Growth, characterization and performance of bulk and nanoengineered molybdenum oxides for electrochemical energy storage and conversion

C.V. Ramana, A. Mauger, C.M. Julien

Growth, characterization and performance of bulk and nanoengineered molybdenum oxides for electrochemical energy storage and conversion

C.V. Ramana[1,2,*], A. Mauger[2], C.M. Julien[2#]

[1]*Center for Advanced Materials Research (CMR), University of Texas at El Paso, El Paso, 500 W University Ave, El Paso, Texas 79968, USA*

2Department of Mechanical Engineering, University of Texas at El Paso, 500 W University Ave, El Paso, Texas 79968, USA

[3]*Institut des Minéralogie, de Physique des Matériaux et de Cosmologie (IMPMC), Sorbonne Université, CNRS-UMR 7590, 4 place Jussieu, 75752 Paris, France*

*Corresponding author: rvchintalapalle@utep.edu (C.V.R.)

#Corresponidng author: christian.julien@sorbonne-universite.fr (C.M.J)

Keywords: Molybdenum oxides; Nanostructures; Cathodes; Anodes; Lithium-ion batteries; Sodium-ion batteries; Intercalation; Conversion

Abstract

Molybdenum oxides (MoO_y) exhibit quite interesting structural, chemical, electrical, optical and electrochemical properties, which are often dependent on the synthetic procedures and fabrication conditions. While these oxides show promise in a diverse applications ranging from electronics to energy storage and micromechanics, engineering the phase and microstructure is the key to achieving the desired properties and performance, especially in electrochemical energy storage and conversion technologies. In the course of development of lithium batteries delivering high-power and high-energy density for powering electric vehicles, here in this paper, we examine the performances of Mo-oxides, which are candidates as electrodes materials primarily for lithium-ion batteries (LIBs), while some aspects considered in sodium-ion batteries (SIBs) or electrochemical supercapacitors (ECs). Due to the wide range of oxidation states (from +6 to +2) they are promising as both positive (cathode) and negative (anode) electrodes of electrochemical cells. Based on their specific structural, chemical, electrical, and optical properties, which are dependent on the growth conditions and the fabrication technique, this review highlights the progress in improving and understanding the electrochemical performance of MoO_y compounds. Various materials ($2.0 \leq y \leq 3.0$) including anhydrous, hydrates, nanorods, nanobelts, composites and thin films of MoO_y are considered. Due to their higher oxidation states, MoO_y have been shown to undergo reversible topotactic lithium intercalation reactions; however, electrochemical features appear strongly dependent on the crystal quality and structural arrangement in the host lattice. Several structural characteristics such as in-situ and ex-situ X-ray diffraction (XRD) patterns, Raman spectra are also presented. The approaches used for performance improvement are summarized, and the causes of first-cycle irreversible capacity loss are discussed in detail. Several sub-stoichiometric MoO_y positive electrodes exhibit excellent cycle life (up to 300 cycles) with high initial coulombic efficiency (80–90%) and large reversible capacity (>300 mAh g^{-1}). Molybdenum oxides also categorized as one of the conversion-type transition-metal oxides and applied as negative electrodes for LIBs and SIBs with a specific capacity approaching 1000 mAh g^{-1}. In addition to the discussion of the key aspects of crystal growth, characterization, and structure-property relationships, the future prospects to design Mo-oxide materials to enhance the structural stability and electrochemical performance are presented.

1. Introduction

Nowadays, a great deal of efforts directed towards the green and sustainable energy development in view of the concerns about climate change and global warming. The major contribution comes from human activities for the energy conversion, especially the fossil fuel combustion for electricity, heat and transportation. The fossil fuels consumption for energy production and transporation presumably result in the emission of green-house gases and subsequently causes the global warming effects. Converting global energy consumption through electrification of alternative forms of transportation requires the use of efficient power sources, with an emphasis on hybrid electric (HEVs), plug-in hybrid electric (PHEVs) and fully electric vehicles (EVs) [1]. Other current applications concern batteries used to solve the intermittence problems of the electricity produced by wind or photovoltaic plants, more and more developed as renewable energy sources, and considered as the only solution to give access of electricity to the sub-Saharan countries in Africa, for example. Moreover, economics and environmental incentives, as well as advances in electricity production via renewable intermittent sources are reshaping the traditional distribution network (smart grid environment, vehicle-to-grid (V2G) infrastructure) [2]. High energy density lithium ion batteries (LIBs) and sodium ion batteries (SIBs) are suitable storage systems for such applications.

The concept of LIB (often called a 'rocking-chair battery') was first formulated by Armand in the late 1970s [3]. In a LIB, the lithium ion moved reversibly between the positive and the negative electrode as intercalation materials of different potentials. This important principle was experimentally established by Lazzari and Scrosati over 60 cycles and implemented with a lithiated WO_2 anode and a TiS_2 cathode, which operate in the potential range 0.8-2.1 volts [4]. In 1991, Sony Corporation announced the first commercialization of a LIB, which consisted of lithium cobaltate $LiCoO_2$ (LCO) as positive electrode and carbon (graphite) as negative electrode in between of which a separator soaked with an organic electrolyte (ionic conductor) [5]. Depending on the choice of the electrodes, the volumetric energy density of LIBs is in the range of 200–350 Wh L^{-1} and on average the gravimetric density is 150 Wh kg^{-1}. However, two critical issues need to be addressed: performance and safety [6]; also, significant improvements of LIBs must be achieved for vehicular applications in both energy density and rate capability. For an analysis of the LIBs deficiencies and possible remedies, see the report by Blomgren [7]. Briefly, the main deficiencies are: (i) low capacity density of the carbonaceous anode, (ii) formation of a resistive solid-electrolyte interphase (SEI), (iii) low specific capacity of the cathode and (iv) limiting cycle life due to the cathode-electrolyte interphase (CEI). Thus, the replacement with new anode and/or cathode materials is needed that could provide high

coulombic efficiency (CE), good power capability, low irreversible capacity, and low cost with little or no loss of capacity density or cell voltage. Due to its disadvantages of high price, cobalt toxicity and a rather small capacity (≈140 mAh g^{-1}) LCO cannot be used as power supply for EVs. The energy density E must satisfy the relation $E = QV$, which imposes high operating cell voltage (V) and large stored capacity (Q) delivered to loads. According to the Faraday law ($Q = nF/M_w$), the capacity is determined by the number of transferred electrons (n) and the molar weight of the active electrode material (M_w). Since, for safety and energetic reasons discussed elsewhere [8], the most feasible methods involve an increase of the capacity and working voltage of the cathode and to avoid the use of graphite as an anode.

Among the transition-metal oxides (TMOs) of diverse compositions and morphological architectures, the various compounds with two- and tri-dimensional structures have been intensively investigated as cathode and anode materials. Molybdenum (Mo) oxides are among those TMOs. Micro- and nano-structured molybdenum oxides (MoO_y) with $2.0 \leq y \leq 3.0$ have shown to be attractive materials in early applications [8]. For example, in 1980s, taking advantages of the superior electrochromic response of MoO_3 to the other materials, General Motors introduced a rear-view electrochromic mirror in Cadillac cars based on MoO_3 [9,10]. MoO_3 is not only a candidate material for energy storage, batteries and supercapacitors [11-14], but also have potential applications in the fields of display devices [15], gas sensors [16-19], electrochromics [20-22], lubricants [23], field-emission-devices [24], organic solar cells [25], organic-light-emitting-diode (OLED) devices [26]. MoO_3 also serves as a precursor for preparing a wide variety of nanomaterials indetended for specific electronic and optoelectronic applications [27-29]. Moreover, MoO_y are important compounds in selective oxidation catalysis [30-32]. MoO_y materials are used industrially as catalysts for partial oxidation of hydrocarbons to carbon acids, selective catalytic reduction of NO_y, production of acrylonitrile, fabrication of acrylic acid and for olefin metathesis reactions [33].

In addition to diverse crystallography and structural features, Mo-oxides posesses interesting electronic structure. With respect to electronic structure, the Mo-oxide phases can be arranged into five groups:

(i) The strictly stoichiometric anhydrous MoO_3 polymorphs (α-, β- and ε-phases), which are nearly insulators (with an unfilled 4d band).

(ii) The nearly-stoichiometric α-$MoO_{3-\delta}$ (with $\delta < 0.03$), which retains the orthorhombic symmetry of α-MoO_3. This set of materials are unintentionally n-type semiconductors at ambient conditions, partly due to intrinsic point defects related to oxygen vacancies (V_O) and molybdenum interstitials (Mo_i) [34].

(iii) The defective $MoO_{3-\delta}$ (with $0.03 < \delta < 0.11$).

(iv) Mo_nO_{3n-1} suboxides (Magnéli phases, n = 4–9), which collapse into ReO_3-type structures with crystallographic shear planes due to the destabilization of the MoO_3 structure by the loss of oxygen [35-40].

(v) The hydrated $MoO_3 \cdot nH_2O$ phases [41].

This review is focused on key issues and trends in research on the material science aspects of a variety of Mo-oxides (MoO_3, MoO_y, Mo_nO_{3n-1}, $MoO_3 \cdot nH_2O$, MoO_2) used in many advanced systems for energy storage and conversion with a special emphasis toward the compounds that are candidates as positive or negative electrodes in rechargeable lithium and sodium batteries. One of the most interesting properties of MoO_y compounds is their intercalation ability, which is possible only if the bonding between the layers or tunnels of the host materials is weak. This technique has been applied to develop nanohybrids and widely used in electrochemical devices and displays because the layered structure facilitates the formation of Mo(VI)/Mo(V) couple [42]. With the realized property enhancements originating from the incorporation of conducting polymers into layered inorganic hosts, interest in MoO_3 nanocomposites have attracted great interest. Various combinations of electronic and/or ionic conductive polymers and MoO_3 have been explored, requiring a wide variety of synthetic methods to effect inclusion of the polymer in the interlamellar gap of the host material [43]. Thus, based on this brief overview, it is very clear that the fundamental understanding of the crystal growth, chemical bonding, structural quality, morphology, surface chemistry, electronic properties of Mo-oxides is critical to tune the synthetic conditions and procedures so as to obtain materials with enhanced electrochemical perfromance. Furthermore, a deeper understanding of the Mo-oxides from a fundamental scientific perspective will enable even design materials with unexpected properties and phenomena, which might be useful for integration into other future applications. Therefore, the synthesis, structural and electrochemical properties of Mo-oxides are thoroughly examined.

This paper is organized as follows. Section 2 is devoted to the properties of anhydrous MoO_3 phases including nanomaterials and MoO_3 used as cathode and anode materials in rechargeable batteries. In Section 3, we expose the properties of $MoO_3 \cdot nH_2O$ hydrates and their derivative products. The non-stoichiometric MoO_y and oxygen deficient molybdenum oxides Mo_nO_{3n-1} are evaluated in Section 4. Finally, Section 5 is devoted to the electrochemical features of MoO_2 used as anode in lithium and sodium batteries. In the very section (conclusions), for completeness, a very short panel devoted to discuss the limit of performance of Mo oxides.

2. Anhydrous molybdenum trioxides

Anhydrous molybdenum trioxides have six polytypic forms. At ambient conditions the thermodynamically stable phase is orthorhombic (α-MoO_3), while hexagonal (*h*-MoO_3) and monoclinic (β -MoO_3, β'-MoO_3, ε-MoO_3 (MoO_3-II) and MoO_3-III) are metastable phases [44]. The crystallographic parameters of anhydrous MoO_3 polymorphs are listed in **Table 1**.

Table 1. Crystallographic parameters of the anhydrous molybdenum trioxides.

Compound	Space group	Cell parameters (Å)			Réf.
		a/α	*b*/ß	*c*/γ	
α-MoO_3	*Pbnm*	3.962	13.850	3.696	[45]
β-MoO_3	*P2₁/n*	7.118	5.366/91.99°	5.568	[46]
β'-MoO_3	*P*2₁/*n*	7.424	7.478/90.09°	7.689	[47]
h-MoO_3	*P*6₃/*m*	10.57	-	3.72	[48]
ε-MoO_3	*P*2₁/*m*	3.954	3.687/103.75°	7.095	[49]

2.1. Orthorhombic α-MoO_3

Molybdenum trioxide exists as mineral *molybdite* (molar mass 143.94 g mol^{-1}, density 4.70 g cm^{-3}, melting point 802 °C).

2.1.1. Brief history

It was Carl Wilhem Scheele who, in 1778, identified molybdenum by separation from lead and isolated the oxide MoO_3 and the molybdenite, MoS_2. In 1861, Adolf Nordenskiold synthesized a MoO_3 crystal by sublimation of ammonium molybdate and determined the crystal axial ratio as *a*:*b*:*c* = 0.3872:1:0.4792. In 1931, it was Haakon Bräkken and Nora Wooster, who reported the crystal structure of MoO_3; the works carried out independently obtained fairly similar results [50,51]; a new axial ratio of 0.282:1:0.265 was determined by X-ray measurements. In 1940s, the Uppsala's group, by means of X-ray methods, revised the crystallographic structure of all forms of molybdenum oxides [52]. In 1950, Oskar Glemser published a series of papers on Mo oxides investigated by X-ray powder technique and electrical resistivity measurements [53]; they also formulated a series of molybdenum oxide hydroxides [54]. Since 1956, MoO_3 has been the subject of numerous studies as a host structure for the intercalation of various atoms or molecules, which lead in particular to molybdenum

bronzes H_xMoO_3 [55]. Since then, a large number of works were devoted to the study of insertion in aqueous environments and in H_2SO_4 [56]. In the 1960s, Morehouse Glicksman [57] investigated the discharge characteristics of MoO_3 in strongly alkaline aqueous electrolyte. In the 1970s, several attempts made to use MoO_3 as a battery electrode [58-60]. The electrochemical behavior of MoO_3 as positive electrode material in organic solvent lithium batteries was investigated for the first time by Campanella and Pistoia [58,59], who recognized the poor solubility of MoO_3 in aprotic solvent and reported the open circuit voltages (OCV) of the Li(s)|Li^+(nonaqueous solvent|MoO_3(s) of ~2.8 V. Further, during the early years of lithium battery research, MoO_3 was actively investigated as lithium insertion compound [42,61-65]. In 1974, the growing interest in lithium anode batteries has led to studies on the properties of MoO_3 in an aprotic medium [66,67]. The lithiated phase of MoO_3 was synthesized both by reaction of n-butyllithium and electrochemically. The maximum *x* value in Li_xMoO_3 obtained by chemical lithiation is 1.55 [62]. Besenhard and Schöllhorn [61] investigated the charge and discharge process of Li//MoO_3 cells using different aprotic electrolytes and have shown the process to be a reversible "*topotactic*" redox reaction to form the ternary phase Li_xMoO_3, which exhibits an increase of the interlayer spacing of ~1 Å. The term "topotactic" refers to solid-state reactions, which are characterized by the fact that defined lattice matrix elements specific to the original solid phase remain unaltered in the course of the reaction with respect to their structural architecture [68]. The Hagenmuller's group reported that the high-temperature lithium molybdenum bronzes monoclinic Li_xMoO_3 ($0.31 \leq x \leq 0.39$ at 560 °C) and $Li_xMo_6O_{17}$ (x= 0.9 display structures different than that of α-MoO_3 itself [69].

2.1.2. Structure

Of the anhydrous MoO_3 polymorphs, the orthorhombic α-MoO_3 phase is the stable form at room temperature and possesses a 2D layered structure [70]. The α-phase MoO_3 can be represented as the double layers of linked distorted MoO_6 octahedra parallel to (010) planes (**Fig. 1**). In each double layer MoO_6 octahedra form edge sharing zigzag rows along the (001) direction and corner haring rows along the (100) direction. Successive layers are held together by weak interlayer forces with an easy cleavage along the (010) planes (**Fig. 1a**). The octahedral coordination of Mo with O characterizes the geometrical structure of MoO_3 with Mo surrounded by four close neighbor O atoms at distances of 1.95, 1.95, 1.73, and 1.67 Å and two O atoms at significantly longer distances of 2.25 and 2.33 Å. These values indicate that the MoO_6 octahedra are distorted and three different types of oxygen neighbors are present in the coordination sphere of Mo. They are termed as terminal (non-bridging) O(1), bridging O(2),

and chain oxygens O(3) (see **Fig. 1c**). The terminal oxygen O(1) is doubly bound to a single Mo at a short bond length of 1.67 Å. O(2) is two-fold coordinated and the Mo–O bonds with bond lengths of 1.79 and 2.25 Å characterize the bridging oxygen located asymmetrically between two Mo centers. The symmetric bridging oxygen O(3) is bound to three Mo atoms, with two equivalent Mo–O bonds (1.94 Å) and a longer Mo–O bond (2.33 Å) [35]. The large work function of MoO_3 of 6.6 eV is due to its closed shell character and the dipole layer created by planes of terminal O(1) oxygen sites which lower the electrostatic potential of the inner Mo-O units. These O(1) sites arise from the high stoichiometry of MoO_3. The oxygen vacancy is most stable at the 2-fold O(2) site. It is a shallow donor and has a small formation energy in the O poor limit so that MoO_3 easily becomes a degenerate semiconductor [71,72]. **Figure 1d** displays the XRD pattern of the layered α-MoO_3 showing fingerprints at 2θ = 12.7°, 23.3°, 25.6°, 27.2°, and 38.9°, which correspond to the (020), (110), (040), (0.21) and (060) planes (JCPDS card no. 05-0508, S.G.), and crystallizes in the unique orthorhombic crystal structure (space group *Pbnm*) with lattice unit-cell constants a = 3.962 Å, b = 13.858 Å and c = 3.697 Å. Unit cell parameters of α-MoO_3 investigated through 80 years are given in **Table 2**. [45,52,73].

Table 2. Unit cell parameters of α-MoO_3 (*Pbnm* S.G.) through 80 years.

Authors (year)	a (Å)	b (Å)	c (Å)	V (Å)^3	Ref.
Bräkken (1931)	3.962	13.855	3.701	203.1	[73]
Wooster (1931)	3.93	13.97	3.67	201	[74]
Magnéli (1950)	3.966	13.85	3.696	203.0	[52]
Kilborg (1963)	3.9628	13.855	3.6964	202.9	[45]
Sitepu (2005)	3.9621(7)	13.855(1)	3.6986(4)	203.0	[75]

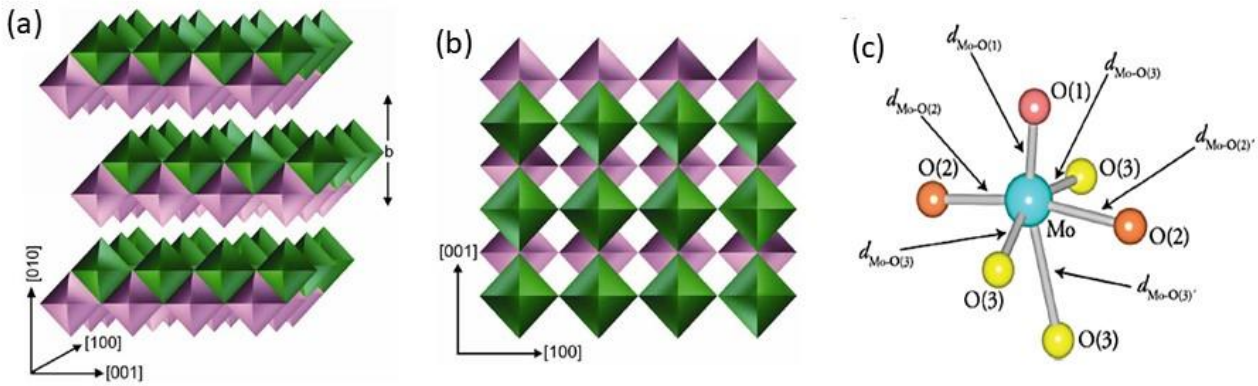

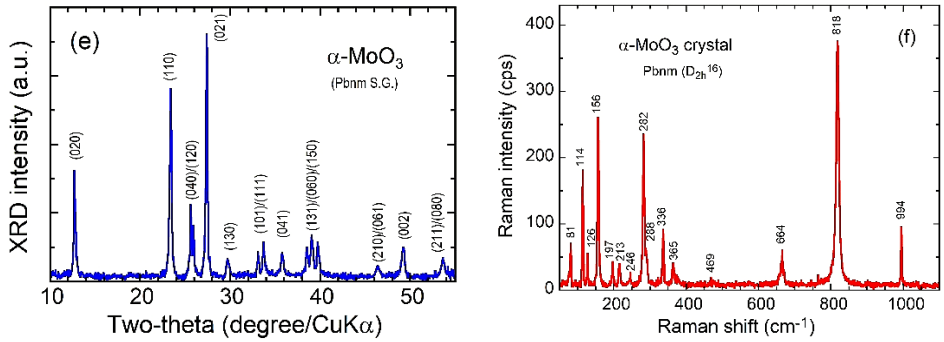

Fig. 1. Structural model for MoO_3 α-phase (a) The unit cell includes four formula units located on double-layer slabs along the (010) direction. (b) The (010) projection of an individual double-layer. (c) The three different types of oxygen neighbors present in the coordination sphere of molybdenum. The Mo-O framework consists of MoO_6 octahedra sharing edges (O2-O2'). (d) XRD pattern of orthorhombic α-MoO_3 (white crystal). (e) Raman spectrum recorded with the excitation laser line λ = 532 nm.

The local structure was investigated using Raman scattering (RS) and Fourier transform infrared (FTIR) spectroscopy, which are effective tools to study the structure of crystalline, disordered and amorphous substances. The vibrational spectrum of a molecule, as observed in Raman studies, is the direct manifestation of forces arising from mutual interactions of electrons and nuclei and the RS spectrum can be analysed in terms of internal and external mode. Thus, from the observed mode frequencies, we can glean information about the force constants which hopefully can then be correlated with electronic structure and bonding theories. Several reports have been devoted to the study of vibrational features of MoO_y materials [41,76-80]. **Figure 1f** shows the RS spectrum of crystalline α-MoO_3. The observed bands are assigned according to the single crystal model of Py and Masche [76]. The Raman spectrum of α-MoO_3 single crystal has characteristic bands at 996 cm^{-1} (A_g, ν_{as} M=O stretch), 823 cm^{-1} (A_g, ν_s M=O stretch), 667 cm^{-1} (B_{2g}, B_{3g}, ν_{as} O–M–O stretch), 473 cm^{-1} (A_g, ν_{as} O–M–O stretch and bend), 380 cm^{-1} (B_{1g}, δ O–M–O scissor), 376 (B_{1g}), 366 cm^{-1} (A_{1g}, δ O–M–O scissor), 334 cm^{-1} (A_g, B_{1g}, δ O–M–O bend), 293 cm^{-1} (B_{3g}, δ O=M=O wagging), 285 cm^{-1} (B_{2g}, δ O=M=O wagging), 247 cm^{-1} (B_{3g}, τ O=Mo=O twist), 216 cm^{-1} (A_g, rotational rigid MoO_4 chain mode, R_c), 197 cm^{-1} (B_{2g}, τ O=Mo=O twist), 159 cm^{-1} (A_g/B_{1g}, translational rigid MoO_4 chain mode, T_b), 129 cm^{-1} (B_{3g}, translational rigid MoO_4 chain mode, T_c), 116 cm^{-1} (B_{2g}, translational rigid MoO_4 chain mode, T_c), 100 cm^{-1} (B_{2g}, translational rigid MoO_4 chain mode, T_a) and 89 cm^{-1} (A_g, translational rigid MoO_4 chain mode, T_a). The Raman bands at 995 and 823 cm^{-1} are the fingerprints of the symmetrical stretching vibration of the terminal Mo=O bonds along the *a*- and *b*-axes (**Table**

3). The bridging oxygens (longer bond distances) along the *c*-axis are the weakly bound oxygens as shown by Mestl et al. [81]. Due to the stoichiometry deviation within the MoO_y samples variations of the Raman bands of localized vibrations, e.g., the 666, 823 or 995 cm^{-1} bands are expected as a displacement of the Mo atom toward the terminal oxygen in the *b*-direction occurs upon the loss of the bridging oxygen, thus weakening the bond to the terminal O atom along the *a*-axis.

Table 3. Raman vibration modes of nanostructured α-MoO_3. Reproduced with permission from [82]. Copyright 2012 Elsevier.

Modes	**Assignment**	**Raman shift (cm^{-1})**					
		[82]	[44]	[78]	[83]	[84]	[41]
A_g	T_a Translation of rigid MoO_4 chain (T_a)	82	-	89	82	82	83
B_{2g}	T_a Translation of rigid MoO_4 chain (T_a)	98	-	100	-	98	98
B_{2g}	T_c Translation of rigid MoO_4 chain (T_c)	116	116	116	115	114	116
B_{3g}	T_c Translation of rigid MoO_4 chain (T_c)	127	130	129	129	128	128
A_g/B_{1g}	δ $(O_2Mo_2)_n$	159	157	159	158	157	156
B_{2g}	δ O_2—Mo—O_2 scissoring	196	198	197	198	197	198
A_g	δ O_2—Mo—O_2 scissoring	218	217	216	216	216	218
B_{3g}	δ O_2—Mo—O_2 scissoring	245	246	247	246	244	246
B_{2g}	δ O_1=Mo=O_1 wagging	283	284	285	284	282	286
B_{3g}	δ O_1=Mo=O_1 wagging	292	291	293	-	-	291
A_g/B_{1g}	δ O_3—Mo—O_3 bending	338	338	334	336	336	338
A_g	δ O_2=Mo=O_2 scissoring	365	365	366	365	365	366
B_{1g}	δ O_2=Mo=O_2 scissoring	379	378	376	379	377	380
A_g	ν_{as} Mo—O_2—Mo bending	471	471	473	-	469	472
B_{2g}/B_{3g}	ν_{as} Mo—O_2—Mo stretching	664	667	667	666	666	666
A_g	ν_s Mo—O_3—Mo stretching	816	817	823	819	818	820
A_g	ν_{as} Mo=O_1 stretching	992	996	996	996	994	996

2.1.3. Synthesis

A variety of synthesis routes have been developed for the preparation of MoO_y materials to control their structure and morphology. They include solid state reaction [85], wet-chemical synthesis [86], sol-gel route [20], precipitation [87], thermal oxidation [88], thermal evaporation [83], flame synthesis process [89], hot-plate method [90], mechanochemical technique [91], electrodeposition [92], electrospinning technique [93,94], solvothermal method [95], spray pyrolysis [96-98], spin coating [99], and template synthesis [100]. Synthesis techniques are briefly reviewed in this section; for a complete view see Ref. [101]. Most of crystallized MoO_y were easily fabricated by heat treatment of either molybdic acid powders (H_4MoO_4) or synthetic hydrated molybdenum trioxide ($MoO_3 \cdot nH_2O$) [102,103].

Different hydrothermal techniques were utilized to grow α-MoO_3 crystals (see **Table 4**) [104-107]. Various raw materials are commonly used including Mo metal powders, acid molybdic (H_4MoO_4), ammonium molybdate ($(NH_4)_2MoO_4$), ammonium molybdate tetrahydrate ($(NH_4)_6Mo_7O_{24}\cdot 4H_2O$), and sodium molybdate (Na_2MoO_4). Zhou et al. [108] fabricated flexible single crystalline nanobelts with widths of 200-500 nm, lengths of 5-10 μm, and thicknesses of ~50 nm via hydrothermal treatment at 180 °C for 24 h of a peroxomolybdic acid solution prepared by reaction of H_2O_2 with Mo metal powders. Li et al. [93] prepared MoO_3 nanofibers (diameter of 200 nm) by a combination method of sol–gel process and electrospinning technique using $(NH_4)_6Mo_7O_{24}\cdot 4H_2O$ with the molar ratio of 1/1.28 dissolved in dilute nitric acid and then mixed with a water–ethanol (v/v 1:4) solution containing citric acid as a chelating agent for the metal ions. Subba-Reddy et al. [106] constructed nanobelts (1–5 µm in length and 100–600 nm in diameter) by hydrothermal method using $MoO_3\cdot nH_2O$ sols prepared by ion exchange of ammonium heptamolybdate tetrahydrate through a proton exchange resin. After ion exchange, a clear light-blue MoO_3 sol (pH ≈ 2.0) was obtained and modified with poly(ethylene glycol) (PEG). Nanocrystalline MoO_3 was synthesized by a sol-gel method using ammonium molybdate tetrahydrate citric acid (CA) as chelating agent with the metal/CA ratio of 1:1 under neutral pH [109]. Pure MoO_3 was obtained by calcination of dried precursor at 500 °C for 5 h in air, while Mo_nO_{3n-1}/C composite was formed under argon atmosphere (**Fig. 2**).

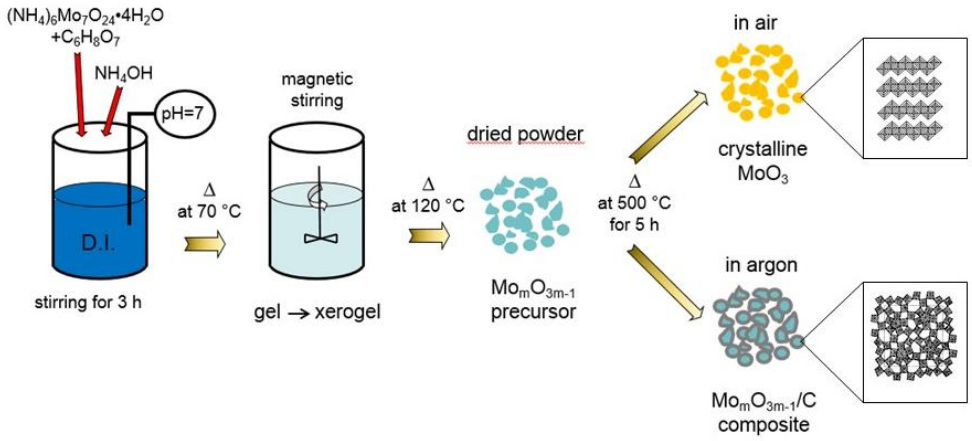

Fig. 2. Overall synthesis process of the crystalline MoO_3 and Mo_mO_{3m-1}/C composite. Copyright Hashem et al. [109]. Copyright 2020 Hashem et al. Under Creative Commons Attribution (CC BY) license.

Table 4. Synthesis of α-MoO_3 through different hydrothermal routes.

Raw material	Additive	Conditions	Ref.
commercial MoO_3 bulk	CTAB [a)]	180 °C/4 days	[110]
Mo metal powders	$H_2C_2O_4{\cdot}2H_2O$	180 °C/5 days	[111]
Na_2MoO_4	0.2 mmol HCl	160 °C/20 h	[112]
$(NH_4)_6Mo_7O_{24}{\cdot}4H_2O$	HNO_3 (pH=4.5-9-6)	140-220 °C/5-62 h	[105]
$(Mo(NO)(NH_2O))^{2+}$	HNO_3	220 °C/7-24 h	[113]
Mo metal powders	H_2O_2	180 °C/24 h	[108]
Na_2MoO_4	4 mmol L^{-1} $HClO_4$	140 °C/24 h	[114]
$Na_2MoO_4{\cdot}2H_2O$	3-diaminopropane	120 °C/48 h	[115]
$Na_2MoO_4{\cdot}2H_2O$	NaCl + GO	180 °C/24 h	[116]
H_2MoO_4	HNO_3/H_2O_2 (1:5 v/v)	120-180 °C/6 h	[117]
MoO_2 powders	H_2O_2	180 °C/10 h	[118]
$MoO_3{\cdot}nH_2O$ sols	poly(ethylene glycol)	180 °C/4 days	[106]

[a)] cetyltrimethylammonium bromide.

The procedure developed by Jiao et al. [119] consists in the wet-chemical synthesis using an ammonium molybdate tetrahydrate solution adjusted at pH = 3.5 with diluted glacial acetic acid with subsequent sintering at 600 °C for 24 h. The conversion of isopolymolybdate anions $Mo_7O_{24}^{6-}$ to neutral Mo_7O_{21} (or α-MoO_3) occurs by combining excess oxygen in $Mo_7O_{24}^{6-}$ with protons from the acidic medium:

$$Mo_7O_{24}^{6-} + 6H^+ \rightarrow 7MoO_3 + 3H_2O. \qquad (1)$$

Chiang et al. [120] investigated the precipitation route using the mixture of an ammonium molybdate tetrahydrate solution with ethylene glycol (dark blue solution), which precipitates after centrifugation and heating at 80 °C for 24 h (white powder). In a typical solid-state reaction, α-MoO_3 crystals obtained from the decomposition of H_4MoO_4 raw powders loaded into porcelain crucibles and positioned in a multi-zone tube furnace with a 300 cm^3 min^{-1} argon flow. After 2-h purge, the furnace temperature is ramped from room temperature to the desired heat-treatment temperature over a 1-h period. This thermal treatment maintained at 750 °C for 2 h provides well-crystallized specimens [121]. **Figure 3** shows the SEM images of samples produced by heat treatment of molybdic acid at temperature $400 \leq T_a \leq 800$ °C. Hydrates contain $MoO_5(H_2O)$ octahedral units, while they are intercalated by water molecules in $MoO_3{\cdot}2H_2O$. During the topotactic dehydration process, the intercalated water is lost first, then neighbouring sheets condense giving the double sheets of the anhydrous MoO_3 phase as the final water is lost (see sketch of **Fig. 4a**). TG and DTA curves of the oxide-hydrate of molybdenum $MoO_3{\cdot}2H_2O$ shown in **Fig. 4b** exhibit four endothermic peaks at annealing temperature (T_a) of 120, 198, 246, and 325 °C corresponding to the various steps for water removal via the formation of the intermediate α-$MoO_3{\cdot}H_2O$. **Figure 4c** presents the XRD patterns of oxide-hydrates heat-treated

in the temperature range 75-800 °C. The phase α-MoO_3 appears after a thermal treatment of the molybdic acid above 750 °C in air. FTIR spectra of $MoO_3 \cdot nH_2O$ (n<l) shows the spectral features of the layered α-$MoO_3 \cdot H_2O$ phase for $T_a \approx 280$ °C. Note the disappearance of the OH stretching mode (3400 cm^{-1}) for T_a>250 °C (**Fig. 4d**). The low-temperature synthesis of MoO_3 nanobelts (15 nm thick) was based on the preparation of $MoO_3 \cdot H_2O$ solution (i.e., colorless solution obtained by dissolution of 20 mmol Na_2MoO_4 in distilled water added with 4 mol L^{-1}perchloric acid and subsequent treatment of a hydrothermal reaction [114].

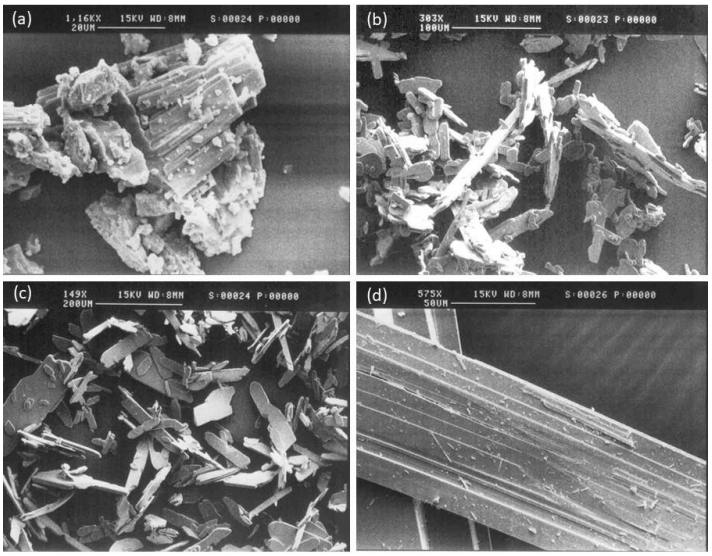

Fig. 3. SEM images of samples produced by heat treatment of $MoO_3 \cdot 2H_2O$ hydrate at (a) 400, (b) 600, (c) 750 and (d) 800 °C. The latter sample is the well crystallized α-MoO_3 phase, which displays the typical elongated shape the layered structure (edge of the platelet).

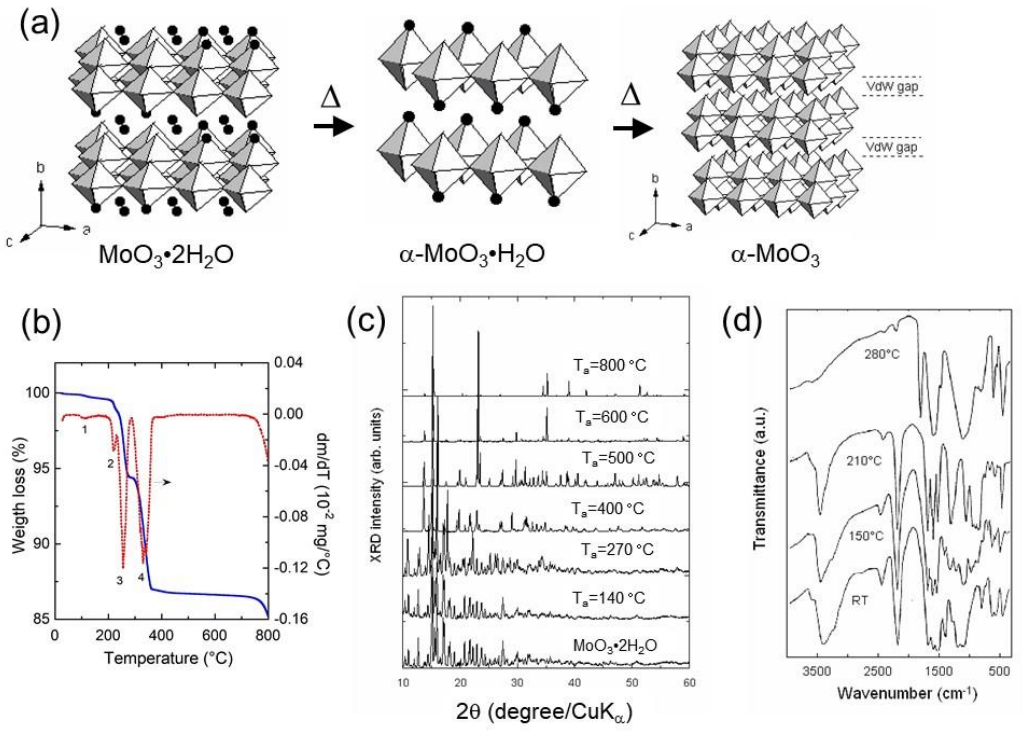

Fig. 4. (a) Sketch of the structural evolution upon heat-treatment of the hydrated $MoO_3 \cdot 2H_2O$ precursor to form α-MoO_3 via the intermediate α-$MoO_3 \cdot H_2O$ phase. (b) TG and DTA curves for oxide-hydrate of molybdenum. The DTA curve exhibits four endothermic peaks at 120, 198, 246, and 325 °C corresponding to the various steps for water removal. (c) X-ray diffraction patterns of oxide-hydrates of molybdenum heat-treated at various temperature in the range 75-600 °C. The phase α-MoO_3 appears after a thermal treatment of the molybdic acid above 750 °C in air. (d) FTIR spectra of dehydrated $MoO_3 \cdot nH_2O$ (n<l). Spectral responses are more complex than that of crystalline MoO_3, but they can be discussed in terms of internal and external modes as usual for oxide lattices.

2.1.4. MoO_3 nanostructures

One major reason for the use of nanosized particles of materials for energy storage comes from their poor transport properties that imply poor rate performance of the electrochemical devices. This is the case for MoO_3 used as electrodes in batteries and supercapacitors. As the electronic conductivity of MoO_3 is $\approx 10^{-8}$ $S \cdot cm^{-1}$ at room temperature, it requires some sophisticated technology such as the use of slurry containing a huge quantity of carbon (carbon "Super P", acetylene black, amorphous carbon, etc.) or deposition at the surface of the grains for enhanced charge carrier transport [122-126]. Achieving high-rate capability depends ultimately on the geometry of the active objects building the positive and negative electrodes.

As the performance of an electrode is governed by the transport of both electrons and ions, the ionic and electronic conductivity of the materials must be considered. For a diffusion process, the characteristic time τ for ionic species *i* (in practice Li^+ or Na^+ ions in the present case) to reach the surface of any active particle of dimension *L* is given by the second Fick's law that applies the chemical diffusion coefficient with D_{Li}^* of moving ions [127]. In the case when the chemical reaction proceeds by a single-phase process, i.e., within a solid solution, τ is given by $\tau = L^2/4\pi D_{Li}^*$. Moreover, decreasing the size of MoO_3 particles is an efficient strategy to mitigate the volume variation of the electrode during Li ions intercalation and deintercalation process. Nanosized MoO_3 particles with different morphologies (**Fig. 5**) include nanoparticles [128], nanobelts [108,129,130], nanowires [131-34], nanofibers [113,135], nanotubes [136-138], nanoflakes [90] and nanoribbons [18]. Designing of porous structure and carbon coating are another most popular strategy to improve the electrochemical performances of MoO_3 [139,140].

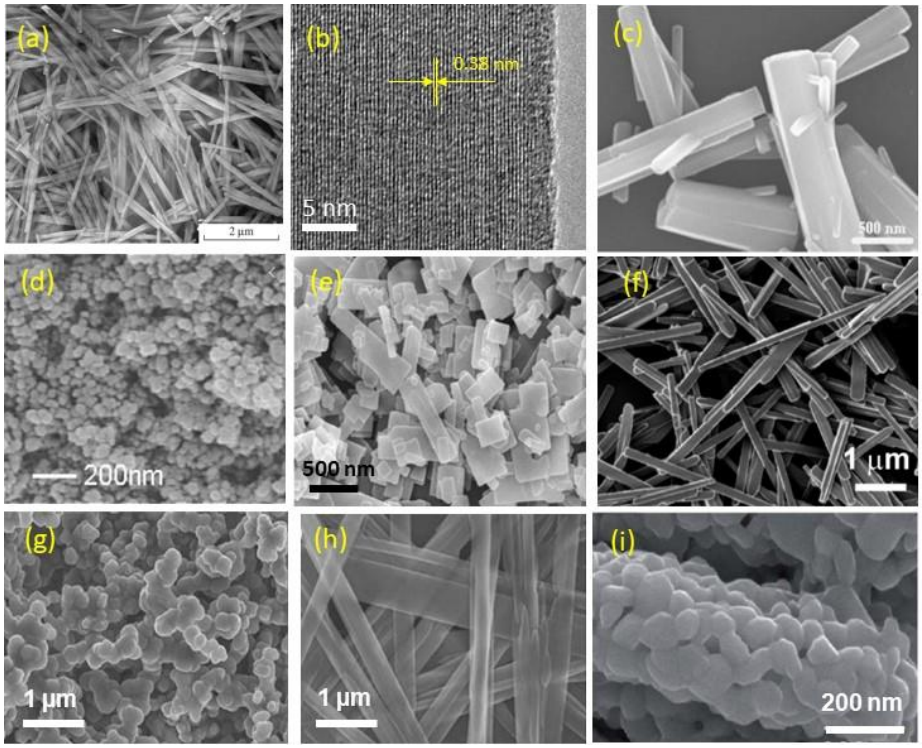

Fig. 5. SEM images of nanostructured a-MoO_3. (a) nanofibers, (b) HRTEM image showing the lattice fringe of 0.38 nm which corresponds to the d_{110} spacing, (c) nanoplatelets, (d) nanospheres, (e) nanoflakes, (f) nanorods, (g) nanosheets, (h) nanoribbons, (i) nanotubes.

2.1.5. MoO_3 thin films

Due to their chromogenic, catalytic properties and ability to host foreign ions, MoO_3 thin films have been applied in electrochromic display devices (see [141] and Refs. therein), optical memory devices [142], gas sensors [17], and lithium microbatteries [143-146]. Currently, there are several approaches available for preparing MoO_3 films with either an amorphous or a polycrystalline structure using physical vapor deposition (PVD) and metal organic chemical vapor deposition (MOCVD) [147] are also used to fabricate MoO_3 in thin film forms. The different techniques include thermal evaporation [148], magnetron sputtering [144,149], chemical vapor deposition [150,151], electrodeposition [152], flash evaporation [153,154], pulsed-laser deposition (PLD) [155-157], electron-beam deposition [158,159], ion-beam deposition [17], sol-gel spin-coating [160,161], and spray pyrolysis [162,163]. Among these methods, magnetron sputtering and pulsed-laser deposition have received considerable attention for industrial purpose because the low temperatures process [164]. MoO_3 films were produced under varying conditions of growth temperature, T_s, and oxygen pressure $p(O_2)$. Analyses indicate that the microstructure of MoO_y thin films is sensitive to growth conditions. For example, RHEED patterns of sputter-deposited Mo oxide films grown at 445 °C with various $p(O_2)$ show that a secondary component phase, i.e., Mo_8O_{23}, is evidenced for films grown at lower $p(O_2)$. Well-textured MoO_3 film without secondary phases is obtained for $p(O_2)$=62.3% [165]. FTIR spectra of PLD MoO_3 films grown at different T_s show that the broad infrared absorption band in the region of 500–1000 cm^{-1} starts to be resolved into strong absorption peaks at around 570, 625, 700, 840, and 985 cm^{-1} at T_s > 200 °C [157], indicating the pure α-MoO_3 phase. In addition, the splitting of IR active mode at 900–1010 cm^{-1} is evidenced for well-crystallized film. X-ray photoelectron spectroscopy (XPS) is also a sensitive tool to evaluated the local environment: (i) the XPS Mo 3d core level spectra evidence the reduction of Mo^{6+} ions to Mo^{5+} ions in non-stoichiometric film and (ii) the broadening of the Mo 3d core level peaks is assigned to the distortion of the oxide matrix [166].

To fabricate nanoscopic MoO_3, methods like template-directed reaction of molybdic acid and the subsequent leaching process [167], and templating against carbon nanotubes have been attempted [168]. Polycrystalline MoO_3 thin films have been prepared by oxidation at high temperature of molybdenum compound layers deposited by chemical vapour deposition (CVD) from molybdenum hexacarbonyl $Mo(CO)_6$ [169].

The main parameter for a thin film microbattery is the delivered gravimetric capacity. Rather than being expressed as the conventional unit of $mAh \cdot g^{-1}$, due to the uncertainty in the film density, technologists prefer the stored charge, Q expressed in µAh or in coulomb, per film surface area and the film thickness, i.e., $\mu Ah \cdot cm^{-2}\ \mu m^{-1}$ or $mC \cdot cm^{-2}\ \mu m^{-1}$. The relation

between the gravimetric capacity, Q_m, of the material and the volumetric capacity of a film, Q_f, is given by:

$$Q_f = 0.36\, d\, Q_m, \qquad (2)$$

where Q_f is expressed in mC·cm^{-2} µm^{-1}, Q_m in mAh·g^{-1}, and d is the density of the material in g·cm^{-3}. Considering the accommodation of 1.5Li per mole of MoO_3, yielding a gravimetric capacity of 280 mAh·g^{-1}, the capacity of a dense film can reach the value of ≈130 µAh·cm^{-2}·µm^{-1}. For certain applications, high-quality films grown by PLD are required. Currently, PLD MoO_3 thin films are grown using a KrF excimer laser (λ = 248 nm) with a fluence of 2 J cm^{-2} (energy of 300 mJ per pulse) and deposited on various substrates heated in the range of $25 \leq T_s \leq 500$ °C under an atmosphere of O_2 flow maintained at a pressure of $0.1 \leq p(O_2) \leq 20$ Pa. In the prior report, Julien et al. showed that the structure analyzed by optical spectroscopy strongly depends on T_s. For T_s < 150 °C, an amorphous phase is formed, the β-MoO_3 monoclinic phase grows at $T_s \approx 200$ °C, and the layered α-MoO_3 orthorhombic phase appears at T_s = 300 °C [170-172]. Al-Kuhaili et al. reported the growth of polycrystalline MoO_3 films on unheated substrates using both XeF and KrF excimer lasers. By tuning the annealing temperature in the range of 300 to 500 °C, both the grain size and surface roughness increased. Films formed using the XeF laser (λ = 351 nm) and annealed at 400 °C have the best stoichiometry of $MoO_{2.95}$ [155]. Analyzing the growth mechanism, Ramana and Julien concluded that the thermochemical reaction during ablation strongly influences the structural characteristics of PLD MoO_3 films. Above T_s = 400 °C, the formation of compositional defects induces structural disorder, i.e., α-β-$MoO_{3-\delta}$ phase mixture [165,173].

The applicability of MoO_3 films as cathode component in Li//MoO_3 microbatteries was demonstrated by the best electrochemical features. Early works have been reviewed by Julien et al. [174,175]. Assuming fully dense MoO_3 films, a theoretical specific capacity ~130 µAh cm^{-2} µm^{-1} is expected compared with 69 µAh cm^{-2} µm^{-1} for $LiCoO_2$. In 1989, Ohtsuka and Yamaki [176] prepared a Li/solid-state electrolyte/$MoO_{3-\delta}$ microbattery by thin film technology, in which the $MoO_{3-\delta}$ cathode film thickness was 1.0 µm. The Li_2O–V_2O_5–SiO_2 thin film electrolyte exhibits a conductivity of 1 × 10^{-4} S cm^{-1} at 25 °C. The Li//$MoO_{3-\delta}$ cell was cycled over 240 times with a capacity of 60 µAh cm^{-2}. In 1994, Julien et al. investigated the influence of the conditions of preparation of MoO_3 thin on their ability to intercalate Li^+ ions have been evaluated [177]. Microbatteries fabricated with cathode films formed at moderate temperature ($T_s \leq 250$ °C) exhibit a monotonous discharge profile but show a strong dependence of the average voltage *vs*. deposition temperature. For T_s =250 °C, the average potential is 2.9 V and the Li uptake is close to 3 Li/Mo. The variation of the cell voltage is generally attributed

to (i) the presence of large crystallites surrounded by amorphous grain boundaries, (ii) the presence of a mixed α-β-phase which may tune the standard potential, and/or (iii) high concentration of oxygen defects in the host structure involving a lower Fermi level in MoO_3 film. An in-depth study of polycrystalline thin films for cathode applications was reported [178]. It was found that the kinetically accessible discharge range was $0 \leq x \leq 1.5$ in Li_xMoO_3 and that the operating potential for the disordered phases was higher than that of the crystal. The OCVs ranged from 3.2–2.5 V and the cells were discharged to 1.5 V vs. Li^+/Li. The chemical diffusion coefficient D_{Li}^* of the crystalline film ranged from 10^{-11}–10^{-12} cm^2 s^{-1} for disordered polycrystalline films with a thermodynamic factor that was approximately two orders of magnitude higher than in MoO_3 crystals. Electrochemical properties of MoO_3 film grown by thermal and flash evaporation have been investigated in cell of 100 µAh capacity [179]. Thermodynamic data show that microbatteries fabricated with films formed at moderate temperature exhibit a monotonous discharge voltage indicating that the Li_xMoO_3 material remains in the single phase even for large degree of intercalation, x. The lithium diffusivity increases with the temperature T_s of preparation of the film and reaches the value of 10^{-11} cm^2 s^{-1} in Li_xMoO_3 for T_s = 250 °C. MoO_y films have been deposited on Ni substrate by rf-sputtering using different flow rate of O_2/Ar mixture ($1.5 \leq \Phi \leq 8.0$ sccm) as sputter gas [180]. Their electrochemical properties appear to be dependent of the oxygen flow rates and the nature of the substrate. At a flow rate of 8.0 sccm, the Li//MoO_y microcell delivers a discharge capacity of 450 µAh cm^{-2} at 5 µA cm^{-2} current density. $\widetilde{D}_{Li}$ increases at least by two orders of magnitude in films grown at high oxygen partial pressure. A value $D_{Li}^* = 2 \times 10^{-12}$ cm^2 s^{-1} is obtained for Φ = 8 sccm. In 2000, Ferreira et al. [181] prepared MoO_y thin films deposited by r.f. reactive sputtering of metallic Mo target in an Ar/O_2 atmosphere. The films with different compositions and crystal structures were obtained by varying the oxygen flow $0.5 \leq \Phi \leq 4.0$. Combined XRD and XPS analyses show that, with the increase of Φ, the microstructures were obtained as: amorphous → ($MoO_{2.8}$ + α-MoO_3) → β-MoO_3 → ($MoO_{2.8}$ + β-MoO_3). The film formed with the β-MoO_3 phase exhibits the best lithium insertion and electrochromism properties.

In 2001, Ohtsuka and Sakurai [144] fabricated an all-solid-state lithium microbattery with thicker cathode layer (4.66 µm) to increase the cell capacity per unit area. The thin film battery architecture deposited on stainless-steel substrate is composed of a thick $MoO_{3-\delta}$ cathode film, Li film anode and Li_2O–V_2O_5–SiO_2 thin film electrolyte. The cathode films (0.49 cm^2 area) with composition Mo_9O_{26} were grown at 100 °C by magnetron sputtering at rf-power of 200 W using a sintering-powdered MoO_3 target in Ar at pressure of Pa. The discharge curves are S-shaped with an average potential of 2.3 V. At discharge current density of 10 mA cm^{-2}, the

battery has discharge capacity of 290 mAh cm^{-2} (56.4 µAh cm^{-2} $µm^{-1}$) at the 40th cycle. Assuming a film of composition Mo_9O_{26} (determined by XRD) with density 4.7 g cm^{-3}, the first discharge capacity is equivalent to 182 mAh g^{-1}.

In 2006, Ramana et al. reported a specific discharge capacity of 90 µAh cm^{-2} $µm^{-1}$ for a PLD α-MoO_3 film deposited at T_s = 400 °C, while only 53 µAh·cm^{-2} $µm^{-1}$ was delivered for T_s = 200 °C [157]. The superiority of MoO_3 cathode material that can be extend the upper limit of rechargeable lithium microbatteries was demonstrated in experiments on lithium thin-film cells fabricated on glass slides [182]. Each cell included a layer of Ti (for adhesion to the glass slide), a patterned layer of Pt that served as a cathode current collector, a cathode layer of MoO_3, a solid electrolyte layer of $Li_{3.3}PO_{3.8}N_{0.22}$ (LiPON), and an anode layer of Li. All the layers were deposited by magnetron sputtering except for the Li layer, which was deposited by thermal evaporation. After 5500 cycles of charge/discharge at a current density of 0.7 mA cm^{-2} the cell operating at temperature 150 °C delivered specific capacity of 140 µAh $cm^{-2}µm^{-1}$, while the cell containing $LiCoO_2$ failed. MoO_3 thin films were prepared by sol-gel process from molybdenum acetylacetonate sol [183]. The films were formed onto silica substrates by spin-coating with subsequent heat treatment at 508 °C for 2 h. SEM images show grains shaping from oval to rod are distributed on the substrates in random orientation. It seems that the size and morphology of micrograins in MoO_3 films depend on the heat treatment temperature, ambient and type of substrates. Comini et al. [184] have obtained needle-like nanoparticles by rf-sputtering technique and continuous planar films with sol-gel method on alumina substrates. Yu and coworkers reported that a porous MoO_3 film prepared by a hydrothermal route and subsequent calcinations in air, delivers a high capacity of 750 mAh g^{-1} at 1C rate, and exhibits long cycle life of 120 cycles with 80 % capacity retention as the anode of LIB [140].

Recently, Moitzheim et al. [185] reviewed the progress toward solid-state 3D thin-film Li-ion microbatteries and discussed the status of the individual components: thin-film cathodes, anodes, and thin-film solid electrolyte. Julien et al. investigated the electrochemical performance of molybdenum-suboxide thin films as anode layers in planar lithium microbatteries [72]. Puppala et al. investigated the microstructure and morphology of PLD MoO_{3-x} thin films' growth for catalytic applications using a femtosecond laser (f-PLD) and a nanosecond excimer-laser (n-PLD). Substantially textured films with a partially crystalline phase prior to annealing were obtained by the f-PDL laser, while the n-PLD-grown MoO_{3-x} films were predominantly amorphous with a smooth surface [186]. Sunu et al. claimed that as-deposited PLD films (T_s = 400 °C, Φ = 4–5 J·cm^{-2}, repetition rate of 15 to 20 Hz, and $p(O_2)$ = 500 Pa) are suboxide-like, i.e., mixture of η--Mo_4O_{11} and χ-Mo_4O_{11}, which transformed to

MoO_3 after annealing at 500 °C in air for 5 h [18]. Several works reported the PLD growth of films $(MoO_3)_{1-x}(V_2O_5)_x$ with $0.0 \leq x \leq 0.3$ prepared at room temperature under an oxygen pressure of 13.3 Pa. The effect of the V_2O_5 content on the coloring switching properties for thermochromic, gasochromic, photochromic, and electrochromic applications was investigated [187,188]. Contrary to pure MoO_3, the electrochromism of MoO_3-V_2O_5 films showed that the Mo oxidation state (+6) did not change considerably upon Li^+ insertion, while V^{5+} was reduced considerably to V^{4+} [187]. A similar improvement of the gas-sensing properties, i.e., the shortest response time and highest transmittance change, was observed for V_2O_5-doped MoO_3 films under an H_2 atmosphere [188]. **Figure 6** presents the structural and electrochemical properties of MoO_3 thin films deposited on Si wafer using PLD technique. The average grain size was estimated to be 50 nm. The α-MoO_3 thin films deposited at T_s=400 °C (500 nm thick) delivers a volumetric capacity of 90 μAh cm^{-2} μm^{-1}.

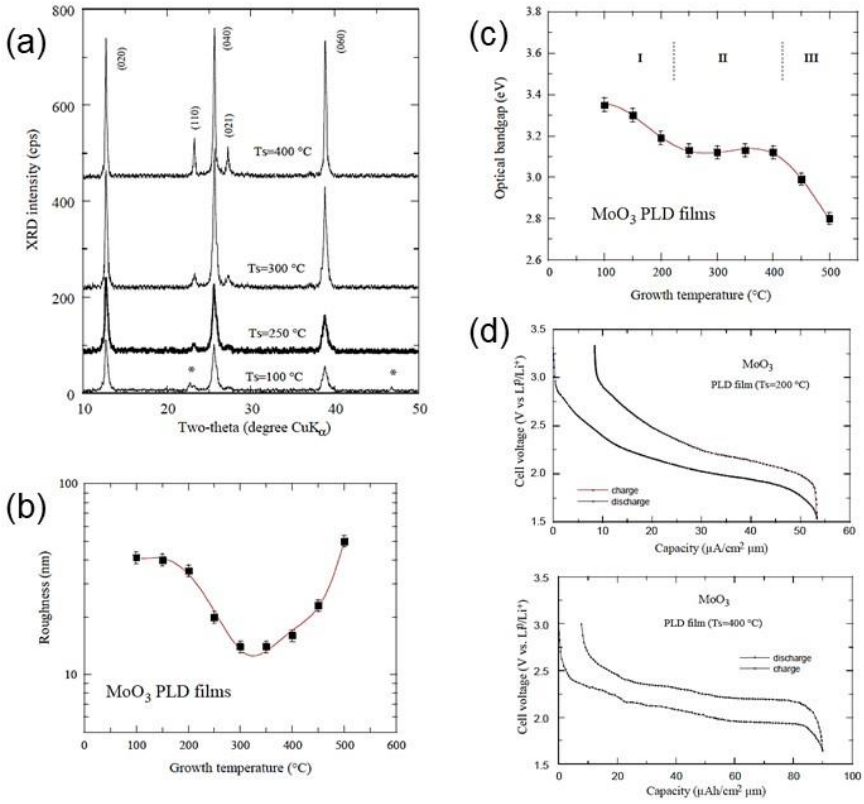

Fig. 6. Structural and electrochemical properties of α-MoO_3 thin films deposited on Si wafer using PLD technique. (a) XRD patterns for different deposition temperature. Asterisks show the peaks due to the β-MoO_3 phase for film deposited at T_s=100 °C. (b) Dependence of the growth temperature on the surface roughness determined by atomic force microscopy; (c) Influence of the growth temperature on the optical band gap. (d) The discharge-charge profiles

of Li//MoO_3 microcells cycled at a current density 10 μA cm^{-2}. A volumetric capacity of 90 μAh cm^{-2} $μm^{-1}$ is obtained for film deposited at T_s=400 °C.

2.1.6. Electronic properties

The chemistry of molybdenum is dominated by the consequences of the considerable extension of its *d*-orbitals and the position of the *d*-electrons redox potential relative to the anion valence band edge. Even prepared at elevated temperatures under atmospheric oxygen pressure, molybdenum trioxide always contains some oxygen defects ($MoO_{3-δ}$). Deb estimated the oxygen vacancy concentration to be $3×10^{-19}$ mol^{-1}, resulting in a formal stoichiometry of (3-δ) = 2.999 [189]. MoO_3 is an n-type semiconductor with indirect bandgap that has reported between 2.9 and 3.3 eV. α-MoO_3 is found to be indirect insulator with the conduction band minimums (CBM) located at Γ point and the valence band maximum (VBM) at *R* point [190]. The introduction of oxygen vacancies in MoO_3 gives rise to electrical conductivity. The valence band is generated by oxygen $2p_π$ orbitals, while the conduction band is formed by overlapping metal 4d and 5s bands. Structural characterization of oxygen defects in $MoO_{3-δ}$ by Raman spectroscopy and X-ray diffraction has been reported by Dieterle et al. [78].

2.1.7. Intercalation properties of MoO_3

The layered crystalline α-MoO_3 is an attractive material for charge storage because of its ability to intercalate ions in a wide range of composition [108,191,192]. Both faradaic and non-faradaic mechanisms can store charge. The latter is the dominant factor in electric double-layer capacitors, in which charge is stored electrostatically from the reversible adsorption of ions onto high-surface-area materials. The other option is to store charge in a faradaic process, which again can take place on a surface, as in pseudocapacitors [193,194], or in the bulk of the material, as in conventional batteries [195]. Due to their reversibility, fairly attractive energy densities, conductivities, and Li diffusion coefficients, and a good availability, MoO_y materials are probably the most promising candidates for anodes in non-aqueous batteries among all second and third row transition metal oxides. A scheme of the modification of the structure of the layered lattice of α-MoO_3 phase due to the intercalation of foreign ions (Li^+, Na^+, K^+, etc) or molecules (polypyrrole) is shown in **Fig. 7**.

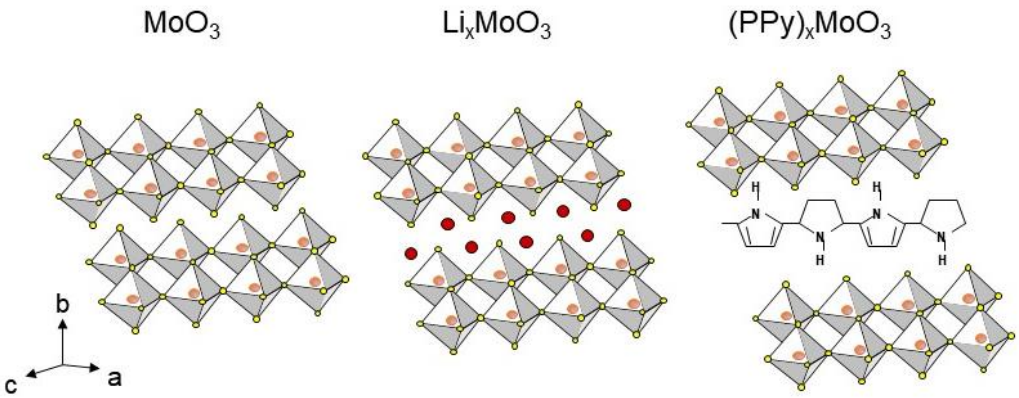

Fig. 7. Scheme of the modification of the structure of the layered lattice of α-MoO_3 phase due to the intercalation of foreign atoms or molecules.

2.1.6.1. Chemical lithiation

Orthorhombic α-MoO_3 powders synthesized by thermal decomposition of molybdic acid containing ammonium ions, $(H_2O)_y$ $(NH_4)_z$ MoO_3, in air at 600 °C for 6 h were lithiated by Hashem et al. [196]. Li_xMoO_3 were prepared by reaction of various amounts of water-free lithium iodide (the molar ratios of Li/Mo $0.1 \leq x \leq 1.0$ in organic solution; dispersions of LiI and MoO_3 powders were stirred for 24 h in dry n-hexane; the n-hexane was renewed two times during this period to remove the liberated iodine. The filtered powder was washed with excess of n-hexane until the filtrate was clear from iodine. The filtered powder was heated at 250 °C under vacuum for 8 h. The major amount of iodine evolved during this reaction step due to the reaction of LiI with MoO_3 and the subsequent liberation of I_2. Structural studies show that a two-phase reaction occurs during chemical lithium insertion into α-MoO_3. The XRD peaks related to the orthorhombic MoO_3 phase disappeared gradually until the formation of completely lithiated phase at $x > 0.25$ in Li_xMoO_3, for which a new peak assigned to (010) refection appeared at about 2θ=11.4°. Mai et al. [197,198] reported the electroactivity of α-MoO_3 nanobelts after lithiation that show superior performance to non-lithiated α-MoO_3 nanobelts. The lithiated phase (light-blue color) was obtained by reaction of MoO_3 with LiCl in aqueous solution for 2 days followed by a hydrothermal process at 180 °C for 24 h. For the non-lithiated MoO_3, the discharge capacity decreased from 301 to 180 mAh g^{-1} after 15 cycles, corresponding to a capacity retention of 60 %, whereas the discharge capacity of lithiated MoO_3 decreased from 240 to 220 mAh g^{-1} after15 cycles, corresponding to a capacity retention of 92%, showing the stability and drastic improvement in the charge-storage capacity of the lithiated MoO_3 nanobelts. Villevieille et al. conducted similar studies on MoO_3 nanobelts

synthetized by hydrothermal route and chemically lithiated using a LiCl solution. The obtained nominal $LiMoO_3$, shows enhanced electrochemical performance (>150 mAh g^{-1} for a loading of 4 mg cm^{-2} at 3C rate) and can be considered as a novel cathode with high specific charge (**Figs. 8a-b**) [199]. High resolution in situ XRD analysis reveals almost no damage to the nanobelt electrode after 50 cycles (**Fig. 8c**).

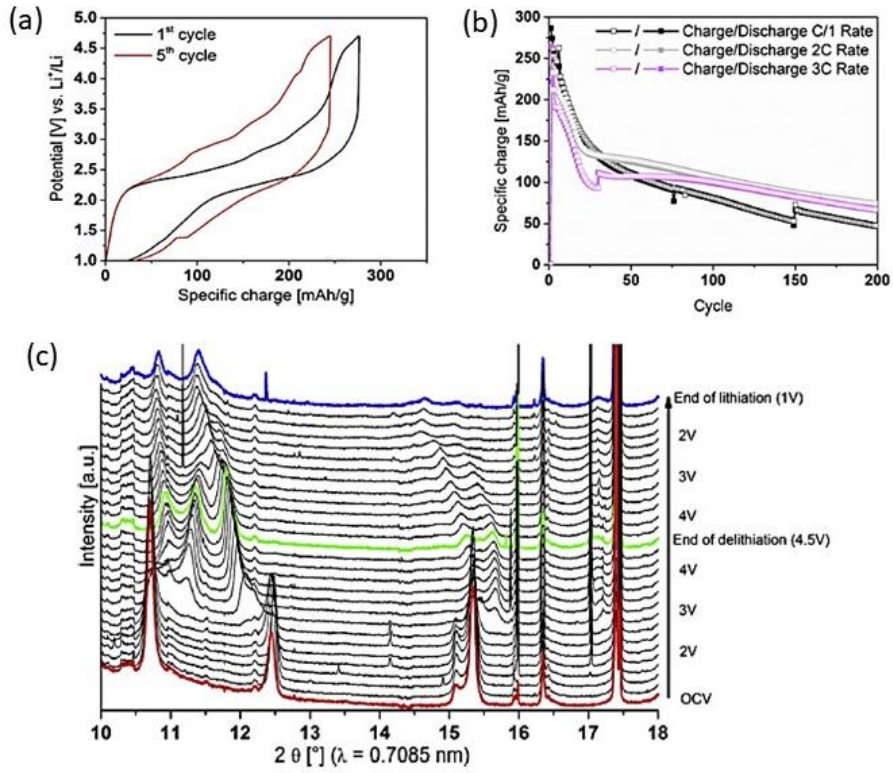

Fig. 8. (a) Galvanostatic curves of $LiMoO_3$ nanobelts prepared using 1 mol of LiCl per MoO_3 cycled at C/10 rate. (b) Cyclability at different C rate. (c) In situ XRD synchrotron pattern collected during the first cycle. In red the starting material before cycling, in green the end of the delithiation process, in blue the end of the lithiation process. Due to the small shift the changes in lattice parameter are less than 1%. Reproduced with permission from [199]. Copyright 2015 Elsevier.

2.1.6.2. Electrochemical lithiation

In principle, many works have demonstrated the suitability of Li^+ ions to intercalate/deintercalate the interlayer spacing (van der Waals gap) of the α-MoO_3 host structure by redox reaction with the accommodation up to 1.5 Li atom per Mo [11,64,135,196,200-203]. In the cut-off potential 3.5-1.5 V vs. Li^+/Li, the overall reversible intercalation/deintercalation reaction is:

$$x\mathrm{Li}^{+} + x\mathrm{e}^{-} + [\mathrm{Mo}^{\mathrm{VI}}]\mathrm{O}_3 \leftrightarrow \mathrm{Li}_x^{+}[\mathrm{Mo}^{(6-x)+}]\mathrm{O}_3, \quad (3)$$

assuming the reduction the transition-metal cations from Mo(VI) to Mo(V) and Mo(IV) oxidation states. Note that the Li^+ coupled electron transfer produces intense blue coloration ($Li_x^+[Mo^{(6-x)+}]O_3$) via strong light absorption of the pristine transparent $[Mo^{VI}]O_3$. **Figure 9a** shows the cyclic voltammograms of the electrode made of crystalline α-MoO_3 powders in the first five cycles at a sweep rate of 0.05 mV s^{-1}. In the first cycle, two sets of cathodic and anodic peaks appear at around the potential of 2.30, 2.73 V and 2.33, 2.48 V, which can be assigned to the insertion/extraction of Li^+ ions between the MoO_6 octahedral interlayers and intralayers, respectively [11]. However, the set of peaks at (2.33, 2.75 V) completely disappeared in the second and subsequent cycles, indicating irreversible capacity losses due to the unrecoverable phase transformation. The first galvanostatic discharge charge profiles of a Li//α-MoO_3 cell and those of subsequent cycles are shown in **Figs. 9b-c**. During the first cycle at C/10 current rate, the host can accommodate almost 1.6 Li/Mo, which corresponds to a specific capacity 265 mAh g^{-1}. A capacity retention of 152 mAh g^{-1} is remained after 100 cycles. The discharge capacities of anhydrous MoO_3 reported by several workers are in the range from 1.3 to 1.6 Li/Mo in the potential range above 1.2 V vs. Li^+/Li [113,196,204]. The capacity of MoO_3 observed here is approximately in good agreement with the theoretical gravimetric capacity of 280 mAh g^{-1}. The disappearance of the irreversible peak (at ca. 2.75 V) in the CV and the absence of voltage plateau at ca. 2.78 V in the galvanostatic discharge curve is related to a structural modulation that occurs upon insertion/extraction of Li^+ ions between the MoO_6 octahedral interlayers and intralayers, respectively, and it is responsible for a capacity loss of ca. 20 mAh g^{-1}. This suggests that part of the Li^+ ions, first introduced during the reduction reaction (discharge), later remain in the lattice. Such an effect has also been observed in V_2O_5 [205] The mechanism of Li-ions intercalation into the α-MoO_3 has been described as the formation of three phases separated by bi-phase domains that are responsible for voltage plateaus in the first discharge curve [11,196,206]. It is believed that the $Li_{0.25}MoO_3$ phase formed at 2.75 V vs. Li^+/Li is at the origin of the irreversible capacity at the end of the first charge. Thus, for subsequent cycles of discharge-charge, the cathode material shuttles from $Li_{0.25}MoO_3$ to $Li_{1.5}MoO_3$ without the appearance of the first plateau. Based on these results, an idealized scheme of the Li intercalation process into the MoO_3 framework is shown in **Fig. 10** [135].

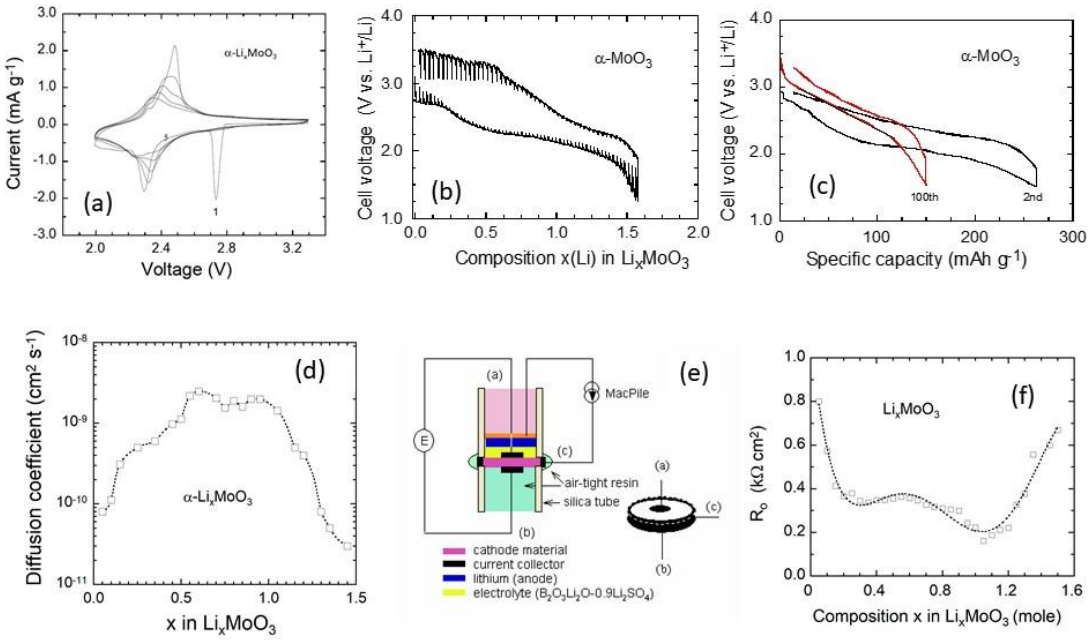

Fig. 9. Electrochemical intercalation of Li ions in crystalline α-MoO_3. (a) Five first cyclic voltammograms of Li//α-MoO_3 cell cycled at a sweep rate of 0.05 mV s^{-1} and cut-off potential 2.0–3.3 V vs. Li^+/Li. (b) First galvanostatic discharge-charge profile recorded at C/10 rate. (c) Electrochemical patterns at the 2nd and 100th cycle. (a) Variation of the chemical diffusion coefficient of Li^+ ions in the α-MoO_3 host network with the degree *x*(Li) of intercalation. (e) Experimental setup of *in situ* measurements of the electrical resistance of the α-MoO_3 electrode upon Li extraction (charge). (f) Composition dependence of the electrode resistance. MoO_3 can be considered such as a good self-limiting over-charge material.

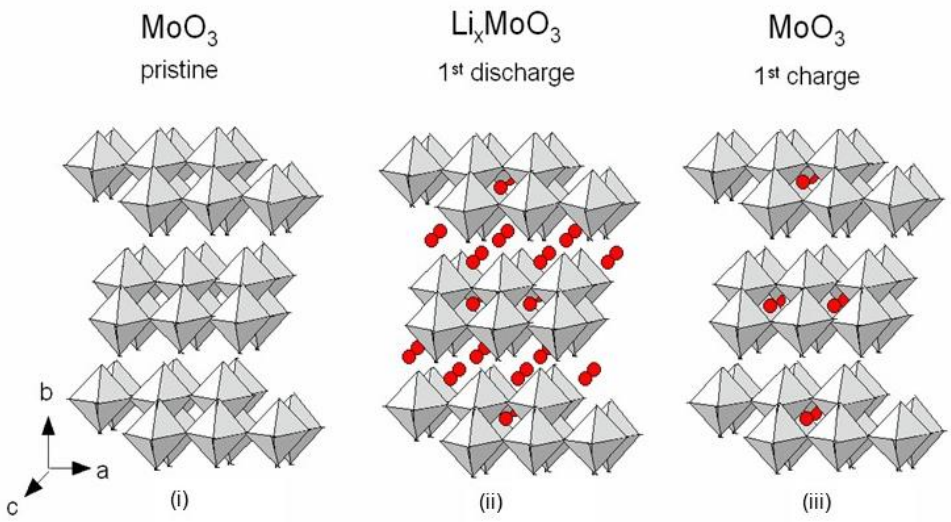

Fig. 10. Idealized scheme of the intercalation process in MoO_3 framework. At the end of the discharge, the chemical composition is $Li_{1.5}MoO_3$, while at the end of the charge, it is $Li_{0.25}MoO_3$. Reproduced with permission from [135]. Copyright 2012 Elsevier.

The chemical diffusion coefficient, D_{Li}^{*}, of Li^{+} ions in the α-MoO_3 host lattice depends on the composition x and the morphology of the material. **Figure 9d** shows the compositional dependence of D_{Li}^{*} determined using the current step method (plot of ΔE vs $t^{-1/2}$) given by the relation [207]:

$$D_{Li}^{*} = \widetilde{D}\frac{RT}{xF}\frac{\Delta x}{\Delta E}, \qquad (4)$$

where $\widetilde{D}$ is the self-diffusion coefficient, R and F are the usual constant and T is the absolute temperature. Dickens reported a chemical diffusion coefficient of 3×10^{-9} cm^2 s^{-1} (self-diffusion of 3×10^{-10} cm^2 s^{-1}) for $Li_{0.3}MoO_3$ [200] A maximum value of ca. 10^{-10} cm^2 s^{-1} has been reported for $x \approx 0.6$. Li mobility was shown to slightly decrease upon subsequent discharge-charge cycles due to irreversible structural and morphological changes of the host matrix [64]. However, when the cell was recharged, reoxidation of Mo produces a resistive compound, which induces a large polarization of the cell at the end of the charge as shown in **Fig. 9a**. This effect could be beneficial for application, thus, MoO_3 can be considered such as a good self-limiting over-charge material. Upon lithiation of Li_xMoO_3, the electronic conductivity increases from 10^{-4} S cm^{-1} for $x = 0$ to ca. 10^{-1} S cm^{-1} for $0.3 \leq x \leq 0.9$ [64]. *In situ* measurements of the electrical resistance of the electrode has been reported by Yebka et al. [204]. The results shown in **Fig. 9f** are in good agreement with the variation of the overpotential at the end of charge. The structural changes occurring in the positive electrode materials during Li electrointercalation were followed by *in situ* XRD measurements (**Fig. 11a**) and Raman spectroscopy (**Fig. 11b**) [204]. **Figure 11a** presents the XRD diagrams of Li_xMoO_3 during the discharge process ($0.0 \leq x \leq 1.5$). These patterns indicate the formation of a two-phase system in the range $0.0 \leq x \leq 0.25$ followed by a single phase Li_xMoO_3 for which the framework structure is almost unchanged during discharge reaction up to 1.5 Li/Mo. However, one can observe the vanishing of Bragg peak at ca. $2\theta = 52°$ for $x > 0.5$Li/Mo. This indicates a continuous structure reorganization corresponding to complete reversibility of the insertion/de-insertion process for the Li_xMoO_3 material in the potential range 3.5-1.2 V. The orthorhombic lattice parameters of $Li_{0.5}MoO_3$ chemically intercalated by n-butyllithium have been reported by Dickens and Reynolds [200] as $a = 3.64$ Å, $b = 16.7$ Å, $c = 3.77$ Å, which result in a slight contraction along the a- and c-direction and an expansion of the b-axis of 20% due to the filling of the interlayer spacing. Such a structural evolution has been reported by Tsumura et al. [11] as shown in **Fig. 11c**. The initial formation of the lithiated phase results in expansion of the interlayer spacing from 0.69 to 1.175 nm.

The evolution of the local structure of α-MoO_3 cathode materials during the first discharge has been studied by Raman spectroscopy. The electrode was washed with DMC solution to remove $LiPF_6$ salt and left in a glove box for 12 h to reach equilibrium. **Figure 11b** shows the Raman spectra of α-Li_xMoO_3 nanofibers as a function of the concentration of Li^+-ions inserted in the range $0 \leq x \leq 1$. At the first discharge, the Raman spectrum of MoO_3 nanofibers shows significant changes. As a general trend, we notice that all the main spectral features observed in MoO_3 are present in the spectrum of Li_xMoO_3 and the broadening of the bands indicate that the Li_xMoO_3 phase is less ordered than the α-MoO_3 lattice. On comparing the Raman features of Li_xMoO_3 and MoO_3, the following considerations can be established: (i) the intensity of the translational modes at low frequency, i.e., 83 and 113 cm^{-1}, is progressively quenched, (ii) some bands are enhanced, i.e., the δ(O_2-Mo-O_2) scissoring B_{3g} and B_{1g} modes at 244 and 377 cm^{-1}, respectively, while some others vanish, i.e., the intense δ(O_1-Mo-O_1) wagging B_{2g} mode at 282 cm^{-1} and the δ(O_2-Mo-O_2) scissoring A_g mode at 364 cm^{-1}, (iii) the single line, corresponding to the Mo=O stretching mode (molybdyl mode) along the *c*-axis broaden and shifted up to 998 cm^{-1} with respect to 994 cm^{-1}, typically observed for the α-phase, and (iv) new spectral features are detected in the spectrum of Li_xMoO_3 (bands at 440, 758, 967 and 1013 cm^{-1}). At least two factors can account for the distinction between the spectra of these materials. First, the non-equivalent character of the transition metals in the lattice of Li_xMoO_3, meaning three kinds of molybdenum oxidation states from Mo^{6+} to Mo^{4+}, which implies the modification in the local environment of MoO_6 octahedra. Second, the Li atom oscillations may couple with some modes of the MoO_3 lattice. These results are consistent with the reported data in the literature, which describe that the lithium insertion process consists in rather moderate local distortions allowing the accommodation of 1.5 Li/mol of oxide without breaking of the orthorhombic symmetry [11]. The structural modifications in Li_xMoO_3 can be also evidenced by the variation of the peak intensities of stretching modes; a decrease of the peak intensity ratio I_{994}/I_{818} with the increase of Li content is shown in **Fig. 11d**.

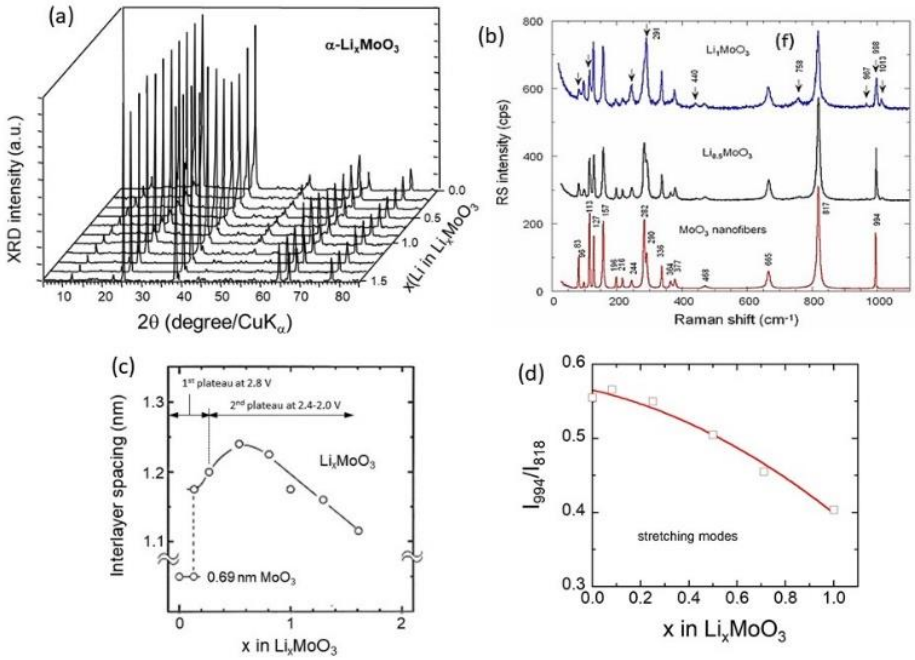

Fig. 11. (a) In-situ XRD patterns taken during the electrochemical lithium intercalation of α-MoO_3 crystal. Around 2θ = 55° the diffraction line vanishes with the increase of Li concentration in the lattice. (b) Raman spectra of pristine and Li_xMoO_3 (x = 0.5 and 1.0). New vibrational modes are marked by asterisks. (c) Change of interlayer spacing between Mo–O octahedron layers of Li_xMoO_3 with lithium composition. Reproduced with permission from [11]. Copyright 1997 Elsevier. (d) Evolution of the Raman peak intensity ratio I_{994}/I_{818} with x(Li).

The mechanism of a phase transition in electrochemical lithium insertion into α-MoO_3 was also investigated by transmission electron microscopy (TEM), X-ray diffraction (XRD) and X-ray photoelectron spectroscopy (XPS) [206,208]. The combined XPS, RBS, and NRA analysis of MoO_3 thin films electrochemically treated at selected potentials between 1.7 and 3.2 V vs. Li^+/Li allowed the dosing of intercalated lithium and the determination of the composition of the lithiated phases. $Li_{0.50}MoO_3$, $Li_{1.20}MoO_3$, and $Li_{0.21}MoO_3$ were obtained after intercalation at 2.58 and 1.73 V and deintercalation at 3.2 V, respectively, showing that ~1.2 mol of Li can be initially intercalated in the potential range 1.7−3.2 V (capacity of 223 mAh g^{-1}), and ~0.2 mol of Li per mol of MoO_3 is trapped in the oxide matrix after the initial stages of intercalation. The Li 1s core level (at E_B = 55.80 eV) is most intense at 1.73 V and does not vanish at 3.2 V. Changes of the electronic structure after intercalation result from the occupation of the Mo 4d states (at E_B = 1.0 eV) originally empty in the pristine oxide [166].

Recently, Guo et al. [209] investigated the electrochemical insertion of proton in α-MoO_3 in acidic electrolyte (i.e., the 4.4 mol L^{-1} H_2SO_4 commonly used in lead-acid batteries). **Figure 12** presents the electrochemical patterns and operando structure changes of initial proton deintercalation in molybdenum bronzes H_xMoO_3 ($0 \leq x \leq 1.68$). Zhang et al. [210] reported how selective H_3O^+ intercalation in a neutral $ZnCl_2$ electrolyte can be achieved for water-proton co-intercalated α-MoO_3. H_2O molecules located between MoO_3 interlayers block Zn^{2+} intercalation pathways while allowing smooth H_3O^+ intercalation/diffusion through a Grotthuss proton-conduction mechanism. Thus, the water-proton insertion provides enhanced specific capacity of 356 mAh g^{-1}, a rate capability of 77.5% at 4 A g^{-1} and a cycling stability of 83% over 1000 cycles.

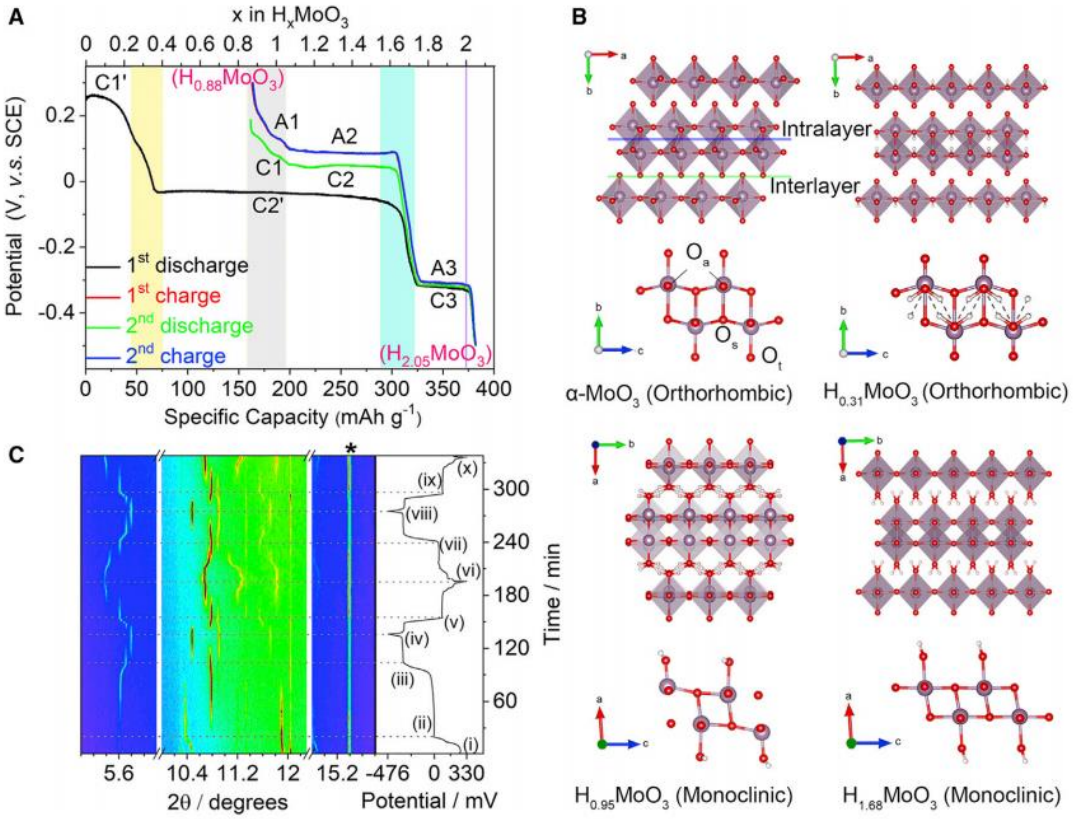

Figure 12. Electrochemistry and operando structure changes of initial proton intercalation (A) The initial galvanostatic charge-discharge profiles of MoO_3 at 1 A g^{-1}. Typical redox processes are labeled as C (cathodic)/A (anodic) *n*, where *n* is the redox index. Note the initial cathodic processes are unique and labeled as C1'/C2'. (B) Structure diagrams of α-MoO_3 and the hydrogen molybdenum bronzes (HMBs) with different hydrogen amounts. The purple, red, and white spheres refer to Mo, O, and H atoms, respectively. Note that these structures were defined by different authors; therefore, the coordinates are different. (C) The contour plot of operando

diffraction data of cell (in 4.4 mol L^{-1} H_2SO_4 electrolyte, galvanostatically tested at 1C), correlated with the electrode potential as a function of time. Copyright Guo et al. [209]. Open access article under the CC BY-NC-ND license.

Several approaches have been conducted to improve the electrochemical performance of MoO_3 electrodes (i.e., capacity retention, long life cycling) including nanocrystallization [130,211-213] core-shell composite [214], carbon-based hybrid [215-217], carbon encapsulation [218], MWCNT-based hybrid [219-221], incorporation into graphene network [222-224], MoO_2 intergrowth [225,226], dual-ion intercalation [210,227], and coating [228-230]. Nanobelts of α-MoO_3 have been modified to $H_xMo(O,N)_3$ through a moderate ammonolysis method, i.e., reaction at 200–300 °C with gaseous NH_3, which diffuses in-between the MoO_3 layers and reacts with terminal oxygen sites. As a consequence, hydrogen is bonded to terminal oxygen, and the unit cell volume significantly shrinks mostly along the *b*-axis. The modified $H_xMo(O,N)_3$ electrode exhibits a specific capacity of ~250 mAh g^{-1} and shows no capacity fading over 300 cycles in the potential window 1.5–3.5 V [227].

2.1.8. MoO_3 anodes for LIBs

Molybdenum trioxide, which can be also categorized as one of the conversion type transition metal oxides, has additional advantageous features of low cost and environmental benignity as well as even higher capacity. However, MoO_3 suffers from serious capacity fading caused by large volume changes and poor rate capability due to low conductivity. Recently, these drawbacks have been mitigated by different strategies, i.e., reduction of particle size to nanoscale and fabrication of composites.

2.1.8.1. MoO_3 nanoparticles

The MoO_3 nanoparticles have been demonstrated as high-capacity Li-ion battery anodes for next-generation electric vehicles [231-235]. Specifically, the MoO_3 anodes have been shown to have approximately three times the Li-ion capacity of commercially employed graphite anodes in thick electrodes suitable for vehicular applications [128,193, 232,236-240]. Researches about MoO_3 as an anode in the potential range down to 0 V (*vs.* Li^+/Li) have shown that MoO_3 can theoretically accommodate 6 Li/Mo providing a specific capacity of 1117 mAh g^{-1}. The overall first lithiation reaction for MoO_3 is described by two reactions: the lithium insertion (addition) at potential >1.5 V up to $x \approx 1.2$ (Eq. 5) and the conversion (transformation) reaction at potential <0.5 V up to $x \approx 6.0$ (Eq. 6) as follows:

$$MoO_3 + xLi^+ + xe^- \rightarrow Li_xMoO_3, \quad (5)$$

$$Li_xMoO_3 + (6-x)Li^+ + (6-x)e^- \rightarrow Mo + 3Li_2O. \quad (6)$$

Note that the amorphization of the material does not alter the overall electrochemical performance of the anode. The conversion reaction yields nanodispersed particles of Mo metal in the Li_2O matrix [241]. **Figure 13** shows the typical first discharge-charge curve of MoO_3 nanofibers as anode materials in lithium battery. Nanofibers were synthesized by hydrothermal method from $MoO_3 \cdot 1.4H_2O$ sols prepared by ion exchange of ammonium heptamolybdate tetrahydrate $(NH_4)_6Mo_7O_{24} \cdot 4H_2O$.

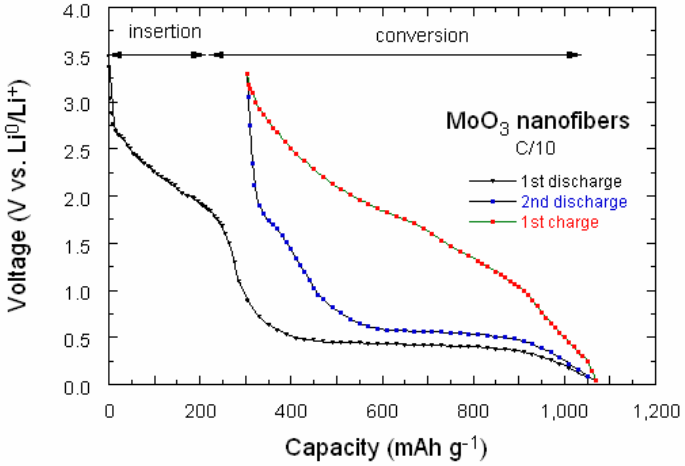

Fig. 13. The typical first discharge-charge curve of MoO_3 nanofibers as anode materials in lithium battery. The overall first lithiation reaction for MoO_3 is described by two reactions: the lithium insertion (addition) at potential >1.5 V up to $x \approx 1.2$ and the conversion (transformation) reaction at potential <0.5 V up to $x \approx 6.0$.

Xia et al. [208] investigated the lithiation mechanism in α-MoO_3 nanobelts using in situ TEM experiments. Results reveal that α-MoO_3 undergoes a two-stage delithiation process. Mo nanograins were first transformed into crystalline $Li_{1.66}Mo_{0.66}O_2$ along with the disappearance of Li_2O and size shrink, followed by the conversion to amorphous Li_2MoO_3. The electrochemical reactions of α-MoO_3 during lithiation and delithiation processes can be expressed as:

$$MoO_3 + 6Li^+ + 6e^- \rightarrow Mo + 3Li_2O, \quad (7)$$

$$Mo + 3Li_2O \rightarrow 1.5Li_{1.66}Mo_{0.66}O_2 + 3.5Li^+ + 3.5e^-, \quad (8)$$

$$1.5Li_{1.66}Mo_{0.66}O_2 \rightarrow Li_2MoO_3 + 0.5Li^+ + 0.5e^-, \quad (9)$$

where Eq. (7) represents the first lithiation and Eqs. (8) and (9) account for the two-stage phase of the subsequent delithiation/lithiation reactions (**Fig. 14**) [208]. This shows that the total

amount of extracted Li is about 4 [132,236]. The theoretical lithium storage capacity of Li_2MoO_3 is calculated to be about 734 mAh g^{-1} according to its weight and the ability of accommodating lithium ions, which is much lower than MoO_3 of 1117 mAh g^{-1}.

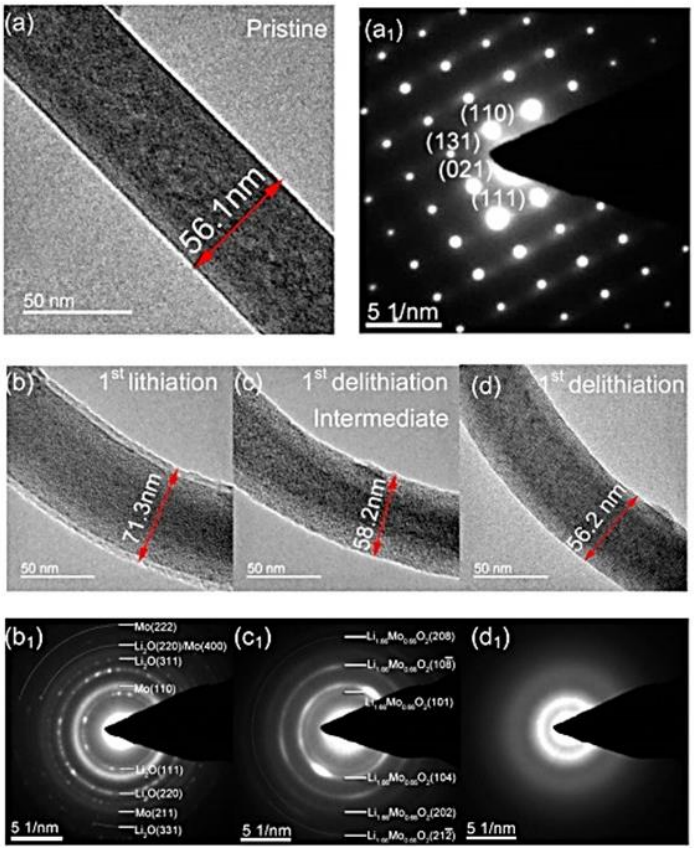

Fig. 14. HRTEM images and electron diffraction patterns (EDP) showing the microstructure evolution of MoO_3 nanobelt in lithiation and delithiation processes. (a) pristine MoO_3 nanobelt with a size of 56.1 nm. (b) The first lithiation. (c) Intermediate stage of the first delithiation. (d) Delithiated MoO_3 nanobelt. EDPs recorded from the nanobelt anode reveal the phase conversion during conversion. Reproduced with permission from [208]. Copyright 2016 American Chemical Society.

Ultralong α-MoO_3 nanobelts (length of 200–300 μm and uniform width of ~0.6–1.5 μm) were hydrothermally synthesized using a molybdenum organic salt precursor. The electrodes fabricated with sodium carboxymethyl cellulose (Na-CMC) binder deliver the specific capacity of over 730 mAh g^{-1} for over 200 cycles at a 0.2C rate. Even cycled at high rates of 1–2C, high capacities of around 430–650 mAh g^{-1} can be still retained [129]. Sasidharan et al. [242] synthesized α-MoO_3 hollow nanospheres (HNSs; outer diameter of 42 nm; hollow cavity of 23 nm) have been using a soft template of polymeric micelles with core–shell–corona architecture. The MoO_3 HNSs electrode delivers a discharge capacity of 263 mAh g^{-1} for the first cycle at a

rate of 0.3C and maintains structural integrity even after subjecting to a high current density 2000 mA g^{-1} (10C rate) The capacity retention is 2.2 times higher than that of dense MoO_3 particles. Ette et al. [243] prepared self-assembled lamellar α-MoO_3 nanoflakes (20-30 nm) using facile polymer (polyvinyl pyrrolidone) assisted solvothermal method. After 50 cycles, a capacity value of 1027 mAh g^{-1} can be extracted at 0.2C rate while at 2C rate it shows capacity of 700 mAh g^{-1}. Riley and coworkers prepared α-MoO_3 nanoparticles using a hot-wire chemical vapor deposition and reported that MoO_3 negative electrodes fashioned into thick electrodes containing 70% MoO_3 nanoparticles (10-40 nm in diameter), active material, 20% poly (vinylidenefluoride) (PVDF), binder, and 10% acetylene black (AB), conductive additive, can deliver a discharge capacity of ~1000 mAh g^{-1} at a reduced rate to C/10 [237]. Later, these workers showed that coating of the electrode with ~8 Å of Al_2O_3 by atomic layer deposition (ALD) achieves better rate capability [244]. It was suggested that the ALD coating enabled better adhesion of the high-volume expansion MoO_3 (≥100%) to the current collector. In a subsequent work, MoO_3 nanoparticles prepared by hot wire chemical vapor deposition (HWCVD) have been demonstrated as high-capacity Li-ion battery anodes for next-generation electric vehicles. The MoO_3 nanoparticles coated with ~8 Å thick Al_2O_3 layer deliver a specific capacity of ~600 mAh g^{-1} at 5C rate [239]. The ALD-coated MoO_3 composite electrode (~15 μm thick) prepared with an Al_3O_3 coating of ~8 Å thick delivers a capacity of ~600 mAh g^{-1} at 5C rate. Zhao and coworkers [245] synthesized MoO_3 hollow microspheres via a template-free solvothermal route and subsequent heat treatment in air. The MoO_3 hollow microspheres have a high specific surface area of 48.2 m^2 g^{-1}, and with such a feature, when tested as a Li-storage anode material, they show a higher discharge capacity of 1377 mAh g^{-1} in the first discharge and a high reversible capacity of 780 mAh g^{-1} after 100 cycles at a rate of 1C (**Fig. 15**). Varghese et al. [246] investigated the performance of full-cell Li-ion batteries based on MoO_3 nanobelts synthesized by hydrothermal process as cathode and prelithiated MoO_3 as anode. At 1 A g^{-1} current density, the Li_xMoO_3 anode delivers a capacity of 700 mAh g^{-1} and at 2.5 A g^{-1} current density a capacity of 400 mAh g^{-1} is achieved. The MoO_3//Li_xMoO_3 full-cell delivers initial energy densities of 156 Wh kg^{-1} and shows a CE of 99% over 100 cycles.

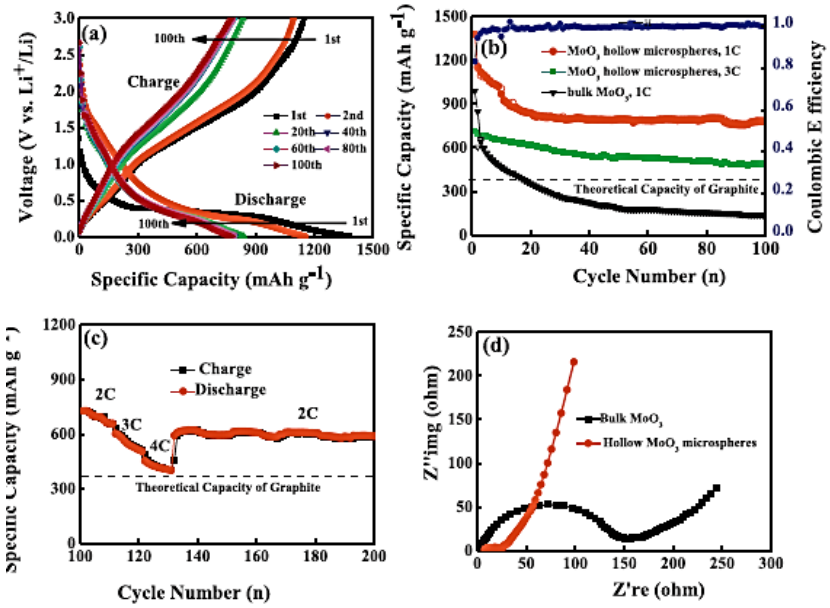

Fig. 15. (a) Discharge/charge voltage profile between 0.01 and 3 V at a rate of 1C of MoO_3 hollow microspheres; (b) cycling performance of MoO_3 hollow microspheres and bulk MoO_3; (c) cycling performance for the different rates (1–4C) of MoO_3 hollow microspheres; (d) electrochemical impedance spectroscopy of the MoO_3 hollow microspheres. Reproduced with permission from [245]. Copyright 2013 Elsevier.

The promising characteristics of both poly(*p*-phenylene) (PPP) and $Na_{0.25}MoO_3$ as anode materials in Li-ion cells, along with substantial amounts of polymer surface impurities resulting from the hydrothermal method, have led us to develop a new technique for the inclusion of PPP in MoO_3 [247]. Thus, the electrochemical reactivity of MoO_3 utilizing a conversion reaction has been widely investigated [129,236]. Reversible lithium-ion insertion in MoO_3 nanoparticles deposited by electrophoresis on stainless steel substrate have been reported by Lee et al. [128]. A stable capacity of 630 mAh g^{-1} was obtained for 150 cycles between 0.005 and 3.5 V. In contrast micron-sized particles of MoO_3 showed significant capacity fade after only several cycles. These thin films employed neither conductive additive nor binder as in traditional electrodes. Despite stable cycling at a rate of C/2, the reversible capacity was only 60% of the theoretical maximum of MoO_3, 1117 mAh g^{-1}. **Table 5** summarizes the electrochemical performance of MoO_3 nanoparticles as anode materials for LIBs prepared by various methods.

Table 5. Electrochemical performance of MoO_3 nanoparticles as anode materials for LIBs prepared by various methods. Relevant cycle number is given in brackets.

Material [a)]	Synthesis	Specific capacity (mAh g^{-1})	Current rate (mA g^{-1})	Ref.
HMPs	Solvothermal	780	1C (100)	[245]
NBs (52 nm thick)	Precipitation	300	1000 (100)	[246]
NPs (10-40 nm thick)	Hot-wire CVD	940	C/10 (40)	[237]
NBs (0.6-1.5 μm width)	Hydrothermal	730	0.2C (200)	[129]
NBs (~200 nm width)	Hydrothermal	387	2000 (80)	[248]
MoO_3 microspheres	Spray-pyrolysis	345	2000 (300)	[249]
NFs	Ultrasonication	795	550 (100)	[250]
NSs (20-30 in diameter)	Hot-wire CVD	630	150 (150)	[251]

[a)] HMPs: hollow microspheres; NBs: nanobelts; NPs: nanoparticles; NFs: nanofibers; NSs: nanospheroids.

2.1.8.2. MoO_3 nanocomposites

The MoO_3 nanocomposites act as high capacity anode materials for lithium-ion batteries and exhibits good cyclic behavior. A variety of appealing strategies including carbon-based nanocomposites have been utilized to minimize the volume expansion/contraction and particle aggregation associated with the Li-insertion and extraction processes [232, 252,253]. MoO_3-based nanocomposites include: MoO_3@carbon [232,252], MoO_3@graphene [254-257], MoO_3@rGO [223,258-260], MoO_3@metal [261,262], and MoO_3@metal oxides [238,263,264].

Tao and coworkers [252] synthesized a MoO_3–carbon nanocomposite from a mixture of MoO_3 nanoparticles (2–180 nm) and graphite by a controlled ball milling procedure. The initial capacity of the MoO_3/graphite (1:1 by weight) composite exceeds the theoretical capacity of 745 mAh g^{-1}, and the stable capacity of 700 mAh g^{-1} (94% of the theoretical capacity) still retains after 120 cycles. The electrode performance is linked with the unique nanoarchitecture of the composite and is compared with the performance of MoO_3-based anode materials reported in the literature previously (nanoparticles, ball milled powders, and carbon-coated nanobelts). The high value of capacity and good cyclic stability of MoO_3-carbon nanocomposite are attractive in respect to those of the reported MoO_3 electrodes [254]. Hussan et al. [232] synthesized MoO_3 nanobelts, diameter of 150 nm and a length of 5–8 μm, by a simple hydrothermal route followed by carbon coating. The C–MoO_3 nanobelts exhibit excellent cycling stability after being cycled at a current rate of C/10, maintaining their capacity at 1064 mAh g^{-1} after 50 cycles. Highly uniform MoO_3 nanoparticles were prepared using hot-wire chemical vapor deposition (HWCVD) for use as active negative electrodes in high-energy LIBs [183]. An optimized reversible high capacity of ~1050 mAh g^{-1} was obtained for an electrode fabricated from active material, acetylene black and PVDF (70:10:20) with a 250 °C pre-heat treatment.

Xue et al. [238] have synthesized α-MoO_3 nanobelts and SnO_2/α-MoO_3 core-shell nanobelts, which show extraordinarily high reversible capacity as LIB anodes. The initial coulombic efficiency (ICE) of α-MoO_3 nanobelts and SnO_2/α-MoO_3 core-shell nanobelts is 70.8% and 69.7%, respectively. The low ICE is probably attributed to the formation of solid electrolyte interphase (SEI) layer. In the following cycles, both α-MoO_3 nanobelts and SnO_2/α-MoO_3 core-shell nanobelts show high coulombic efficiency (>96.0%). The reversible capacity of SnO_2/α-MoO_3 core-shell nanobelts is ~2200 mAh g^{-1}, much higher than that of pure α-MoO_3 nanobelts (~1400 mAh g^{-1}). For pure α-MoO_3 nanobelts, during the first lithiation process, three peaks can be observed at 2.25, 0.4 and 0.07 V. The peak at 2.25 V, only observed in the first discharge process, is probably ascribed to the formation of SEI layer. The other two peaks can be attributed to the lithiation process. In the subsequent lithiation processes, all the peaks (at 0.07, 0.3, 0.53, 1.29 and 1.48 V) are reversible, which can be attributed to the lithiation with different site energies and phase-transition process of α-MoO_3 nanobelts. For SnO_2/α-MoO_3 core-shell nanobelts, during the first lithiation process, the irreversible peak, also observed at 2.25 V, can be ascribed to the formation of SEI layer. In the following lithiation processes, a new and reversible peak at ~0.7 V is observed, corresponding to the formation of $Li_{22}Sn_5$ alloys [238]. MoO_3 nanoplates were used as anode material for aqueous supercapacitors with higher energy density and relatively higher power density in comparison with traditional activated carbon [240]. MoO_3 nanowires were synthesized using a biomolecule-assisted hydrothermal approach and were demonstrated to be an excellent pseudocapacitor material. A specific capacitance 30 F g^{-1} was reported [193]. The nanocomposite MoO_3/C was synthesized by a facile one-pot citric-nitrate method, where the carbon (from glucose – ratio MoO_3:C = 10:3 in weight corresponding to 23 wt.% carbon) was introduced *in situ*, and therefore uniformly dispersed in MoO_3 host, forming a homogeneous core-shell structure (thin carbon layer of 10-15 nm). The MoO_3/C anode exhibits superior electrochemical performance, a specific capacity of about 500 mAh g^{-1} in the voltage range of 0.01–3.0 V vs. Li^+/Li can be maintained after 100 cycles [126]. Wang et al. [234] fabricated synergistic TiO_2-MoO_3 core-shell nanowire array anode for high energy and high power lithium-ion batteries via a combination of hydrothermal and electrodeposition process. The TiO_2-MoO_3 (1:1 mass ratio) hybrid exhibit a first specific capacity of 670 mAh g^{-1}, retention of ~400 mAh g^{-1} at 250 mA g^{-1} current rate after 200 cycles and good rate capability (up to 2 A g^{-1}). The areal capacity is also as high as 3.98 mAh cm^{-2}.

Martinez-Garcia et al. [265] presented the electrochemical performance of a low lithiation potential of 0.2 V vs. Li^+/Li for pristine MoO_3 nanoplatelets and Si-decorated (0.3 wt.%). MoO_3 (Si@MoO_3). The products of lithiation were identified as Li_2MoO_4 and $Li_{1.333}Mo_{0.666}O_2$,

respectively. The initial cyclic voltammogram of Si@MoO_3 carried out in the 3.0 – 0.005 V potential range exhibits three cathodic peaks at 2.6, 2.18 and 0.02 V during (reduction process). Upon oxidation to 3.0 V, the anodic peaks are observed at 0.75, 1.23, 1.5, and 2.72 V. At subsequent cycle, the features over 2.0 V disappear and a new cathodic peak starts evolving at a potential of 1.45 V after the second polarization. Si-decorated MoO_3 nanoplatelets exhibit enhanced capacity of 1037 mAh g^{-1} with exceptional cyclability when charged/discharged at high current densities of 10 A g^{-1}. Mesoporous orthorhombic MoO_3 nanowire bundles with diameters 10-30 nm and lengths of up to 2 μm were prepared by topotactic chemical transformation from triclinic α-$MoO_3 \cdot H_2O$ nanorods under vacuum condition at 260 °C The electrochemical measurements indicate that the high reversible capacities of 955 mAh g^{-1} can be retained over 150 cycles at 200 mA g^{-1} [266]. Single-crystalline α-MoO_3 nanobelts with uniform width of ~200 nm and length at the micrometer level are first synthesized by a simple water-based hydrothermal route [248]. The α-MoO_3 film electrode exhibits a reversible specific capacity of ~1000 mAh g^{-1} at 50 mA g^{-1} and a stable capacity retention of 387–443 mAh g^{-1} at 2000 mA g^{-1}.

Graphene oxide-encapsulated α-MoO_3 nanoribbons (GO/MoO_3) composite was prepared by a self-assembly process. The great potential of this unique hybrid architecture as anode for Li-ion battery is revealed by a high specific capacity (up to 823 mAh g^{-1} after 70 cycles at 200 mA g^{-1}), an excellent cycling performance (with more than 754 mAh g^{-1} after 200 cycles at 1 A g^{-1}) and a greatly-enhanced high-rate capability (displaying a high discharge capacity of 710 mAh g^{-1} after 30 cycles at 3 A g^{-1}) [267]. Ni et al. [268] fabricated the MoO_{3-x}/CNTs composite via hydrothermal synthesis and controlled reduction in Ar/H_2 atmosphere, which consists of 63 mol% MoO_3 and 37 mol% MoO_2. When evaluated as an anode in the 0.05–3.0 V voltage range, the MoO_3/CNTs hybrid retains a capacity of 421 mAh g^{-1} after 100 cycles at 200 mA g^{-1}, and deliver 293 and 202 mAh g^{-1} at current densities of 2 and 4 A g^{-1}, respectively. MoO_3@C nanofibers were synthesized by electrospinning the Mo precursor with polyvinyl pyrrolidone (PVP), followed by annealing. The as-prepared MoO_3@C nanofibers deliver a discharge capacity of 623 mAh g^{-1} after 100 cycles at 500 mA g^{-1}, and 502 mAh g^{-1} even at 1000 mA g^{-1} [124]. Ding et al. [122] adopted a facile two-step method in which pristine bulk MoO_3 is first converted into MoO_3 nanorods (MoO_3 NRs) through mechanical grinding, to buffer the continuous volume changes, and then coated with amorphous carbon (a-C) through simple stirring and heating. Electrochemical tests reveal that the a-C/MoO_3 NRs exhibits outstanding specific capacity of 856 mAh g^{-1} after 110 cycles at a current density of 0.1C and cycle life of 485 mAh g^{-1} after 300 cycles at 0.5C and 373 mAh g^{-1} after 400 cycles at 0.75C. Yang et al.

[269] aimed to expanded the interlayer spacing and enhanced the electrical conductivity of α-MoO_3 by introducing glucose in the layered framework. It is found that glucose functioned as a cage to hold the pulverized MoO_{3-x} pieces, while the subsequent conversion reaction of between Li_2O, Mo and Li_xMoO_3 occurred in confined space, which maintained electrodes structural integrity. MoO_{3-x}@G exhibits superior specific capacity of 607 mAh g^{-1} after 200 cycles at 1 A g^{-1} and a coulombic efficiency kept stable near 100%. The exceptional performance of MoO_{3-x}@G is attributed to the capacitive contribution and high reversible reaction. Cao et al. [270] hybridized nanostructured MoO_3 particles with foam-like carbon nanoflakes (CNFs) via the pyrolysis of molybdenum 2-ethtlhexanoate ($C_{48}H_{90}MoO_{12}$) at a low temperature of 300 °C under ambient atmosphere. Electrochemical tests of the MoO_3/CNFs composite as anode material for LIBs show a high discharge capacity of 791 mAh g^{-1} after 100 cycles at 500 mA g^{-1} and even ~600 mAh g^{-1} at a high rate of 2000 mA g^{-1} (**Fig. 16**).

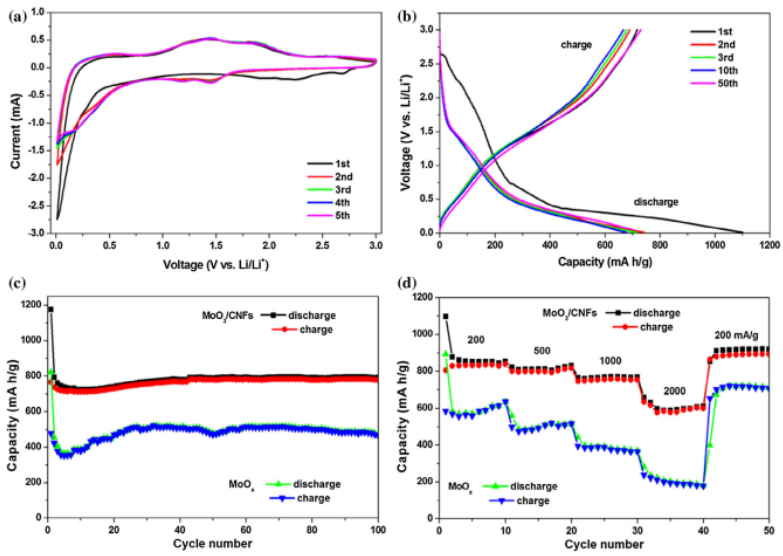

Fig. 16. (a) CV curves and (b) discharge-charge profiles of the MoO_3/CNFs. (c) Cycle performance at 500 mA g^{-1} and (d) rate performance at current densities ranging from 200 to 2000 mA g^{-1} for the MoO_3/CNFs and MoO_y electrodes. Reproduced with permission from [270]. Copyright 2018 Elsevier.

Ultrathin N-doped carbon layer encapsulated MoO_3 nanosheets have been synthesized by a simultaneous pyrolysis–reduction process of dodecylamine-intercalated MoO_3 composites at 600 °C under a nitrogen atmosphere. The as-fabricated nanosheets can reach high initial charge and discharge capacities of 1610 and 1359 mAh g^{-1}, respectively, and show remarkable cycle stability with a specific capacity of 1250 mAh g^{-1} after 60 cycles at 0.3C rate. High specific

discharge capacities are maintained at fast C rates, e.g., 1370, 1010, 940, 610, 490 and 370 mAh g^{-1} at 0.3C, 1C, 2C, 4C, 10C, and 20C, respectively [218]. A nanocomposite α-MoO_3/MWCNT was synthesized via a surfactant-assisted solvothermal process followed by low-temperature calcination [271]. When the discharge/charge current density is increased from 0.1 to 2 A g^{-1}, the reversible charge capacity is only decreased from 1138 to 941 mAh g^{-1}, giving a capacity retention of 82.7%. After 300 cycles at a current of 0.5 A g^{-1}, a high discharge capacity of 1350 mAh g^{-1} is maintained. Martinez-Garcia et al. [265] presented the electrochemical performance of a low lithiation potential of 0.2 V vs. Li^+/Li for pristine MoO_3 nanoplatelets and Si-decorated (0.3 wt.%). MoO_3 (Si@MoO_3). The products of lithiation were identified as Li_2MoO_4 and $Li_{1.333}Mo_{0.666}O_2$, respectively. The initial cyclic voltammogram of Si@MoO_3 carried out in the 3.0 – 0.005 V potential range exhibits three cathodic peaks at 2.6, 2.18 and 0.02 V during (reduction process). Upon oxidation to 3.0 V, the anodic peaks are observed at 0.75, 1.23, 1.5, and 2.72 V. At subsequent cycle, the features over 2.0 V disappear and a new cathodic peak starts evolving at a potential of 1.45 V after the second polarization. Si-decorated MoO_3 nanoplatelets exhibit enhanced capacity of 1037 mAh g^{-1} with exceptional cyclability when charged/discharged at high current densities of 10 A g^{-1}. Mesoporous orthorhombic MoO_3 nanowire bundles with diameters 10-30 nm and lengths of up to 2 μm were prepared by topotactic chemical transformation from triclinic α-$MoO_3 \cdot H_2O$ nanorods under vacuum condition at 260 °C The electrochemical measurements indicate that the high reversible capacities of 955 mAh g^{-1} can be retained over 150 cycles at 200 mA g^{-1} [266]. Single-crystalline α-MoO_3 nanobelts with uniform width of ~200 nm and length at the micrometer level are first synthesized by a simple water-based hydrothermal route [248]. The α-MoO_3 film electrode exhibits a reversible specific capacity of ~1000 mAh g^{-1} at 50 mA g^{-1} and a stable capacity retention of 387–443 mAh g^{-1} at 2000 mA g^{-1}. A porous MoO_3 film was prepared by electrodeposition on Ni foam substrates and exhibits a capacity of 650 mAh g^{-1} at a current density of 3 A g^{-1} as anodes for LIBs [139]. A MoO_3/C nanocomposite synthesized using the electrospinning method with 42% carbon takes the morphology of nanofibers, with the diameter of 50-200 nm. The MoO_3/C anode cycled in a 3.0–0.01 V potential window at current density of 40 mA g^{-1} retains a discharge capacity of 710 mAh g^{-1} after 100 cycles. When the load current density is increased to 800 mAg^{-1}, the composite delivers a discharge capacity of 300 mAh g^{-1} after 100 cycles [125]. Sun et al. [272] reported on the synthesis of single wall carbon nanotubes (SWNTs)-bridged MoO_3 nanosheets as anode material for LIBs. The MoO_3/SWNTs composite as fabricated via a liquid phase exfoliation of layered MoO_3 crystallites producing multilayer MoO_3 nanosheets dispersed in isopropanol and mixed with solution processed

SWNTs in the same solvent. The MoO_3/SWNTs hybrid leads to a specific capacity of 865 mAh g^{-1} at 100 mA g^{-1} after 100 cycles, with a coulombic efficiency approaching 100% and a capacity fading of 0.02% per cycle. The MoO_3@$CoMoO_4$ hybrid was fabricated by a facile one-step hydrothermal method [273]. Galvanostatic charge–discharge tests show that the hybrid anode delivers a capacity of 586 mAh g^{-1} at the high current density of 1 Ag^{-1} and an enhanced cyclic capacity of 887 mAh g^{-1} after 140 cycles at the current density of 200 mA g^{-1}. Reduced graphene oxide wrapped hollow MoO_3 nanorods (MoO_3@rGO) were fabricated by freeze drying method [274]. The MoO_3@rGO composite delivers a high reversible capacity of 842 mAh g^{-1} at 0.1 A g^{-1} rate, excellent cycling stability of 778 mAh g^{-1} at 0.1 A g^{-1} after 200 cycles and excellent rate capability (455 mAh g^{-1} at 2 A g^{-1}).

Recently, a novel composite of α-MoO_3 nanobelts and single-walled carbon nanohorns (SWCNHs) has been synthesized by a microwave hydrothermal method. Tested as a anode material for LIBs, the α-MoO_3/SWCNH composite displays a specific capacity of 654 mAh g^{-1} at 1C rate, excellent rate capability (275 mAh g^{-1} at 5 C), and outstanding cycle life (capacity retention of >99% after 3000 cycles at 1C) without any cracking of the electrode [275]. Feng et al. [276] produced SnO_2/MoO_3 nanoparticles encapsulated in plate-like graphite via simple hydrothermal synthesis and dry ball milling. The SnO_2–MoO_3–C displays high ICE of 70%, high reversible specific capacity of 1338 $mAhg^{-1}$ at 0.2 A g^{-1} current rate after 300 cycles (715 $mAhg^{-1}$ at 5 A g^{-1}. Long-term cyclic tests show a capacity of 571 $mAhg^{-1}$ at 2 A g^{-1} after 1000 cycles. Zhao et al. [277] designed a core–sheath structured MoO_3@MoS_2 composite via in situ growth of few-layered MoS_2 nanoflakes on the surface of the biotemplated MoO_3. The electrochemical tests show that the composite possesses a high specific capacity of 1545 mAh g^{-1} at 100 mA g^{-1} and coulombic efficiency (above 98%) after 150 cycles. Teng et al. [278] developed a hierarchically nanostructured composite of MoO_3-NiO/graphene. Ultrafine MoO_3 nanosheets and NiO nanoparticles were homogeneously anchored on the graphene layers. Tested as anode material for LIB, this ternary composite exhibits specific capacities of 1164 mAh g^{-1} at 100 mA g^{-1} after 50 cycles and 946.9 mAh g^{-1} at 1000 mA g^{-1} after 180 cycles. A fibrous CNTs/MoO_3 composite, in which CNTs anchored with MoO_3 nanoplates was synthesized by electrospinning process of the $MoO_2(acac)_2$-PAN-CNTS complex in solution and subsequent annealing. The anode composite has high specific capacities of 972 mAh g^{-1} after 100 cycles at 1 A g^{-1} and 905 mAh g^{-1} after 800 long-term cycles at 2 A g^{-1}. Rate capability tests show discharge capacities of 599 and 374 mAh g^{-1} at 5 and 10 mAh g^{-1} rate, respectively [279]. The ternary composite MoO_3/V_2O_5/C having the morphology of nanofibers with the diameter of 200~500 nm was synthesized by electrospinning combined with heat treatment.

Electrochemical tests of the composite containing ~40% carbon retains a specific capacity of 737 mAh g^{-1} after 200 cycles at 0.2 A g^{-1} current density, and its coulomb efficiency is 93% [280]. **Table 6** summarizes the electrochemical performance of MoO_3 nanocomposites as anode materials for LIBs prepared by various methods.

Table 6. Electrochemical performance of MoO_3 nanocomposites as anode materials for LIBs prepared by various methods. Relevant cycle number is given in brackets.

Material [a)]	Synthesis	Specific capacity (mAh g^{-1})	Current rate (mA g^{-1})	Ref.
MoO_3 NBs/CNTs	Hydrothermal	166	5C (500)	[281]
MoO_3@GNS	Electrostatic	833	200 (70)	[267]
MoO_3/C NBs	Hydrothermal	1000	100 (50)	[215]
$MoO_{3-\delta}$/CNTs	Hydrothermal	421	200 (100)	[268]
C/MoO_3 NBs	Hydrothermal	1064	110 (50)	[232]
MoO_3@C NFs	Electrospinning	623	500 (100)	[124]
MoO_3 NPs/C	Ball milling	700	150 (120)	[252]
aC-MoO_3 NRs	Mechanical grinding	485	0.5C (385)	[122]
$MoO_{3-\delta}$/graphene	Vacuum drying	607	1000 (200)	[269]
MoO_3/CNFs	Pyrolysis	791	500 (100)	[270]
MoO_3/N-doped C	Pyrolysis–reduction	1250	0.3C (60)	[218]
MoO_3/MWCNT	Solvothermal	1350	500 (300)	[271]
MoO_3/C layer (10-15 nm)	Hydrosol-gel	500	100 (100)	[126]
MoO_3/C microspheres	Spray-pyrolysis	808	1000 (100)	[282]
SnO_2/α-MoO_3 NBs	Ultrasonication	1895	C/10 (50)	[238]
MoO_3/C	Electrospinning	300	800 (100)	[125]
MoO_3/29%C microballs	Spray-pyrolysis	733	2000 (300)	[249]
MoO_3/graphene	In situ hydrothermal	869	50 (80)	[253]
MoO_3/graphene	Spray-pyrolysis	1296	2000 (100)	[283]
MoO_3/SWCNHs	Microwave hydrothermal	654	1000 (3000)	[275]
MoO_3/graphene (1:1 in wt.)	Sonication	574	500 (100)	[284]
MoO_3/rGO	Freeze drying	778	100 (200)	[274]
SnO_2/MoO_3/C	Hydrothermal	1338	200 (300)	[276]

[a)] CNFs: carbon nanofibers; SWCNHs: single-walled carbon nanohorns.

Xia et al. [215] designed a polyporous MoO_3/C nanobelt anode material by a hydrothermal route with $(NH_4)_6Mo_7O_{24}{\cdot}4H_2O$ and activated carbon. The carbon component (8 wt.%) present in the composite serves as a physical barrier preventing the aggregation of the MoO_3 nanoparticles, and offers good electronic conductivity for electrode reaction. The MoO_3/carbon nanobelts exhibit a high specific capacity of 1000 mAh g^{-1} after 50 cycles at a current density of 0.1 A g^{-1} and retain a discharge capacity of 675 mAh g^{-1} at a current density of 5 A g^{-1} and long-term cycle stability to 550 cycles. In situ XRD examination on MoO_3/C electrode is

performed to understand the reaction mechanism of lithium with MoO_3 in initial process (**Fig. 17**).

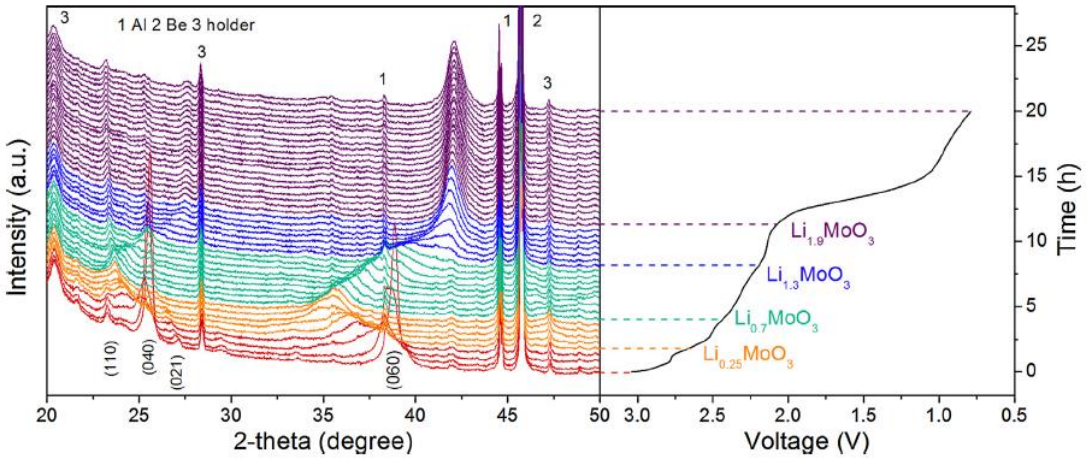

Fig. 17. In situ XRD results recorded during the first discharge of the MoO_3/C cell. During the initial lithiation process, the intensities of (040) and (060) peaks strongly decrease, indicating a phase transition from pristine MoO_3 to a lithium-inserted phase. The nanobelts anode delivers a specific capacity of 1014 mAh g^{-1} at 100 mA g^{-1} rate after 50 cycles in cut-off 0.01-3.0 V. Reproduced with permission from [215]. Copyright 2015 Elsevier.

2.1.9. Anodes for SIBs

MoO_3 is considered as an appealing choice of anode for sodium-ion batteries (SIBs) because of its high theoretical capacity of 1117 mAh g^{-1} (i.e., considering the charge transfer of $6e^-$/Mo). However, the poor cycling stability and capacity fade results from the large volume change upon Na^+ storage. Hence, several investigations offer new possibilities to bypass multiple material challenges facing current sodium electrodes.

The first experimental evidence of the electrochemical insertion of sodium in the orthorhombic MoO_3 lattice has been reported in 1995 by Spahr et al. [202]. Specific capacity of up to 240 mAh g^{-1} (at 0.15 mA cm^{-2} current density) was obtained using 0.5 mol L^{-1} $NaClO_4$ solution in propylene carbonate (PC) as electrolyte. In the first cycle (**Fig. 18a**), a very sharp reduction peak found in the cyclic voltammogram at a potential of about 2.4 V vs. Na^+/Na indicates the formation of a sodium bronze, Na_xMoO_3. It is further reduced to $Na_{x+y}MoO_3$. Subsequently, *y* moles of sodium are cycled rather reversibly. The galvanostatic discharge-charge curves (**Fig. 18b**) suggest the formation of the molybdenum bronze of sodium, Na_xMoO_3 [285] with $0 < x < 0.4$ at a voltage plateau of 2.5 V followed by a second plateau at about 1.8 V. A maximum Na uptake of ~1.5 mole is obtained at a potential limit of 1 V vs. Na^+/Na. In

2013, Hariharan reported the sodium storage in commercial α-MoO_3 powder (anode loading ~1.5 mg cm^{-2}) using 2016-coin-type cell with 1 mol L^{-1} $NaClO_4$ dissolved in ethylene carbonate (EC) and propylene carbonate (PC) as electrolyte (**Figs. 18c-e**) [233]. The sodiation and desodiation capacities of 771 and 410 mAh g^{-1} were delivered in the voltage window 0.04–3.0 V with average voltage profiles lying below 1.0 V. During sodiation (**Fig. 18c**), the voltage dropped from OCV (2.6 V) to reach a small plateau (i) at ca. 2.3 V. resulting the formation of sodium bronze Na_xMoO_3. Beyond the first Na^+ insertion plateau, the voltage profile in the region 1.8-1.2 V corresponds to additional insertion of Na in MoO_3 leading to the $Na_{x+y}MoO_3$, followed by a long sloping tail. MoO_3 anode also shows favorable rate performance and long cycle life of 117 mAh g^{-1} over 500 cycles at 0.2C (0.223 A g^{-1}). The real-time sodiation/desodiaton behaviors of α-MoO_3 during electrochemical cycling was observed by Xia et al. [286] investigating the *in situ* TEM and the electron diffraction patterns of α-MoO_3 nanobelts. The EELS measurements show that upon the first sodiation, α-MoO_3 initially forms an amorphous Na_xMoO_3 phase and is subsequently sodiated into intermediate phase of crystalline $NaMoO_2$, finally resulting in the crystallized Mo nanograins embedded within the Na_2O matrix. During the first desodiation process, Mo nanograins are firstly re-oxidized into intermediate phase $NaMoO_2$ that is further transformed into amorphous Na_2MoO_3, resulting in an irreversible phase transformation. The overall electrochemical reactions can be expressed by the relations:

$$MoO_3 + 6Na^+ + 6e^- \rightarrow Mo + 3Na_2O, \quad (10)$$

$$Mo + 3Na_2O \leftrightarrow Na_2MoO_3 + 4Na^+ + 4e^-, \quad (11)$$

where Eq. (10) states for the first sodiation and Eq. (11) for the subsequent desodiation/sodiation.

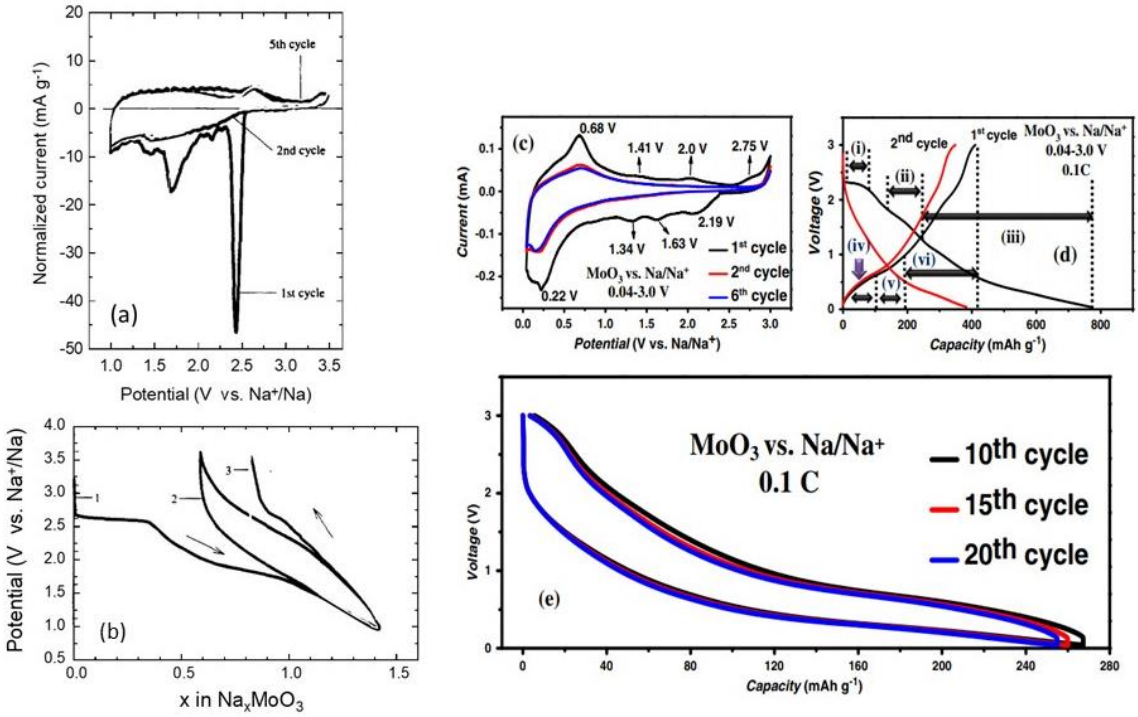

Fig. 18. Electrochemical patterns of the sodium intercalation in commercial α-MoO_3 powders. (a) Cyclic voltammogram in 0.5 mol L^{-1} $NaClO_4$/PC at 20 μV s^{-1} sweep rate. (b) Galvanostatic discharge charge curves in 0.5 mol L^{-1} $NaClO_4$/PC at 0.15 mA cm^{-2} (first three cycles). Reproduced with permission from [202]. Copyright 1995 Elsevier. Electrochemical patterns of the sodium intercalation in α-MoO_3 powders prepared by precipitation of phosphomolybdic acid. (c) Cyclic voltammogram of MoO_3 vs. Na^+/Na in the window 0.04–3.0 V recorded at 0.058 mV s^{-1}. (d) First and second galvanostatic voltage profiles of MoO_3 vs. Na^+/Na at 0.1C (0.1117 A g^{-1}) in the window 0.04–3.0 V. (e) Voltage profiles showing hysteresis at selected cycles. Reproduced with permission from [233]. Copyright 2013 Elsevier.

Sreedhara et al. [287] fabricated a 3D MoO_3-rGO composite from MoO_3 nanosheets chemically tagged with optimum amounts of rGO. The MoO_3-(10 wt.%)-rGO composite exhibits remarkable electrochemical stability (first discharge capacity of 1061 mAh g^{-1} at C/20 rate; ICE of 88%; capacity retention of 665 mAh g^{-1} after 100 cycles), cyclability and high rate capability over a wide range of operating currents (0.05-1C). At 1 C, the MoO_3–(10 wt.%)-rGO dislays a capacity of 330 mAh g^{-1}. Jiang et al. [288] demonstrated a surface phosphorylation strategy to mitigate the degradation of 3D MoO_3 array electrodes, which allows to sustain a capacity of 265 mAh g^{-1}, or ~90% of the initial value, at a rate of 2 A g^{-1} over 1500 cycles. Kinetic analysis unveils a capacitance-dominated Na^+ storage behavior, owing to the enhanced electron mobility imparted by oxygen vacancies that are simultaneously introduced by

phosphorylation. Liu et al. [289] prepared a nanocomposite of MoO_3 nanobelts coated with polypyrrole (PPy) as anode material and investigated the electrochemical performance of the full cell formed by PPy@MoO_3 as anode and $Na_{0.35}MnO_2$ as cathode in 0.5 mol L^{-1} Na_2SO_4 aqueous electrolyte, which delivers an energy density of 20 Wh kg^{-1} at 80 Wkg^{-1} and even maintain 18 Wh kg^{-1} at 2.6 kWkg^{-1}.

Yang et al. reported the synthesis of MoO_3 nanoplates (MoO_3 NPs) from Mo-based metal–organic frameworks via a facile heating treatment [235]. When used as an anode in SIB, the material showed a discharge capacity of 154 mAh g^{-1} at 50 mA g^{-1} after 1200 cycles. Even at 500 mA g^{-1}, it exhibits a specific capacity 217 mAh g^{-1} after 500 cycles. It is believed that the nanoplate morphology prevents the pulverization caused by volume expansion in SIBs. Li et al. [290] reported that MoO_{3-x} grown on flexible carbon cloth, with a well-controlled oxygen vacancy, exhibits a specific capacity of ~150 mAh g^{-1} after 200 cycles at 0.1 A g^{-1} current rate in the voltage range 4.0-1.0 V vs. Na^+/Na, and long-life performance of 79 mAh g^{-1} after 2000 cycles at 1 A g^{-1}. The oxygen vacancy in $MoO_{3-\delta}$ is responsible for the two-plateau voltage profile, in contrast to the sloping feature observed in α-MoO_3. Xu et al. [291] demonstrated the beneficial effect of oxygen vacancies (OVs) in $MoO_{3-\delta}$ nanosheet anode for SIBs. A series of measurements show that the OVs increase the electric conductivity and Na-ion diffusion coefficient, and that the ultrathin Al_2O_3 coating promotes the effective reduction of cycling-induced solid-electrolyte interphase. The Al_2O_3 coated $MoO_{3-\delta}$ nanosheets exhibited high reversible capacity and great rate capability with the capacities of 283.9 (50 mA g^{-1}) and 179.3 mAh g^{-1} (1 A g^{-1}) after 100 cycles. Rod-like α-MoO_3 is successfully designed by alternating voltage induced electrochemical synthesis (AVIES) approach with subsequent control of the morphology and texture of MoO_3 by applying various calcination temperature of 300–600 °C [292]. When utilized for SIBs, it presents the high charge capacities of 305 mAh g^{-1} at 1C rate and 143 mAh g^{-1} at 10C. Even after 3000 cycles at 10C, a significant capacity of 108 mAh g^{-1} is still delivered. Zhu et al. [293] fabricated an amorphous MoS_2/MoO_3/nitrogen-doped carbon composite using a reaction that partially sulfurizes organic–inorganic hybrid material Mo_3O_{10}($C_2H_{10}N_2$) (named as MoO_y/ethylenediamine) nanowire precursors at low temperature of 300 °C. Tested in sodium cell, the composite retains 539 mAh g^{-1} after 200 cycles at 300 mA g^{-1} and maintains 340 mA h g^{-1} at 1000 mA g^{-1} after 220 cycles. The α-MoO_3 nanosheets vertically grown on activated carbon fiber cloth exhibit a discharge capacity of 2.5 mAh cm^{-2} (1621 mAh g^{-1}) at 0.1 mA cm^{-2} and capacity retention of 90% after 200 cycles at 0.2 mA cm^{-2} [294]. Zhang et al. [259] prepared MoO_3/reduced graphene oxide (MoO_3/rGO) composites via one-step hydrothermal method, and evaluated as anode materials for SIBs. The MoO_3/rGO composite

with 6 wt.% rGO delivers the highest reversible capacity of ~208 mAh g^{-1} at 50 mA g^{-1} after 50 cycles. **Table 7** summarizes the electrochemical performance of MoO_3 composites as anode materials for SIBs prepared by various methods.

Table 7. Electrochemical performance of MoO_3 composites as anode materials for SIBs prepared by various methods. Relevant cycle number is given in brackets.

Material	Synthesis	Specific capacity (mAh g^{-1})	Current rate (mA g^{-1})	Ref.
α-MoO_3	Precipitation	117	223 (500)	[233]
MoO_3-rGO	Sonication+hydrothermal	330	1000 (100)	[287]
MoO_3 NPs	Heat treatment	154	50 (1200)	[235]
MoO_3 arrays	Surface phosphorylation	265	2000 (1500)	[288]
MoO_{3-x}	Grown on carbon cloth	79	1000 (2000)	[290]
Al_2O_3/MoO_{3-x}	Coating	179	1000 (100)	[291]
Rod-like α-MoO_3	Electrochemical	108	10C (3000)	[292]
MoS_2/MoO_3/N-doped C	Organo-metallic	538	300 (200)	[293]
MoO_3 NSs/C fibers	Hydrothermal	1458	65 (200)	[294]
MoO_3/rGO	Hydrothermal	208	50 (50)	[259]
MoO_3/rGO	Spray-drying	1115	500 (100)	[223]
MoO_3/rGO	Spray-drying	1000	0.5C (100)	[295]
MoO3/$MoSe_2$	Solvothermal+annealing	540	500 (200)	[296]

2.2. Monoclinic β-MoO_3

MoO_3 in its β-modification presents a great interest in many applications such as catalysts [297,298], gas sensors [299] and batteries [300]. It was revealed that β- MoO_3 exhibits better response than that of α-MoO_3 in some catalysis reactions due to the high acidity of Lewis acid sites on the surface of β-MoO_3 [301]. Therefore, a metastable β-MoO_3 which has been reported to have high catalytic property in methanol oxidation to formaldehyde [302] due to the overall symmetry of this phase.

2.2.1. Structure

Since 1986, the β-phase MoO_3 with distorted 3D ReO_3-related structure similar to WO_3 is known from the work of McCarron [46,303,304]. This novel metastable phase with monoclinic symmetry results from the thermal treatment of spray-dried powders of aqueous molybdic acid solutions [46]. The β-MoO_3 phase ($P2_1/c$ S.G., a = 7.118 Å, b = 5.366 Å, c = 5.568 Å, β = 91.99°, and JCPDS: 00-047-1081) has a crystal structure similar to ReO_3 (cubic, $Pm\bar{3}m$), which possesses a three-dimensional network of ReO_6 octahedra sharing the six corners. Its structure

is markedly different from the crystal structure of α-MoO_3, in which the MoO_6 octahedral units share corner oxygen atoms in the direction of the *c*-direction, and edge sharing occurs in the direction of the *c*-axis (inset **Fig. 19a**). The absence of van der Waal forces is due to adjacent MoO_6 octahedra sharing corners, which form a 3D monoclinic network. As shown in (**Fig. 19a**) the XRD pattern of β-MoO_3 is characterized with two dominant peaks at 2θ = 22.9° and 24.9° corresponding to the (001) and (200) planes, respectively. **Fig. 19b** shows the Raman spectrum of β-MoO_3, which differs than the α-MoO_3 spectral features. The peaks at 775, 840 and 904 cm^{-1} are the Raman profiles corresponding to the Mo-O stretching modes of β-MoO_3. The absence of peak in the high-frequency range (ν > 904 cm^{-1}) indicates that no oxygen atoms are singly coordinated [305].

Phuc et al. [306] reported the existence of a new metastable β-MoO_3 green phase synthesized from MoO_2Cl_2 solution derived from H_2MoO_4 powder and concentrated HCl solution. This new phase crystallizes in a triclinic structure similar to that of WO_3 and is stable up to 435 °C. The XRD pattern exhibits three main reflection at 22.9°, 24.0°, and 24.9°, which are indexed as (002), (020) and (200) of the triclinic symmetry ($P\bar{1}$ space group) [307]. The Raman spectrum of the β-MoO_3 green phase displays Mo—O—Mo vibration modes located at 767, 842 and 898 cm^{-1} along with a weak peak at 708 cm^{-1}, which does not exist in the spectrum of the β-MoO_3 yellow phase. The β'-MoO_3 phase was prepared by heating the $D_{0.99}MoO_3$ intercalate in oxygen at 200 °C, driving off D_2O. The structure of β'-MoO_3 was determined from neutron powder diffraction as monoclinic ($P2_1/n$ S.G., a = 7.4245(1) Å, b = 7.4783(1) Å, c = 7.6897(1) Å, β = 90.090(2)°) is isostructural with the room temperature monoclinic modification of WO_3 [47].

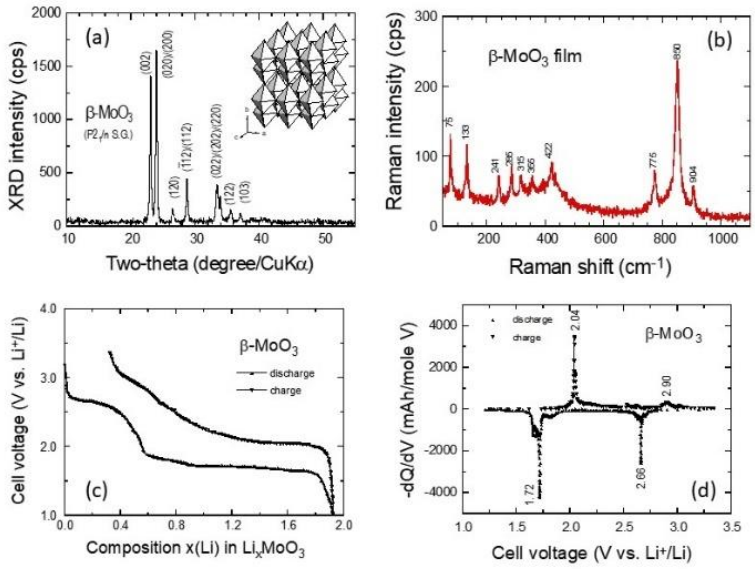

Fig. 19. (a) XRD pattern of the β-MoO_3 yellow phase ($P2_1/c$ space group). (b) Raman spectrum recorded with the excitation line at λ = 532 nm. (c) GCD profile carried out at C/10 rate. (d) Differential capacity plot (-d*Q*/d*V*) vs. *V*.

2.2.2. Synthesis

The synthesis of the metastable β-MoO_3 phase is limited due to the difficulty in finding suitable molybdenum source such as ammonium molybdate, molybdic acid, polyoxomolybdate. The first successful preparation of β-MoO_3 was reported by McCarron [46] who employed a soft-chemical route. The synthesis consists of the dehydration of blue molybdic acid ($Mo_{36}O_{112}(H_2O)_{16})_8$ solution, which is obtained via cation exchange of Na_2MoO_4 solution (1 mol L^{-1} of Na_2MoO_4 only gives 0.1 mol L^{-1} of blue molybdic acid solution). Mizushima et al. [301] reported that this method consumes a lot of water and also has very low yield, i.e., the Mo content in the final solution was only 3.3% of the initial value. In 2011, Mizushima et al. synthesized the β-MoO_3 phase (yellow powders) by a soft chemical transformation of α-MoO_3 via the addition of HNO_3 to an aqueous solution of α-MoO_3, followed by drying and calcination [308]. Yao et al. synthesized β-MoO_3 from sodium molybdate solution [299] but α-MoO_3 was detected in the final product. β-MoO_3 crystal has a yellow color [46,306,309-311]. Moreover, β-MoO_3 can reportedly be obtained by a novel method of freeze drying the same molybdic acid solution [312]. These methods yield a mixture of α-MoO_3 and β-MoO_3. Juárez Ramírez and Martínez-de-la-Cruz [310] produced pure β-MoO_3 free from the α phase through vacuum drying. This method, however, requires a very long drying time. In 2005, Mizushima et al. [311] reported a new preparation method for pure

β-MoO_3 using a generalized rotary evaporator. The simple evaporation of a cation-exchanged molybdic acid solution forms pure α-MoO_3 crystallites (bright yellow powder) after calcination at 573 K, whereas the addition of a small amount of nitric acid to the solution resulted in selective formation of the β-phase. The preparation of β-MoO_3 thin films has reported by several workers. Porous high surface area thin films of nanosheet-shaped (50-100 nm thick) monoclinic β-MoO_3 were deposited onto platinized Si substrates using patch antenna-based atmospheric microplasma processing [313]. β-MoO_3 thin films were prepared by reactive rf sputtering deposition at low substrate temperature of 200 °C under a 65%Ar+35%O_2 gas mixture at the pressure of 0.13 Pa [314]. Nearly a pure β-phase was formed (i.e., well-resolved XRD reflections at ca. 2θ = 23.0, 25.0, 47.5 and 51.8° corresponding to the (011), (200), (022) and (400) of the $P2_1/c$ structure, respectively**)**, which exhibits a preferred *a*-axis orientation when the annealing temperature is in the range of 300-350 °C. MoO_3 films were electrodeposited on fluorine-doped tin oxide (FTO) glass substrates from sodium-molybdate (Na_2MoO_4) solutions. The monoclinic β-phase was obtained by manipulating the cyclic voltammetry conditions [299]. Characterization of the MoO_3 films grown by molecular beam epitaxy on *c*-plane sapphire substrates was conducted by Koike et al. [315]. XRD and Raman measurements revealed that amorphous, (100) β-phase, and (010) α-phase MoO_3 films were preferentially grown at 150, 200, and 350 °C, respectively. Their optical bandgap energies were estimated to be ~3.5 eV for the amorphous, ~3.7 eV for the β-phase, and ~4.1 eV for the α-phase films. The β-phase films were completely transformed into stable α-phase films at 600 °C.

A transformation from the β to α phase took place spontaneously at the temperature ranging from 387 to 450 °C, according to several reports [304,316-318]. Topotactic transition of metastable β-MoO_3 to orthorhombic α-MoO_3 has been reported as a result of thermal treatments at temperature 350 °C and above. The presence of the β-phase of MoO_3 at low temperature ~250 °C is supported by Kuzmin [316], Julien [317] and McEvoy [318], who have shown that sintering in air of hydrated, amorphous molybdenum oxide at relatively low temperatures produces a morphological change from an amorphous phase to a metastable, monoclinic β-MoO_3. Raman microprobe spectroscopy experiments have revealed that two phases of MoO_3 coexist. Some regions exhibit characteristic Raman shifts of 997, 821, and 668 cm^{-1} that are unique to α-MoO_3 while other regions exhibit Raman stretches at 850 and 776 cm^{-1} that are specific to β-MoO_3 [319].

2.2.3. Li intercalation

Pristine β-MoO_3 exhibits an electrical conductivity below 10^{-7} S cm^{-1} [320], which implies to build an electrode using of carbon additive. In 2003, Juárez Ramírez and Martínez-de-la-Cruz demonstrated the ability of β-MoO_3 obtained through soft chemistry methods to accommodate electrochemically Li^+ ions [300,310]. Electrochemical experiments were carried out in Swagelok-type cells using Li foil as negative electrode and a 1 mol L^{-1} $LiPF_6$ in ethylene carbonate (EC)/dimethyl carbonate (DMC) as electrolyte. The cathode electrode was made of β-MoO_3 powders, carbon black and ethylene–propylene–dieneterpolymer (EPDT) in a 90:9:1 ratio. Lithium insertion in β-MoO_3 proceeds at least in a two-step reduction process. The maximum amount of lithium inserted leads to a specific capacity of 370 mAh g^{-1} (gravimetric energy density of 666 Wh kg^{-1}). However, a total loss of 25% occurs after the first charge-discharge cycle due to structural transformations with variable Li_xMoO_3 composition. For several discharge/charge cycles, the Li//β-MoO_3 cell is able to maintain 280 mAh g^{-1} at 400 µA cm^{-2} current density. Porous β-MoO_3 nanosheets (50-100 nm thick) produced by atmospheric microplasma were applied to LIBs [313]. The insertion/de-insertion of Li^+ ions was performed in 1 mol L^{-1} $LiN(SO_2CF_3)_2$ in EC:DEC (1/1, v/v) electrolyte. The cyclic voltammogram displays cathodic peaks at 2.2 and 1.6 V and the anodic peaks at 1.7 and 2.1 V. At galvanostatic current of 10 μA g^{-1}, the discharge process proceeds through several steps and two-phase regions are observed at 1.7 and 2.7 V, respectively. The charge capacity is 370 mAh g^{-1} and corresponds to a mole fraction of 2 Li atoms per Mo atom. McEvoy et al. [321] investigated the Li-ion insertion energetics and kinetics of β-MoO_3 films prepared by electrodeposition from acidic peroxo-polymolybdate solutions. Films deposited on ITO-coated glass substrates and sintered in the temperature range 250-350 °C display an intermixed α-β-MoO_3 structure. In $LiClO_4$/propylene carbonate solution, the electrochemical response for films sintered at $T \geq 250$ °C exhibits three sets of distinguishable redox peaks. This response is assigned to the faradaic electron transfer and to a large capacitive charge during Li^+ insertion. The smaller anodic peak area after the first cycle suggests that the insertion/deinsertion process is only 60% reversible. It is more likely due to some fraction of Li^+ becoming trapped in the film due to the irreversible formation of a molybdenum bronze (i.e., $Li_{x+2}Mo^{VI}_{1-x}Mo^{V}_{x-z}Mo^{IV}_{z}O_{3-y-z}$). **Figure 19c** shows the typical first discharge charge curve of a β-MoO_3 film prepared by pulsed-laser deposition on silicon wafer at T_s = 250 °C. The OCV of the Li//β-MoO_3 cell is 3.20 V vs. Li^+/Li. In the potential range 3.2-1.0 V, the transfer of 1.92 e^-/Mo occurs during the discharge at C/10 rate (36 mA g^{-1}) yielding a specific capacity of 357 mAh g^{-1}. The first charge occurs with a coulombic efficiency of 83%. The two distinct sets of redox reaction are determined by the plot

of the differential capacity (-dQ/dV) vs. V at 2.66/1.72 V and 2.90/2.04 V for the anodic and cathodic peaks, respectively (**Fig. 19d**).

2.3. Hexagonal h-MoO_3

Hexagonal molybdenum trioxide (h-MoO_3) is known for one century when, in 1906, Rosenheim described the preparation of a molybdic acid hydrate by precipitation of an aqueous solution of ammonium paramolybdate, $(NH_4)_6[Mo_7O_{24}]_3$ $4H_2O$, acidified with HNO_3 [322]. In 1969, the Roseheim's process was used by Peters for the XRD analysis of the isolated precipitates [323]. In 1980s, several workers revised the structure of hexagonal molybdates [324,325]. Caiger et al. [325] reported that the "hexagonal MoO_3" series corresponds to the partially dehydrated and de-ammoniated ammonium decamolybdate $NH_4Mo_5O_{15}OH{\cdot}2H_2O$. Mc Carron et al. investigated the crystal structure of h-MoO_3 with incorporation of sodium and proton in the tunnels [324]. Functional modifications and diversified applications of h-MoO_3 can be found in Refs. [325-331]

2.3.1. Structure

The framework of hexagonal h-MoO_3 is constructed from zigzag chains of MoO_6 octahedra linked to each other by corner sharing along the c direction giving large one-dimensional tunnels (**Fig. 20a**). The h-MoO_3 phase can generally be formulated as $(A_2O)_x{\cdot}MoO_3{\cdot}(H_2O)_y$, where A is an alkali-metal ion or ammonium ion, and the exact values of x and y depend on the details of the preparation and subsequent treatment [101,332-334]. The salient structural feature for crystalline h-MoO_3 is the presence of tunnel (~3 Å in diameter) running along the c axis, in which cations or water molecules can be sitting. Each tunnel is enclosed by 12 MoO_6 octahedra linked by sharing corners along the a and b directions and by edges along the c direction (**Fig. 20a**). The tunnel structure in h-MoO_3 exhibits better intrinsic properties than α-MoO_3, such as high sensitivity, coloration efficiency, and faster response. The sample prepared via the precipitation of molybdenum oxide from an ammonium paramolybdate solution, by the addition of nitric acid has a "sea-urchin" shape composed of h-MoO_3 nanorods (SEM images in **Fig. 20b**) [335]. **Figure 20c** depicts the XRD pattern of crystalline h-MoO_3. The diffraction peaks appeared at 2θ = 9.62°, 16.72°, 19.34°, 25.68°,29.26°, 33.86° and 35.32° can be attributed to the planes of (100) (110) (200) (210) (300) (220) and (310), respectively of the hexagonal structure (space group $P6_3/m$) with lattice parameters a= 10.53 Å and c = 14.97 Å (JCPDS card No. 21-0569) [13,27,28,332,335]. However, using Rietveld refinements, XRD reflections were successfully indexed with a= 10.55 Å and c = 3.72 Å [48]. A structural transformation from

hexagonal to stable orthorhombic α-MoO_3 phase was observed at 350 °C [107]. The publication by Lunk et al. [334] aimed to dispel the confusion concerning the identity of the hexagonal molybdenum trioxide (HEMO) phases variously described in the literature. The reported HEMO composition are characterized by virtually identical XRD patterns with unit cell parameters a ≈ 10.60 Å and c ≈ 3.72 Å. As occurred in the case of MnO_2 hollandite, the presence of large cations into the tunnel can stabilize the h-MoO_3 structure [337]. However, the growth of crystalline h-MoO_3 without large cations incorporated into the tunnels can be obtained from two methods: one is the hot liquid-phase process [335], and the other is the liquid-phase process followed by autoclaving and vacuum heat-treatment [27,332]. The crystallinity and phase purity of as-synthesized nanorods were evidenced by micro-Raman spectrum (**Figure 20d**), which exhibits sharp high-frequency peaks at 980, 915, 902 and 888 cm^{-1} assigned to the symmetrical and asymmetrical stretching modes of Mo=O double bond. The peak at 818 cm^{-1} is assigned to the stretching mode of Mo_2−O and the band at 694 cm^{-1} is the scissoring vibration of the O-Mo-O bonds. Raman peaks at 395, 412 and 495 cm^{-1} are attributed to the bending modes of O-Mo-O bonds, while the peaks at 247 and 220 cm^{-1} are assigned to the twisting vibration of O-Mo-O bonds [48,338,339]. Raman peaks in the low-frequency (174 and 145 cm^{-1}) belong to the external lattice modes.

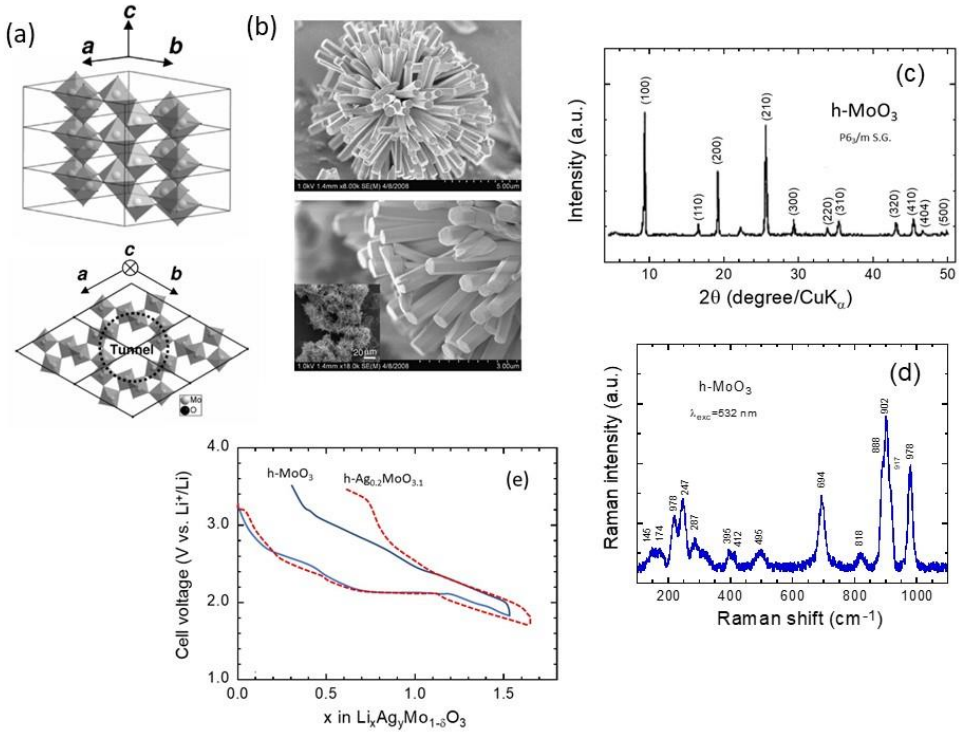

Fig. 20. (a) Crystallographic structure of h-MoO_3. The unit cell is shown by a thin black line. (b) SEM images of h-MoO_3 nanorods: projected view (top) and side view (bottom). Reproduced with permission from [335]. Copyright 2009 Elsevier. (c) XRD pattern of h-MoO_3 with

reflection indexed with $P6_3/m$ S.G (JCPDS card No. 21-0569). (d) Raman spectrum of h-MoO_3 recorded with the laser excitation λ_{exc} = 532 nm. (e) Galvanostatic discharge-charge profiles recorded at 50 µA cm^{-2} current density for h-MoO_3 electrode with empty tunnels and h-$Ag_{0.2}MoO_{3.1}$ electrode. Reproduced with permission from [340]. Copyright 1995 Elsevier.

2.3.2. Synthesis

The metastable hexagonal form of *h*-MoO_3 has been successfully prepared starting from the ammonium molybdate, using a "chimie douce" reaction [107,332,341-345]. In the precipitation method, a mixture of ammonium heptamolybdate tetrahydrate $(NH_4)_6Mo_7O_{24}\cdot 4H_2O$ and concentrated nitric acid (37% HNO_3) heated to a temperature in the range 55-85 °C was used [13,107,346]. Hydrothermal technique has been widely used for the synthesis of h-MoO_3 [332,333,347]. Zheng et al. [332] prepared h-MoO_3 nanobelts by a simple hydrothermal route from peroxomolybdate solution with the presence of sodium nitrate as a mineralizer. It was demonstrated that the high openness degree in the tunnel structure of h-MoO_3 provides larger spatial locations for cation insertion/extraction and diffusion. Song et al. prepared the high purity h-MoO_3 phase via chemical precipitation, hydrothermal treatment and calcination. In the procedure of precipitation, the concentrated HCl played a key role for the formation of the metastable h-MoO_3 [13]. Atuchin et al. [28] prepared h-MoO_3 nanocrystals in the form of well-faceted straight hexagonal rods with an aspect ratio of $l/d \simeq 60$. Han et al. [348] demonstrated that rod-shaped h-MoO_3 were obtained by hydrothermal method using a low concentration of nitric acid (0.1-1.0 mol L^{-1} HNO_3), while higher concentration leads the nanostructured α-MoO_3 phase. Hexagonal and truncated hexagonal shaped MoO_3 nanoplates (MoO_3 HNP) were synthesized through a simple vapor-deposition method in Ar atmosphere under ambient pressure without the assistant of any catalysts. The nanoplates have a large area surface. The Raman spectrum shows a significant size effect on the vibrational property of MoO_3 HNP [344]. Hexagonal MoO_3 nanoparticles were synthesized by hydrothermal method (T = 90 °C for 12 h) from a solution of 0.2 mol L^{-1} ammonium molybdate in 10 ml of distilled water added with 5 ml of concentrate HNO_3. When heated to T > 150 °C, h-MoO_3 transforms to the layered α-MoO_3 phase [107,326]. Using chemical precipitation, the h-MoO_3 phase with unique rod-like morphology was synthesized by Song et al. [13]. Guan et al. [349] obtained a nanodisk of hexagonal h-MoO_3 by heat treatment of rhodamine B/molybdic acid aggregates (RBMA). Dhage et al. [29] fabricated *h*-MoO_3 nanorods via the probe sonication route using ammonium molybdate, urea and sodium dodecyl sulphate at 70 °C. Irmawati and Shafizah [344] produced pure h-MoO_3 nanocrystals through the acid washing method, which consists in

the reduction of the basic aqueous solution of ammonium heptamolybdate tetrahydrate and ammonium carbonate from pH of 8.85 to 1.95-2.10 by addition of 5 mol L^{-1} HNO_3 (lattice parameters a = 10.55 Å and c = 14.89 Å). Pan and coworkers [48] prepared nano- and microrods h-MoO_3 using modified liquid-phase processes with concentrated HNO_3 and H_2SO_4 and determine the hexagonal structural patterns as $a \approx 10.57$ Å and $c \approx 3.72$ Å. The fabricated rods have a BET total surface area of ~3 m^2 g^{-1}, with crystallite size ranging from 33 to 46 nm. Zheng et al. [332] synthesized h-MoO_3 nanobelts by a simple hydrothermal route from peroxomolybdate solution with the presence of sodium nitrate as a mineralizer.

2.3.3. Li intercalation

Due to the many empty sites in the tunnel structure, i.e., hexagonal tunnel and trigonal cavity (**Fig. 20e**), the h-MoO_3 electrode exhibits a high capacity on Li^+ battery application [324,325,332,340,350-351]. In the early work by Gao et al. [340], the lithium intercalation/deintercalation reaction was studied on h-MoO_3 with empty tunnels and Ag-containing tunnels. In the discharge curves carried out at 30 µA cm^{-2} in the potential range 1.7-3.5 V vs. Li^+/Li (**Fig. 20e**), the voltage plateau at x = 0.7 indicates a two-phase region with lattice parameters a = 10.559(5) Å and c = 3.725(3) Å (i.e., 0.97% volume change). For the hexagonal $Ag_{0.2}MoO_{3.1}$ electrode, the ICE was reduced to ~60%. Electrochemical tests, carried out at current density of 0.1 mA cm^{-2} in the voltage range 1.2–4.0 V vs. Li^+/Li, show excellent performances with an initial reversible discharge specific capacity of 402 mAh g^{-1}, i.e., insertion of 2.2 Li/Mo. Xu et al. reported a first discharge voltage plateau at ~1.8 V for hydrothermally synthesized h-MoO_3 [352]. Tang et al. [353] fabricated h-MoO_3/graphene composites using a facile hydrothermal method via a template effect of GO on catalyzing the phase transition from α-MoO_3 to h-MoO_3. The galvanostatic charge/discharge tests of this composite as anode of Li cell exhibit a first reversible capacity of 987 and 739 mAh g^{-1} after 30 cycles under the current density of 100 mA g^{-1} in the voltage range of 0.01–3 V vs. Li^+/Li. Recently, Joseph et al. [354] fabricated MoO_3 microrods with hexagonal structure as an Al-ion intercalation host material and show its use as an electrode for an aqueous Al-ion battery. h-MoO_3 microrods yield a discharge capacity of ~300 mAh g^{-1} for 150 cycles at a current density of 3 A $g^{-1}$and 90 % capacity retention after 400 cycles. Xiao et al. [355] used a solution-based method to synthesized 2D h-MoO_3 nanosheets Mo was dissolved in H_2O_2 to produce the molecular peroxomolybdate precursor solution mixed with NaCl microcrystals as lattice-matched templates. 2D h-MoO_3 was tested in a 1 mol L^{-1} $LiClO_4$ solution with a 1:1 mixture of ethylene carbonate and dimethyl carbonate. Intriguingly, a gravimetric capacity of 996 C g^{-1} (277 mAh

g^{-1}, 1.49 Li/Mo) at 2 mV s^{-1} was much larger than that previously reported for mesoporous α-MoO_3 in 1 mol L^{-1} $LiClO_4$ with propylene carbonate.

The coloration properties from facile Li^+ ion insertion/extraction in electrochromic devices was demonstrated by several workers. Zheng et al. [332] showed that the performances concerning photochromism on two types of MoO_3 nanobelt suspensions show that the photochemical efficiency of h-MoO_3 is more excellent than that of α-MoO_3. Electrochromic performance of the h-MoO_3 nanobelts coated film was tested in a three-electrode cell cycled between -1.0 and -2.0 V vs. SCE with 1 mol L^{-1} $LiClO_4$ in propylene carbonate as electrolyte and graphite plate as the counter electrode. Two strong and wide transmittance peaks at ~620 and 590 nm imply that the MoO_3 nanobelt film can display from green-blue to dark blue color at different voltages. Huang et al. [211] reported the synthesis of h-MoO_3 nanorods (average length of 20-50 mm and a width of 1-10 mm) using a hydrothermal treatment at 180 °C for 24 h of a solution of $(NH_4)_6Mo_7O_{24}\cdot 4H_2O$ adjusted at pH~1 by addition of 8 mol L^{-1} HNO_3. Electrochemical properties of h-MoO_3 (**Fig. 21**) were examined as anode for LIB over 100 cycles at 0.1C rate. The discharge capacity of 780 mAh g^{-1} (2nd cycle) rapidly drops to 132 mAh g^{-1} after 100 cycles, merely 14% of the 2nd cycle. The structure of h-MoO_3 leads to poor capacity stability. After 20 cycles, the hexagonal framework transforms to agglomerated bulk structure with slow Li^+/e^- transfer kinetic and finally nanorods are pulverized after 100 cycles (**Fig. 21d**). **Table 8** lists the electrochemical performance of some h-MoO_3 anode materials for LIBs. Electrochemical properties of h-MoO_3 have been also investigated by Song et al. [350]. The first reversible discharge specific capacity can reach 402 mAh g^{-1} (2.2 Li/Mo uptake) at 0.1 mA cm^{-2} current density in the voltage range 1.2–4.0 V *vs.* Li^+/Li.

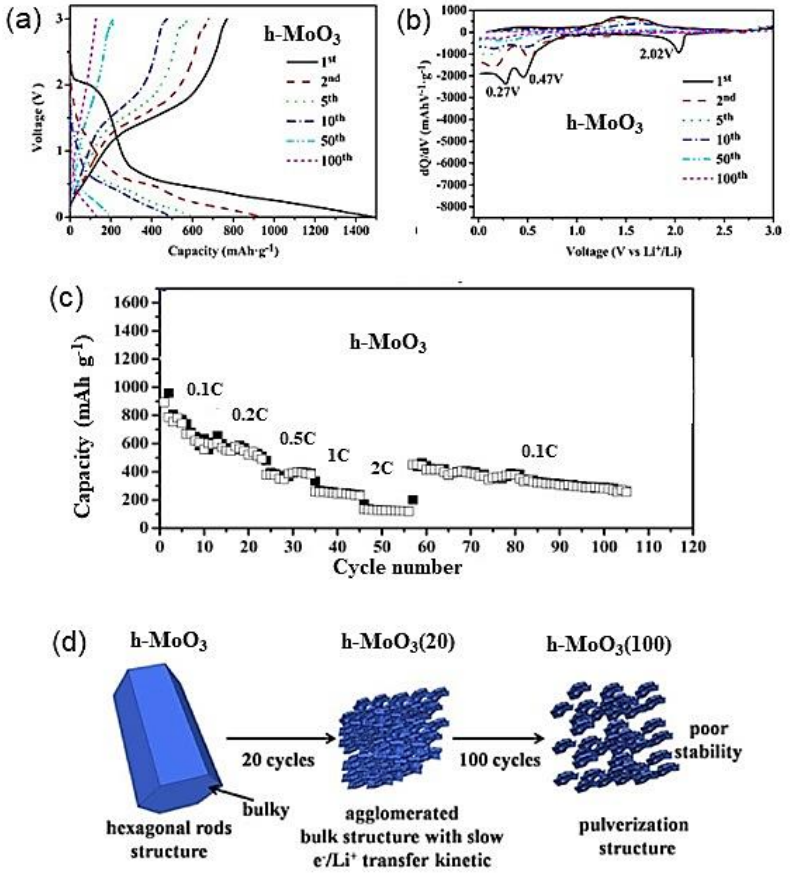

Fig. 21. (a) Galvanostatic charge-discharge curves in different cycles carried out at 0.1C rate of h-MoO_3. (b) Differential capacity vs; voltage curves. (c) Rate capability of h-MoO_3 at rates between 0.1 and 2C. (d) Schematic illustration of the structural changes upon cycling. Reproduced with permission from [211]. Copyright 2016 Elsevier.

Table 8. Electrochemical performance of h-MoO_3 anode materials for LIBs.

Material	Synthesis	Specific capacity (mAh g^{-1})	Current rate (mA g^{-1})	Ref.
h-MoO_3 NRs	Hydrothermal	132	0.1C (100)	[211]
h-MoO_3/graphene	Hydrothermal	739	100 (30)	[353]
h-MoO_3 NRs	Solvothermal	780	0.1C (150)	[356]

2.4. Monoclinic MoO_3-II phase

The metastable MoO_3-II (ε-MoO_3) phase was highlighted by Mc Carron and Calabrese [357] from the combination of high pressure and high temperature (60 kbar and 700 °C), using a tetrahedral anvil apparatus at elevated temperature. Using a soft-chemical synthesis of the high-pressure phase of molybdenum trioxide, MoO_3-II, has been described by Baker et al. [49]. A topotactic dehydration of either the white molybdenum trioxide monohydrate $MoO_3 \cdot H_2O$, or

the hemihydrate $MoO_3 \cdot ½H_2O$ provides a convenient synthetic route to the high-pressure phase. The structural filiations between the various molybdenum trioxide and trioxide hydrate phases are delineated, and simple mechanistic models for the transformations have been proposed, which involves a change in the stacking sequence of the Mo-O layers. MoO_3-II is the high-pressure modification of α-MoO_3. Like the α-MoO_3 layered structure, the individual $MoO_{3/3}O_{2/2}O_{1/1}$ layers of MoO_3-II and α-MoO_3 are virtually identical. The stacking sequence of the layers of MoO_3-II (*AAA* stacking) differs from that of α-MoO_3 (*ABA* stacking), which is equated with an improved packing efficiency for the layers of MoO_3-II versus those of α-MoO_3 (**Fig. 22**). Its structure is monoclinic, $P2_1/m$ S.G., with unit cell parameters a = 3.954(l) Å, b = 3.687(2) Å, c = 7.095(4) Å and β = 103.75(4)° (4.75 g cm^{-3}). In contrast, Åsbrink et al. [358] reported the lattice parameters of α-MoO_3 as a function of pressure up to 7.4 GPa at ambient temperature, but did not find any high-pressure phase transition. Liu et al. [44] demonstrated that the MoO_3-II phase can be achieved at 12 GPa and room temperature. The lattice parameters refined within the $P2_1/m$ space group for the new phase were a=3.860(3) Å, b=3.711(6) Å, c =6.329(4) Å, β = 104.811°, and unit cell volume V=87.66(5) $Å^3$ (Z=2). The metastable MoO_3-II phase is relatively more stable than h-MoO_3 but can convert rapidly to stable orthorhombic phase α-MoO_3 at temperatures above 200 °C [8,357]. Another high-pressure phase, the monoclinic MoO_3-III phase ($P2_1/c$ S.G.), has been observed at pressure of 25 GPa at room temperature. The lattice parameters refined within the $P2_1/c$ space group for the MoO_3-III phase were a=5.749(2) Å, b =4.804(6) Å, c=6.095(3) Å, β =116.73(5)°, and unit cell volume V=150.36(5) $Å^3$ (Z=4). The Raman spectrum of MoO_3-III did not display the peak associated with the unique molybdyl bond (νMo=O stetch) confirming this phase is not a layered structure. The stretching modes at 786, 834 and 893 cm^{-1} reveal the Mo-O bonds in the corner-sharing MoO_6 octahedra. The MoO_3-III phase is likely a distortion of the ReO_3-type structure [44].

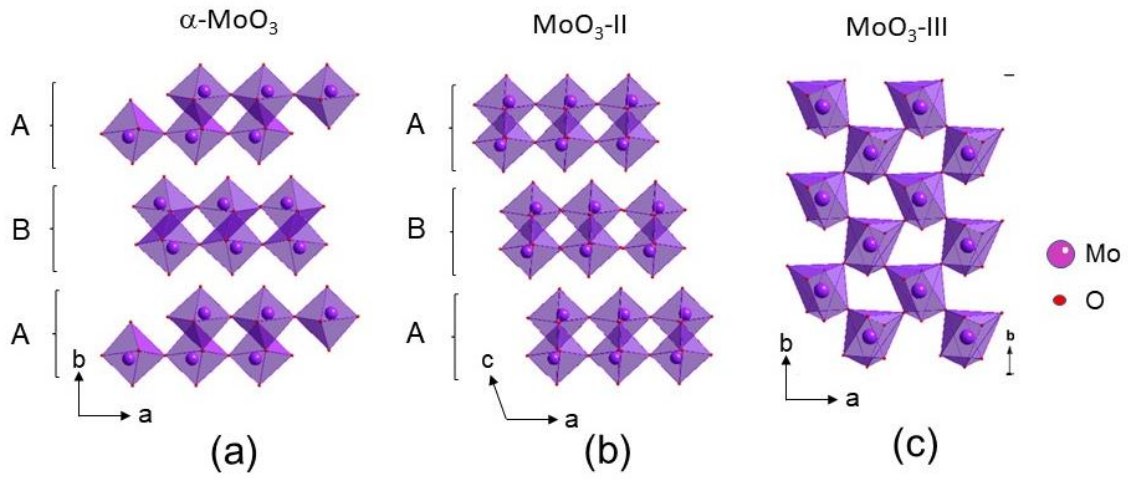

Fig. 22. Crystallographic structures of molybdenum trioxides. (a) Orthorhombic α-MoO_3 structure with *ABA* stacking. (b) Monoclinic $P2_1/m$ MoO_3-II structure with *AAA* stacking. Mo atoms of the *B* layer within MoO_6 a mirror plane compared with α-MoO_3. (c) Monoclinic $P2_1/c$ structure of the high-pressure phase MoO_3-III. Purple circles represent the Mo atoms and red circles the O atoms. Reproduced with permission from [44]. Copyright 2009

2.5. Bronzes of Molybdenum

In 1895, the first molybdenum bronze was synthesized by Stavenhagen and Engels [359]. The sodium molybdenum bronze $Na_6Mo_7O_{24}$ ($3NaO{\cdot}7MoO_3$) was produced by electrolytic reduction of fused sodium molybdate. Under water, the bronze appears as indigo blue, shiny metal needles that lost some of their metallic sheen when drying and turned a dark blue color. In 1970, Réau et al. [69] investigated the monoclinic Li_xMoO_3 phases, which refer to violet-blue bronzes prepared in a range of stoichiometry with $0.31 \leq x \leq 0.39$. The main interest of molybdenum bronzes was motivated by their transport anomalies (charge-density wave instabilities). In the 1980s, molybdenum bronzes were studied as low-dimensional metallic conductors, with the generic formula $A_xMo_yO_z$ where *A* is hydrogen or alkali metal. They are distinguished by their color: red bronzes ($Li_{0.33}MoO_3$, $K_{0.33}MoO_3$), blue bronzes ($K_{0.3}MoO_3$), and purple bronzes ($Li_{0.9}Mo_6O_{17}$, $Na_{0.9}Mo_6O_{17}$) [360-363]. In 1984, McCarroll and Greenblatt reported the synthesis of several single crystals of Li_xMoO_3 bronze with different compositions: violet-red $Li_{0.9}Mo_6O_{17}$, violet-blue $Li_{0.32}MoO_3$ and blue $Li_{0.04}MoO_3$ [364]. A lithium-ion battery was fabricated with a lithium molybdenum bronze as anode [365]. The molybdenum bronze $Li_xMoO_3{\cdot}\varepsilon H_2O$ with $0.20 \leq x \leq 0.30$ and $\varepsilon \leq 0.1$ was prepared in a preferred embodiment, using a method that prevent the co-intercalation of proton. For instance, $Li_xMoO_3{\cdot}\varepsilon H_2O$ is formed from MoO_3 suspended in aqueous solution in argon atmosphere, by simultaneous addition of sodium dithionite and hydrated lithium molybdate. In the voltage range 3.5-0.005 V vs. Li, the composite electrode exhibits a capacity retention of 72% after 20 cycles.

3. Hydrated Mo-O phases

3.1. Structure

A rich family of crystalline molybdenum(VI) oxide hydrates (MOHs), $MoO_3{\cdot}nH_2O$, are known for $1 \leq n \leq 2$, which include the monoclinic dihydrate, $MoO_3{\cdot}2H_2O$, two monohydrates, the yellow monoclinic $MoO_3{\cdot}H_2O$, and the white triclinic $MoO_3{\cdot}H_2O$, a white hemihydrate, $MoO_3{\cdot}½H_2O$, and a white orthorhombic $MoO_3{\cdot}⅓H_2O$ (**Table 9**). The $MoO_3{\cdot}⅔H_2O$ hydrate has been also reported [366]. The structure of $MoO_3{\cdot}2H_2O$ is made of layers of $MoO_5(OH_2)$

octahedra exchanging their oxygens in the equatorial plane and stacking along the *b*-direction [367]. Yellow monohydrate (β-$MoO_3 \cdot H_2O$) displays a structure with equatorial sharing oxygens and axial Mo-OH_2 and Mo=O bonds [368]. White monohydrate (α-$MoO_3 \cdot H_2O$) has a triclinic structure (space group $P\bar{1}$, JCPDS card No. 16-1449) closely related to that α-MoO_3 and crystallizes in well-shaped needles. Its structure is formed by edge-sharing octahedra parallel to the *b*-direction and includes Mo-OH_2, Mo=O and Mo-O_3 bonds [369]. The $MoO_3 \cdot ½H_2O$ structure is built of layers parallel to the b-direction formed of edge-sharing distorted MoO_6 octahedra and $MoO_5(OH_2)$ octahedra [370]. $MoO_3 \cdot ⅓H_2O$ presents slightly distorted MoO_6 octahedra leading to a base-centered orthorhombic structure [41,309,371].

Table 9. Crystallographic parameters of the various molybdenum oxide hydrates.

Compound	Space group	Cell parameters (Å)		
		a/α	*b*/β	*c*/γ
$MoO_3 \cdot H_2O$	$P2_1/c$	7.55	10.69/91.0°	7.28
α-$MoO_3 \cdot H_2O$	*P1*	7.388	3.70/113.6°	6.673/91.6°
$MoO_3 \cdot 2H_2O$	$P2_1/n$	10.476	13.822/91.6°	10.606
$MoO_3 \cdot ⅓H_2O$	*Pbnm*	7.697	12.647	7.338
$MoO_3 \cdot ½H_2O$	*P2/m*	9.658	3.71/102.4°	7.087
h-$MoO_3 \cdot ½H_2O$	$P6_3/m$	10.584	-	3.728

During the dehydration process of molybdic acid, several hydrated phases are formed. Yellow monoclinic mono-hydrate $MoO_3 \cdot H_2O$ is formed by the topotactic loss of the intralayer water molecule on the dehydration of $MoO_3 \cdot H_2O$ [368]. The white monoclinic hemi-hydrate (*n*=1/2) was prepared by precipitation from nitric acid solution [368], and by ion exchange method from sodium molybdate [366]. White orthorhombic $MoO_3 \cdot ⅓H_2O$ was grown by hydrothermal treatment at 110 °C of aqueous solution of molybdic acid [309]. By dehydration of molybdic acid, the monoclinic β-MoO_3 with ReO_3-type structure is formed which transforms to the orthorhombic α-MoO_3 phase above 400 °C [70,154].

The different steps are observed as endothermic peaks in TGA curves indicating multi-step dehydration and structural rearrangements of the MOH framework (**Fig. 4**). Above 325 °C, β-MoO_3 and α-MoO_3 phases are formed. A broad exothermic peak at 480 °C originates from the irreversible phase transformation from monoclinic to orthorhombic structure. The phase transformation is associated with loss of oxygen observed particularly for the samples heat

treated above 750°C leading sub-oxide such as $MoO_{2.8}$ (Mo_5O_{14}) [121]. The DSC curve of $MoO_3 \cdot H_2O$ shows three broad endothermic peaks at 198, 246, and 325 °C on heating in argon atmosphere at the rate 2 °C min^{-1}, which is correlated with the weight losses. At the first stage 33% of the water molecules was removed forming the product $MoO_3 \cdot \frac{1}{3}H_2O$.

Günter [368] reported that the dehydration process is a topotactic-like reaction with a slight expansion in both axial direction and an increase in symmetry; in molybdenum trioxide, the coordination octahedra partly share edges instead of corners only, which explains the change in the lattice constants and in symmetry. The low-temperature phase β-MoO_3 (bright yellow colour) is formed around 450 °C, while the layered α-MoO_3 phase (white transparent) is formed at 750 °C. Some samples with black colour are formed at 750 °C, indicating an oxygen-deficient $MoO_{3-\delta}$ structure. The dehydration mechanism of Mo mono hydrate (molybdic acid) can be summarized by the relation

$$MoO_3 \cdot H_2O \rightarrow MoO_3 \cdot \tfrac{2}{3}H_2O + \tfrac{1}{3}H_2O\uparrow \rightarrow MoO_3 \cdot \tfrac{1}{3}H_2O + \tfrac{1}{3}H_2O\uparrow$$
$$\rightarrow \beta\text{-}MoO_3 + \tfrac{1}{3}H_2O\uparrow \rightarrow \alpha\text{-}MoO_3 \rightarrow MoO_{3-\delta}, \qquad (12)$$

Vibrational spectra of $MoO_3 \cdot H_2O$ and dehydrated products obtained after heat treatment were studied by Raman spectroscopy, which appears to be a sensitive technique to distinguish unambiguously inter-lamellar MoO_6 octahedra from octahedra sharing two common edges. The Raman spectrum of the product heated above 470 °C exhibits superposition the spectral features of β-MoO_3 and α-MoO_3 crystal. Moreover, FTIR spectra of dehydrated $MoO_3 \cdot nH_2O$ (n<l) shown in **Fig. 4c** are also more complex than that of crystalline MoO_3, but spectral features can be discussed in terms of internal and external modes as usual for oxide lattices. The highest frequency bands are due to the symmetric stretching mode of the shortest Mo=O bond (the so-called molybdyl-mode), whereas the next highest bands are assigned to the stretch of intermediate bridging Mo-O bonds (longer Mo-O distances). The bending modes due to O-Mo-O bonds are located in the medium frequency range [77], while the external modes appear below 300 cm^{-1}. FTIR results (**Fig. 4c**) clearly show the change in the local structure of the MOs for annealing treatment T>250 °C of starting $MoO_3 \cdot H_2O$ in good agreement with XRD patterns (**Fig. 4b**). Here, the modifications of the crystallinity can be deduced using the shape and frequency of the four groups of peaks. At intermediate heat treatment we observe the bands attributed to the mixed phase during the transformation from β-MoO_3 to α-MoO_3 [309].

Camacho-López et al. [372] reported that the $MoO_3 \cdot 1.4H_2O$ glassy phase transforms to the amorphous $MoO_3 \cdot 0.7H_2O$ phase prior to its crystallization, while the sample heated at 500 °C crystallizes into the orthorhombic α-MoO_3 with micro-crystallites having an average size of 6.8

μm. The local structure of products obtained by dehydration was investigated by Raman spectroscopy as shown in **Fig. 23** with the correspond SEM images of the as-prepared samples. In the Mo-O stretching mode region (100-600 cm^{-1}) the broad bands are due to the highly disordered $MoO_5(H_2O)$ octahedral units in the amorphous hydrated sample (a-$MoO_3 \cdot 1.4H_2O$). These bands are centered on those of the Raman spectrum of the polycrystalline $MoO_3 \cdot 1H_2O$ phase, so the patterns of $MoO_3 \cdot 1.4H_2O$ are the features envelop of $MoO_3 \cdot 1H_2O$. The sample a-$MoO_3 \cdot 1.4H_2O$ heated at 120 °C for 1 h transforms to $MoO_3 \cdot 0.7H_2O$. The overall decrease of the Raman signal is due to the enhancement of the electrical conductivity (decrease of the penetration depth of the light) of the partially dehydrated sample [319]. The Raman spectrum exhibits the spectral features at 705, 850 and 948 cm^{-1} of the $MoO_3 \cdot 1.4H_2O$ with additional vibrations at 665 and 983 cm^{-1} assigned to the Mo-O3 stretch (B_{2g}, B_{3g} mode) and M=O stretch (A_g mode) of the $MoO_3 \cdot 0.7H_2O$ phase, respectively. These structural changes are related to water removal, which induces shorter Mo=O bonds and the less octahedral distortion. For well-crystallized α-MoO_3, the peak at 983 cm^{-1} shows a red shift to 995 cm^{-1} and becomes a narrow line due to its non-polar character. It is worth noting that the line shape of the stretching modes is a function of the particle size growing with the annealing temperature of the glassy phase. Thus, the phonon confinement is observed in the case of MoO_3 crystallization, i.e., the Raman peaks broadened and little asymmetry is observed at 819 cm^{-1}. When MoO_3 nano-particles formed were large in diameter ($L \geq 40$ nm) no significant downshift can be observed. The frequency of the stretch of terminal Mo=O shows a step at ca. T_a=120 °C.

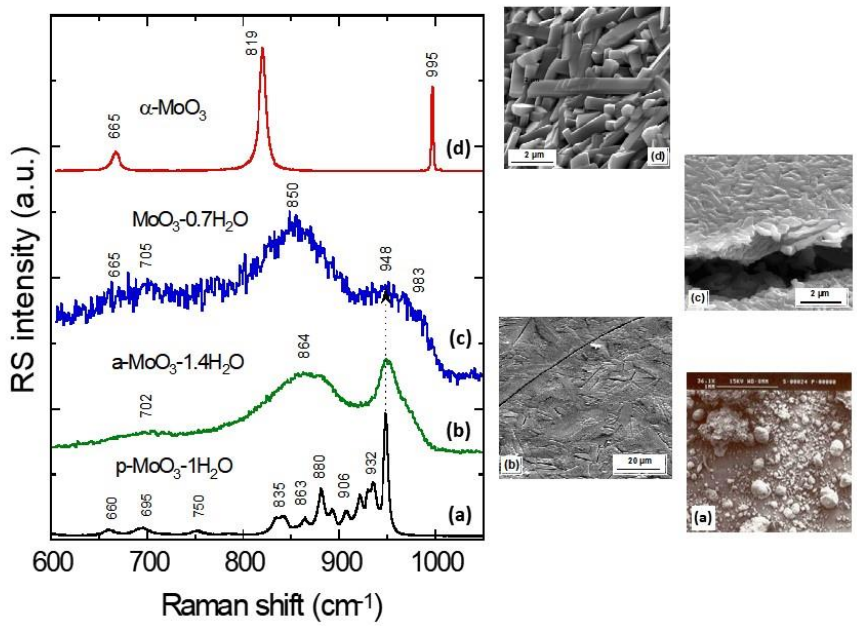

Fig. 23. Raman spectra for four different molybdenum trioxide phases: the $MoO_3 \cdot 1H_2O$ polycrystalline powders, the $MoO_3 \cdot 1.4H_2O$ hydrated phase, the partially $MoO_3 \cdot 0.7H_2O$

dehydrated phase, and the orthorhombic α-MoO_3 phase with their corresponding SEM images.

Haro-Poniatowski et al. [102] have reported the preparation of hydrated MoO_3 by acidification of sodium molybdate (Na_2MoO_4) solution and have also revealed the dependence of the morphology and color of the resulting product on the drying procedure. Using Raman scattering techniques, they demonstrated the evolution of the sample from a low temperature glass phase to a high temperature glass phase then crystallization under laser radiation. The thermally induced structural transformations in hydrated MoO_3 samples prepared by acidification of Na_2MoO_4 solution have been investigated dynamically by combined analytic techniques such as thermo-Raman spectroscopy, thermogravimetry, differential thermal calorimetry and X-ray diffraction [103]. Results reveal that the structural evolution proceeds through an amorphous phase after dehydration processes, formation of sub-microcrystals, the possible MoO_3-II phase and the α-MoO_3 phase. The structural evolution under a flow of nitrogen gas indicated that the sample formed after dehydration could be oxygen deficient $MoO_{3-\delta}$. Du et al. [373] prepared the $MoO_3 \cdot 0.55H_2O$ phase by sonication of ammonium molybdate solution added to a mixture of 3-mercaptopropyltrimethoxysilane (MPTS) with anhydrous toluene. The light-blue sample obtained after vacuum drying at 70 °C for 6 h has a hexagonal structure with lattice parameters α = 10.581 Å, c = 3.720 Å (JCPDS card No. 76-1003). $MoO_3 \cdot 0.55H_2O$ was converted into α-MoO_3 till the temperature reached 400 °C.

3.2. Electrical conductivity

Figure 24 shows the temperature dependence of the electrical conductivity, σ_{dc}, of MOHs heat-treated at various temperatures in the range 140-458 °C. It is well known that transition-metal oxides can be non-stoichiometric. MoO_3 is such a material. Mo^{5+} ions can be produced as a consequence of the formation of oxygen vacancies. The conduction process has been described as a carrier hopping mechanism between localized states [18]. Small polarons are formed around these ions, due to the highly polar structure of this oxide. A thermally activated electronic hopping between lower and higher valence states is responsible for the electric transport. Also, it has been pointed out that the number of vacancies in MoO_3 films is indicated by the colour of the film [177]. The electrical conductivity curves shown in **Fig. 24** are typical of a hopping mechanism. The activation energies of the high-temperature regime are in the range 0.5-0.7 eV. The increase in σ_{dc} suggests a decrease of the O/Mo ratio due to the oxygen

loss in annealed materials. The highly treated samples (T_a=458 °C) have the highest electrical conductivity values.

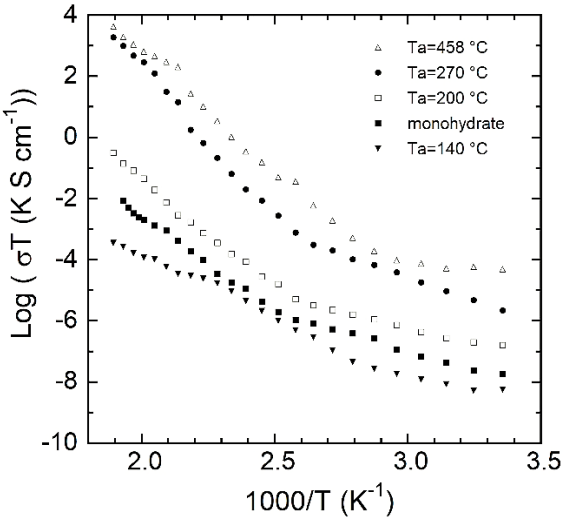

Fig. 24. Arrhenius plots of the electrical conductivity of molybdenum monohydrate $MoO_3 \cdot 1H_2O$ and products heat-treated at various temperatures in the range 140-458 °C.

3.3. Intercalation in $MoO_3 \cdot nH_2O$

Molybdate-based layered hybrids derived by intercalating organic guest species into the interlayer spaces of MoO_6 layers have also been a hot research topic, and the as-obtained organic–inorganic hybrids can be used as the precursors to prepare MoO_3 nanostructures [167,374-376]. Afsharpour et al. [374] synthesized molybdenum oxide nanohybrids using yellow molybdic acid and amino-carboxylates as the starting materials in an ethanol-water (1:3) mixed solution, and α-MoO_3 nanostructures with high surface areas were obtained by calcining the as-obtained nanohybrids at 600 °C. Niederberger et al. [167] prepared molybdenum oxide-amine hybrid composites by hydrothermally treating the ethanol-water mixed suspension of yellow $MoO_3 \cdot 2H_2O$ and amines at 120 °C, and the molybdenum oxide-amine hybrid composites were used as the precursor to synthesize a-$MoO_3 \cdot H_2O$ nanofibers. Shukoor et al. [375] systematically investigated the intercalation behaviors of amines with various n-alkyl lengths into yellow molybdic acid ($MoO_3 \cdot 2H_2O$) in ethanol/water (1/3, v/v) solutions, and the as-obtained hybrids were transformed to MoO_3 rods, scrolls and disks by 33% HNO_3 treatment. In these intercalation reactions, elevated temperatures are usually necessary. Chen et al. [374] investigated molybdate-based inorganic–organic hybrids, which are formed from the reaction of white molybdic acid ($MoO_3 \cdot H_2O$) powders and n-octylamine at room temperature, for sensing applications.

The suitability of MOHs as 3-volt electrode materials for non-aqueous lithium batteries has been assessed by several workers [121,319,366,377-379]. In early studies of electrochemical lithium insertion in MOHs Kumagai et al. [201,380,381]. Discharge profiles and kinetics are dependent on the amount of "structural water" into the host lattice. Compositional range was reported to be more than 2.5 Li/Mo reversibly inserted into crystalline $MoO_3 \cdot 2H_2O$, which is higher than the 1.5 Li/Mo obtained for anhydrous α-MoO_3. Numerous hydrated forms of $MoO_3 \cdot y(H_2O)$ (y = 0.3~0.6) were prepared using the Freedman's method by hydrothermal acidification of Na_2MoO_4 solution with 6 mol L^{-1} HCl. The orthorhombic structure was obtained at HCl/Na_2MoO_4 ratio of 2.0~1.5 and 150~180 °C, while a hexagonal network was formed at lower ratio. The as-prepared $MoO_3 \cdot 0.58(H_2O)$ has crystallographic parameters a = 3.955 Å, b = 13.805 Å, c = 3.684 Å and V = 201.1 $Å^3$. As shown in the XRD patterns (**Fig. 25a**), the (021) reflection intensity is sensitive with the annealing temperature. The initial discharge-charge curves in 1 mol L^{-1} $LiClO_4$ in propylene carbonate as electrolyte at 0.2 mA cm^{-2} current density and cycling performance are shown in **Figs 25b-c**. The maximum first discharge capacity of 335 mAh g^{-1} is delivered by the $MoO_3 \cdot 0.58(H_2O)$ electrode heat-treated at 200 °C. However, a rapid decrease in specific capacity is observed after few cycles (**Fig. 25c**) [382]. The same group of workers reported the suitability of $MoO_3 \cdot H_2O$ to deliver a discharge capacity of about 400 mAh g^{-1} with a voltage plateau around 2.5 V vs. Li^+/Li. The $MoO_3 \cdot H_2O$ crystal was found to be changed from a monoclinic to orthorhombic structure with lattice parameters of a = 5.285 Å, b = 10.824 Å, c = 5.237 Å on discharge to 0.5 e^-/Mo [201]. Similar synthesis process was used to prepared yellow $MoO_3 \cdot 2H_2O$ powders in 1 mol L^{-1} Na_2MoO_4 aqueous solution with 3 mol L^{-1} HCl at 100 °C. Starting from an initial value of about 340 mAh g^{-1} obtained at a discharge exchange rate of C/10, the specific capacity continuously decreases with cycling. However, after the tenth cycle in the potential limits 3.8-2.0 V about 300 mAh g^{-1} are still available against only 240 mAh g^{-1} in the case of conventional MoO_3 [383]. Komaba et al. [336] showed that the orthorhombic $x(Li_2O) \cdot MoO_3 \cdot y(H_2O)$ electrode which was hydrothermally formed from Li_2MoO_4 system underwent electrochemical lithium intercalation up to Li/Mo ≈ 1.6 (>300 mAh $(g_{oxide})^{-1}$) on electroreduction until 1.3 V vs. Li^+/Li.

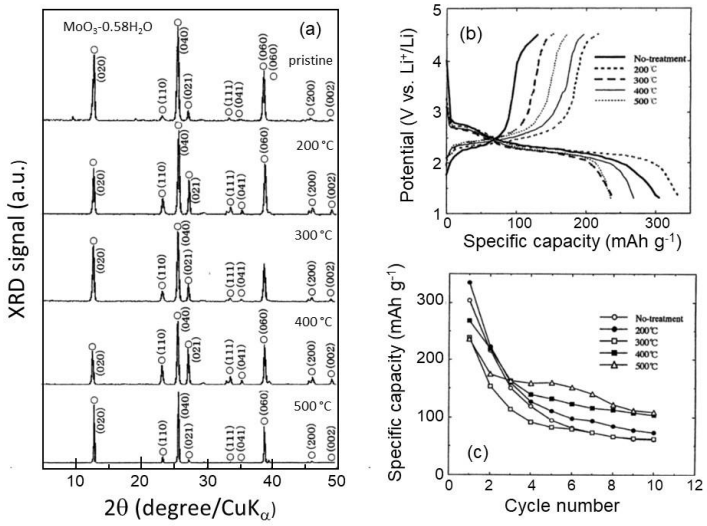

Fig. 25. (a) XRD patterns of orthorhombic $MoO_3 \cdot 0.58(H_2O)$ electrode prepared at 150 °C with H^+/Na^+ ratio of 2.0 and its heat-treated products (o: orthorhombic phase). (b) Initial discharge-charge curves in 1 mol L^{-1} $LiClO_4$ in propylene carbonate as electrolyte at 0.2 mA cm^{-2} current density. (c) cycling performance. On line at https://books.google.fr/books?hl=fr&lr=&id=Ju5viChENAwC&oi=fnd&pg=PR6&dq=intercalation+compounds+for+battery+materials.

It was made clear as a general trend that the discharge capacity of MOHs increases with decreasing water content, but cycle life increases with increasing water content in the compositional range $0.33<n<1.0$. Julien et al. [121,366,377] reported the discharge curves performed on MOHs from open circuit potential down to 2.5 V vs. Li^+/Li (-0.77 V vs. Ag/AgCl). This general trend has been also observed for MoO_3 thin films prepared by electrodeposition from peroxo-polymolybdate solutions [318]. Amorphous oxide-hydrate of molybdenum $MoO_3 \cdot 2H_2O$ was obtained during the synthesis of β-MoO_3 by cation exchange of an aqueous solution of $Na_2MoO_4 \cdot 2H_2O$ passed through a cation exchange resin (Dowex 50WX8-200). As a product of this process, a solution with a pale green color and a pH of 2 was obtained. This solution was placed in a 50 ml vessel that was connected to a vacuum pump for 36 h. In this time, all water was removed slowly and a green powder was obtained as a residue [378]. Electrochemical lithium insertion in amorphous $MoO_3 \cdot 2H_2O$ led to a specific capacity of the cell of 490 mAh g^{-1}. This value exceeds notably the capacity developed by anhydrous β-MoO_3 (370 mAh g^{-1}). Kumagai et al. [380] investigated $x((NH_4)_2O) \cdot MoO_3 \cdot y(H_2O)$ (with x = 0.075-0.042, y = 0.40-0.043) as cathode materials in Li cells. At current densities of 0.5 mA cm^{-2} and an average discharge voltage of 2 V, theoretical energy densities of ca. 600 Wh kg^{-1}

have been predicted, which are considerably higher than in the case of completely dehydrated molybdenum oxides. However, the performance of $x((NH_4)_2O)\cdot MoO_3\cdot y(H_2O)$ decreases drastically with subsequent cycling. The differing discharge mechanisms for the latter compounds (heterogeneous reaction) and MoO_3 (homogeneous reaction) has been discussed on the grounds of discharge characteristics, XRD data, and structural models. The maximum amount of lithium (~3.3 Li/Mo) incorporated in amorphous $MoO_3\cdot 2H_2O$ leads to a specific capacity of 490 mAh g^{-1}. The charge–discharge curve showed a good reversibility in the potential range from 3.2 to 1.1 V *vs.* Li^+/Li, where the cell voltage decreased monotonously as a function of the degree of lithium inserted [378].

Monoclinic monohydrate, $MoO_3\cdot 1H_2O$, having only one coordinated water molecule, shows a discharge capacity of about 200 mAh g^{-1} of acid weight equivalent and a discharge potential around 2.5 V vs. $Li^{\cdot+}/Li$. This electrode material displays a good charge-discharge cyclic behaviour at a capacity below 1 Li/Mo, while keeping the original layered lattice on cycling. Guzman et al. [366] studied a crystalline $MoO_3\cdot 1H_2O$ electrode prepared by sol-gel method, while Yebka et al. used commercial molybdebum-trioxide hydrate powders [319]. **Figure 27** presents the electrochemical behavior of the crystalline $MoO_3\cdot 1H_2O$ investigated at the current rate of C/10 (cathode loading of 2.3 mg cm^{-2}). In the potential voltage 1.5-3.0 V vs. Li^+/Li, the first discharge occurs a Li uptake identical to that of anhydrous MoO_3 (1.5Li/Mo). The electroinsertion of Li ions occurs mainly in two steps in the potential range between 3.0 and 1.5 V (compositional range $0.0 \leq x \leq 1.5$): a first plateau at ca. 2.85 V in the range $0 \leq x \leq 0.25$ and at wide plateau at ca. 2.35 V with a sloppy region in between, which corresponds to a single-phase insertion mechanism (**Fig. 26a**). The $MoO_3\cdot 1H_2O$ electrode delivers a first discharge capacity of 344 mAh g^{-1}, which maintains at ~200 mAh g^{-1} after 100 cycles (**Fig. 26b**). The discharge/charge curves have been modelled using the Armand's model with two adjacent domains including an ion-ion interaction term for each voltage region [3]. The electrochemical behaviour of anhydrous sample shows higher discharge capacity than that of hydrated MoO_3 (262 mAh g^{-1}). $MoO_3\cdot 1H_2O$ has only a coordinated water molecule in the structure. It is obvious that this open structure is favourable to the lithium insertion. The temperature dependence of the discharge-charge shows that $Li//MoO_3\cdot 1H_2O$ cells can operate efficiently at different temperatures in the range of 25-50 °C. However, in the case of $Li//MoO_3\cdot 1H_2O$ operating at 50 °C, the cell voltage range is about 5% less than for the material operating at 25 °C. Amorphous $MoO_3\cdot 1H_2O$ electrode exhibits stepwise discharge behaviour, including two plateaus: the first step up to $0.3e^-$/Mo and the second one up to $1.0e^-$/Mo. A

discharge capacity of 260 mAh g^{-1} is delivered in the potential range corresponding to 1.5 e^-/Mo [366].

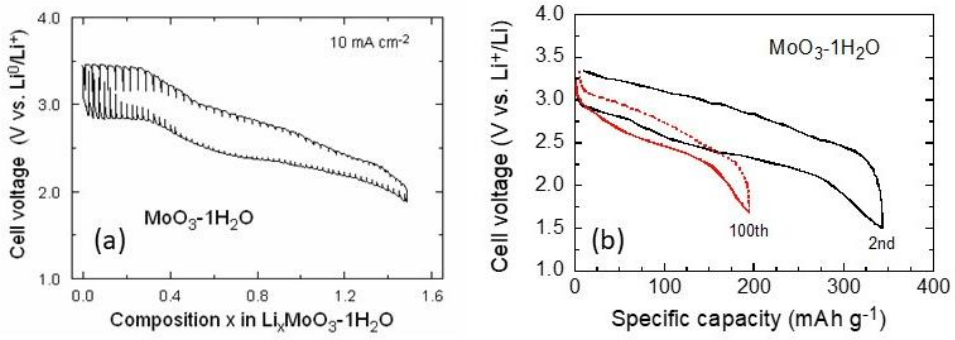

Fig. 26. (a) First galvanostatic discharge-charge curve of the MoO_3•$1H_2O$ positive electrode recorded at C/10 rate in the potential range 2.0-3.5 V vs. Li^+/Li. (b) Electrochemical patterns of MoO_3•$1H_2O$ at the 2nd and 100th cycle.

The electrochemical features of the crystalline MoO_3·½H_2O electrode are rather similar with the appearance of three plateaus at. ca. 2.5, 1.75 and 1.5 V (**Fig. 27a**). This electrochemical behaviour is attributed to the large cavities available for Li ions, which prevent repulsive forces between inserted ions. The structure of MoO_3·½H_2O may be described as an alteration of linear double rows of edge-sharing distorted MoO_6 and $MoO_5(H_2O)$ octahedral [309]. In the potential range 3.0-1.0 V, the MoO_3 hemihydrate electrode delivers a first discharge capacity of 353 mAh g^{-1} for a charge transfer of ~1.5e^-/Mo. The cyclability of MoO_3·½H_2O (**Fig. 27b)** shows the electrode cycled 100 times at C/10 rate retains a capacity of 201 mAh g^{-1}. **Figure 27c** presents the XRD patterns of Li_xMoO_3·½H_2O as a function of the amount of Li electrochemically inserted. The monoclinic structure remains largely unchanged upon lithiation with the strongest (001) reflection line shifted toward lower angles (inset **Fig. 27c**). This result suggests that, on discharging, Li^+ ions are inserted between the layers leading to a small increase of the interlayer spacing, which can be explained by a model of rigid hydrated-MoO_3 layers in their original state separated by intercalated Li cations. **Figure 27d** displays the FTIR absorption spectra of pristine and Li intercalated products. The FTIR spectra of $Li_{0.15}MoO_3$·½H_2O and $Li_{0.15}MoO_3$·½H_2O samples show new bands at 1780, 1200, 1148, 1117 and 1087 cm^{-1}. The band at 1780 cm^{-1} is assigned to the stretching vibration $\nu_{C=O}$ of propylene carbonate molecules. Its position is shifted towards lower energies compared with pure propylene carbonate suggesting that solvent molecules are bonded at the surface of the oxide network. The bands situated in the region 1200-1080 cm^{-1} are attributed to the stretching mode of Li atoms inserted between layers vibrating against the nearest neighboring oxygen atoms [366].

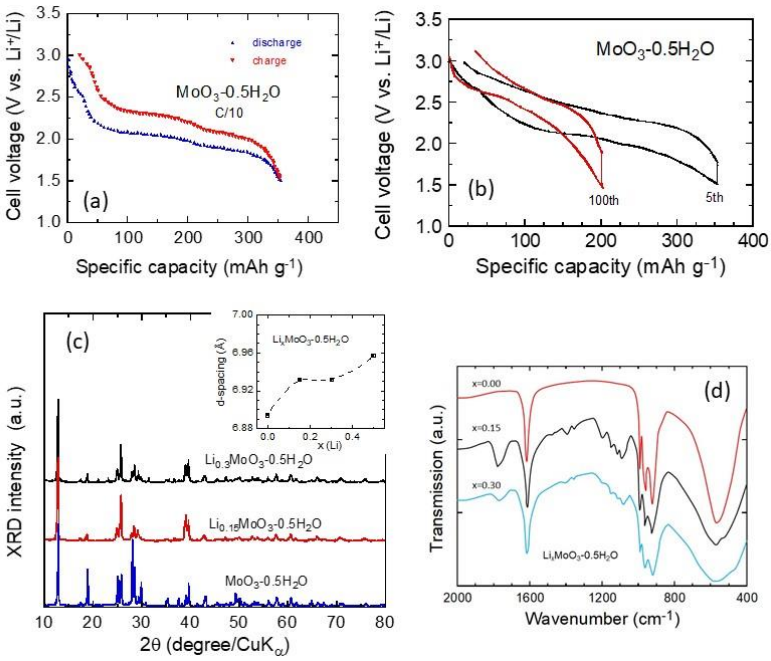

Fig. 27. (a) Typical discharge curves of amorphous $MoO_3 \cdot ½H_2O$ powders cycled at C/10 rate in the potential window3.0-1.5 V vs. Li^+/Li. (b) Electrochemical patterns of $MoO_3 \cdot ½H_2O$ at the 5th and 100th cycle. (c) XRD patterns of lithiated $MoO_3 \cdot ½H_2O$ powders using electrochemical titration. The insert shows the variation of the d-spacing vs. x(Li) (reflection at $2\theta = 12.8°$). (d) FTIR absorption spectra of pristine $MoO_3 \cdot ½H_2O$ and electrochemically Li inserted $Li_xMoO_3 \cdot ½H_2O$ (x = 0.15 and 0.3).

$MoO_3 \cdot 0.66H_2O$ powders were prepared by heating molybdic acid ($MoO_3 \cdot H_2O$) at T_a=216 °C [121,317,319]. **Figures 28a-b** show the typical discharge-charge curves of $Li_xMoO_3 \cdot ⅔H_2O$//Li cells cycled at C/10 rate in the potential range 3.5-1.5 V vs. Li^+/Li, which exhibit electrochemical patterns as follows: (i) an initial OCV of ~3.5 V, (i) a Li uptake 1.5 Li per Mo atom providing a discharge capacity of 260 mAh g^{-1}, (iii) a large voltage plateau at ca. 2.2 V, and (iv) the discharge capacity remains at 162 mAh g^{-1} after 100 cycles. Note the absence of the first discharge voltage plateau in the $0.0 < x < 0.25$ observed in discharge profiles of other MOHs and of anhydrous MoO_3, which show the strong dependence of the water content on the Li insertion process in MOH frameworks. The S-shaped behaviour of the discharge-charge curves of the $MoO_3 \cdot ⅔H_2O$ electrode suggests single-phase reaction $Li_xMoO_3 \cdot ⅔H_2O$ in the range $0.0 \leq x \leq 1.5$. Structural changes in Li-intercalated were analysed using in situ XRD in $MoO_3 \cdot ⅔H_2O$/$LiClO_4$-PC electrolyte/Li cell (**Fig. 28c**) and Raman spectroscopy (**Fig. 28d**). The Raman spectrum of $MoO_3 \cdot ⅔H_2O$ is in fair agreement with the spectrum of MoO_3 [77]. Bands located at 120 and 150 cm^{-1} are assigned to vibrations of the $(O_2Mo_2)_n$ chains while bands

located at 335, 440 and 657 cm^{-1} are attributed to the vibration of the O- Mo_3. After lithium insertion, we observed features as follows. (i) The intensities of original Raman-active vibrations decrease drastically and the background increases. (ii) The background also increases as the frequency shift increases, probably owing to the modification of the electronic band structure upon intercalation. (iii) The low-frequency part of the spectrum remains almost unchanged, indicating that the layered structure of $MoO_3 \cdot ⅔H_2O$ is maintained. (iv) New peaks appear at 562, 546, and 278 cm^{-1}, which are assigned to a longitudinal and transverse intercalation mode [384], in which intercalant species vibrate strongly against the host lattice. Moreover, the reversible insertion behaviour has been also observed by Raman measurements. The original Raman spectrum has been recovered on discharge-charge cycling. Note that the change in colour with increasing Li content seems to start from the physical edges of the sample proceeding along the crystal imperfections (grain boundaries, micro cracks, planer defects, etc.) to a uniform coloration of the crystal [385]. **Figure 28e** shows the interplanar distance, d_{int}, deduced from the position of the (200) reflection peak as a function of the Li concentration within the $MoO_3 \cdot ⅔H_2O$ framework. *In situ* XRD patterns were recorded during charge and discharge in the potential range 3.4-1.2 V. The shift toward lower 2θ position of the (200) line reveals that Li ions are inserted between layers upon discharge the cell, resulting in a significant increase in the interlayer spacing of about 6%. Layer separation in spite of the reduced dimensions of Li ions (0.69 Å, *CN*=6) is constantly reported for layered compounds. Besenhard and Schollhorn demonstrated an interlayer separation of 1 Å for x = 1 for the parent oxide Li_xMoO_3 [61]. An expansion of 12% for d_{int} in the basic structure of $Mo_{18}O_{52}$ has been observed by Pasquali et al [386]. The lattice expansion in Li_xMoO_3 does not increase continuously with the degree of intercalation, x, but shows a maximum in the vicinity of x = 0.1. Similar situation has been observed for molybdenum bronzes H_xMoO_3 [387].

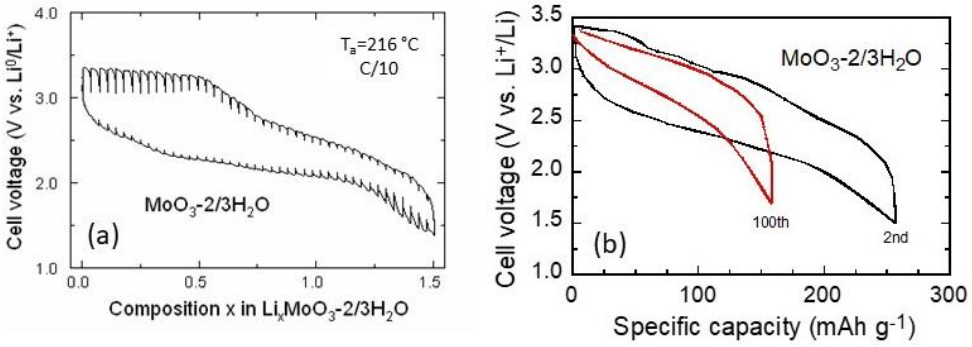

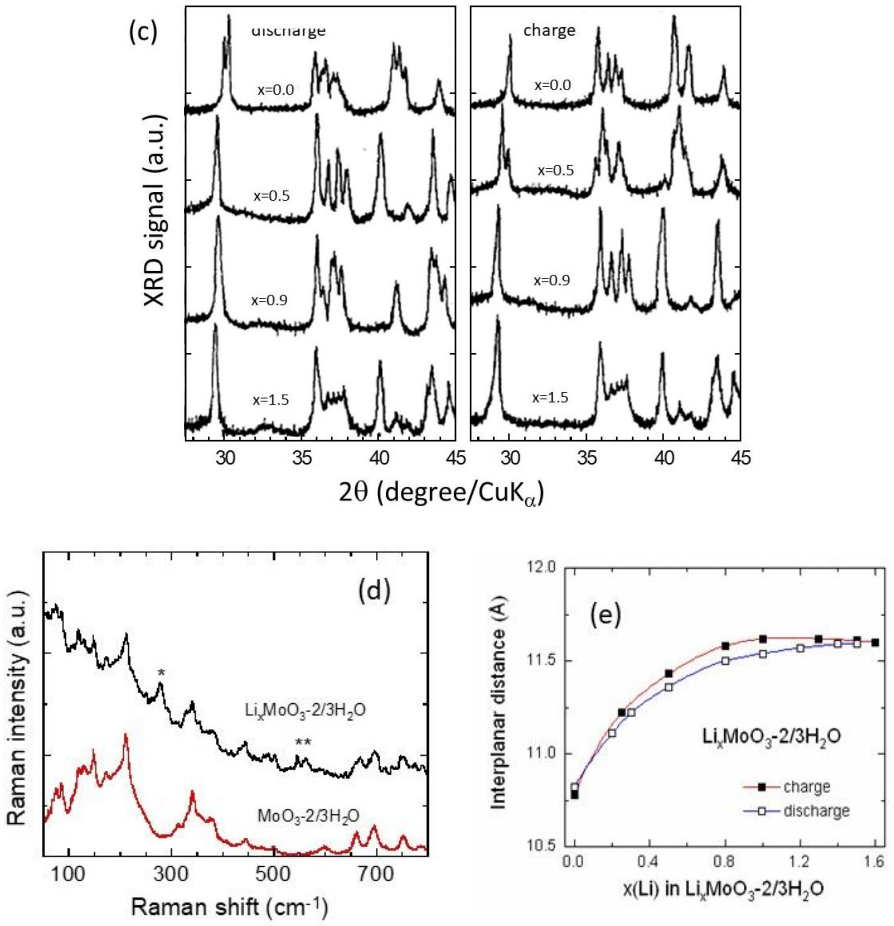

Fig. 28. (a) Galvanostatic discharge-charge curve of the $MoO_3 \cdot ⅔H_2O$ positive electrode. Electrochemical measurements were performed at a rate of C/5. (b) Electrochemical patterns of $MoO_3 \cdot ⅔H_2O$ at the 2nd and 100th cycle. (c) In situ XRD patterns of Li-intercalated $MoO_3 \cdot ⅔H_2O$ in $LiClO_4$-PC electrolyte. (d) Raman spectra of molybdenum hydrate $Li_xMoO_3 \cdot ⅔H_2O$ and its lithium intercalated product. New peaks marked by stars are the fingerprints of Li ions located in the interlayer space. (e) Variation of the interplanar distance deduced from the (200) Bragg peak with the Li concentration within the $MoO_3 \cdot ⅔H_2O$ framework. In-situ XRD patterns were recorded during charge (■) and discharge (●) in the potential range 3.4-1.2 V.

Using a vacuum drying technique Ramirez et al. have prepared an amorphous hydrate molybdenum oxide a-$MoO_3 \cdot 2H_2O$ [310]. Electrochemical lithium insertion in a-$MoO_3 \cdot 2H_2O$ shows a maximum amount of Li incorporated of ~3.3 Li/Mo, which leads to a specific capacity of 490 mAh g^{-1} [378]. This value exceeds by more than 20% the specific capacity developed by its homolog crystalline form (400 mAh g^{-1}). The charge–discharge curves show a good reversibility in the potential range from 3.2 to 1.1V vs. Li$^+$/Li, where the cell voltage decreased monotonously as a function of the degree of lithium inserted. Yuan and Si prepared a triclinic

α-$MoO_3 \cdot H_2O$ sample by direct chemical reaction of Mo powders and H_2O_2 with the formation of precursor $MoO_2(OH)(OOH)$. Partly dehydrated α-$MoO_3 \cdot xH_2O$ with x=0.936, 0874 and 0.752 were prepared by vacuum dehydration at 110, 150 and 165 °C, respectively (**Fig. 29**) [379]. **Figure 29c** presents the first two galvanostatic discharge–charge curves for the triclinic α-$MoO_3 \cdot H_2O$ and its dehydrated products (loading ~2 mg) tested in 2016-type coin cell with Li metal anode cycled at 0.1 A g^{-1} current density in the potential range 3.0-0.001 V vs Li^+/Li. These profiles show a broad plateau at 0.2 V ascribed to the conversion reaction involving the transformation of $Li_xMoO_3 \cdot H_2O$ to Mo and Li_2O matrix.

Recently, Yu et al. [388] demonstrated a water-incorporation strategy to expand the interlayer gap of α-MoO_3, in which water molecules take the place of the non-bridging oxygen of layered lattice. The incorporated H_2O molecules expand the interlayer channel dimension, i.e., increase of the b-lattice parameter to 15.02 Å compared to α-MoO_3 (13.85 Å). The composition $MoO_{2.92} \cdot 0.07H_2O$ was determined by TGA. The modified α-MoO_3 electrode exhibits specific capacity of 963 C g^{-1} at 0.1 mV s^{-1}, and boosted cycling stability, i.e., a capacity of 455 C g^{-1} is maintained after 600 cycles at 100 mA g^{-1}. A fast-kinetics dual-ion-intercalation energy storage device was assembled by combining the Li^+ intercalation α-$MoO_3 \cdot nH_2O$ anode with an anion-intercalation graphite cathode in 2 mol L^{-1} $LiPF_6$ electrolyte. Operating within a 1.0–3.5 V voltage window an energy density of 44 Wh L^{-1} was delivered (based on the whole device). The significant role of the incorporated H_2O molecules in accelerating the diffusion of Li^+ within the $MoO_{2.92} \cdot 0.07H_2O$ lattice was studied by galvanostatic titration. The D_{Li}^* values 2.4×10^{-12}–3.5×10^{-10} cm^2 s^{-1}) are substantially higher than those in α-MoO_3 (3.9×10^{-13}–6.0×10^{-11} cm^2 s^{-1}).

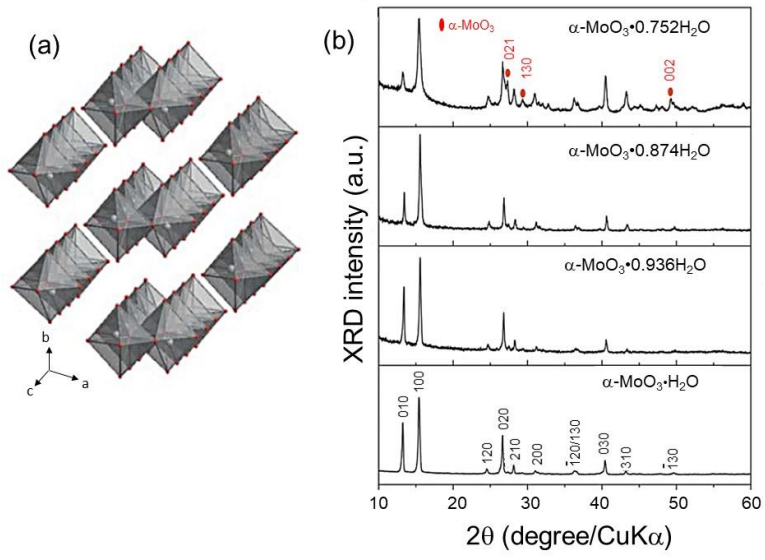

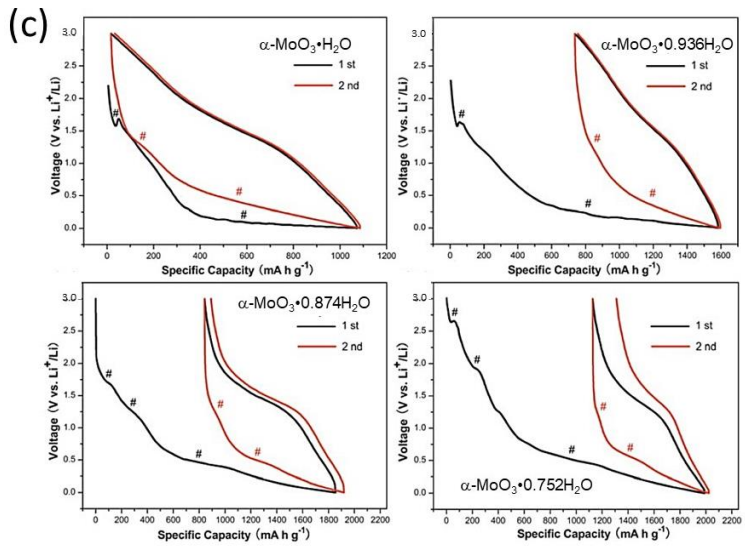

Fig. 29. (a) The crystal structure of the triclinic monohydrated molybdenum oxide α-$MoO_3 \cdot 1H_2O$. (b) XRD patterns of pristine α-$MoO_3 \cdot 1H_2O$ and its partially dehydrates α-$MoO_3 \cdot 0.936H_2O$, α-$MoO_3 \cdot 0.874H_2O$, and α-$MoO_3 \cdot 0.752H_2O$. (c) The first two discharge-charge profiles of α-$MoO_3 \cdot xH_2O$ cycled at 0.1 A g^{-1} current density between 3.0 and 0.001 V vs. Li^+/Li. Reproduced with permission from [379]. Copyright 2013 The Royal Society of Chemistry.

4. Oxygen deficient $MoO_{3-\delta}$

4.1. $MoO_{3-\delta}$ suboxides

$MoO_{3-\delta}$ suboxides with stoichiometric deviation $\delta < 1$ belong to the class of materials that offer a tunability of their intrinsic electronic properties from wide bandgap semiconductor MoO_3 to semi-metallic MoO_2 [8]. Upon inducing oxygen defects, Mo^{6+} ions can be reduced to Mo^{5+} and finally Mo^{4+}, the oxygen vacancies not only increase the interlayer spacing and the electrical conductivity of MoO_3, but also enhance charge storage kinetics [389]. The varieties of oxidation states in oxygen-deficient $MoO_{3-\delta}$ compounds make them highly attractive in the field of energy storage and conversion and they have found applications in LIBs [236,390], solid state thin-film microbatteries [72,173,], electrochemical supercapacitors [194,391], gas sensors [392], electrochromic devices [231], solar cells [393,394], anode interlayers for photovoltaic devices [395], smart windows [396], light-emitting diodes [397], etc. These devices take advantage of the changes in the degree of crystallinity, cationic environment, stoichiometry deviation, band gap energy and electronic conductivity, which can be controlled by the growth conditions.

4.1.1. Structure

Regarding the electronic structure, the defective oxygen generates gap states, which change the optical appearance, i.e., the oxides exhibit color transitions from transparent to yellow and eventually grayish/blue. Thus, the molybdenum suboxides phases can be classified in three groups: (i) the nearly-stoichiometric $MoO_{3-\delta}$ (with $\delta < 0.03$), which retains the orthorhombic symmetry, is unintentionally an *n*-type semiconductor at ambient conditions, partly due to intrinsic point defects related to oxygen vacancies (V_O) and molybdenum interstitials (Mo_i) [34], (ii) the defective $MoO_{3-\delta}$ (with $0.03 < \delta < 0.11$) and (iii) Mo_nO_{3n-1} suboxides (Magnéli phases, $n = 4–9$), which collapse into ReO_3-type structures with crystallographic shear planes due to the destabilization of the MoO_3 structure by the loss of oxygen [35-40]. The schematic representation of the crystal structure of the layered α-MoO_3 phase and the vacancies of the three inequivalent oxygen positions O1 (apical), O2 (corner-sharing) and O3 (edge-sharing) are shown in **Fig. 30** [398]. An O1 vacancy ($V_{O(1)}$) leads to two localized electrons on the neighboring Mo that are thus in the Mo^{4+} ($4d^25s^0$) configuration; O2 and O3 vacancies create a bipolaron with electrons localized on two separate Mo^{5+} sites in the first and second coordination spheres for $V_{O(2)}$ and on the opposite side of the vacancy for $V_{O(3)}$ [399]. At higher vacancy concentration, the shear structure is energetically more favorable than the point defects [400]. Inzami et al. accurately explored the effect of oxygen nonstoichiometry on the electronic structure and properties of the oxygen-deficient $MoO_{3-\delta}$ material using a van der Waals density functional calculation [398]. It is shown that: (i) the electronic structure of layered MoO_{3-d} is highly sensitive to changes in oxygen stoichiometry as Mo^{6+} has an empty 4d shell; (ii) the layered structure efficiently screens the structural perturbations caused by oxygen vacancies, and (iii) the oxygen deficiency gives rise to Mo 4d gap states with energy levels dependent on the type of oxygen vacancy.

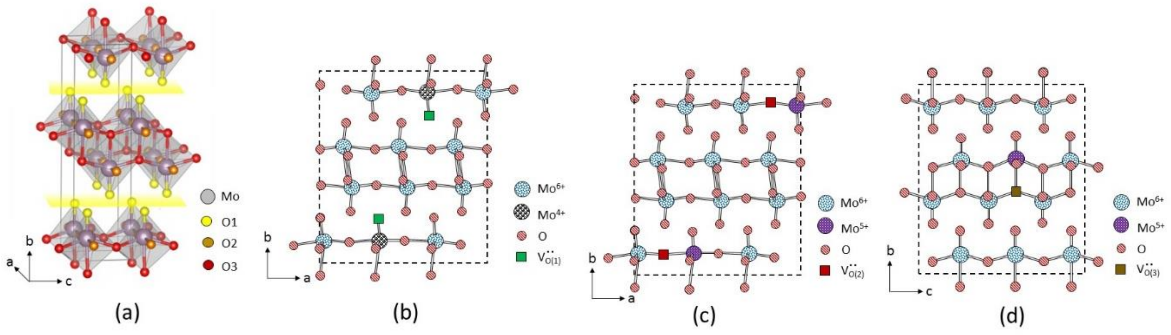

Fig. 30. Crystal structure of the layered α-MoO_3 phase (a) and the vacancies of the three inequivalent oxygen positions O1 (apical) (b), O2 (corner-sharing) (c) and O3 (edge-sharing) (d). Adapted from [398]. Copyright 2016 American Chemical Society.

Figure 31 shows a schematic diagram of the electronic states of molybdenum oxides as a function of the oxygen vacancies. The electronic character varies from insulator (MoO_3) to semiconductor ($MoO_{3-\delta}$) and finally to metal-like (Mo_9O_{26}), in agreement with conductivity measurements [399]. It is well established that increasing δ in $MoO_{3-\delta}$ can lower the bandgap [401]. The electron distribution in pure MoO_3 follows the ionic model (Mo^{6+} and O^{2-}) corresponding to the Mo $4d^0$ configuration. For non-stoichiometric MoO_3 oxides, extended Mo 4*d* states, which then lie in the bandgap as gap states due to the occurrence of Mo^{5+} and Mo^{4+} ions, are filled by electrons donated from oxygen vacancies. The formation of oxygen deficiency (termed also as sub-stoichiometric) not only produces an increase of the electrical conductivity σ_e [402,403] owing to the additional gap states, but also increases the surface energy of the particles and promotes electrochemical reactions [397,399]. Magnetic susceptibility measurements showed that MoO_3, MoO_2 and Mo_nO_{3n-1} shear suboxides in between are all feebly paramagnetic.

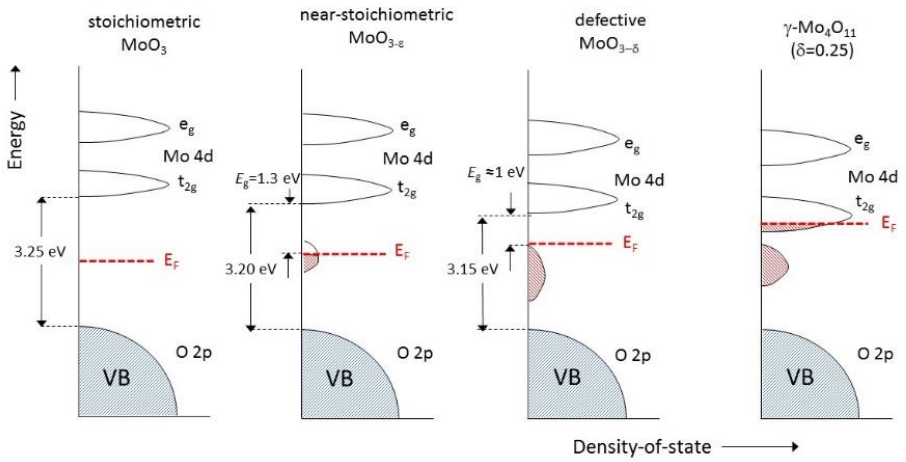

Fig. 31. Schematic diagram of the electronic states of molybdenum oxides as a function of the oxygen vacancies. The electronic character varies from insulator (MoO_3, $\sigma_e > 10^{-9}$ S cm^{-1}) to semiconductor (defective Mo_9O_{26}, $\sigma_e \approx 10^{-1}$ S cm^{-1}) to metal-like (γ-Mo_4O_{11}, $\sigma_e \approx 10^{2}$ S cm^{-1}). Copyright Lakshmi-Narayana et al. [72]. Open access article under the CC BY-NC-ND license.

4.1.2. Determination of δ

X-ray photoelectron spectroscopy (XPS) is an appropriate tool to evaluate the stoichiometry of oxygen deficient $MoO_{3-\delta}$ compounds. From the Mo 3d core level spectra, the presence of Mo in low valence states, i.e., Mo^{5+} and Mo^{4+}, can be evidenced by fitting the XPS $3d_{5/2}$ and $3d_{3/2}$ peaks at binding energies around 235 and 232 eV, respectively (**Table 10**) [85,404].

Table 10. Standard binding energies of Mo 3d levels for molybdenum at different oxidation states [405].

Peak assignment	Binding energy (eV)	
	$3d_{5/2}$	$3d_{3/2}$
Mo^{6+}	232.5	235.7
Mo^{5+}	231.5	234.7
Mo^{4+}	230.1	233.3
Mo^{3+}	229.3	232.5
Mo^{2+}	228.4	232.6
Mo^{0}	227.7	230.9

Based on the deconvolution of the Mo 3d core-level peaks by using equal-width Gaussian peaks $3d_{5/2}$ and $3d_{3/2}$ spin-orbit components, the ratio of Mo^{6+}/Mo^{5+} in a sub-stoichiometric $MoO_{3-\delta}$ oxide is calculated by the following equation [406]:

$$k = \frac{Mo^{6+}}{Mo^{5+}} = \frac{R(Mo^{6+}3d_{5/2})+R(Mo^{6+}3d_{3/2})}{R(Mo^{5+}3d_{5/2})+R(Mo^{5+}3d_{3/2})}, \quad (13)$$

where k is the ratio of the quantity of Mo^{6+}/Mo^{5+} calculated from the ratio of the integrated peak area (R), the valence state for molybdenum can be calculated by the relation [407]:

$$\phi = \frac{6}{1+k^{-1}} + \frac{5}{1+k}, \quad (14)$$

and the stoichiometric deviation is given by:

$$\delta = 3 - \frac{\phi}{2}. \quad (15)$$

As an example, **Figure 32a** shows the XPS spectra of oxygen vacancies-rich α-$MoO_{3-\delta}$ nanobelts synthesized by hydrothermal process. Blue $MoO_{3-\delta}$ nanobelts were obtained by calcining the MoO_3 powder $NaH_2PO_2 \cdot H_2O$ at 250 °C for 1 h in N_2 atmosphere. A graphene nanomesh carbon nanotube/$MoO_{3-\delta}$ (GC/$MoO_{3-\delta}$) nanocomposite with more O-vacancy defects was also characterized [408]. For the pristine MoO_3 nanobelts, the atomic ratio of Mo^{5+}/Mo^{6+} is calculated to be 0.132 giving $\delta = 0.02$, whereas is greatly increased to 0.308 for the GC/$MoO_{3-\delta}$ nanocomposite, indicating the partial reduction of MoO_3, $\delta = 0.12$. Consequently, the electrons occupied in 4d band increase with δ improving the electrical conductivity to 0.83×10^{-5} S cm^{-1}

(two orders of magnitude higher than that of pristine pure MoO_3). Diffuse reflectance spectra show that the bandgap is reduced largely from 3.25 to 2.95 eV with the increase of O-vacancy concentration.

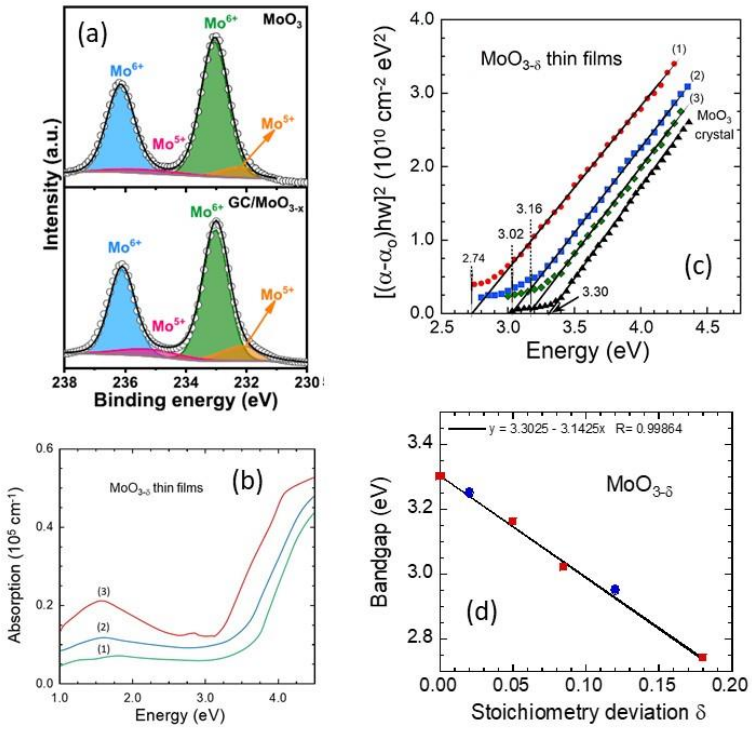

Fig. 32. (a) XPS core-level spectra of Mo 3d for the oxygen vacancies-rich α-$MoO_{3-\delta}$ nanobelts. Reproduced with permission from [408]. Copyright 2019 Elsevier. (b) UV-Vis absorption spectra of flash-deposited α-$MoO_{3-\delta}$ thin films at different substrate temperatures: (1) 30 °C, (2) 120 °C, and (3) 250 °C. (c) Plot of $[(\alpha-\alpha_0)\hbar\omega]^2$ vs. photon energy for thin films and MoO_3 crystal. The intercepts at $\alpha = 0$ (full lines) give the bandgap energy. (d) variation of the bandgap with the stoichiometric deviation. Reproduced with permission from [153]. Copyright 1995 Elsevier.

Ultraviolet-visible spectroscopy can be also used to determine the stoichiometric deviation in $MoO_{3-\delta}$ (**Figs. 32b-c**) [153]. The increase of O-vacancy concentration results in the enhanced absorbance from 300 to 1000 nm. The fundamental absorption edge occurs at about 4 eV with a high value of the absorption coefficient 3×10^4 cm^{-1}. A broad absorption band in the red region, i.e., 1.5 eV, corresponds to the excitation of trapped electrons into the conduction band. As a result, various degrees of coloration occurred. It is worth noting that the coloration of the films is associated with the absorption edge shift. For example, films grown at room temperature are white and transparent, whereas films deposited at higher substrate temperatures

(T_s > 120°C) are deeply colored. The intrinsic absorption edge of the films was evaluated in terms of the direct transition. The optical absorption coefficient α is calculated by the expression:

$$\alpha = \frac{1}{d} ln\left\{\frac{(1-R)^2}{2T} + \sqrt{\left[\frac{(1-R^2)}{2T}\right]^2 + R^2}\right\}, \quad (16)$$

where d is the sample thickness, T the transmittivity and R the reflectivity determined from the optical transmission and reflection spectra, respectively (**Fig. 32b**). The theory of interband absorption near the threshold shows that α vary according the equation:

$$\alpha h\nu = B(h\nu - E_g)^n, \quad (17)$$

where h is the Planck constant, ν the frequency, B the probability parameter, E_g is the optical bandgap and n an exponent, which characterizes the transition process (n = ½ for direct allowed transitions). Thus, the Tauc plot $[(\alpha-\alpha_0)\hbar\omega]^2$ vs. photon energy yields a linear behavior in the region of strong absorption near the absorption edge, as shown in **Fig. 32c**. Extrapolating the linear portion of this straight portion to α = 0 gives the optical bandgap. The optical bandgap of crystalline MoO_3 is E_g = 3.05 eV. As shown in **Fig. 32d**, the bandgap of $MoO_{3-\delta}$ suboxides decreases linearly with the increase of the stoichiometric deviation in the range $0 \leq \delta \leq 0.15$.

4.1.3. Li insertion in $MoO_{3-\delta}$

Generally, the oxygen deficient $MoO_{3-\delta}$ oxides, as cathode or anode materials, exhibits several appealing characteristics for lithium-ion storage, including high specific capacity, good stability against cycling and fast charge transport kinetics [132]. The bulk structure of $MoO_{3-\delta}$ under reductive and oxidative reaction conditions was investigated in situ with time-resolved X-ray absorption spectroscopy (XAS) [409]. The $MoO_{3-\delta}$ suboxide phases (with $0 < \delta < 0.25$) exhibit Li-insertion capacity much higher than that of stoichiometric MoO_3 phase, which justifies the efforts to fabricate them under the form of thin films. For the development of these technologies, oxygen vacancies are easily generated in the $MoO_{3-\delta}$ materials prepared in a thin film architecture by optimizing the deposition conditions [410]. Jung et al. [236] investigated the electrochemical reactivity of ball-milled $MoO_{3-\delta}$ as anode materials for lithium-ion batteries. High-energy ball-milling converts highly-crystalline MoO_3 bulk powders into partially reduced low crystalline $MoO_{3-\delta}$ materials with a reduced particle size. Oxygen deficiency gradually increases as the ball milling time increases. Bulk MoO_3 powders were partially reduced to give nanostructured $MoO_{2.929}$, $MoO_{2.903}$, and $MoO_{2.895}$ by ball-milling for 4, 6, and 8 h, respectively. When tested in the 0.01–3 V *vs.* Li^+/Li range the first discharge

capacity is beyond 1100 mAh g^{-1}, which is indicative of a complete conversion reaction. The lithiation in $MoO_{3-\delta}$ suboxides occurs with two steps: intercalation (>1.5 V) and conversion (<0.5 V), although their voltage profiles become smother than that of MoO_3 bulk. Additionally, incomplete re-oxidation during subsequent charge results in the formation of MoO_2 instead of MoO_3, which in turn affects the reactivity in subsequent cycles. As compared to bulk MoO_3, ball-milled $MoO_{3-\delta}$ showed significantly enhanced cycle performance. The anode material ball-milled for 8 h has 64.4% discharge efficiency at the 35th cycle against 27.6% for bulk at the 10th cycle, which has been attributed to the nano-texture wherein nanometer-sized particles aggregate to form secondary ones. Jegal et al. [390] prepared a mixed-valence $MoO_{3-\delta}$/CNT nanocomposite (x<0.1) using a one-pot microwave-assisted hydrothermal reaction in which 5 nm $MoO_{3-\delta}$ nanoparticles are coated on the surfaces of CNT. The nanocomposite had a reversible discharge capacity of could deliver discharge capacities of 770, 700, and 570 mAh g^{-1} at current densities of 450, 900, and 1800 mA g^{-1}, respectively.

Highly dispersed ultra-small MoO_y nanoparticles (1.5-3.5 nm) anchored on N-doped 3D hierarchically porous carbon (3D-MoO_y@CN) were prepared using an efficient in-situ chelating and hard-templating strategy. An optimized 3D-MoO_y@CN heat-treated at 700 °C delivers specific capacities of 742 and 431 mAh g^{-1} at current density of 100 and 1000 mA g^{-1} after 1000 cycles, respectively. This excellent performance is attributed to the unique hierarchical porous morphology (specific BET surface area of 109 m^2 g^{-1} and pore volume of 0.30 cm^3 g^{-1}) structure with strong binding of the ultra-small MoO_y nanoparticles onto N-doped carbon surface, which can avoid the agglomeration and alleviate the volume expansion of MoO_y nanoparticles in the charge-discharge process [406]. $MoO_{3-\delta}$ nanowires were synthesized in a hot-filament chemical vapor deposition reactor in which molybdenum filaments were resistively heated to 775 °C in 10 sccm of oxygen at a pressure of ~150 Pa [134]. Structural characterization revealed the $Mo_{17}O_{47}$ phase. It has been shown that $Mo_{17}O_{47}$ nanowire arrays can retain a capacity of 630 mAh g^{-1} for up to 20 cycles at a current density of 50 mA g^{-1}. Also, it has been reported that a 10-nm silicon coated $MoO_{3-\delta}$ hybrid architectures, deposited by microwave plasma CVD have shown a capacity retention of 780 mAh g^{-1}. Sun et al. [411] designed vertically aligned oxygen-deficient α-$MoO_{3-\delta}$ nanoflake arrays as 3D cathode for advanced all-solid-state thin film lithium batteries (TFLIBs). The α-$MoO_{3-\delta}$ electrode were fabricated by magnetron sputtering of metal Mo target. The Li/LIPON/$MoO_{3-\delta}$ 3D-TFLIB exhibits high specific capacity of 266 mAh g^{-1} at 50 mA g^{-1} current density, good rate performance (110 mAh g^{-1} at 1000 mA g^{-1}), and excellent cycle performance (92.7% capacity retention after 1000 cycles).

Sun et al. prepared MoO_y nanobelts with different quantities of oxygen vacancies through a "sauna reaction" and tested their performance in LIBs [412]. The number of oxygen vacancies depends on the duration for the production of H_2 by the reaction of the carbon cloth and water vapor to reduce MoO_3. The as-obtained MoO_y nanobelts deliver a reversible capacity of 400 $mAh \cdot g^{-1}$ at 1 $A \cdot g^{-1}$ after 200 cycles without obvious capacity loss. Furthermore, MoO_y exhibits an excellent rate capability (400 and 267 $mAh \cdot g^{-1}$ at 100 and 200 $mA \cdot g^{-1}$ current rate, respectively. Wang et al. [225] investigated the MoO_3-MnO_2 intergrown nanoparticles (6-8 nm in size) composite prepared by one-step hydrothermal synthesis as anode for LIBs. The composite attains an initial specific capacity of 2034 mAh g^{-1} and stays 1446 mAh g^{-1} after 50 cycles at a rate of 0.5C in the voltage range of 0.01-2.0 V. The synergistic effect of MoO_3 and MnO_2 during intergrowth is attributed to the incorporation of Mn^{4+} is incorporated into the MoO_3 lattice to modify its crystal structure, i.e., creation of oxygen deficiency. Carbon nanotube-wired and oxygen-deficient $MoO_{3-\delta}$ nanobelts ($MoO_{3-\delta}$/CNTs) were constructed via hydrothermal synthesis with subsequent controlled reduction in H_2/Ar gas mixture [268]. The MoO_3/CNTs composite, evaluated as an anode in the 0.05–3.0 V potential window, is able to retain a specific capacity of 421 mAh g^{-1} after 100 cycles at 200 mA g^{-1}, and delivers 293 and 202 mAh g^{-1} at current densities of 2 and 4 A g^{-1}, respectively. Zhang et al. [413] prepared several oxygen deficient α-$MoO_{3-\delta}$ cathode materials using H_2 plasma etching process. From XPS measurements, the composition is calculated to be $MoO_{2.912}$ and $MoO_{2.870}$ for MoO_3 etched for 10 and 20 min, respectively, which is confirmed by the appearance of the Raman peak at 1008 cm^{-1} as a result of oxygen vacancy. The $MoO_{2.912}$ electrode shows the best performance delivering a first specific capacity of 224 mAh g^{-1} at 1 A g^{-1} rate, which declines slowly to 67 mAh g^{-1} over 1000 cycles.

In a SIBs, the oxygen vacancies of $MoO_{3-\delta}$ play also an important role. They can enhance the electric conductivity and Na-ion diffusion coefficient [291]. Li and coworkers revealed how oxygen vacancies of MoO_y influenced the performance of the SIBs [290]. $MoO_{2.97}$, which possesses only a few oxygen vacancies exhibits the best specific capacity (176.6 $mAh \cdot g^{-1}$ at 50 $mA \cdot g^{-1}$) and a ~8% capacity loss over 2000 cycles compared with the highest capacity at the 500^{th} cycle. The voltage profile of $MoO_{2.5}$ displays a two-plateau behavior suggesting the stabilized function of oxygen vacancies during the charge/discharge cycling. Yi et al. reported that oxygen-deficient MoO_3 demonstrates excellent performances in Li-S batteries. The cells with $MoO_{3-\delta}$ cathode deliver a capacity of 690 mAh g^{-1} after 200 cycles at 0.2C, demonstrating a significant improvement of the capacity retention. Furthermore, at the current rate of 1C, $MoO_{3-\delta}$ cell displays a high initial capacity of 775 mAh g^{-1} and an enhanced surplus capacity

of 480 mAh g^{-1} after 600 cycles [414]. Wu et al. [226] adopted a carbon-free strategy for an advanced LIB anode material, which consists of a mixture of MoO_3 and MoO_2. MoO_2 nanoparticles treated with a smaller fraction of O_2 (0.2% O_2 in N_2) show mixed phases which can be attributed to MoO_2, MoO_3, as well as a small fraction of Mo_4O_{11}. A high specific capacity up to 930.6 mAh·g^{-1}, long cycle-life (>200 cycles) and high rate capability. $MoO_{3-\delta}$ nanobelts with different concentrations of oxygen vacancies were synthesized by a one-step hydrothermal process using different concentrations of ethanol as the reductant [415]. With the increasing amount of ethyl alcohol in the hydrothermal reaction, the sample color gradually changes from white (pure α-MoO_3) to dark (MoO_2+Mo_4O_{11}). Mo^{5+} in $MoO_{3-\delta}$ appears blue and MoO_2 looks black. $MoO_{3-\delta}$ nanobelts, tested as anode for LIBs in a voltage window of 0.01–3.0 V vs. Li^+/Li, can maintain a high specific capacity of ~500 mAh g^{-1} at a high current density of 1 A g^{-1} and can retain a high specific capacity of 641 mAh g^{-1} after 50 cycles at 100 mA g^{-1} and 420 mAh g^{-1} after 100 cycles at 500 mA g^{-1}.

4.2. $MoO_{3-\delta}$ thin films

$MoO_{3-\delta}$ thin films have been easily prepared using a broad variety of physical vapor deposition (PVD) methods, including thermal evaporation [194,416,417], magnetron sputtering [418,419], dip-coating [394], pulsed layer deposition (PLD) [115,173,420,421]. However, few works report the spin-coating deposition of $MoO_{3-\delta}$ via a low-temperature solution process [422]. α-$MoO_{3-\delta}$ thin films with low resistivity were fabricated on glass substrate via conducting a two-step annealing treatment on the thin film deposited by thermal evaporation method. A heat-treatment in air enables the formation of the α-phase layered structure (resistivity of 10^6 Ω·cm), whereas an annealing in N_2 gives rise to the lowest resistivity of 5.4 Ω·cm without deteriorating crystal structure [417]. The increase in carrier concentration was assigned to the presence of ionized oxygen vacancy during the N_2 annealing as illustrated by the following equation:

$$O_O^x + 2Mo^{6+} \rightleftharpoons V_O^{\cdot\cdot} + 2Mo^{5+} + \frac{1}{2}O_2(g). \qquad (18)$$

Like stoichiometric MoO_3, sub-stoichiometric $MoO_{3-\delta}$ thin films can be obtained by evaporation in a vacuum at relatively low temperature (T < 500 °C) or in reducing atmosphere. However, few works explore the effect of oxygen deficiency and electrical conduction enhancement on energy storage properties [423]. Parashar demonstrated that the deposition temperature plays a crucial role on the composition of $MoO_{3-\delta}$ thin film deposited by magnetron sputtering in argon plasma. At working pressure of 0.5 Pa and RF power of 75 W, the film

deposited at T_s = 250 °C is a mixture of α-MoO_3 and Mo_4O_{11} phases, while a pure α-MoO_3 phase is grown at T_s = 350 °C [418]. Sub-stoichiometric $MoO_{3-\delta}$ thin films were deposited on SiO_2 glass and stainless-steel substrate using conventional RF sputtering technique [144]. The films fabricated in an Ar gas atmosphere at a sputtering gas pressure of 4 Pa, a radio-frequency power of 200 W, a substrate temperature of 100 °C and a deposition rate of 1.16 µm h^{-1} exhibit the Mo_9O_{26} structure (dark-blue color) with the crystallographic (010) plane oriented parallel to the substrate surface. The OCV of the Mo_9O_{26} thin-film electrode (4.6 µm thick) was 2.7 V. The discharge capacities of the 1st, 10th and 21st cycles were 398, 318 and 289 µAh cm^{-2}, respectively, at a current density of 10 mA cm^{-2}. Recently, He and coworkers [419] prepared sputtered MoO_y thin films with different oxygen contents (fixed Ar flow rate of 10 sccm and variable O_2 flow rate from 0.4 to 1.5 sccm corresponding to 3.8%-13%). $MoO_{2.95}$, $MoO_{2.43}$, $MoO_{2.7}$, and $MoO_{1.45}$ thin films were obtained with O_2 concentration of 13.0%, 8.6%, 6.5% and 3.8%, respectively, showing that the decrease of the oxygen content pushes the Fermi level very close to the conduction band. Puppala et al. investigated the microstructure and morphology of PLD $MoO_{3-\delta}$ thin films growth for catalytic applications using a femtosecond laser (f-PLD) and a nanosecond excimer-laser (n-PLD). Substantially textured films with a partially crystalline phase prior to annealing were obtained by the f-PDL laser, while the n-PLD-grown $MoO_{3-\delta}$ films were predominantly amorphous with a smooth surface [186]. Sunu et al. claimed that as-deposited PLD films (T_s = 400 °C, Φ = 4–5 J cm^{-2}, repetition rate of 15 to 20 Hz, and p(O_2) = 500 Pa) are suboxide-like, i.e., mixture of η-Mo_4O_{11} and χ-Mo_4O_{11}, which transformed to MoO_3 after annealing at 500 °C in air for 5 h [392].

Recently, the effects of operational conditions on structural, electronic and electrochemical properties on molybdenum suboxides ($MoO_{3-\delta}$) thin films were investigated [72]. Three classes of samples are obtained with different degrees of stoichiometric deviation without post-treatment: (i) amorphous $MoO_{3-\delta}$ ($\delta < 0.05$) (ii) nearly-stoichiometric samples ($\delta \approx 0$) and (iii) suboxides $MoO_{3-\delta}$ ($\delta > 0.05$). The suboxide films $0.05 \leq \delta \leq 0.25$ deposited on Au/Ti/SiO_2/flexible-Si substrates with appropriate processing conditions show high electrochemical performance as an anode layer for lithium planar microbatteries. In the realm of simple synthesis, the $MoO_{3-\delta}$ film deposited at 450 °C under oxygen pressure of 13 Pa is a mixture of α-MoO_3 and Mo_8O_{23} phases (15:85). The electrochemical test of the 0.15MoO_3-0.85Mo_8O_{23} ($MoO_{2.894}$) film shows a specific capacity of 484 µAh cm^{-2} μm^{-1} after 100 cycles of charge-discharge at a constant current of 0.5 A cm^{-2} in the potential range 3.0-0.05 V. This capacity value corresponds to the insertion of ~5.78 Li^+/Mo, is close to the theoretical maximum (5.79 Li^+/Mo). **Figure 33** presents the electrochemical performance of the $MoO_{3-\delta}$ deposited at

450 °C under oxygen pressure of 13 Pa [72]. Amorphous MoO_y thin films prepared by reactive magnetron sputtering deposition (total $Ar+O_2$ gas flow kept at 40 sccm at 0.8 Pa using 20% O_2) consists of a mixture of amorphous MoO_3 and MoO_2 phases [424]. The a-MoO_y thin films (1.1 µm thick) exhibit a high capacity of 338 µAh·cm^{-2} (about 845 mAh·g^{-1}) at a current density of 90 µA cm^{-2} even after 100 discharge/charge cycles, and have a rate capacity of 158 µAh cm^{-2} at a high current density of 2000 µA cm^{-2}.

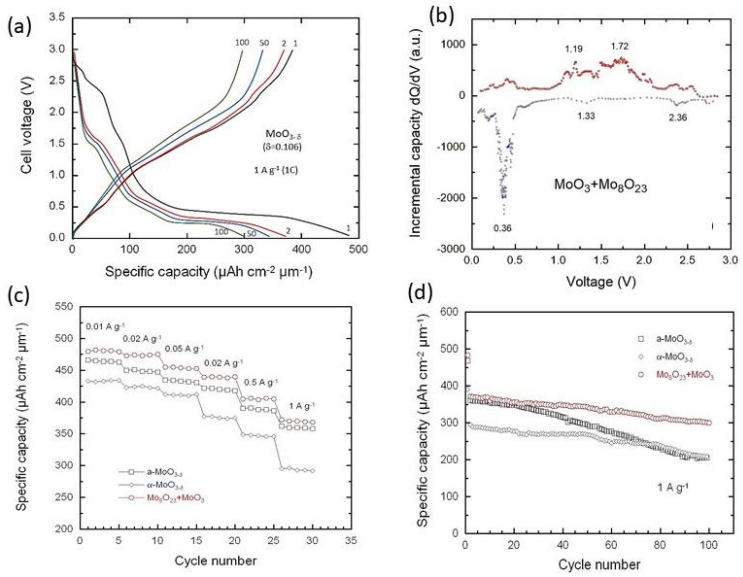

Fig. 33. Electrochemical tests of the MoO_3-Mo_8O_{23} (15:85) thin film in Li cells with 1 mol L^{-1} $LiPF_6$ dissolved in ethylene carbonate and dimethyl carbonate (EC:DMC; 1:1 *w*/*w*) as aprotic electrolyte. (a) Galvanostatic charge discharge profiles of a cell cycled at 1 A g^{-1} current density in the voltage range 3.0–0.05 V. (c) Differential capacity (-d*Q*/d*V* vs. *V*) of the first lithiation-delithiation cycle. (c) Rate capability. (d) Cyclability over 100 cycles at 1 A g^{-1} compared with amorphous $MoO_{3-\delta}$ and α-$MoO_{3-\delta}$ film deposited at 300 °C. Copyright Lakshmi-Narayana et al. [72]. Open access article under the CC BY-NC-ND license.

5. Magnéli-type Mo oxides

In the Mo-O binary system, there is the series Mo_nO_{3n-1}, which crystallizes in the so-called Magnéli phases described in details by Kihlborg [37] (see crystallographic parameters in **Table 11**). They are oxygen deficient relative to MoO_3. The removal of oxygen and accompanied partial reduction of Mo(VI) cations introduce crystallographic shear maintaining the layered framework. These oxides have been identified as derived from MoO_3 by shear mechanism with networks of MoO_6 octahedra. These units are connected in three dimensions with empty parallel tunnels involving the presence of potential sites for hosting Li^+ ions. The crystal structures of

the Mo_nO_{3n-1} molybdenum oxides, with their respective single unit cells are shown in **Fig. 34**. Since 1980s, quasi-2D layered Mo_nO_{3n-1} compounds with commensurate/incommensurate periodic lattice distortion (PLD) have attracted great attention due to their fascinating property of charge-density-wave (CDW) [425,426]. These intermediate molybdenum oxides are believed to be also catalytically active [427]. Furthermore, they exhibit a rich phase polymorphism and a variety of morphologies.

Table 11. Structural parameters of Mo_nO_{3n-1} molybdenum oxides.

Compound	Space group	Cell parameters (Å)			Ref.
		a/α	*b*/β	*c*/γ	
$Mo_{17}O_{47}$	*Pba*2	21.61/90°	19.63/90°	3.951/90°	[38]
Mo_9O_{26}	*P*2/*c*	14.45	4.00/96.0°	16.750	[36]
Mo_8O_{23}	*P*2/*a*	16.88	4.052/106.19°	13.39	[428]
η-Mo_4O_{11}	$P2_1/a$	6.695/90°	5.440/94.31°	324.573/90°	[429]
γ-Mo_4O_{11}	*Pnam*	24.49/90°	6.752/90°	5.457 /90°	[430]
Mo_5O_{14}	*P*4/*nmm*	23.00	-	3.937	[431]
$Mo_{18}O_{52}$	$P\bar{1}$	8.145/102.67	11.89/67.82°	21.23/109.97°	[35]

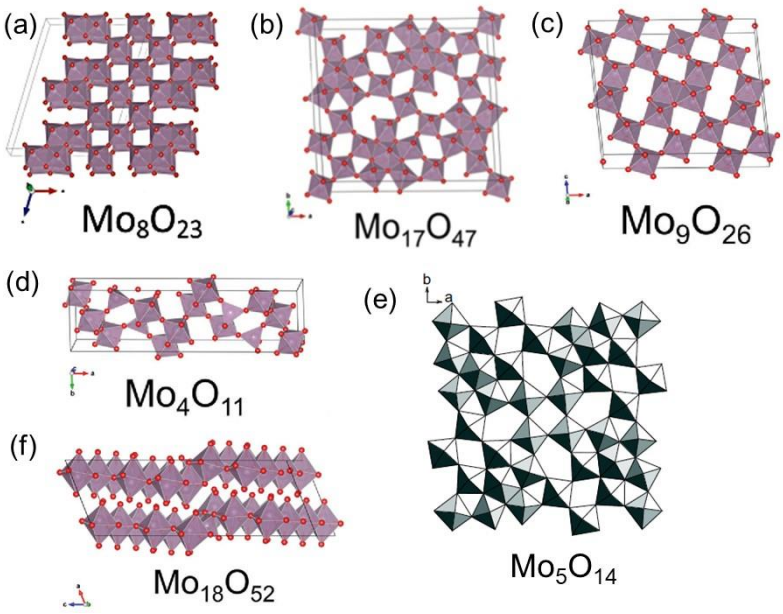

Fig. 34. Crystal structures of Magnéli Mo_nO_{3n-1} phases. Reproduced with permission from [400]. Copyright 2017 Royal Society of Chemistry.

In 1951, Glemser and Lutz [54] investigated the structure of several molybdenum blue oxides, the crystallized samples Mo_8O_{23} and Mo_9O_{26}, amorphous blue oxide hydrates $MoO_{2.75}{\cdot}nH_2O$ and $MoO_{2.80}{\cdot}nH_2O$, and crystallized blue hydroxides $Mo_4O_{10}(OH)_2$ and $Mo_2O_4(OH)_2$, which are closely related to the starting material MoO_3. The Mo_nO_{3n-1} phases

include Mo_4O_{11} [432,433], Mo_5O_{14} [434], Mo_6O_{17}, Mo_8O_{23} [36], Mo_9O_{26} [40], $Mo_{18}O_{52}$ [35,435] and $Mo_{17}O_{47}$, which are formed by a mixture of Mo oxidation states between +6 and +4. As experimental results, the topotactic reaction of lithium into the MoO_y framework and reversibility have been demonstrated [66,67], and extent of lithiation depend on the stoichiometry of the Mo_nO_{3n-1} phases. Due to their tunneling structure with empty cavities, the Mo_nO_{3n-1} phases are performant cathode materials in non-aqueous lithium cells [61,436-439]. Christian and co-workers [440] shown that of the oxides Mo_4O_{11} ($MoO_{2.75}$), $Mo_{17}O_{47}$ ($MoO_{2.765}$), Mo_8O_{23} ($MoO_{2.889}$), and Mo_9O_{26} ($MoO_{2.875}$) the greatest reversible capacity (1.5 Li/Mo) after several deep discharge-charge cycles was exhibited by $Mo_{17}O_{47}$ in cells with $LiClO_4$/propylene carbonate electrolyte in the potential range 2.9-1.4 V (**Table 12**).

Table 12. Electrical and electrochemical characteristics of Mo_nO_{3n-1} oxides.

Compound	ρ (Ω cm)	Li uptake (Li/Mo)	
		1st cycle	20th cycle
$Mo_{18}O_{52}$	10	0.7	0.3
Mo_8O_{23}	1	1.0	0.4
Mo_4O_{11}	0.01	1.5	0.75
$Mo_{17}O_{47}$	0.05	1.5	0.8
Mo_5O_{14}	0.02	1.45	-

5.1. Mo_4O_{11} ($MoO_{2.75}$)

The Mo_4O_{11} phase has two 2D modifications (metal-like), orthorhombic γ-Mo_4O_{11} [441] and monoclinic η-Mo_4O_{11} [442]; in the metallic η-Mo_4O_{11} phase the layers with the ReO_3-type are ordered parallel to each other, whereas in γ-Mo_4O_{11} they are arranged like the mirror image of the former ones [443]. Cignini et al. [436] investigated the electrochemical behavior of the orthorhombic Mo_4O_{11} phases in Li cells with different electrolytes. The higher specific capacity of 340 mAh g^{-1} was delivered in $LiClO_4$/PC. A Li//Mo_4O_{11} cell, discharged at 0.5 mA cm^{-2}, has given 610 Wh kg^{-1}, based on the weight of Li and Mo_4O_{11}. When the discharge for Mo_4O_{11} is stopped above 2 V corresponding to $x < 0.7$ e^-/Mo), the lattice of this oxide is essentially retained, while at 1.5 V, the Mo_4O_{11} structure is greatly altered with the appearance of new phases.

5.2. Mo_5O_{14} ($MoO_{2.8}$)

The crystal structure of Mo_5O_{14} (denoted as *θ*-Mo oxide) is tetragonal (*P*4/*mbm* S.G.). The lattice consists of either distorted MoO_6 octahedra and MoO_7 pentagonal bi-pyramids which are coupled together by edge- and corner-sharing [431]. As shown in **Fig. 34e**, the pentagonal bipyramids are edge sharing with the neighbored octahedra perpendicular to the fivefold axis

and tunnels are parallel to the *c*-axis. Few works reporting the lithiation of Mo_5O_{14} are available in the literature [121,436,410,444]. Preliminary patterns of the fully lithiated Mo_5O_{14} crystal suggest that the unit cell expands in the *b*-direction and contracts in both the *a*- and *c*-directions upon insertion of lithium [440]. Among the Mo_nO_{3n-1} oxides, Mo_4O_{11}, $Mo_{17}O_{47}$, and Mo_8O_{23}, the compound $Mo_{17}O_{47}$ has the highest intercalation cyclability. Its average discharge voltage is 1.85 V, and its reversible discharge capacity is 1.5 Li/Mo. Its theoretical specific energy is 490 Wh kg^{-1}. Cignini et al. reported a specific capacity of 310 mA g^{-1} for Mo_5O_{14} as the positive electrode of a primary Li cell discharged at 0.5 mA cm^{-2} and 1.0 V cut-off. [436]. Nazri and Julien [121] showed that $MoO_{2.8}$, an oxygen-deficient Mo_5O_{14} prepared by dehydration and annealing treatment of molybdic acid powder ($MoO_3 \cdot 1H_2O$) at 750 °C, exhibits a high electrical conductivity of 10^{-2} S cm^{-1}. Such a material displays an excellent reversible capacity (1.45 e^-/Mo) in cells with 1 mol L^{-1} $LiClO_4$ in propylene carbonate (PC) electrolyte in the potential range 3.3–1.3 V vs. Li^+/Li. The open-circuit voltage is 3.1 V vs. Li/Li^+. The first discharge displays a stepped behavior with a voltage plateau at ca. 2.2 V followed by a potential decline for $x > 0.7$ e^-/Mo. This compound can be assigned to the $Mo_3^{6+}Mo_2^{5+}$ valence distribution. If reversible lithium incorporation produced all Mo^{4+}, the expected lithium uptake would be 8/5(1.6) e^-/Mo; a value close to that measured by electrochemical titration. The gravimetric capacity of 326 mAh g^{-1} was much higher than the 280 mAh g^{-1} of anhydrous MoO_3. Shembel et al. [445] reported the electrochemical performance of e-Mo_4O_{11} synthesized from ammonium molybdate electrolyte in thin-layer binder-free electrodes. A first discharge capacity of 900 mAh g^{-1} is delivered at 30 mA g^{-1} current density. The reversible discharge capacity can exceed 225 mAh g^{-1} for more than 170 cycles.

Oxygen deficient $MoO_{3-\delta}$ nanoparticles (200 nm thick) were prepared by a citrate sol-gel using ammonium heptamolybdate tetrahydrate as a source of Mo and heat treated with a small fraction of zirconia under reducing atmosphere [446]. The structural analyses reveal that the composite is a blend formed by layered α-MoO_3, orthorhombic oxygen deficient phases $MoO_{3-\delta}$ with $\delta = 0.25$ (γ-Mo_4O_{11}) and α-$ZrMo_2O_8$. At C/10 rate, the composite delivered a stable reversible capacity of 135 mAh g^{-1} after the 50th cycle. At a rate of 2C the reversible capacity is maintained at 118 mAh g^{-1}. An amorphous Mo_nO_{3n-1}/carbon nanocomposite ($n \approx 5$) was fabricated from a citrate–gel precursor heated at moderate temperature (500 °C) in inert (argon) atmosphere. The as-prepared Mo_5O_{14}-type/C material is compared to α-MoO_3 synthesized from the same precursor in air. Thermal gravimetry and elemental analysis indicate the presence of 25.8 ± 0.2% of carbon in the composite. The RS spectrum of Mo_5O_{14}/C demonstrates an oxygen deficiency in the molybdenum oxide and the presence of a partially graphitized carbon.

Outstanding improvement in electrochemical performance is obtained for the Mo_5O_{14} encapsulated by carbon (325 mAh g^{-1} at the 50th cycle at 70 mA g^{-1}) in comparison with the carbon-free MoO_3 (95 mAh g^{-1}). The high performance of the Mo_5O_{14}/C composite is clearly revealed with a specific discharge capacity of 155 mAh g^{-1} at 10C rate (7 A g^{-1}) [109]. Mo_4O_{11} nanoparticles were decorated onto ultralight graphene sheets (HRG) self-assembled with sulfur homogeneously dispersed onto the surface were used as the cathode material for a lithium sulfur battery [447]. The Mo_4O_{11}−HRG/S cathode deliver a specific capacity of ~900 mAh g^{-1} at 0.1C rate after 80 cycles at cut-off of 1.5 V. Tysyachny et al. [448] investigated the transport properties of the electrolytic oxide Mo_4O_{11} as cathode material of lithium battery. The average values of D_{Li}^{*} in Mo_4O_{11} determined by cyclic voltammetry are in the range from 3.0 to 6.4×10^{-12} cm^2 s^{-1}.

5.3. Mo_8O_{23} ($MoO_{2.875}$)

Mo_8O_{23} has a monoclinic crystal structure (*P2/a* S.G.), which derived from that of ReO_3 by a shear mechanism, is formed by slabs, 8 MoO_6 octahedra thick, mutually connected by edge-sharing between octahedra. It is a 3D framework characterized by intersecting channels and of cavities (**Fig. 34a**). Besenhard and Schollhorn [61] reported that cathodes containing Mo_8O_{23} can be galvanostatically reduced resulting in the first uptake of ~1 e^- per Mo in 0.35 mol L^{-1} $LiAlCl_4$/DME electrolyte, which reduced to 0.4 Li after 20 cycles. Pistoia and co-workers examined the electrochemical properties of Mo_8O_{23} as cathode in lithium cells. Fiordiponti et al. [439] reported that Li cells containing the monoclinic Mo_8O_{23} cathode show a stepwise discharge curve with particularly noticeable knees for $0.2<x<0.3$, $0.6<x<0.7$, and $0.8<x<0.9$, which does not prevent a complete reversibility. For high values of Li content, more serious structure alterations start to take place to which the sharp fall of potential may be attributed. Mo_8O_{23} exhibits at first a shrinkage of the unit cell until 0.2Li/Mo, which is attributed to the large empty cavities with at least 12 coordinating sites, followed by a lattice re-expansion. At 1.0 mA cm^{-2} and 2.0 V cut-off, 85 mAh g^{-1} (0.89 e^-/Mo) and 200 Wh kg^{-1} were obtained. Mo_8O_{23} maintains good recharge efficiencies for over 15 cycles. The chemical diffusion coefficient Li ions in $Li_xMo_8O_{23}$ was measured in the range $0.0<x<0.8$. D_{Li}^{*} reaches a maximum value of 5 ×10^{-9} cm^2 s^{-1} at *x* near to 0.3.

5.4. $Mo_{18}O_{52}$ ($MoO_{2.889}$)

$Mo_{18}O_{52}$ crystallized with the triclinic symmetry ($P\bar{1}$ S.G.). Its network maintains the layered structure of MoO_3 (**Fig. 34f**). Ressler et al. [449] investigated the bulk structural

modification of Mo-O oxides by the reduction of MoO_3 with propene and the oxidation of MoO_2 with oxygen. The formation of a $Mo_{18}O_{52}$-type shear structure consists of generation of oxygen vacancies at the (100) or (001) facets by reaction with propene and a vacancy diffusion in the MoO_3 bulk. Kaiser et al. [450] prepared Mo_nO_{3n-1} compounds by the solid-state reaction of powdered α-MoO_3 with Mo in the spark-plasma synthesis (SPS) process at temperatures up to 973 K: $Mo_{18}O_{52}$ (x = 2.889), $Mo_{17}O_{47}$ (x = 2.760), and γ-Mo_4O_{11} (x = 2.750), which show different thermoelectric properties. $Mo_{18}O_{52}$, which appears to be an intrinsic narrow-gap semiconductor (activation energy ≈ 0.3 eV), exceptionally low thermal conductivity over the full temperature range (0.5–0.9 W m^{-1} K^{-1}), while γ-Mo_4O_{11}, and $Mo_{17}O_{47}$ show poor metallic conductivity. The highest power factor is achieved by $Mo_{17}O_{47}$ (30 W m^{-1} K^{-2} for 440 ≤ T ≤ 610 K). Preliminary electrochemical tests of $Mo_{18}O_{52}$ in 0.35 mol L^{-1} $LaAlCl_4$/DME were conducted at 0.3 mA cm^{-2} current density. The galvanostatic reduction in the potential window from -0.1 to -2.8 V vs. SCE yields 1.5 e^- per Mo [61]. Investigations of $Mo_{18}O_{52}$ by Pistoia et al. [438] show that this non-stoichiometric $Mo_{18}O_{52}$ oxide displays a high-rate capability as cathode for secondary Li cells. In a cell with 1 mol L^{-1} $LiClO_4$/PC electrolyte, it can intercalate reversibly up to 1.35 Li/Mo (250 mAh g^{-1}) at current density in the range 1.0 mA cm^{-2} and 1 V cut-off, forming ternary phases. In a cell with 2 mol L^{-1} $LiAsF_6$/methyl formate electrolyte, it delivers 340 mAh g^{-1} (1.81 e^-/Mo charge transfer). Li^+-ion diffusion is relatively fast in the $Mo_{18}O_{52}$ channels (D^*_{Li}= 10^{-9} cm^2 s^{-1}) and gives rise to a structure, in which Li^+ is tetrahedrally coordinated by oxygen.

5.5. Mo_9O_{26} ($MoO_{2.889}$)

Mo_9O_{26} has the same composition than $Mo_{18}O_{52}$, but crystallizes with a monoclinic structure (*P*2/*c* S.G.), which derives from the metastable ReO_3-type modification β-MoO_3.

5.6. $Mo_{17}O_{47}$ ($MoO_{2.765}$)

Christian et al. [440] obtained their best results with $Mo_{17}O_{47}$. Li//$Mo_{17}O_{47}$ cells could be cycled over 35 times at current densities of 0.5 mA cm^{-2} and average discharge voltages of 1.85 V. The $Mo_{17}O_{47}$ framework accommodates 1.5 electrons per Mo during the first cycle, which reduces to 0.8e^- at the 20th cycle. Among the Mo_nO_{3n-1} oxides, $Mo_{17}O_{47}$ has the highest intercalation cyclability. From these figures, the theoretical specific energy is 400 Wh kg^{-1}. Meduri et al. [132] prepared MoO_{3-x} nanowire arrays with diameters of ~90 nm in a hot-filament chemical vapor deposition reactor at 775 °C in 10 sccm of oxygen at a pressure of 146 Pa. XRD and Raman characterization indicate an oxygen deficient $Mo_{17}O_{47}$ orthorhombic

phase. The initial discharge capacity retention of ~770 mAhg^{-1} at a current density of 25 mA g^{-1} in the range 0.1-3.5 V corresponds to 4.1 Li^+ ions per MoO_{3-x}. A capacity of ~630 mAh g^{-1} is retained for up to 20 cycles at a current density of 50 mA g^{-1}. Hugues et al. [449] considered that, among Mo oxides with formulae between MoO_2 and MoO_3, $Mo_{17}O_{47}$ is the best cathode materials, which can supply current densities of 15 mA cm^{-2}.

6. Molybdenum Dioxide MoO_2

Molybdenum dioxide occurs as the mineral *tugarinovite* (molar mass 127.94 g mol^{-1}, density 6.47 g cm^{-3}, insoluble in water, melting point 1100 °C).

6.1. Structure

MoO_2 crystallizes with the monoclinic structure with space group $P2_1/c$ (C_{2h}^5), which can be viewed as a distorted rutile phase (**Fig. 35a**). This structure is composed of MoO_6 octahedra joined by edge-sharing, which form a (1×1)-tunnelling network (**Fig. 35b**). The lattice parameters of MoO_2 are a = 5.6109 Å, b = 4.8562 Å, c = 5.6285 Å, and β = 120.95° (JCPDS card No. 66-6787) [452,453]. The unit cell comprises four formula units. The metal atoms as well as the two inequivalent oxygen atoms occupy the general Wyckoff positions (4*e*). An interesting feature of MoO_2 is that its metallic ground state (electrical resistivity 6.9 × 10^{-4} Ω cm) (**Fig. 35c**) [454]. The *d* orbital can be separated into two sub-bands, i.e., t_{2g} and e_g bands by the crystal field. The t_{2g} band has a lower energy level and is partially filled by the two electrons, and the e_g band is empty and has a higher energy level located above the Fermi energy (**Fig. 35d**). This metallicity indeed differentiates MoO_2 from insulating MoO_3.

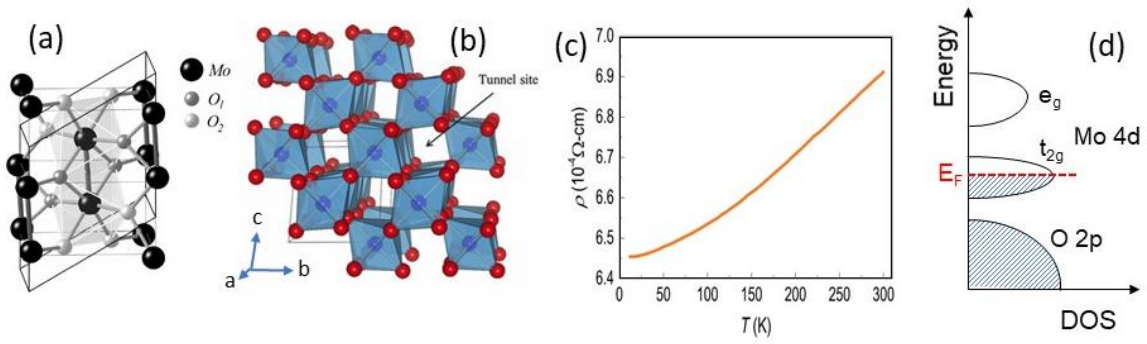

Fig. 35. (a) The distorted rutile structure of MoO_2 (monoclinic, $P2_1/c$ S.G.). (b) View of the (1 × 1) tunnels in the rutile network. (c) Temperature-dependent resistivity. It shows a typical metallic behavior. The lowest resistivity is around 6.45 × 10^{-4} Ω cm. reproduced with permission from [454]. Copyright 2014 Royal society of Chemistry. (d) Schematic band

diagram. The *d* orbital can be separated into two sub-bands, i.e., t_{2g} and e_g bands by the crystal field. The t_{2g} band has a lower energy level and is partially filled by the two electrons, and the e_g band is empty and has a higher energy level located above the Fermi energy.

6.2. Lithium insertion

Importantly, MoO_2 is considered to be one of the most studied anode systems for lithium-ion batteries [455,456]. The lithium ions are inserted in the octahedral interstitial sites that are located in the tunnels between chains to form Li_xMoO_2 as reported 30 years ago [457,458]. MoO_2 as Li-ion battery anode was systematically studied by Auborn and Barberio in 1987 for the first time [459] who demonstrated a relatively large capacity of 400-600 mAh g^{-1}.

The lithiation of MoO_2 is a subject of debate since different mechanisms have been described, i.e., insertion reaction and conversion reaction delivering a theoretical gravimetric capacity of 838 mAh g^{-1} and a theoretical volumetric capacity of 1357 mAh cc^{-1} [460,461]. The first lithiation mechanism is an insertion-type reaction, which took place in the bulk and amorphous MoO_2 electrodes with only one-electron reduction as described by the equation [457]:

$$MoO_2 + xLi^+ + xe^- \leftrightarrow Li_xMoO_2, \quad (19)$$

with $0 \leq x \leq 0.98$. The second mechanism is a conversion reaction that gradually resolves Li_xMoO_2 as described by the equation [462]:

$$Li_xMoO_2 + 3.02Li \leftrightarrow 2Li_2O + Mo. \quad (20)$$

that evidences the formation of metallic Mo and Li_2O. In-situ XRD structural investigations of the lithium ions insertion into MoO_2 have shown that the original monoclinic lattice ($P2_1/c$ S.G.) transforms to another monoclinic structure ($P2_1/c$ S.G.) via an orthorhombic phase (*Pnnm* S.G.). **Figure 36** presents the crystal structure of monoclinic MoO_2, orthorhombic Li_xMoO_2 and $Li_{0.98}MoO_2$. [463].

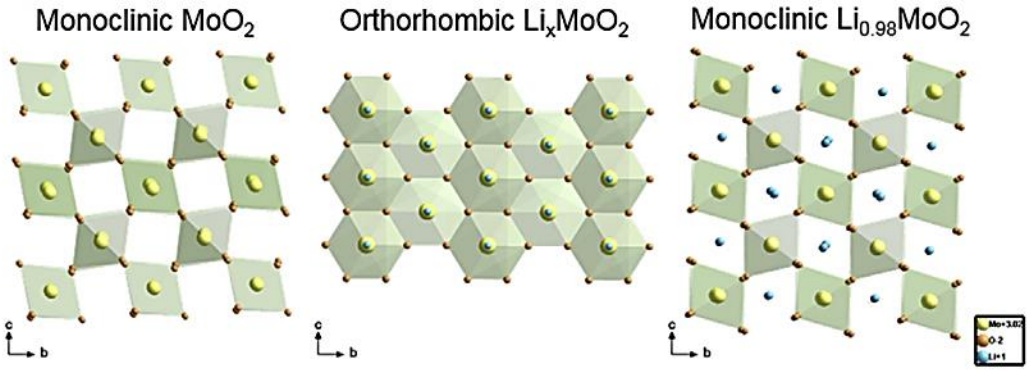

Fig. 36. The crystal structure of monoclinic MoO_2, orthorhombic Li_xMoO_2 and $Li_{0.98}MoO_2$. reproduced with permission from [463]. Copyright 2016 Elsevier.

The volume change associated with the Li insertion is only 11%. Based on Li^+ insertion and extraction reaction, the phase transition MoO_2 to $LiMoO_2$ occurs in the potential range 2.5-1.0 V on discharge (reduction) and vice versa on charge (oxidation) [455,457,464]. In the first cycle, two pronounced reduction peaks were observed at 1.49 and 1.20 V, which may arise from the phase transition from orthorhombic to the monoclinic phase due the Li insertion [465]. Ku et al. [466] demonstrated that structural defects in amorphous MoO_2 electrodes can serve as a reversible Li^+ storage site for lithium secondary batteries. An unexpectedly high Li^+ storage capacity (up to four Li per MoO_2 unit), which is larger by a factor of four than that for the crystalline counterpart. The conversion-type lithiation is discarded for this electrode from the absence of Mo metal and Li_2O in the lithiated α-MoO_2 electrode with high specific capacity up to 810 mAh g^{-1}. In comparison to MoO_3, MoO_2 has superior electronic conductivity, less charging potential, and higher volumetric capacity, which are highly important for application as an anode material in LIBs [467,468]. **Figure 37** presents the typical electrochemical behavior of a MoO_2 composite anode for LIB [468].

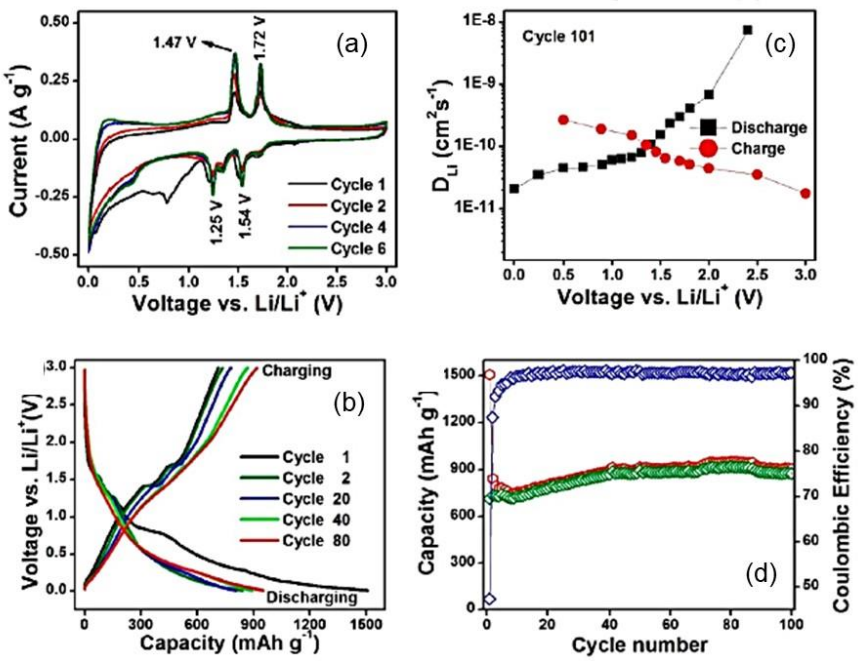

Fig. 37. Typical electrochemical properties of a MoO_2 composite anode for LIB. (a) Cyclic voltammograms conducted at a sweep rate of 58 μV s^{-1} in the voltage range of 0.005−3.0 V. CV curves contain strong redox couples centered at 1.25/1.47 and 1.54/1.72 V, which corresponds to Li intercalation and deintercalation into MoO_2 according to Eq. 1. (b) Galvanostatic discharge-charge profiles of Li_xMoO_2 recorded at 100 mA g^{-1} current rate. (c) Chemical diffusion coefficient of Li ion in MoO_2 anode measured after 100 discharging/charging cycles. (d) Cyclability and coulombic efficiency over 100 cycles at 100

mA g^{-1} current rate. Reproduced with permission from [468]. Copyright 2016 American Chemical Society.

MoO_2 has been synthesized using various techniques [469]: template method [455,470-473], hydrothermal method [467,474-478], reduction of MoO_3 [479-481], soft chemistry route [464,465,482], spray pyrolysis [483-485], carbothermal reaction [486], ion-exchange route [487], and so on. Traditionally, molybdenum dioxide is prepared by reducing MoO_3 with hydrogen at high temperature and the product grows as micrometer size [479,480]. Manthiram et al. [488] and Liu et al. [489] reported the preparation of MoO_2 powders by a reduction process in solution reaction routes, but their products showed a limited success because their low-dimensional nanosized powders. Liang et al. [477] prepared MoO_2 nano-particles by a hydrothermal reaction route. The results show the resulting spherical, sheet-like and bar-shaped samples present a single phase MoO_2 with monoclinic structure. SnO_2/MoO_3 nanowires were synthesized by a combination of hydrothermal (preparation of a white MoO_3 precipitate from the yellowish solution of MoO_2 powders dissolved in H_2O_2) and wet chemical (decoration of MoO_3 nanowires by SnO_2 nanoparticles by mixing MoO_3 with $SnCl_2$ with addition of HCl) routes [228].

6.3. MoO_2 anode for LIBs

The characteristic lithium-intercalation properties of spherical MoO_2 powders imply there is a correlation between their nano-sized structure and an irreversible phase transition after the initial discharge process. MoO_2 anode materials were made with various morphologies: nanobelts [490], nanorods [474,491], nanoporous powders [455,492], nanospheres [473,477] and nanosheets [493]. Rod type-MoO_2 was synthesized by two steps: preparation of hexagonal MoO_3 powders with rod shape followed by an ethanol-assisted reduction in 5% H_2/Ar atmosphere [335]. Zhang et al. [474] have prepared uniform MoO_2 nanorods by a facile hydrothermal method, and the resultant samples were lithiated by subsequent treatment with LiCl solution. After lithiation, the MoO_2 nanorods possessed a similar crystalline structure to the unlithiated sample. At a current density of 20 mA g^{-1}, the lithiated specimen with better coulombic efficiency displayed a preferable cycling performance and exhibited excellent reversible charge-discharge capacity, while the unlithiated MoO_2 exhibited more irreversible behavior. MoO_2 nanosheets were synthesized for the first time by a solvothermal route using an ionic liquid [494]. When used as anode, the MoO_2/C nanosheets exhibit a high reversible capacity of 620 mAh g^{-1} at 100 mA g^{-1} for 20 cycles.

Since 2000, many works achieve improved electrochemical performance of MoO_2 anode materials. Different architectures have been proposed including 2D [495,496] and 3D assemblies [455,460,493,497]. Spherical type-MoO_2 was prepared by ultrasonic spray pyrolysis of aqueous ammonium molybdate and 5-20% sucrose in 550-650 °C under 5% H_2/Ar atmosphere [484]. Shi et al. [455] prepared highly ordered mesoporous MoO_2 by using phosphomobyldic acid as precursor and silica KIT-6 as hard template via nanocasting strategy. The mesoporous MoO_2 electrode shows a first discharge capacity of 960 mAh g^{-1} ($Li_{4.6}MoO_2$) and a charge capacity of 630 mAh g^{-1} (Li_3MoO_2) in the potential range of 0.01-3.0 V. Sun et al. [498] fabricated MoO_2 monolith using cotton cloth that is utilized as a binder-free alternative anode that exhibits a high reversible Li-storage capacity of 719 mAh g^{-1} at 200 mA g^{-1} after 30 cycles. Manthiram and Tsang [464] synthesized amorphous $MoO_{2+\delta}$ (δ=0.3) at ambient temperatures by a reduction of aqueous potassium molybdate solution with potassium borohydride. The amorphous sample exhibits excellent cyclability with a capacity of over 200 mAh g^{-1} in the range 3 to 1 V in lithium cells with electrochemical behavior distinctly different from that of crystalline MoO_2. MoO_2 nanoparticles (~100 nm) were synthesized by reduction of MoO_3 with ethanol vapor. This anode material exhibits good rate capability for the LIBs It displays an initial charge capacity of 318 mAh g^{-1}, which maintains 100% after 20 cycles in the range of 0.01–3.00 V at a current density of 5 mA cm^{-2}, and around 85% of the retrievable capacity is in the range of 1.0–2.0 V [467].

Tremella-like MoO_2 consisting of nanosheets (NSs) were prepared using a Fe_2O_3-assisted hydrothermal reduction of MoO_3 in ethylenediamine aqueous solution [493]. As an anode material for LIB, MoO_2 NSs deliver a reversible capacity of 538 mAh g^{-1} with the coulombic efficiency of 70% at the current density of 0.5 mA cm^{-2} in the first cycle and sustains ~300 mAh g^{-1} at 5.0 mA cm^{-2} after 22 cycles. Ultrafine MoO_2 nanorods (~5 nm diameter) were successfully synthesized by a nanocasting method using mesoporous silica SBA-15 as hard template. The ultrafine MoO_2 nanorod electrode exhibits a first discharge capacity of 775 mAh g^{-1} ($Li_{3.7}MoO_2$) at C/20 rate in the voltage range 3.0-0.01 V. The capacity even reaches 830 mAh g^{-1} after 29 cycles [491]. MoO_2 powder electrode was electrochemically activated [499] at high temperature. The lithiation behavior occurs by a one-electron reduction (by addition reaction) at room temperature. At elevated temperatures, this electrode is lithiated with four-electron reduction by addition and continued conversion reaction. This phenomenon is named "thermoelectrochemical activation" because the extension from one- to four-electron reduction is achieved by a simple charge–discharge cycling made at elevated temperatures. This MoO_2 electrode delivers a reversible specific capacity that is close to the theoretical four-electron

capacity (838 mAh g^{-1}) with an excellent cycle performance at room temperature. A template-free solvothermal method has been developed to synthesize yolk–shell MoO_2 microspheres [500]. They are composed of both a uniform porous shell of 80 nm in thickness and a porous core constructed from primary MoO_2 nanocrystal clusters of 20 nm in size. Yolk–shell MoO_2 microspheres can deliver a high specific capacity of 955 mAh g^{-1} in the first discharge at a current density of 50 mA g^{-1}, and retain a reversible capacity of 847 mA g^{-1} after 50 cycles.

6.4. MoO_2 composites

Several strategies have demonstrated the ability to mitigate the particle pulverization as a consequence of Li insertion and extraction and to improve the MoO_2 electrochemical performance via the fabrication of nanocomposites including carbonaceous materials. By scaling down to the particle size, it results in shortening the transport paths for both ions and electrons, while the carbonaceous matrix maintains high conductivity, large surface area and chemical stability. The composites studied as lithium battery anodes include various carbon forms, such as carbon cloth [501], carbon coating [490,502-504], MoO_2/C spheres [460], MoO_2/carbon hybrid nanowires [482], MoO_2/Mo_2C composite [461,487], MoO_2/ordered mesoporous carbon [471,505]. Nitride-coating [506] and Mo_2N nanolayer-coating [507] are also attractive synthetic approaches.

Uniform carbon-coated MoO_2 nanospheres synthesized a one-pot hydrothermal method [502] exhibit significant improved electrochemical performance for high-rate lithium storage. Carbon-coated MoO_2 lengthened a few micrometers produced by carbothermal reduction of MoO_3 nanobelts were further ball-milled to reduce the particle size below 100 nm. C/MoO_2 nanoparticles demonstrate a discharge capacity of 248 mAh $(g_{MoO2})^{-1}$ at 150 mA g^{-1} (0.5C rate) with an average operation voltage of 1.3 V. This anode material is also suitable for high rate charge and discharge, reaching 129 mAh g^{-1} for charge and 146 mAh g^{-1} for discharge even at 30C-rates (9 A g^{-1}) [486]. Luo et al. [503] fabricated carbon-coated MoO_2 nanofibers (with a uniform carbonaceous shell of ~3 nm in thickness and a hierarchical core made of primary MoO_2 nanocrystal clusters of ~20 nm in size) through a controlled route based on single-nozzle electrospinning, air stabilization, and reduction/carbonization processes. These nanofibers exhibit a highly reversible capacity as high as 762.7 mAh g^{-1} over 100 cycles. Carbon coated MoO_2 nanobelts were synthesized via a hydrothermal method followed by calcination under inert atmosphere, using α-MoO_3 nanobelts as the precursor and self-template, ethanol as the reducer and glucose as the carbon source [490]. Electrochemical tests of this anode material show a reversible capacity of 769 mAh g^{-1} at a current density of 100 mA g^{-1} in the first cycle,

and retain 80.2% of the capacity after 30 cycles. Zhou et al. [462] have evaluated C-coated MoO_2 nanocomposite, i.e., interconnected MoO_2 nanocrystals with carbon nanocoating, prepared by one-pot hydrothermal route that show high specific capacities of ~640 mAh g^{-1} at 200 mA g^{-1} and ~575 mAh g^{-1} at 400 mA g^{-1}. Chen et al. [470] designed a novel MoO_2–ordered mesoporous carbon (MoO_2–OMC) hybrid through a two-step solvothermal chemical reaction route. Electrochemical tests reveal a first discharge capacity of 1642 mAh g^{-1} with an ICE of 63.6%, and a reversible capacity as high as 1049 mAh g^{-1} even after 50 cycles at a current density of 100 mA g^{-1}. The MoO_2–OMC hybrid demonstrates an excellent high rate capability with capacity of ~600 mAh g^{-1} even at a charge current density of 1600 mA g^{-1} after 50 cycles. A nano-sized MoO_2/C composite was synthesized using a spray pyrolysis technique, and investigated as an anode material for Li-ion batteries. Spherical MoO_2/C particles with the monoclinic phase ($P2_1/c$ S.G.) were obtained without any impurities, and with a primary particle size in the range 30–50 nm [483]. Liu et al. [475] synthesized MoO_2/C composite nanospheres with cage-like structure by a simple hydrothermal reduction process using ammonium molybdate tetrahydrate ($(NH_4)_6Mo_7O_{24}\cdot 4H_2O$) and ascorbic acid as a structure directing agent, reductive agent and carbon source. These porous structured electrodes can deliver a capacity of 692.5 mAh g^{-1} after 80 charge–discharge cycles at a current density of 200 mA g^{-1} and can maintain excellent cycling stability (about 550 mAh g^{-1} after 475 cycles). Nanostructured monolithic hybrid mat made of C/$MoO_{2+\delta}$ nanofibers were fabricated through an electrospinning process by thermal treatment in N_2. The free-standing anode C/$MoO_{2+\delta}$ composite exhibits a reversible capacity as high as 877 mAh g^{-1} after 250 cycles at a current density of 200 mA g^{-1}. A capacity of ~448 mAh g^{-1} could be maintained after 1000 cycles at 2000 mA g^{-1} rate [508]. Recently, Qing et al. [509] fabricated the composite MoO_2/VC via a facile hydrothermal route, where vitamin C (VC) is a source of carbon. This composite LIB anode displays a discharge capacity of ~300 mAh g^{-1} at 0.5 A g^{-1} after 120 cycles.

Several MoO_2/Mo_2C heterostructures have been fabricated as anode materials for LIBs [461,487,510]. MoO_2/Mo_2C heteronanotubes were fabricated by a one-step carbothermal reduction by using a mesoporous carbon CMK-3 acting as template and reactant [461]. Mo_2C is an electrochemical inactive compound, which exhibits a high conduction of ~10^{-2} S cm^{-1} and minimizes the charge transfer resistance of the composite. Cycled at 200 and 1000 mA g^{-1} for 140 cycles, the discharge capacities of the MoO_2/Mo_2C heteronanotubes remain to be 790 and 510 mAh g^{-1}, respectively. Ihsan et al. [510] synthesized MoO_2/Mo_2C/C spheres through hydrothermal and calcination processes that demonstrates not only high cycling performance, but also good rate capability when they are used as anode materials for LIBs. After 100 cycles

at 100 mA g^{-1}, the discharge capacities of the $MoO_2/Mo_2C/C$ spheres as anode materials remain at 800 mAh g^{-1}.

Zhang et al. [460] synthesized uniform hierarchical MoO_2/C spheres through calcination of a MoO_3/resin precursor generated via a hydrothermal method in the presence of resorcinol, formaldehyde and $(NH_4)_6Mo_7O_{24}\cdot 4H_2O$. Used as an anode material, these spheres exhibit an initial capacity of ~400 mAh g^{-1} at 0.5 A g^{-1} and high cycling performance after 400 cycles with capacities of ~600 and ~500 mAh g^{-1} at 0.5 and 1.0 A g^{-1} rate, respectively. MoO_2/carbon nanowires were prepared by a method based on organic–inorganic hybrid nanocomposites with nanometer periodic structures [482]. The MoO_2/C hybrid nanowires show good rate capability even at the high current density of 1000 mA g^{-1} as anode material for LIBs.

MoO_2-loaded porous carbon hollow sphere composite materials were synthesized using MoO_2 nanoparticles with an average size of ~12 nm uniformly dispersed in the shells of the porous carbon hollow spheres (PCHS) [511]. The MoO_2/PCHS composite containing 44.2% of MoO_2 revealed a reversible capacity of 574 mAh g^{-1} at a current density of 50 mA g^{-1}. After 80 cycles, this composite still retained a capacity of 640 mAh g^{-1} due to the presence of porous carbon, which prevents volume change or aggregation of the MoO_2 nanoparticles during the Li ion insertion/extraction process. Zeng et al. [471] synthesized the nanocomposite of MoO_2-ordered mesoporous carbon (MoO_2–OMC) using a carbon thermal reduction route. This nanocomposite exhibits a large reversible capacity of 689 mAh g^{-1} after 50 cycles at a current density of 50 mA g^{-1}. This nanocomposite offered a better accommodation of the strain and volume changes and a shorter path for Li-ion and electron transport, leading to the improved capacity and enhanced rate capability of the anode material for LIBs.

Carbon-coated MoO_2 nanobelts were fabricated via a hydrothermal route followed by calcination under inert atmosphere, using α-MoO_3 nanobelts as the precursor and self-template, ethanol as the reducer and glucose as the carbon source. The C/MnO_2 NBs anode materials exhibit a reversible capacity of 769 mAh g^{-1} at a current density of 100 mA g^{-1} in the first cycle, and retain 80.2% of the capacity after 30 cycles [490]. Nanorods (250 nm in diameter), which consist of α-MoO_3 core and β-MnO_2 shell (46 nm thick, tetragonal phase) were synthesized by a two-step hydrothermal process [214]. The α-MoO_3@β-MnO_2 nanorods show a reversible capacity of 1475 mAh g^{-1} at 0.1C rate and retains at 1127 mAh g^{-1} after 50 cycles. Even at high current rate of 6C, the reversible capacity is 394 mAh g^{-1} and retains at 286 mAh g^{-1} after 50 cycles. A heterostructure, which consists of MoO_2 nanoparticles anchored and embedded in the 1D N-doped carbon matrix were fabricated using the organic–inorganic $Mo_3O_{10}(C_6H_8N)_2\cdot 2H_2O$ hybrid nanowires as a precursor and self-template. The nanowires were

calcined at 650 °C for 5 h under an Ar flow (50 mL min^{-1}) to yield the MoO_2/N-C heteronanowires. Tested at a current density of 2 A g^{-1}, the MoO_2/N-C composite delivers a reversible capacity of 700 mAh g^{-1} after 400 cycles, which still remains 570 mAh g^{-1} even after 1500 cycles [512]. Nanoporous 3D MoO_2 single crystals were partially covered with a few atomic layers of MoS_2 to form MoS_2/MoO_2 nanonetworks, which exhibit a reversible discharge specific capacity of 1233 mAh g^{-1} at a current density of 100 mA g^{-1}. When discharged at 200 and 500 mA g^{-1}, the capacities are 1158 and 826 mhA g^{-1} [513]. Wang et al. [514] prepared a mesoporous MoO_2@C nanocomposite using oleic acid to reduce the MoO_3 precursor and to simultaneously coat the resultant 1D MoO_2 nanorods with carbon layers (BET surface area of 45.7 m^2 g^{-1}, and pore size of 3.8 nm). The MoO_2@C electrode exhibits a high capacity of 1034 mAh g^{-1} at 0.1 A g^{-1}, and a capacity of 155 mAh g^{-1} at a super-high current rate of 22 A g^{-1}. When, the Li/MoO_2@C half cells cycled at 0.5 and 10 A g^{-1} retain 861 and 312 mAh g^{-1} capacity after 140 and 268 cycles, respectively. Recently, Zhang et al. [515] reported the design and fabrication of a composite, which consists of encapsulated MoO_2 nanocrystals into flexible carbon nanofibers, using a needle-free electrospinning method combined with the subsequent carbonization process. The MoO_2/C nanofiber membrane as self-supporting anode exhibits a discharge capacity of 450 mAh g^{-1} after 500 cycles at 2000 mA g^{-1}. **Table 13** summarizes the electrochemical performance of various MoO_2 composites as anode materials for LIBs.

Table 13. Electrochemical performance of various MoO_2 composites as anode materials for Li-ion batteries. The relevant cycle number is displayed in brackets.

Material	Synthesis	Reversible capacity (mAh g^{-1})	Current rate (mA g^{-1})	Ref.
Nano MoO_2	Rheology	402	100 (40)	[516]
MoO_2/Mo_2N	Reduction of MoO_3	815	100 (150)	[517]
MoO_2/graphene	Chemical vapor deposition	986	50 (150)	[518]
MoO_2/C	Ion exchange	574	100 (100)	[519]
MoO_2/C	Carbothermal reduction	500	100 (50)	[471]
MoO_2/C hollow spheres	Solvothermal	580	200 (200)	[520]
Mesoporous MoO_2	Template casting	750	42 (30)	[455]
Activated MoO_2	Electrochemical activation	850	100 (30)	[521]
MoO_2 HCSMSs	Hydrolysis	420	50 (30)	[522]
W-doped MoO_2	Nanocasting	670	75 (20)	[492]
C/WO_x/MoO_2	Hydrothermal	670	90 (50)	[523]
MoO_2/C NWs	Solvothermal	500	200 (20)	[482]
C/MoO_2 NSs	Hydrothermal+annealing	675	838 (30)	[502]
MoS_2/MoO_2	Sulfur assisted	654	500 (80)	[513]
C/MoO_2 NBs	Hydrothermal+annealing	617	100 (30)	[490]
MoO_2 monolith	Morphosynthesis	719	200 (20)	[498]

α-MoO_3@β-MnO_2	Two-step hydrothermal	286	6C (50)	[214]
MoO_2/N-doped C NWs	Calcination	700	2000 (400)	[512]
C-coated MoO_2	Hydrothermal	312	10000 (268)	[514]
MoO_2/flexible C	Electrospinning	450	2000 (500)	[515]

6.5. MoO_2/graphene composites

To overcome the sluggish lithiation/delithiation kinetics of micron-scale particles, several graphite-based nanocomposites have been created such as graphite oxide [524], and graphene (GR) [465,525,526], graphene oxide (GO) [465,527-529], and reduced graphene oxide (rGO) [530-534]. Using a microwave-assisted hydrothermal process and subsequent thermal annealing, Palanisamy et al. [535] prepared 3D porous self-assembled MoO_2/graphene microspheres. Such hybrid is built from interconnected MoO_2 nanoparticles (3-5 nm) in the graphene matrix. The MoO_2/graphene composite anode delivers a high reversible capacity of ~1300 mAh g^{-1} after 80 cycles at C/10 rate and excellent rate capability (913 and 390 mAh g^{-1} at 2C and 5C rates, respectively). Sun et al. [465] have investigated self-assembled hierarchical MoO_2/graphene nanoarchitectures fabricated on a large scale through a facile solution-phase process and subsequent reduction of the Mo-precursor/graphene composite. The as-formed MoO_2/graphene nanohybrid (containing 11.2 wt.% graphene) as an anode material for LIBs exhibits not only a highly reversible capacity but also an excellent cycling performance as well as good rate capability, a specific capacity of 597 mAh g^{-1} is delivered after 70 cycles at current density of 1000 mA g^{-1}. Tang et al. [528] reported the electrochemical performance of MoO_2/graphene nanocomposite synthesized via a two-step of hydrothermal-calcination method. When used as anode material for LIBs, the MoO_2/graphene composite shows a first discharge capacity of 674 mAh g^{-1} with a reversible capacity of 430 mAh g^{-1}. Significantly, the composite can also deliver a reversible capacity of as high as1009 mAh g^{-1} after 60 charge/discharge cycles. Chen et al. [481] reported the electrochemical properties of hierarchical nanocomposites including MoO_2 nanocrystal-functionalized graphene synthesized by in-situ reduction process. The discharge capacity is still up to 997 mAh g^{-1} after 50 cycles and 370 mAh g^{-1} after 200 cycles at 10C rate.

Nanostructured MoO_2/GO composites, which consists of a mixture of MoO_2 nanorods and nanoparticles uniformly distributed at the surface of GO sheets, were synthesized by a simple solvothermal method of a GO suspension with $(NH_4)_6Mo_7O_{24}$ and HNO_3 in ethanol at 160 °C for 16 h [524]. The MoO_2/GO with 10 wt.% GO tested in lithium half-cell delivered an initial capacity of 800 mAh g^{-1} at current density of 0.8 A g^{-1} corresponding to Li uptake of 3.43 moles and a reversible capacity of 720 mAh g^{-1} at a current density of 100 mA g^{-1} and 560 mAh g^{-1} at

a high current density of 800 mA g^{-1} after 30 cycles. The improved reversible capacity, rate capacity, and cycling performance of the composites are attributed to synergistic reaction between MoO_2 and GO. MoO_2/rGO composites fabricated by hydrothermal route followed by a heat treatment at 500 °C for 2 h [530]. The MoO_2-based materials have monoclinic crystal structure, and worm like shape with average dimensions of 100-200 nm width and 0.5-1 μm length. There are two steps of Li ion intercalation/de-intercalation for the MoO_2/rGO anode at the potential ranging from 1.0 to 3.5 V vs. Li^+/Li, locating at 1.60/1.75 and 1.25/1.40 V, respectively with a first discharge capacity of 221 mAh $g^{-1}$and R_{SEI} and R_{CT} resistances of 2-4 Ω and below 5 Ω, respectively. Petnikota et al. [468] studied the insertion of Li and conversion mechanism of MoO_2 (below 0.8 V) in exfoliated graphene oxide/MoO_2 composites as anode materials. Graphene oxide was used as a reducing agent of MoO_3 (molar ratio of 4:1) and as a source for exfoliated graphene oxide (EGO) to fabricate EGO/MoO_2 composites with 46 wt.% graphene. The small particle size of ~33 nm indicates that agglomeration of MoO_2 has been controlled with the increased amount of EGO. The initial capacity of 713 mAh g^{-1} increased slightly to 878 mAh g^{-1} after 100 cycles at 100 mA g^{-1} current rate in the voltage window 0.005-3.0 V. Kinetics investigated by cyclic voltammetry revealed high values of the diffusion coefficients of Li ions in the range 6×10^{-10}-1×10^{-11} cm^2 s^{-1} during Li_xMoO_2 lithiation ($0 < x < 4$). Hu et al. [478] prepared MoO_2/GO composites via hydrothermal route at 200 °C for 24 h using Mo powder and exfoliated GO produced by sonication. MoO_2 nanoparticles (5−15 nm in size) were homogeneously dispersed on GO. When tested as an anode material for lithium, the MoO_2/GO composite displayed an initial specific capacity of 780 and 500 mAh g^{-1} at 0.1 and 0.5 A g^{-1}, respectively. The beneficial contribution of exfoliated GO was evidenced by EIS measurements, as the charge transfer resistance of 44 W for MoO_2/GO was much lower than 300 W for pure MoO_2 nanoparticles, due to more conductive pathway for Li-ion transportation. Huang and coworkers [536] fabricated a composite of MoO_2 nanoparticles (~100 nm) anchored on GO for sodium-ion battery anodes. This MoO_2/GO hybrid (15 wt.% GO) yielded a discharge capacity of 483 mAh g^{-1} (~2318 mAh cm^{-3}) at the current density of 100 mA g^{-1} and a capacity fading of 0.019% per cycle over the first 1000 cycles. Tang et al. reported the electrochemical properties of rGO-wrapped MoO_2 porous nanobelts (rGO/MoO_2 NBs) synthesized using a reduction process of the GO-MoO_3 hybrids with Ar/ethanol vapor at 400 °C for 12 h [537]. The full-scale multi-electron conversion reaction in rGO/MoO_2 NBs (with 8 wt.% rGO) led to a high reversible capacity of 974 mAh g^{-1} at the current density of 60 mA g^{-1} after 6th cycle and, after initial activation, a specific capacity of 420 mAh g^{-1} was retained at the end of 1900 cycles at 5 A g^{-1} rate. Zhu et al. [216] demonstrated that rGO/MoO_2 nanobelt composite (with 19.4

wt.% rGO) synthesized by a simple thermal reduction of MoO_3 and GO at 550 °C for 2 h in a 10% H_2/Ar atmosphere had a BET specific surface area and pore volume of 17.68 m^2 g^{-1} and 0.09 cm^3 g^{-1}, respectively. This self-assembled hybrid shows attractive electrochemical performance as LIB anodes with specific discharge capacity reaching 584 mAh g^{-1} after 100 cycles at 1 A g^{-1}.

In 2017, Ju and coworkers [538] designed a TiO_2/rGO/MoO_2@Mo composite electrode for ESC. This architectural nanostructure with 3D walnut-shape synthesized by one-step hydrothermal method was composed of amorphous TiO_2 decorating the rGO/MoO_2 surface grown on Mo foam. It exhibited a specific capacitance of 1636 F g^{-1} at 1.25 A g^{-1} with only 3.5% capacitance loss after 5000 cycles. Tightly anchored MoO_2 nanoparticles (10-20 nm in size) deposited on the basal plane of rGO were fabricated using a green supercritical methanol (scMeOH) route. When tested as an anode in lithium cells, the composite with 37 wt.% MoO_2 loading (BET surface area of 14.3 m^2 g^{-1}, 15% porosity) delivered a reversible capacity of 793 mAh g^{-1} at 50 mA g^{-1} current rate [531]. Graphene oxide flexibly supported MoO_2 porous hybrids were constructed by decomposition of $(NH_4)_2MoO_4$ /GO preforms with the percentage of GO at 4.3, 15.2, and 20.8 wt.%. The lithium storage performance was investigated at the current density of 0.1 A g^{-1} using various MoO_2/GO architectures showing specific capacities of 901, 1127, and 967 mAh g^{-1} after 100 cycles for micrometer MoO_2/GO, MoO_2/GO nanohoneycomb, and layered MoO_2/GO, respectively. The MoO_2/GO nanohoneycomb delivered the capacity of 461 mAh g^{-1} at 5 A g^{-1} current rate with CE of 99.3% [539]. Wang et al. [540] synthesized 2D layered mesoporous-MoO_2/rGO composites (m-MoO_2/rGO) through a novel strategy using silica KIT-6/rGO as a template and ammonium molybdate as a precursor via a nanocasting method with subsequent heat treatment heated up to 600 °C for 6 h at a rate of 2 °C min^{-1} in a mixed gas flow of H_2/Ar (10:90). Analyses of the morphology validated the ordered mesoporous structure with a BET specific surface area of 86 m^2 g^{-1}, a pore size of 3-4 nm in a large domain and a pore volume of 0.19 cm^3 g^{-1}. The m-MoO_2/rGO(1:1) electrode delivered an initial discharge capacity of 1160 mAh g^{-1} at current density of 0.1 A g^{-1} with a capacity loss of 31.9% during the first cycle and a reversible capacity is 801 mAh g^{-1} after 50 cycles.

In 2018, Chen et al. [541] investigated a hierarchical MoO_2@rGO (~10 nm MoO_2 particle size and 21.1 wt.% rGO) composite prepared by hydrothermal route at 200 °C for 2 days, which exhibited outstanding electrochemical performance with a reversible capacity of 708 mAh g^{-1} at a current density of 0.5 A g^{-1} after 50 cycles. A capacity of 473 mAh g^{-1} was maintained when cycled at 2 A g^{-1} current rate. Li et al. [542] utilized Mo particles as both the reductant

for GO and as the Mo source to prepare MoO_2/rGO hybrid anodes. The MoO_2/rGO composite with Mo:GO of 3:1 was used as an efficient cathode catalyst for the oxygen reduction reaction (ORR). Recently, Liu et al. [532] reported the direct growth of MoO_2/rGO hollow sphere composites through hydrothermal technique. This advanced anode materials tested in potassium-ion batteries delivered a reversible specific capacity of 219 mAh g^{-1} after 200 cycles at 50 mA g^{-1} current rate. When cycled at 0.5 A g^{-1}, a high charge specific capacity of 104 mAh g^{-1} was achieved after 500 cycles. Li et al. [543] prepared the MoO_2/Mo-GO hybrids using a freeze-drying technique, which exhibited a high ICE of 97%. A capacity of 550 mAh g^{-1} ws delivered by the MoO_2/Mo-GO anode materials after 150 cycles at 0.1 A g^{-1} rate. Devina et al. [544] used the same technique to prepare MoO_2/rGO composite attached with Mo_2C during carbothermal hydrogen reduction. The MoO_2/Mo_2C/rGO product displayed an increased ICE (77%), long-term cyclability (500 mAh g^{-1} at 50 mA g^{-1} after 150 cycles), and high-rate performance (200 mAh g^{-1} at 1 A g^{-1}) compared with those of the MoO_2/rGO composite (53%; 280 mAh g^{-1} at 50 mA g^{-1} after 150 cycles; 120 mAh g^{-1} at 1 A g^{-1}).

Recently, the fabrication of submicrometer-sized MoO_2@MoS_2/rGO composite with a hierarchical core-shell structure was suggested by Zheng et al. [545]. The three-step synthesis includes: (i) the preparation of the MoO_2@MoS_2 precursor using a solid-state reaction (i.e., MoO_3 and sulfur heated at 600 °C for 1 h in a gas stream of Ar/H_2 (90:10)), (ii) a hydrothermal process at 180 °C for 4 h using a GO suspension, and (iii) a final heat treatment at 400 °C for 2 h in Ar/H_2 flowing gas. The electrochemical tests of the MoO_2@MoS_2/rGO anode showed an initial reversible capacity of 833 mAh g^{-1} with ICE of 80.6% and improved cycling stability (733 mAh g^{-1} after 80 cycles at 0.2 mA g^{-1}). The good rate capability with a capacity of 645 mAh g^{-1} at 4 A g^{-1} was also evidenced. An assembled MoO_2@MoS_2/rGO‖$LiCoO_2$ full cell maintained a reversible capacity of 694 mAh g^{-1} (based on the mass of MoO_2@MoS_2/rGO) at 0.2 mA g^{-1} after 40 cycles. Electrochemical performance of MoO_2/rGO composite anodes for LIBs from the recent literature are summarized in **Table 14**.

Table 14. Electrochemical performance of MoO_2/GO composites as anode materials for LIBs. The relevant cycle number is displayed in brackets.

Material [a)]	Synthesis[a)]	Reversible capacity (mAh g^{-1})	Current rate (mA g^{-1})	Ref.
MoO_2/GR	layer-by-layer assembly	676	48 (100)	[546]
MoO_2/GR	sonication in water (11.2)	597	1000 (70)	[465]
MoO_2/rGO	hydrothermal @200 °C/24 h	503	100 (30)	[478]
MoO_2/rGO	hydrothermal @400 °C/3 h (10.4)	1009	100 (60)	[528]

MoO_2/rGO	solid state reaction (22.0)	640	200 (50)	[526]
MoO_2/GO	thermal reduction @550 °C/2 h (51.7)	752	100 (100)	[547]
MoO_2/Gr	hydrothermal @180 °C/26 h (33.2)	769	540 (83)	[525]
MoO_2/N-rGO	hydrothermal @180 °C/24 h	400	1000 (5)	[548]
MoO_2/exfol-rGO	solid-state graphenothermal (46.0)	878	100 (100)	[468]
MoO_2 NSs/rGO	in situ reduction of MoO_3	1003	100 (100)	[549]
MoO_2/GO	solvothermal @160 °C/ 16 h (10.0)	500	800 (30)	[524]
MoO_2/rGO	solid-state reaction @500 °C (15.0)	276	100 (1000)	[536]
MoO_2/rGO	hydrothermal @200 °C/2 days (21.1)	708	500 (50)	[541]
MoO_2/rGO	thermal reduction @550 °C (19.4)	584	1000 (100)	[542]
MoO_2/rGO/ NBs	surfactant-free self-assembly	420	5000 (1900)	[216]
MoO_2 NBs/rGO	supercritical methanol route	793	50 (50)	[531]
MoO_2/Mo-GO	freeze-drying (5.0)	550	100 (150)	[543]
MoO_2/rGO	solid state reaction @500 °C (15.2)	1127	100 (150)	[539]
MoO_2 NBs/rGO	freeze-drying (8.0)	420	5000 (1900)	[537]
m-MoO_2/rGO	nanocasting (50)	801	100 (100)	[540]
MoO_2@MoS_2/rGO	hydrothermal @180 °C/4 h	733	200 (80)	[545]
MoO_2 NPs/graphene	hydrothermal @180 °C/12 h	765	60 (40)	[550]

[a)] graphene content in wt.%.

6.6. Lithium molybdate $LiMoO_2$

Molybdenum also forms several stable phases with lithium including $LiMoO_2$ [551], Li_2MoO_3 [552], $Li_4Mo_3O_8$ [553] and non-stoichiometric compounds such as $Li_{0.74}MoO_2$ [551]. There were few reports on the structure, physico-chemical properties and electrochemistry of $LiMoO_2$ [554,555]. However, its structure has been the subject of debate. Several groups have claimed that $LiMoO_2$ crystallizes with the rock-salt-like structure isomorphs to the layered α-$NaFeO_2$ [551,554,556,557]. These groups did not consider the accepted theoretical predictions for 3D-systems according to which the structure would distort, while Hibble et al. [558] have determined that $LiMoO_2$ adopts the monoclinic *C*2/*m* space group by refinement of by neutron scattering data. The structure is best described with a = 10.543(6) Å, b = 2.8626(5) Å, c = 10.899(6) Å, and β = 153.29°. The schematic representation is given in **Fig. 38a**. Ben-Kamel et al. [555] synthesized $LiMoO_2$ by a carbothermal method using citric acid as a chelating agent with a subsequent thermal treatment at 800 °C for 72 h in air. Analysis of the crystal structure by Rietveld refinements shows that lithium molybdate crystallizes in the monoclinic system (R_{Bragg} = 1.24%) instead of the rhombohedral structure (R_{Bragg} = 8.53%). This result is confirmed by the Raman spectroscopy experiment, which displays twelve bands instead of two for the rhombohedral ($R\bar{3}m$) structure. **Figure 38b** represents the charge–discharge profile of the Li//$LiMoO_2$ cell cycled in the potential range 2–4 V at current density of C/24. Almost 0.9Li can be extracted when the cell is charged at 4.0 V vs. Li^+/Li. A good reversibility at the first cycle with the capacity retention of 168 mAh g^{-1}, which can be

compared with the theoretical value 198 mAh g^{-1}. Measurements reveal the presence of multiple phase transitions during the lithium extraction process: the S-shaped potential corresponds to the extraction of 0.5Li in Li_xMoO_2, the formation of an ordered composition close to x=0.5 and a plateau at 3.6 V attributed to the existence of a two-phase system, i.e., $Li_{0.1}MoO_2$ and $Li_{0.5}MoO_2$. The differential capacity curve (inset **Fig. 38b**) displays a sharp peak at ca. 3.6 V corresponding to the voltage plateau observed in the charge–discharge curves and redox contributions of the single-phase regime appearing at 2.9 and 3.1 V vs. Li^+/Li. Measurements of Li ion kinetics reveal that diffusion coefficients for the $LiMoO_2$ electrode are in the range of 10^{-12}–10^{-10} cm^2 s^{-1} (**Fig. 38c**). The rate capability of $LiMoO_2$ compared with that of $LiNi_{0.8}Co_{0.2}O_2$ is shown in **Fig. 38d**.

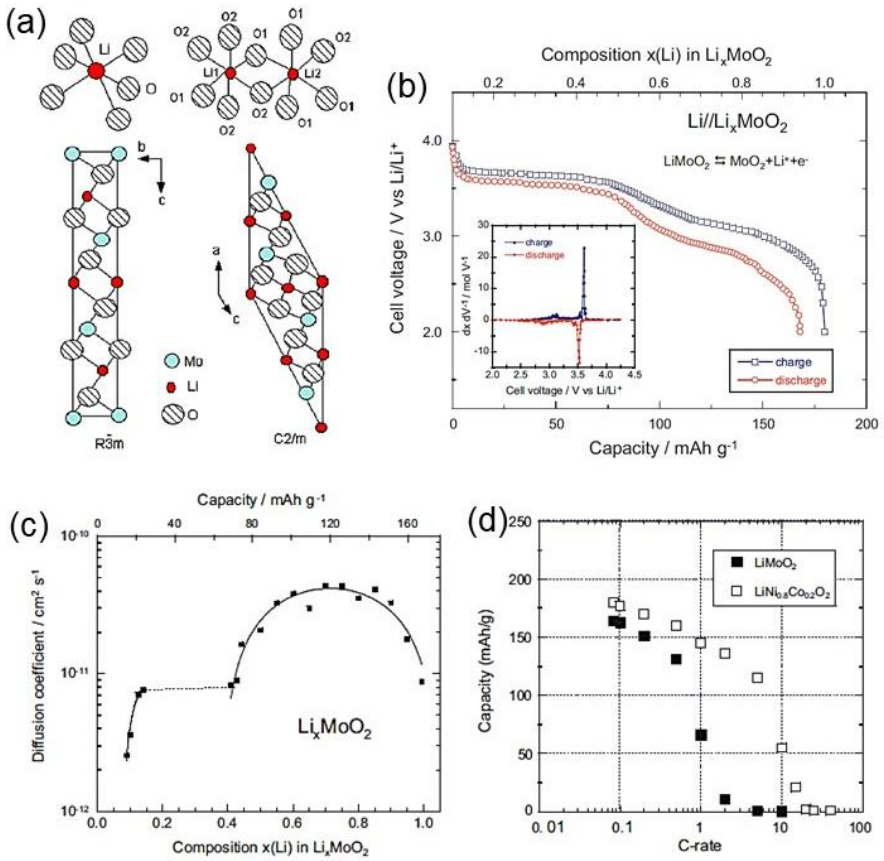

Fig. 38. (a) Schematic representation of the rhombohedral ($R\bar{3}m$) and monoclinic ($C2/m$) structures of $LiMoO_2$. (b) Charge–discharge profile of the Li// $LiMoO_2$ cell cycled in the potential range 2–4 V at C/24 rate. The electrode was $LiMoO_2$ powders synthesized at 600 °C for 72 h ($C2/m$ S.G.) and the electrolyte was 1 mol L^{-1} $LiPF_6$ in 1:1 EC/DMC. The insert shows the differential capacity dQ/dV vs. cell voltage obtained at the second cycle. (c) Evolution of the chemical diffusion coefficient of Li^+ ions in the Li_xMoO_2 cathode material as a function of the composition x. (d) Rate capability of the $LiMoO_2$ electrode recorded at the 5th cycle. Data

obtained for the layered $LiNi_{0.8}Co_{0.2}O_2$ cathode are shown for comparison. Reproduced with permission from [555]. Copyright 2012 Elsevier.

6.7. Lithium molybdate Li_2MoO_3

Because of high lithium storage capacity, high first coulombic efficiency, low cost and Mo(IV)/Mo(VI) redox couple, Li_2MoO_3, can serve as anodes [559] as well as cathodes for LIBs [560,561]. Li_2MoO_3 has a theoretical Li^+ extraction/insertion capacity of 339 mAh g^{-1} simply by a single Mo^{4+}/Mo^{6+} redox reaction. Li_2MoO_3 synthesized through ball milling and thermal reduction presents a first discharge capacity of about 835 mAh g^{-1} with an ICE of 97.6% at a current density of 100 mA g^{-1}; a discharge capacity of 902 mAh g^{-1} is preserved after 150 cycles [559]. Phase-pure Li_2MoO_3 powders were prepared by reducing commercial Li_2MoO_4 at 650 °C for 24 h in flowing H_2/Ar (10:90 v/v) [562]. A fresh electrode delivers ~80 mAh g^{-1} after 20 cycles at 10 mA g^{-1} with ICE of 98.9%, whereas the capacity of aged Li_2MoO_3 (obtained after 120 days in relative humidity <10%) decreases drastically (75% capacity loss at the 2nd cycle). Kumakura et al. [563] prepared a Li_2MoO_3/C composite with the simple addition of acetylene black. As a cathode material tested in the range 1.5-4.3 V, it delivers a first specific capacity of 230 mAh g^{-1}. The polycrystalline Li_2MoO_3 synthesized via simple liquid chemical reaction, followed by thermal reduction in H_2/Ar (5:95 v/v) atmosphere exhibits a first discharge capacity of 836 mAh g^{-1} (ICE = = 94.5%) at a current density of 100 mA g^{-1} over a voltage window of 0.01–3.0V. After 200 cycles at 300 mA g^{-1}, a discharge capacity of 654 mAh g^{-1} is preserved and the composite still keeps a discharge capacity of 489 mAh g^{-1} at 1600 mA g^{-1} current rate [564]. Recently, Mao et al. [565] investigated the electrochemical performance of layered Li_2MoO_3 microspheres prepared from MoO_2 microsphere as a self-template. Due to their enhanced mesoporous structure, Li_2MoO_3 microspheres deliver specific capacities of 247 and 76 mAh g^{-1} at current densities of 34 and 1000 mA g^{-1}, respectively. **Table 15** list the electrochemical performance of some Li_2MoO_3 used as cathode and anode of LIBs.

Table 15. Electrochemical performance of Li_2MoO_3 cathode/anode materials for LIBs. Relevant cycle number is given in brackets.

Material	Synthesis	Specific capacity (mAh g^{-1})	Current rate (mA g^{-1})	Ref.
Cathode				
$Li_2Mo_{0.9}Co_{0.1}O_3$	Solid phase	140	5 (50)	[566]
C/Li_2MoO_3	Ball milling	180	20 (50)	[567]
C/Li_2MoO_3	Solid state reaction	150	16 (35)	[563]

Li_2MoO_3 bulk	Reduction reaction	80	10 (20)	[562]
Anode Li_2MoO_3	Liquid chemical reaction	654	300 (200)	[564]

6.8. Other lithium molybdates

Monoclinic $Li_{1.33}Mo_2O_4$ was prepared by low temperature ion exchange of lithium for sodium in $Na_xMo_2O_4$ [568]. The study of the $Li//Li_{0.3}Mo_2O_4$ electrochemical cells shows that the electrode material can reversibly accommodate up to 1.7 Li per Mo_2O_4 unit formula at an average of 3.0 V resulting in a theoretical energy density of 530 Wh kg^{-1} for the $Li_2Mo_2O_4$ cathode material. Structural studies indicate that $Li_xMo_2O_4$ is a multiphase intercalation system over the range of composition $0.3<x<2.0$. Li_2MoO_4 nanoparticles (hexagonal phenacite-like structure) have investigated as anode materials for LIBs [569,570]. Liu and coworkers [570] synthesized 1D Li_2MoO_4 nanostructures (nanorods and nanotubes) via a sol-gel method adding Li_2CO_3 and MoO_3 powders into distilled water with citric acid as an assistant agent and carbon source. The materials display initial discharge/charge capacities of 688/319 mAh g^{-1} (carbon-free powders), 750/420 mAh g^{-1} (carbon-free nanorods), 850/476 mAh g^{-1} (carbon-free nanotubes), 1016/648 mAh g^{-1} (carbon-coated nanotubes). After 50 cycles at 90 mA g^{-1} current rate, the carbon-coated Li_2MoO_4 nanotubes deliver a specific capacity of 550 mAh g^{-1}. Crystallographic parameters of lithium molybdates are listed in **Table 16**.

Table 16. Crystallographic parameters of lithiated Mo oxides.

Compound	Structure	Cell parameters (Å)		
		a/α	*b*/β	*c*/γ
$Li_{1.3}Mo_2O_4$	monoclinic	10.666	2.885/99.5	4.953
β-Li_2MoO_3	monoclinic	4.990	8.642/99.5°	10.092

6.9. MoO_2 anodes for SIBs

The application of MoO_2 as anode material for SIBs has made rapid progress, and the energy density has been improved greatly [571,572]. Several approaches have been conducted to improve the electrochemical performance of MoO_2 anodes (i.e., capacity retention, long life cycling) including core-shell composite [573,574], carbon-based hybrid [536,575-577], and element doping [578]. Bao et al. [575] fabricated nanosized MoO_2 on 3D porous carbon using a simple hydrothermal method with subsequent calcination. The porous MoO_2/C composite

(with surface area of 171.6 m^2 g^{-1}) exhibits the specific charge capacity of ~463 mAh g^{-1} in the first cycle at 0.1 A g^{-1}. A reversible capacity of ~367 mAh g^{-1} can be maintained after 200 cycles. Jiang et al. [577] prepared a MoO_2/C nanocomposite using a simple hydrothermal method. This composite delivers a charge capacity of 557 mAh g^{-1} at 0.1C in the first cycle and has a good cycling stability for Na storage. Cui et al. [579] synthesized MoO_2@C nanoflowers through a grinding method followed by an annealing process. The MoO_2@C hybrid was tested at 0.1 A g^{-1} and showed a reversible charge capacity of 172 mAh g^{-1}. In the long-term cycling test (1 A g^{-1}, 1000 cycles), a reversible charge capacity of 166 mAh g^{-1} remained. He et al. [580] reported a MoO_2-C composite with MoO_2 nanosheets embedded in carbon matrix. The charge capacity vs. Na^+/Na after 100 cycles is ~367 mAh g^{-1}. Zhao et al. [581] synthesized a MoO_2 nanoparticles anchored graphene oxide, and the material exhibited a reversible charge capacity of 345 mAh g^{-1} after 100 cycles at 0.1 A g^{-1}. MoO_2 combined carbon dots (CDs) with nanoparticle stacking structure were fabricated via a facile hydrothermal route [509]. The MoO_2/CDs granules (50 nm in size) exhibit a discharge capacity of 236 mAh g^{-1} at 0.5 A g^{-1} after 300 cycles in 1 mol L^{-1} $NaClO_4$ in ethylene carbonate (EC) and dimethyl carbonate (DMC) (1:1 in volume) as SIB electrolyte. MoO_2 nanoparticles (≈100 nm) anchored on graphene oxide (MoO_2/GO) were fabricated as SIB for anodes. The discharge gravimetric capacity of the MoO_2/GO hybrid is stabilized at 345 mAh g^{-1} (volumetric capacity ≈1656 mAh cm^{-3}) at the current density of 100 mA g^{-1} after 100 cycles. After 1000 cycles, the capacity loss is only 19% and the electrode is still able to deliver 276 mAh g^{-1} [536]. Valdez et al. [582] prepared MoO_2/C composite fiber anodes using precursors solutions with different concentrations of MoO_2/PAN, which were force-spun into microfibrous mats and subsequently stabilized in air at 280ºC and calcined at 700ºC under Ar atmosphere. The MoO_2/C composite exhibits a discharge capacity of 300-400 $mAhg^{-1}$ after 100 cycles at 100 mAg^{-1}. Recently, Zhang et al. proposed the used of 2 wt.% vinylene carbonate (VC) additive to improve the cyclic stability of MoO_2 microspheres anode for SIBs. After 1000 cycles at 300 mA g^{-1} current rate, the MoO_2 electrode exhibits a capacity retention of 96.5% (~110 mAh g^{-1}) [583].

7. Concluding remarks

This review article shed light on the promising design strategies of molybdenum oxides for high kinetic energy storage. The technology of the molybdenum oxides used in energy storage devices from the 1980s to the recent progress was discussed. Due to their low molecular weight and their favourable electrochemical and solid-state properties, MoO_y compounds appeared attractive as cathode and anode materials in electrochemical energy storage systems. Three

major classes of Mo oxides, which exhibit various structural properties, have be distinguished: (i) anhydrous Mo oxides (MoO_3, Mo_nO_{3n-1}, MoO_2), (ii) molybdenum-oxide hydrates ($MoO_3 \cdot nH_2O$), and (iii) nanostructured MoO_y. A comparison between the electrochemical features of the molybdenum-oxide hydrates with different degrees of dehydration and their anhydrous products shows that oxide-hydrates materials have a good cyclability with a discharge capacity of 160 mAh g^{-1} at the 100^{th} cycle. This value was greater than that of anhydrous MoO_3. In a series of $MoO_3 \cdot nH_2O$ including sol-gel compounds, the main factor affecting the performance is expected to be the water content, which influencing the electrical conductivity and structural properties. Thermodynamics and kinetics of lithium-ion insertion are functions of the structural arrangement of the MoO_6 octahedra in the host lattice. Diffusion coefficients can be modelled using either a simple model for site occupancy or an ideal lattice gas model. A raw MoO_3 powder prepared by heat-treatment of molybdic acid in proper conditions exhibits the highest conductivity and displays the best electrochemical features for Li-ion insertion. Despite the attractive energy and power densities of the molybdenum oxides, these cathode materials belong to the class of 3-volt systems. The new development of nanostructured oxygen deficient MoO_y, and MoO_y-based composites as well, are promising electrodes materials for electrochemical energy storage devices due to their enhanced electronic conductivity, particularly supercapacitors and microbatteries, because they can instantaneously provide a high energy density with long cycle life.

Existing LIBs utilise graphite as anode with moderate theoretical capacity (372 mAh g^{-1}) and limited fast-charging capabilities. Hence, the attractive electrochemical performances of the MoO_3 and MoO_2 composite networks benefit from the synergistic effects of the unique nanoarchitectures and the integrity of these anode materials. Monodispersed MoO_y nanocrystals encapsulated in carbon matrix not only provide interfacial storage but also improve the transport kinetics of electrons and lithium ions. Extensive efforts have been made to overcome the defect of capacity degradation in MoO_2 anode, and the preparation of MoO_2/carbon composite materials has proven to be an effective way. The mesoporous nature of the MoO_2/C nanocomposite and the thin-layer carbon coating are believed to contribute to the enhanced electrochemical performance, which not only feature the efficient four-electron conversion reaction for Li^+ storage, but also effectively tolerate volume expansion during the cycling. In this review, we have also seen that with many distinctive properties, stoichiometric MoO_3 and MoO_2 can sustain high-rate capability as high-power battery electrodes to power electric vehicles. It is worthy to note that MoO_3 is a material used in various devices such as gas sensors, catalysts, recording materials, electrochromic devices, and so on.

References

[1] W. Su, H.R. Eichi, W. Zeng, M.-Y. Chow, A survey on the electrification of transportation in a smart grid environment, IEEE Trans. Ind. Inform. 8 (2012) 1-10.

[2] K. Zaghib, A. Mauger, C.M. Julien, Rechargeable lithium batteries for energy storage in smart grids, in: *Rechargeable lithium batteries: from fundamentals to applications*, A.A. Franco (Ed.), Woodhead Publ. Ltd, Cambridge (2015) chapter 12, pp. 319-351.

[3] M. Armand, Intercalation electrodes, in: *Materials for Advanced Batteries*, D.W. Murphy, J. Broadhead, B.C.H. Steele (Eds.), Plenum Press, New York (1980) pp 145-161.

[4] M. Lazzari, B. Scrosati, A cyclable lithium organic electrolyte cell based on two intercalation electrodes, J. Electrochem. Soc. 127 (1980) 773-774.

[5] H. Zhang, C. Li, G.G. Eshetu, S. Laruelle, S. Grugeon, K. Zaghib, C.M. Julien, A. Mauger, D. Guyomard, T. Rojo, N. Gisbert-Trejo, S. Passerini, X. Huang, Z. Zhou, P. Johansson, M. Forsyth, From solid solution electrodes and the rocking-chair concept to today's batteries, Angew. Chem. Int. Ed. 132 (2020) 542–546.

[6] A. Mauger, C.M. Julien, Critical review on lithium-ion batteries: are they safe? Sustainable? Ionics 23 (2017) 1933-1947.

[7] G.E. Blomgren, The development and future of lithium ion batteries, J. Electrochem. Soc. 164 (2017) A5019-A5025.

[8] I.A. de Castro, R.S. Datta, J.Z. Ou, A. Castellanos-Gomez, S. Sriram, T. Daeneke, K. Kalantar-zadeh, Molybdenum oxides–from fundamentals to functionality, Adv. Mater. 29 (2017) 1701619.

[9] G.A. Nazri, C. Julien, Far-infrared and Raman spectroscopy of molybdenum oxide single crystal, General Motors Publications, GMR Laboratories, Warren, MI, GMR-7403 (1991).

[10] J. Desmond, S. McCormack, P. McNamara, P. Lawlor, Rearview mirror assembly, European Patent 0,615,882A2 (Assessed on 18 March 1994).

[11] T. Tsumura, M. Inagaki, Lithium insertion/extraction reaction on crystalline MoO_3, Solid State Ion. 104 (1997) 183–189.

[12] W. Li, F. Cheng, Z. Tao, J. Chen, Vapor-transportation preparation and reversible lithium intercalation/deintercalation of α-MoO_3 microrods, J. Phys. Chem. B 110 (2006) 119–124.

[13] J. Song, X. Ni, L. Gao, H. Zheng, Synthesis of metastable h-MoO_3 by simple chemical precipitation, Mater. Chem. Phys. 102 (2007) 245–248.

[14] T. Brezesinski, J. Wang, S.H. Tolbert, B. Dunn, Ordered mesoporous α-MoO_3 with iso-oriented nanocrystalline walls for thin-film pseudocapacitors, Nat. Mater. 9 (2010) 146-151.

[15] B. Tian, G. Williams, D. Ban, H. Aziz, Transparent organic light-emitting devices using a MoO_3/Ag/MoO_3 cathode, J. Appl. Phys. 110 (2011) 104507.

[16] D. Mutschall, K. Holzner, E. Obermeier, Sputtered molybdenum oxide thin films for NH_3 detection, Sens. Actuators B 36 (1996) 320–324.

[17] A.K. Prasad, D.J. Kubinski, P.I. Gouma, Comparison of sol-gel and ion beam deposited MoO_3 thin film gas sensors for selective ammonia detection, Sens. Actuators B 93 (2003) 25–30.

[18] D. Kwak, M. Wang, K.J. Koski, L. Zhang, H. Sokol, R. Maric, Y. Lei, Molybdenum trioxide (α-MoO_3) nanoribbons for ultrasensitive ammonia (NH_3) gas detection: integrated experimental and density functional theory simulation studies, ACS Appl. Mater. Interfaces 11 (2019) 10697-10706.

[19] A.M. Taurino, A. Forleo, L. Francioso, P. Siciliano, M. Stalder, R. Nesper, Synthesis, electrical characterization, and gas sensing properties of molybdenum oxide nanorods, Appl. Phys. Lett. 88 (15) (2006) 152111.

[20] S.-Y. Lin, C.-M. Wang, K.-S. Kao, Y.-C. Chen, C.-C. Liu, Electrochromic properties of MoO_3 thin films derived by a sol–gel process, J. Sol-Gel Sci. Technol. 53 (2010) 51-58.

[21] D.G. Kim, S.H. Kim, Y.D. Kim, Electrochromic property of MoO_3 thin films deposited by chemical vapor transport synthesis, Jpn J. Appl. Phys. 50 (2011) 102601.

[22] R. Sivakumar, K. Shanthakumari, A. Thayumanavan, M. Jayachandran, C. Sanjeeviraja, Molybdenum oxide (MoO_3) thin film based electrochromic cell characterization in 0.1 M $LiClO_4$ PC electrolyte, J. Surf. Eng. 25 (2009) 548-554.

[23] J. Wang, K.C. Rose, C.M. Lieber, Load-independent friction: MoO_3 nanocrystal lubricants, J. Phys. Chem. B 103 (1999) 8405-8409.

[24] J. Zhou, N.-S. Xu, S.-Z. Deng, J. Chen, J.-C. She, Z.-L. Wang, Large-area nanowire arrays of molybdenum and molybdenum oxides: synthesis and field emission properties, Adv. Mater. 15 (2003) 1835–1840.

[25] L. Cattin, M. Morsli, F. Dahou, S.Y. Abe, A. Khelil, J.C. Bernède, Investigation of low resistance transparent MoO_3/Ag/MoO_3 multilayer and application as anode in organic solar cells, Thin Solid Films 518 (2010) 4560–4563.

[26] J. Yun, W. Jang, T. Lee, Y. Lee, A. Soon, Aligning the band structures of polymorphic molybdenum oxides and organic emitters in light-emitting diodes, Phys. Rev. Appl. 7 (2017) 024025.

[27] J. Song, X. Ni, D. Zhang, H. Zheng, Fabrication and photoluminescence properties of hexagonal MoO_3 rods, Solid State Sci. 8 (2006) 1164-1167.

[28] V.V. Atuchin, T.A. Gavrilova, V.G. Kostrovsky, L.D. Pokrovsky, I.B. Troitskaia, Morphology and structure of hexagonal MoO_3 nanorods, Inorg. Mater. 44 (2008) 622–627.

[29] S.R. Dhage, M.S. Hassan, O.-B. Yang, Low temperature fabrication of hexagon shaped h-MoO_3 nanorods and its phase transformation, Mater. Chem. Phys. 114 (2009) 511–514.

[30] R. Schlögl, A. Knop-Gericke, M. Hävecker, U. Wild, D. Frickel, T. Ressler, R.E. Jentoft, J. Wienold, G. Mestl, A. Blume, O. Timpe, Y. Uchida, In situ analysis of metal-oxide systems used for selective oxidation catalysis: how essential is chemical complexity, Topics Catal. 15 (2001) 219-228.

[31] X. Ma, J. Gong, X. Yang, S. Wang, A comparative study of supported MoO_3 catalysts prepared by the new "slurry" impregnation method and by the conventional method: Their activity in transesterification of dimethyl oxalate and phenol, Appl. Catal. A 280 (2005) 215-223.

[32] J. Huang, X. Wang, S. Li, Y. Wang, ZnO/MoO_3 mixed oxide nanotube: a highly efficient and stable catalyst for degradation of dye by air under room conditions, Appl. Surf. Sci. 257 (2010) 116–121.

[33] E. Gallei, E. Schwab, Development of technical catalysts, Catal. Today. 51 (3-4) (1999) 535–546.

[34] E.D. Hanson, L. Lajaunie, S. Hao, B.D. Myers, F. Shi, A.A. Murthy, C. Wolverton, R. Arenal, V.P. Dravid, Systematic study of oxygen vacancy tunable transport properties of few-layer MoO_{3-x} enabled by vapor-based synthesis, Adv. Func. Mater. 27 (2017) 1605380.

[35] L. Kihlborg, The crystal structure of $Mo_{18}O_{52}$ and the existence of homologous series of structures based on MoO_3, Ark. Kemi 21 (1963) 443–460.

[36] A. Magnéli, The crystal structures of Mo_9O_{26} (beta'-molybdenum oxide) and Mo_8O_{23} (beta-molybdenum oxide), Acta Chem. Scand. 2 (1948) 501–517.

[37] L. Kihlborg, Studies on molybdenum oxides, Acta Chem. Scand. 13 (1959) 954–962.

[38] L. Kihlborg, The crystal structure of $Mo_{17}O_{47}$, Acta Chem. Scand. 14 (1960) 1612–1622.

[39] S. Åsbrink, L. Kihlborg, A study of the crystal symmetry and structure of orthorhombic Mo_4O_{11} by least squares techniques, Acta Chem. Scand. 18 (1964) 1571–1573.

[40] M. Sato, O. Onoda, Y. Matsuda, Structural transitions in Mo_nO_{3n-1} (n = 9 and 10), J. Phys. C Solid State Phys. 20 (1987) 4763–4771.

[41] L. Seguin, M. Figlarz, R. Cavagnat, J.-C. Lassègues, Infrared and Raman spectra of MoO_3 molybdenum trioxides and MoO_3-$x$$H_2O$ molybdenum trioxide hydrates, Spectrochim. Acta Part A Mol. Biomol. Spectrosc. 51 (1995) 1323–1344.].

[42] M.S. Whittingham, Chemistry of intercalation compounds: metal guests in chalcogenide hosts, Prog. Solid State Chem. 12 (1978) 41-99.

[43] T.A. Kerr, H. Wu, L.F. Nazar, Concurrent polymerization and insertion of aniline in molybdenum trioxide: Formation and properties of a $[poly(aniline)]_{0.24}MoO_3$ nanocomposite, Chem. Mater. 8 (1996) 2005–2015.

[44] D. Liu, W.W. Lei, J. Hao, D.D. Liu, B.B. Liu, X. Wang, X.H. Chen, Q.L. Cui, G.T. Zou, J. Liu, S. Jiang, High-pressure Raman scattering and x-ray diffraction of phase transitions in MoO_3, J. Appl. Phys. 105 (2009) 023513.

[45] L. Kihlborg, Least squares refinement of crystal structure of molybdenum trioxide, Ark. Kemi. 21 (1963) 357-364.

[46] E. M. McCarron III, β-MoO_3: a metastable analogue of WO_3, J. Chem. Soc. Chem. Commun. (1986) 336-338.

[47] J.B. Parise, E.M. McCarron III, W. Sleight, A new modification of ReO_3-type MoO_3 and the deuterated intercalation compound from which it is derived: $D_{0.99}MoO_3$, Mater. Res. Bull. 22 (1987) 803-811.

[48] W. Pan, R. Tian, H. Jin, Y. Guo, L. Zhang, X. Wu, L. Zhang, Z. Han, G. Liu, J. Li, G. Rao, H. Wang, W.Chu, Structure, optical, and catalytic properties of novel hexagonal metastable h-MoO_3 nano- and microrods synthesized with modified liquid-phase processes, Chem. Mater. 22 (2010) 6202−6208.

[49] B. Baker, T.P. Feist, E.M. McCarron III, Soft chemical synthesis of a high-pressure phase of molybdenum trioxide: MoO_3-II, J. Solid State Chemistry 119 (1995) 199-202.

[50] H. Bräkken, Die kristallstrukturen der trioxide von chrom, molybdän und wolfram, Z. Krist. 78 (1931) 484-488.

[51] N. Wooster, The crystal structure of molybdenum trioxide, MoO_3, Z. Krist. 80 (1931) 504-512.

[52] G. Andersson, A. Magneli, On the crystal structure of molybdenum trioxide trioxide, Acta Chem. Scand. 4 (1950) 793-797.

[53] O. Glemser, G. Lutz, Über molybdänoxyde, Z. Anorg. Allgem. Chem. 263 (1950) 2-14.

[54] O. Glemser, G. Lutz, Z. Über molybdänblau, Anorg. Allgem. Chem. 264 (1951) 17-33

[55] O. Glemser, G. Lutz, G. Meyer, Über niedere molybdänhydroxyde, Z. Anorg. Allg. Chemie 285 (1956) 173.

[56] R. Schöllhorn, R. Kuhlmann, J.O. Besenhard, Topotactic redox reactions and ion exchange of layered MoO_3 bronzes, Mater. Res. Bull. 11 (1976) 83-90.

[57] C. Morehouse, R. Glicksman, An investigation of the discharge characteristics of groups VI-VIII oxides in an alkaline electrolyte, J. Electrochem. Soc. 107 (1960) 361-365.

[58] L. Campanella, G. Pistoia, MoO_3: A new electrode material for nonaqueous secondary battery applications, J. Electrochem. Soc. 118 (1971) 1905-1908.

[59] L. Campanella, G. Pistoia, Polarographic behavior of MoO_3 in butyrolactone solutions, J. Electrochem. Soc. 120 (1973) 383-384.

[60] J.P. Gabano, Y. Jumel, J. P. Gomis, Electrodes for secondary lithium batteries, 144th Electrochem. Soc. Meeting, Boston (1973) Abstr. 134.

[61] M.S. Whittingham, The role of ternary phases in cathode reactions, J. Electrochem. Soc. 123 (1976) 315-320.

[61] J.O. Besenhard, R. Schöllhorn, The discharge reaction mechanism of the MoO_3 electrode in organic electrolytes, J. Power Sources 1 (1976) 267-276.

[62] M.S. Whittingham, M.B. Dines, n-butyllithium – An effective, general cathode screening agent, J. Electrochem. Soc. 124 (1977) 1387-1388.

[63] J.O. Besenhard, J. Heydecke, H.P. Fritz, Characteristics of molybdenum oxide and chromium oxide cathodes in primary and secondary organic electrolyte lithium batteries. Part II. Transport properties, Solid State Ion. 6 (1983) 215-224.

[64] J.O. Besenhard, J. Heydecke, E. Wudy, H.P. Fritz, W. Foag, Characteristics of molybdenum oxide and chromium oxide cathodes in primary and secondary organic electrolyte lithium batteries. Part II. Transport properties, Solid State Ion. 8 (1983) 61-71.

[65] F. Bonino, L.P. Bicelli, B. Rivolta, M. Lazzari, F. Festorazzi, Amorphous cathode materials in lithium-organic electrolyte cells: tungsten and molybdenum trioxides, Solid State Ion. 17 (1985) 21-28.

[66] F.W. Dampier, The cathodic behavior of CuS, MoO_3, and MnO_2 in lithium cells, J. Electrochem. Soc. 121 (1974) 656-659.

[67] M. Gargalit, Discharge behavior of Li/MoO_3 cells, J. Electrochem. Soc. 121 (1974) 1460-1461.

[68] R. Schöllhorn, Reversible topotactic redox reactions of solids by electron/ion transfer, Angew. Chem. Int. Ed. 19 (1980) 983-1003.

[69] J.M. Réau, C. Fouassier, P. Hagenmuller, Sur quelques nouveaux bronzes oxygène de molybdène, J. Solid State Chem. 1 (1970) 326-331.

[70] C. Julien, G.A. Nazri, Transport properties of lithium-intercalated MoO_3, Solid State Ion. 68 (1994) 111-116.

[71] Y. Guo, J. Robertson, Origin of the high work function and high conductivity of MoO_3, Appl. Phys. Lett. 105 (2014) 222110.

[72] A. Lakshmi-Narayana, O.M. Hussain, C.V. Ramana, M. Camacho-Lopez, A. Abdel-Ghany, A. Hashem, A. Mauger, C.M. Julien, Molybdenum-suboxide thin films as anode layers in planar lithium microbatteries, Electrochem (Basel) 2 (2020) 160-186.

[73] H. Bräkken, Die kristallstrukturen der trioxide von chrom, molybdän und wolfram, Z. Krist. 78 (1931) 484-488.

[74] N. Wooster, The crystal structure of molybdenum trioxide, MoO_3, Z. Krist. 80 (1931) 504-512.

[75] H. Sitepu, B.H. O'Connor, D.J. Li, Comparative evaluation of the March and generalized spherical harmonic preferred orientation models using X-ray diffraction data for molybdite and calcite powders, Appl. Crystallogr. 38 (2005) 158-167.

[76] M.A. Py, K. Maschke, Intra- and interlayer contributions to the lattice vibrations in MoO_3, Phys. B+C 105 (1981) 370–374.

[77] G.A. Nazri, C. Julien, Far-infrared and Raman studies of orthorhombic MoO_3 single crystal, Solid State Ion. 53–56 (1992) 376–382.

[78] M. Dieterle, G. Weinberg, G. Mestl, Raman spectroscopy of molybdenum oxides - Part I. Structural characterization of oxygen defects in MoO_{3-x} by DR UV/VIS, Raman spectroscopy and X-ray diffraction, Phys. Chem. Chem. Phys. 4 (2002) 812–821.

[79] I.R. Beattie, N. Cheetham, M. Gardner, D.E. Rogers, Calculation of the vibrational frequencies of polyatomic molecules, including those of crystals, J. Chem. Soc. A (1971) 2240-2245.

[80] M.A. Py, P.E. Schmid, J.T. Vallin, Raman scattering and structural properties of MoO_3, Nuovo Cim. B 11. 38 (1977) 271–279.

[81] G. Mestl, N.F.D. Verbruggen, E. Bosch, H. Knözinger, Mechanically activated MoO_3. 5. Redox behavior, Langmuir 12 (1996) 2961–2968.

[82] H. Sinaim, D.J. Ham, J.S. Lee, A. Phuruangrat, S. Thongtem, T. Thongtem, Free-polymer controlling morphology of α-MoO_3 nanobelts by a facile hydrothermal

synthesis, their electrochemistry for hydrogen evolution reactions and optical properties, J. Alloys Compd. 516 (2012) 172-178.

[83] T. Siciliano, A. Tepore, E. Filippo, G. Micocci, M. Tepore, Characteristics of molybdenum trioxide nanobelts prepared by thermal evaporation technique, Mater. Chem. Phys. 114 (2009) 687-691.

[84] L.G. Pereira, L.E.B. Soledade, J.M. Ferreira, S.J.G. Lima, V.J. Fernandes Jr., A.S. Araújo, C.A. Paskocimas, E. Longo, M.R.C. Santos, A.G. Souza, I.M.G. Santos, Influence of doping on the preferential growth of α-MoO_3, J. Alloys Compd. 459 (2008) 377-385.

[85] S.S. Sunu, E. Prabhu, V. Jayaraman, K.I. Gnanasekar, T.K. Seshagiri, T. Gnanasekaran, Electrical conductivity and gas sensing properties of MoO_3, Sens. Actuators B 101 (2004) 161–174.

[86] M.E. Kurtoglu, T. Longenbach, Y. Gogotsi, Synthesis of quasi-oriented α-MoO_3 nanobelts and nanoplatelets on TiO_2 coated glass, J. Mater. Chem. 21 (2011) 7931-7936.

[87] S. Berthumeyrie, J.-C. Badot, J.-P. Pereira-Ramos, O. Dubrunfaut, S. Bach, P. Vermaut|, Influence of lithium insertion on the electronic transport in electroactive MoO_3 nanobelts and classical powders: Morphological and particle size effects, J. Phys. Chem. C 114 (2010) 19803–19814.

[88] Q.P. Ding, H.B. Huang, J.H. Duan, J.F. Gong, S.G. Yang, X.N. Zhao, Y.W. Du, Molybdenum trioxide nanostructures prepared by thermal oxidization of molybdenum, J. Cryst. Growth 294 (2006) 304–308.

[89] L. Cai, P.M. Rao, X. Zheng, Morphology-controlled flame synthesis of single, branched, and flower-like α-MoO_3 nanobelt arrays, Nano Lett. 11 (2011) 872-877.], hot plate method [90] B. Yan, Z. Zheng, J. Zhang, H. Gong, Z. Shen, W. Huang, T. Yu, Orientation controllable growth of MoO_3 nanoflakes: Micro-Raman, field emission, and birefringence properties, J. Phys. Chem. C 113 (2009) 20259–20263.

[91] A. Gopala Krishna, R.V.S.S.N. Ravikumar, T. Vijaya Kumar, S.D. Ephraim, B. Ranjith, M. Pranoy, S. Dola, Investigation and comparison of optical and Raman bands of mechanically synthesised MoO_3 Nano powders, Mater. Today: Proc. 3 (2016) 54–63.

[92] T.M. McEvoy, K.J. Stevenson, Elucidation of the electrodeposition mechanism of molybdenum oxide from iso- and peroxo-polymolybdate solutions, J. Mater. Res. 19 (2004) 429–438.

[93] W. Li, S. Zhao, B. Qi, Y. Du, X. Wang, M. Huo, Fast catalytic degradation of organic dye with air and MoO_3:Ce nanofibers under room condition, Appl. Catal. B 92 (2009) 333–340.

[94] S. Li, C. Shao, Y. Liu, S. Tang, R. Mu, Nanofibers and nanoplatelets of MoO_3 via an electrospinning technique, J. Phys. Chem. Solids 67 (2006) 1869–1872.

[95] A. Michailovski, J.-D. Grunwaldt, A. Baiker, R. Kiebach, W. Bensch, G.R. Patzke, Studying the solvothermal formation of MoO_3 fibers by complementary in situ EXAFS/EDXRD techniques, Angew. Chemie Int. Ed. 44 (2005) 5643–5647.

[96] A. Bouzidi, N. Benradame, H. Tabet-Derraz, C. Mathieu, B. Khelifa, R. Desfeux, Effect of substrate temperature on the structural and optical properties of MoO_3 thin films by spray pyrolysis technique. Mater. Sci. Eng. B 97 (2003) 5-8.

[97] H. Martinez, J. Torres, M.E. Rodriguez-Garcia, L.D. Lopez-Carreno, Gas sensing properties of nanostructured MoO_3 thin films prepared by spray pyrolysis, Phys. B Cond. Matter 407 (2012) 3199-3202.

[98] A.A. Mane, A.V. Moholkar, Orthorhombic MoO_3 nanobelts based NO_2 gas sensor, Appl. Surf. Sci. 405 (2017) 427-440.

[99] A. Klisinska, A.S. Mamede, E.M. Gaigneaux, Effect of the nature of the precursor on the morphology of MoO_3 thin films spin-coated on Si (100), Thin Solid Films 516 (2008) 2904-2912.

[100] L. Fang, Y. Shu, A. Wang, T. Zhang, Template-free synthesis of molybdenum oxide-based hierarchical microstructures at low temperatures, J. Cryst. Growth. 310 (2008) 4593–4600.

[101] H. Ren, S. Sun, J. Cui, X. Li, Synthesis, functional modifications, and diversified applications of molybdenum oxides micro-/nanocrystals: A review. Cryst. Growth Des. 18 (2018) 6326–6369.

[102] E. Haro-Poniatowski, C. Julien, B. Pecquenard, J. Livage, M.A. Camacho-López, Laser-induced structural transformations in MoO_3 investigated by Raman spectroscopy, J. Mater. Res. 13 (1998) 1033–1037.

[103] R. Murugan, A. Ghule, C. Bhongale, H. Chang, Thermo-Raman investigations on structural transformations in hydrated MoO_3, J. Mater. Chem. 10 (2000) 2157–2162.].

[104] S. Wang, Y. Zhang, X. Ma, W. Wang, X. Li, Z. Zhang, Y. Qian, Hydrothermal route to single crystalline α-MoO_3 nanobelts and hierarchical structures, Solid State Commun. 136 (2005) 283–287.

[105] X.W. Lou, H.C. Zeng, Hydrothermal synthesis of α-MoO_3 nanorods via acidification of ammonium heptamolybdate tetrahydrate, Chem. Mater. 14 (2002) 4781–4789.

[106] C.V. Subba Reddy, E.H. Walker, C. Wen, S.-I. Mho, Hydrothermal synthesis of MoO_3 nanobelts utilizing poly(ethylene glycol), J. Power Sources 183 (2008) 330–333.

[107] A. Chithambararaj, A.C. Bose, Hydrothermal synthesis of hexagonal and orthorhombic MoO_3 nanoparticles, J. Alloys Compd. 509 (2011) 8105–8110.

[108] L. Zhou, L. Yang, P. Yuan, J. Zou, Y. Wu, C. Yu, α-MoO_3 Nanobelts: A high performance cathode material for lithium ion batteries, J. Phys. Chem. C 114 (2010) 21868–21872.

[109] A.M. Hashem, A.E. Abdel-Ghany, R.S. El-Tawil, S. Indris, H. Ehrenberg, A. Mauger, C.M. Julien, Amorphous Mo_5O_{14}-type/carbon nanocomposite with enhanced electrochemical capability for lithium-ion batteries, Nanomaterials 10 (2020) 8.

[110] R.-Q. Song, A.-W. Xu, B. Deng, Y.-P. Fang, Novel multilamellar mesostructured molybdenum oxide nanofibers and nanobelts: Synthesis and characterization, J. Phys. Chem. B 109 (2005) 22758-22766.

[111] G.S. Zakharova, C. Täschner, V.L. Volkov, I. Hellmann, R. Klingeler, A. Leonhardt, B. Büchne, Solid State Sci. 9 (2007) 1028–1032.

[112] L. Cheng, M. Shao, X. Wang, H. Hu, Single-crystalline molybdenum trioxide nanoribbons: Photocatalytic, photoconductive, and electrochemical properties. Chem. Eur. J. 15 (2009) 2310–2316.

[113] K. Dewangan, N. Nikkan Sinha, P.K. Sharma, A.C. Pandey, N. Munichandraiah, N. S. Gajbhiye, Synthesis and characterization of single-crystalline α-MoO_3 nanofibers for enhanced Li-ion intercalation applications, CrystEngCom 13 (2011) 927-933.

[114] X.-L. Li, J.-F. Liu, Y.-D. Li, Low-temperature synthesis of large-scale single-crystal molybdenum trioxide (MoO_3) nanobelts, Appl. Phys. Lett. 81 (2002) 4832.

[115] Y. Shen, R. Huang, Y. Li, S. Yao, Synthesis and photochromic properties of 1,3-diaminopropane-induced MoO_3 powder, Appl. Surf. Sci. 258 (2011) 414– 418.

[116] X. Yang, H. Ding, D. Zhang, X. Yan, C. Lu, J. Qin, R. Zhang, H. Tang, H. Song, Hydrothermal synthesis of MoO_3 nanobelt-graphene composites, Cryst. Res. Technol. 46 (2011) 1195–1201.

[117] I. Shakir, M. Shahid, H.W. Yang, D.J. Kang, Structural and electrochemical characterization of α-MoO_3 nanorod-based electrochemical energy storage devices, Electrochim. Acta 56 (2010) 376–380.

[118] I. Shakir, M. Shahid, S. Cherevko, C.-H. Chung, D.J. Kang, Ultrahigh-energy and stable supercapacitors based on intertwined porous MoO_3–MWCNT nanocomposites, Electrochim. Acta 58 (2011) 76– 80.

[119] L. Jiao, H. Yuan, Y. Si, Y. Wang, M. Zhao, Y. Wang, A novel method for synthesis of microstructure MoO_3, Mater. Lett. 59 (2005) 3112–3114.

[120] T.H. Chiang, H.C. Yeh, The synthesis of α-MoO_3 by ethylene glycol. Materials (Basel) 6 (2013) 4509-4625.

[121] G.A. Nazri, C. Julien, Studies of lithium intercalation in heat-treated products obtained from molybdic acid, Ionics 2 (1996) 1–6.

[122] J. Ding, S.A. Abbas, C. Hanmandlu, L. Lin, C.S. Lai, P.C. Wang, L.J. Li, C.W. Chu, C.C. Chang, Facile synthesis of carbon/MoO_3 nanocomposites as stable battery anodes, J. Power Sources 348 (2017) 270-280.

[123] M. Xu, J. Tang, H. Wu, G.F. Zheng, Mesoporous carbon coated molybdenum oxide nanobelts for improved lithium ion storage, RSC Adv. 4 (2014) 29586-29590.

[124] X. Li, J.T. Xu, L. Mei, Z.J. Zhang, C.Y. Cui, H.K. Liu, J.M. Ma, S.X. Dou, Electrospinning of crystalline MoO_3@C nanofibers for high-rate lithium storage, J. Mater. Chem. A 3 (2015) 3257-3260.

[125] C.Q. Feng, H. Gao, C.F. Zhang, Z.P. Guo, H.K. Liu, Synthesis and electrochemical properties of MoO_3/C nanocomposite, Electrochim. Acta 93 (2013) 101-106.

[126] Q. Xia, H.L. Zhao, Z.H. Du, J. Wang, T.H. Zhang, J. Wang, P.P. Lv, Synthesis and electrochemical properties of MoO_3/C composite as anode material for lithium-ion batteries, J. Power Sources 226 (2013) 107-111.

[127] C.M. Julien, A. Mauger, A. Vijh, K. Zaghib, *Lithium Batteries: Science and Technology*; Springer: Heidelberg, Germany, 2016.

[128] S.-H. Lee, Y.-H. Kim, R. Deshpande, P.A. Parilla, E. Whitney, D.T. Gillaspie, K.M. Jones, A.H. Mahan, S. Zhang, A.C. Dillon, Reversible lithium-ion insertion in molybdenum oxide nanoparticles, Adv. Mater. 20 (2008) 3627-3632

[129] Z. Wang, S. Madhavi, X.W. Lou, Ultralong α-MoO_3 nanobelts: synthesis and effect of binder choice on their lithium storage properties, J. Phys. Chem. C 116 (2012) 12508-12503.

[130] D. Yan, X. Luo, H. Zhang, G. Zhu, L. Chen, G. Chen, H. Xu, A. Yu, Single crystalline α-MnO_3 microbelts derived from a bio-templating method for superior lithium storage application, J. Alloys Compd. 688 (2016) 481-486.

[131] L. Mai, F. Yang, Y. Zhao, X. Xu, L. Xu, B. Hu, Y. Luo, H. Liu, Molybdenum oxide nanowires: synthesis and properties, Mater. Today 14 (2011) 346-353.

[132] P. Meduri, E. Clark, J.H. Kim, E. Dayalan, G.U. Sumanasekera, M.K. Sunkara, MoO_{3-x} nanowire arrays as stable and high capacity anodes for lithium ion batteries. Nano Lett. 12 (2012) 1784−1788.

[133] P. Allen, L. Cai, L. Zhou, C. Zhao, P.M. Rao, Rapid synthesis of thin and long $Mo_{17}O_{47}$ nanowire-arrays in an oxygen deficient flame, Sci. Rep. 5 (2016) 27832.

[134] X. He, K. Zhang, X. Zhao, P. Zhang, M. Chen, Z. Zheng, Z. Han, T. Zhu, Y. Tong, X. Lu, Stabilized molybdenum trioxide nanowires as novel ultrahigh-capacity cathode for rechargeable zinc ion battery, Adv. Sci. 6 (2019) 1900151.

[135] A.M Hashem, H. Groult, A. Mauger, K. Zaghib, C.M. Julien, Electrochemical properties of nanofibers α-MoO_3 as cathode materials for Li batteries, J. Power Sources 219 (2012) 126-132.

[136] S. Hu, X. Wang, Single-walled MoO_3 nanotubes, J. Am. Chem. Soc. 130 (2008) 8126-8127.

[137] S. Hu, X. Ling; T. Lan, X. Wang, Cluster-based self-assembly route toward MoO_3 single-walled nanotubes, Chem. Eur. J. 16 (2010) 1889-1896.

[138] J.V. Silveira, J.A. Batista, G.D. Saraiva, J.M. Filho, A.G. Sousza Filho, S. Hu, X. Wang, Temperature dependent behavior of single walled MoO_3 nanotubes: A Raman spectroscopy study. Vibrat. Spectr. 54 (2010) 179-183.

[139] G. Zhao, N. Zhang, K. Sun, Electrochemical preparation of porous MoO_3 film with a high rate performance as anode for lithium ion batteries, J. Mater. Chem. A 1 (2012) 221–224.

[140] X. Yu, L. Wang, J. Liu, X. Sun, Porous MoO_3 film as a high-performance anode material for lithium-ion batteries, ChemElectroChem 1 (2014) 1476-1479.

[141] P.M.S. Monk, R.J. Mortimer, D.R. Rosseinsky, *Electrochromism and Electrochromic Devices*, Cambridge Univ. Press, Cambridge, 2007.

[142] T. Abhijith, T. V. Arun Kumar, V. S. Reddy , Organic bistable memory devices based on MoO_3 nanoparticle embedded Alq_3 structures, Nanotechnology 28 (2017) 095203.

[143] C. Julien, O.M. Hussain, L. El-Farh, M. Balkanski, Electrochemical studies of lithium insertion in MoO_3 films, Solid State Ion. 53-56 (1992) 400-404.

[144] H. Ohtsuka, Y. Sakurai, Characteristics of Li/MoO_{3-x} thin film batteries, Solid State Ion. 144 (2001) 59-64.

[145] C.V. Ramana, V.V. Atuchin, H. Groult, C.M. Julien, Electrochemical properties of sputter-deposited MoO_3 films in lithium batteries, J. Vacuum Sci. Technol. A 30 (2012) 04D105.

[146] C.M. Julien, A. Mauger, Pulsed laser deposition films for microbatteries, Coatings (Basel) 9 (2019) 386.

[147] R. Martinez, J.R. Vargas, V. Santes, E. Gomez, Preparation of molybdenum oxide thin films by MOCVD. J Alloys Compd. 434-435 (2007) 701-703.

[148] N. Miyata, T. Suzuki, R. Ohyama, Physical properties of evaporated molybdenum oxide films, Thin Solid Films 281–282 (1996) 218-222.

[149] C.V. Ramana, V.V. Atuchin, V.G. Kesler, V.A. Kochubey, L.D. Pokrovsky, V. Shutthanandan, U. Becker, R.C. Ewing, Growth and surface characterization of sputter-deposited molybdenum oxide thin films. Appl. Surf. Sci. 253 (2007) 5368-5374.

[150] T. Maruyama, T. Kanagawa, Electrochromic properties of molybdenum trioxide thin films prepared by chemical vapor deposition, J. Electrochem. Soc. 142 (1995) 1644-1647.

[151] T. Ivanova, A. Szekeres, M. Gartner, D. Gogova, K.A. Gesheva, Spectroscopic characterization of CVD-molybdenum oxide films, Electrochim. Acta 46 (2001) 2215-2219.

[152] A. Guerfi, L.H. Dao, Electrochromic molybdenum oxide thin films prepared by electrodeposition, J. Electrochem. Soc. 136 (1989) 2435-2436.

[153] C. Julien, A. Khelfa, O.M. Hussain, G.A. Nazri, Synthesis and characterization of flash-evaporated MoO_3 thin films, J. Cryst. Growth 156 (1995) 235-244.

[154] C. Julien, B. Yebka, G.A. Nazri, Temperature dependence of the vibrational modes of MoO_3, Mater. Sci. Eng. B 38 (1996) 65-71.

[155] M. Al-Kuhaili, S.A. Durrani, I.A. Bakhtiari, Pulsed laser deposition of molybdenum oxide thin films, Appl. Phys. A 98 (2009) 609-615.

[156] A. Pardo, J. Torres, Substrate and annealing temperature effects on the crystallographic and optical properties of MoO_3 thin films prepared by laser assisted evaporation, Thin Solid Films 520 (2012) 1709-1717.

[157] C.V. Ramana, O.M. Hussain, C.M. Julien, Electronic properties and performance upon lithium intercalation of MoO_3 thin films grown by PLD, ECS Trans. 1-15 (2006) 1-7.

[158] M. Yahaya, M.M. Salleh, I.A. Talib, Optical properties of MoO_3 thin films for electrochromic windows, Solid state Ion. 113-115 (1998) 421-423.

[159] R. Sivakumar, R. Gopalakrishnan, M. Jayachandran, C. Sanjeeviraja, Characterization on electron beam evaporated α-MoO_3 thin films by the influence of substrate temperature, Current Appl. Phys. 7 (2007) 51–59.

[160] C.-S. Hsu, C.-C. Chan, H.-T. Huang, C.-H. Peng, W.-C. Hsu, Electrochromic properties of nanocrystalline MoO_3 thin films, Thin Solid Films 516 (2008) 4839-4844.

[161] M. Epifani, P. Imperatori, L. Mirenghi, M. Schioppa, P. Siciliano, Synthesis and characterization of MoO_3 thin films and powders from a molybdenum chloromethoxide, Chem. Mater. 16 (2004) 5495-5501.

[162] A. Boukhachem, C. Bouzidi, R. Boughalmi, R. Ouerteni, M. Kahlaoui, B. Ouni, H. Elhouichet, M. Amlouk, Physical investigations on MoO_3 sprayed thin film for selective sensitivity applications, Ceram. Int. 40 (2014) 13427-13435.

[163] R. Pandeeswari, B.G. Jeyaprakash, Nanostructured α-MoO_3 thin film as a highly selective TMA sensor, Biosens. Bioelectr. 53 (2014) 182-186.

[164] V. Nirupama, M. Chandra Sekhar, T.K. Subramanyam, S. Uthanna, Structural and electrical characterization of magnetron sputtered MoO_3 thin films. J. Phys. Conf. Ser. 208 (2010) 012101.

[165] C.V. Ramana, V.V. Atuchin, L.D. Pokrovsky, U. Beker, C.M. Julien, Structure and chemical properties of molybdenum oxide thin films, J. Vac. Sci. Technol. A 25 (2007) 1166–1171.

[166] J. Swiatowska-Mrowiecka, S. de Diesbach, V. Maurice, S. Zanna, L**.** Klein, E**.** Briand, I**.** Vickridge, P**.** Marcus, Li-ion intercalation in thermal oxide thin films of MoO_3 as studied by XPS, RBS, and NRA, J. Phys. Chem. C 112 (2008) 11050–11058.

[167] M. Niederberger, F. Krumeich, H.-J. Muhr, M. Müller, R. Nesper, Synthesis and characterization of novel nanoscopic molybdenum oxide fibers, J. Mater. Chem. 11 (2001) 1941-1945.

[168] B.C. Satishkumar, A. Govindaraj, M. Nath, C.N.R. Rao, Synthesis of metal oxide nanorods using carbon nanotubes as templates, J. Mater. Chem. 10 (2000) 2115-2119.

[169] A. Abdellaoui, G. Lévêque, A. Donnadieu, A. Bath, B. Bouchikhi, Iteratively derived optical constants of MoO_3 polycrystalline thin films prepared by CVD, Thin Solid Films 304 (1997) 39-44.

[170] E. Haro-Poniatowski, M. Jouanne, J.F. Morhange, C. Julien, R. Diamant, M. Fernandez-Guasti, G.A. Fuentes, J.C. Alonso, Micro-Raman characterization of WO_3 and MoO_3 thin films obtained by pulsed laser irradiation, Appl. Surf. Sci. 127 (1998) 674–678.

[171] C.V. Ramana, O.M. Hussain, C.M. Julien, Effect of growth temperature on the optical properties of pulsed-laser deposited MoO_3 thin films, Mater. Sci. Indian J. 1 (2005)10–15.

[172] C.V. Ramana, O.M. Hussain, C.M. Julien, Electronic properties of MoO_3 thin films grown by PLD and ARE techniques and their performance upon lithium intercalation, Extended Abstract of the 208th ECS Meeting, Los Angeles, CA, USA (16–21 October 2005= p. 885.

[173] C.V. Ramana, C.M. Julien, Chemical and electrochemical properties of molybdenum oxide thin films prepared by reactive pulsed-laser assisted deposition, Chem. Phys. Lett. 428 (2006) 114–118.

[174] C. Julien, Thin film technology and microbatteries, in: *Lithium Batteries - New Materials, Developments and Perspectives*, G. Pistoia (Ed.), Elsevier Science B.V., Amsterdam, The Netherlands (1994), pp.167-237.

[175] C. Julien, Lithium microbatteries, in: *Materials for Lithium-ion Batteries*, C. Julien, Z. Stoynov (Eds.), Kluwer Acad. Publ., Dordecht, The Netherlands (2000), pp. 381-400.

[176] H. Ohtsuka, J. Yamaki, Electrical characteristics of $Li_2O–V_2O_5–SiO_2$ thin films, Solid State Ion. 35 (1989) 201-206.

[177] C. Julien, G.A. Nazri, J.P. Guesdon, A. Goreinstein, A. Khelfa, O.M. Hussain, Influence of the growth conditions on electrochemical features of MoO_3 film-cathodes in lithium microbatteries, Solid State Ion. 73 (1994) 319-326.

[178] C. Julien, A. Khelfa, J.-P. Guesdon, A. Gorenstein, Lithium intercalation in MoO_3: a comparison between crystalline and disordered phases, Appl. Phys. A 59 (1994) 173-178.

[179] C. Julien, L. El-Farh, M. Balkanski, O.M. Hussain, G.A. Nazri, The growth and electrochemical properties of metal-oxide thin films: lithium intercalation, Appl. Surf. Sci. 65-66 (1993) 325-330.

[180] B. Yebka, C. Julien, Lithium intercalation in sputtered MoO_3 films, Ionics 3 (1997) 83-88.

[181] F.F. Ferreira, T.G. Souza Cruz, M.C.A. Fantini, M.H. Tabacniks, S.C. de Castro, J. Morais, A. de Siervo, R. Landers, A. Gorenstein, Lithium insertion and electrochromism in polycrystalline molybdenum oxide films, Solid State Ion. 136-137 (2000) 357-363.

[182] W. West, J. Whitacre, MoO_3 cathodes for high-temperature lithium thin-film cells, NASA Tech Briefs NPO-41099 (2007) 19.

[183] W. Jiebing, X. Rui, W. Shimin, T. Wufeng, T. Hua, S. Jing, Preparation and characterization of molybdenum oxide thin films by sol-gel process, J. Sol-Gel Sci. Technol. 27 (3) (2003) 315-319.

[184] E. Comini, G. Faglia, G. Sberveglieri, C. Cantalini, M. Passacantando, S. Santucci, Y. Li, W. Wlodarski, W. Qu, Carbon monoxide response of molybdenum oxide thin films deposited by different techniques, Sens. Actuators B 68 (2000) 168-174.

[185] S. Moitzheim, B. Put, P. Vereecken, Advances in 3D thin-film Li-ion batteries, Adv. Mater. Interfaces 6 (2019) 1900805.

[186] H.K. Puppala, A.T. Pelton, R.A. Mayanovic, A comparative characterization study of molybdenum oxide thin films grown using femtosecond and nanosecond pulsed laser deposition, Mater. Res. Soc. Adv. 1 (2016) 2585–2590.

[187] M.A. Ashrafi, M. Ranjbar, H. Kalhori, H. Salamati, Pulsed laser deposition of Mo-V-O thin films for chromogenic applications, Thin Solid Films 621 (2017) 220–228.

[188] C.C. Chang, J.Y. Luo, T.K. Chen, K.W. Yeh, T.W. Huang, C.H. Hsu, W.H. Chao, C.T. Ke, P.C. Hsu, M.J. Wang, Pulsed laser deposition of $(MoO_3)_{1-x}(V_2O_5)_x$ thin films: Preparation, characterization and gasochromic studies, Thin Solid Films 519 (2010) 1552–1557.

[189] S.K. Deb, Physical properties of a transition metal oxide: optical and photoelectric properties of single crystal and thin film molybdenum trioxide, Proc. R. Soc. A 304 (1477) (1968) 211–231.

[190] Q. Qu, W.-B. Zhang, K. Huang, H.-M. Chen, Electronic structure, optical properties and band edges of layered MoO_3: A first-principles investigation, Comput. Mater. Sci. 130 (2017) 242-248.

[191] C. Julien, G.A. Nazri, *Solid State Batteries, Materials Design and Optimization*, Kluwer, Boston, 1994.

[192] T.M. McEvoy, K.J. Stevenson, Spatially resolved measurement of inhomogeneous electrocoloration/insertion in polycrystalline molybdenum oxide thin films via chronoabsorptometric imaging, J. Am. Chem. Soc. 125 (2003) 8438-8439.

[193] R. Liang, H. Cao, D. Qian, MoO_3 nanowires as electrochemical pseudocapacitor materials, Chem. Commun. 47 (2011) 10305-10307.

[194] H.-S. Kim, J.B. Cook, H. Lin, J.S. Ko, S.H. Tolbert, V. Ozolins, B. Dunn, Oxygen vacancies enhance pseudocapacitive charge storage properties of MoO_{3-x}, Nat. Mater. 16 (2017) 454-462.

[195] N.A. Chernova, M. Roppolo, A.C. Dillon, M.S. Whittingham, Layered vanadium and molybdenum oxides: batteries and electrochromics, J. Mater. Chem. 19 (2009) 2526-2552.

[196] A.M. Hashem, M.H. Askar, M. Winter, J.H. Albering, J.O. Besenhard, Two-phase reaction mechanism during chemical lithium insertion into α-MoO_3, Ionics 13 (2007) 3-8.

[197] L. Mai, B. Hu, W. Chen, Y. Qi, C. Lao, R. Yang, Y. Dai, Z.L. Wang, Lithiated MoO_3 nanobelts with greatly improved performance for lithium batteries, Adv. Mater. 19 (2007) 3712–3716.

[198] L. Mai, B. Hu, Y. Qi, Y. Dai, W. Chen, Improved cycling performance of directly lithiated MoO_3 nanobelts, Int. J. Electrochem. Sci. 3 (2008) 216-222.

[199] C. Villevieille, A. Gorzkowska-Sobas, H. Fjellvag, P. Novak, Freeze-dryed Li_xMoO_3 nanobelts used as cathode materials for lithium-ion batteries: A bulk and interface study, J. Power Sources 297 (2015) 276-282.

[200] P.G. Dickens, G.J. Reynolds, Transport and equilibrium properties of some oxide insertion compounds, Solid State Ion. 5 (1981) 331-334.

[201] N. Kumagai, N. Kumagai, K. Tanno, Electrochemical characteristics and structural changes of molybdenum trioxide hydrates as cathode materials for lithium batteries, J. Appl. Electrochem. 18 (1988) 857-862.

[202] M.E. Spahr, P. Novak, O. Haas, R. Nesper, Electrochemical insertion of lithium, sodium, and magnesium in molybdenum(VI) oxide, J. Power Sources 54 (1995) 346-351.

[203] J.W. Bullard III, R.L. Smith, Structural evolution of the MoO_3(010) surface during lithium intercalation, Solid State Ion. 2003, 160, 335–349.

[204] B. Yebka, G.A. Nazri, C.M. Julien, In-situ structural features of Li-intercalated molybdenum trioxide with layer- and fiber-like frameworks, Proc. Electrochem. Soc. 20 (2003) 491-496.

[205] F. Leroux, B.E. Loene, L.F. Nazar, Electrochemical lithium intercalation into a polyaniline/V_2O_5 nanocomposite, J. Electrochem. Soc. 143 (1996) L181.

[206] Y. Iriyama, T. Abe, M. Inaba, Z. Ogumi, Transmission electron microscopy (TEM) analysis of two-phase reaction in electrochemical lithium insertion within α-MoO_3, Solid State Ion. 135 (2000) 95-100.

[207] S. Basu, W.L. Worrel,l Chemical diffusion of lithium in Li_xTaS_2 and Li_xTiS_2 at 30 °C. In: Vashishta P, Mindy JN, Shenoy GK (eds) Fast ion transport in solids. North-Holland, Amsterdam (1979) pp 149-152.

[208] W. Xia, Q. Zhang, F. Xu, L. Sun, New insights into electrochemical lithiation/delithiation mechanism of α-MoO_3 nanobelt by in situ transmission electron microscopy, ACS Appl. Mater. Interfaces 8 (2016) 9170-9177.

[209] H. Guo, D. Goonetilleke, N. Sharma, W. Ren, Z. Su, A. Rawal, C. Zhao, Two-phase electrochemical proton transport and storage in α-MoO_3 for proton batteries, Cell Rep. Phys. Sci. 1 (2020) 100225.

[210] H. Zhang, W. Wu, Q. Liu, F. Yang, Xin Shi, X. Liu, M. Yu, X. Lu, Interlayer engineering of α-MoO_3 modulates selective hydronium intercalation in neutral aqueous electrolyte. Angew. Chem. Int. Ed. 59 (2020) 2-10.

[211] J. Huang, J. Yan, J. Li, L. Cao, Z. Xu, J. Wu, L. Zhou, Y. Luo, Assembled-sheets-like MoO_3 anodes with excellent electrochemical performance in Li-ion battery, J. Alloys Compd. 688 (2016) 588-595.

[212] R. Nadimicherla, R. Zha, L. Wei, X. Guo, single crystalline flowerlike α-MnO_3 nanorods and their application as anode material for lithium-ion batteries, J. Alloys Compd. 687 (2016) 79-86.

[213] B. Mendoza-Sánchez, T. Brousse, C. Ramirez-Castro, V. Nicolosi, P.S. Grant, An investigation of nanostructured thin film α-MoO_3 based supercapacitor electrodes in an aqueous electrolyte, Electrochim. Acta 91 (2013) 253-260.

[214] Q. Wang, D.-A. Zhang, Q. Wang, J. Sun, L.-L. Xing, X.-Y. Xue, High electrochemical performances of α-MoO_3@MnO_2 core-shell nanorods as lithium-ion battery anodes, Electrochim. Acta 146 (2014) 411-418.

[215] Q. Xia, H. Zhao, Z. Du, Z. Zeng, C. Gao, Z. Zhang, X. Du, A. Kulka, K. Swierczek, Facile synthesis of MoO_3/carbon nanobelts as high-performance anode material for lithium ion batteries, Electrochim. Acta 180 (2015) 947–956.

[216] Y. Zhu, X. Xu, G. Chen, Y. Zhong, R. Cai, L. Li, Z. Shao, Surfactant-free self-assembly of reduced graphite oxide-MoO_2 nanobelt composites used as electrode for lithium-ion batteries. Electrochim. Acta 211 (2016) 972-981.

[217] Z. Yu, H. Jiang, D. Gu, J. Li, L. Wang, L. She, A new way to prepare MoO_3/C as anode of lithium ion battery for enhancing the electrochemical performance at room temperature, J. Electrochem. Sci. Technol. 7 (2016) 170-178.

[218] J. Qiu, Z. Yang, Y. Li, N-doped carbon encapsulated ultrathin MoO_3 nanosheets as superior anodes with high capacity and excellent rate capability for Li-ion batteries. J. Mater. Chem. A 3 (2015) 24245–24253.

[219] B. Mendoza-Sánchez, P.S. Grant, Charge storage properties of a α-MoO_3/carboxyl-functionalized single-walled carbon nanotube composite electrode in a Li ion electrolyte, Electrochim. Acta 98 (2013) 294-302.

[220] I. Shakir, M. Sarfraz, Evaluation of electrochemical charge storage mechanism and structural changes in intertwined MoO_3–MWCNTs composites for supercapacitor applications Electrochim. Acta 147 (2014) 380-384.

[221] L.S. Aravinda, U. Bhat, B.R. Bhat, Binder-free MoO_3/multiwalled carbon nanotube thin film electrode for high energy density supercapacitors, Electrochim. Acta 112 (2013) 663-669.

[222] Y. Hao, X. Wang, Y. Zheng, J. Shen, J. Yuan, A. Wang, L. Niu, S. Huang, Uniform Pt nanoparticles incorporated into reduced graphene oxides with MoO_3 as advanced anode catalysts for methanol electro-oxidation, Electrochim. Acta 198 (2016) 127-134.

[223] G.D. Park, J.H. Kim, Y.J. Choi, Y.C. Kang, Large-scale production of MoO_3-reduced graphene oxide powders with superior lithium storage properties by spray-drying process, Electrochim. Acta 173 (2015) 581-587.

[224] W. Zeng, G. Zhang, S. Hou, T. Wang, H. Duan, Facile synthesis of graphene@NiO/MoO_3 composite nanosheet arrays for high-performance supercapacitors, Electrochim. Acta 151 (2015) 510-516.

[225] S. Wang, Q. Li, W. Pu, Y. Wu, M. Yang, MoO_3-MnO_2 intergrown nanoparticles composite prepared by one-step hydrothermal synthesis as anode for lithium ion batteries, J. Alloys Compd. 663 (2016) 148-155.

[226] D. Wu, R. Shen, R. Yang, W. Ji, M. Jiang, W. Ding, L. Peng, Mixed molybdenum oxides with superior performances as an advanced anode material for lithium-ion batteries, Sci. Rep. 7 (2017) 44697.

[227] X.-J. Wang, R. Nesper, C. Villevieille, P. Novák, Ammonolyzed MoO_3 nanobelts as novel cathode material of rechargeable Li-ion batteries, Adv. Energy Mater. 3 (2013) 606–614.

[228] I. Shakir, M. Shahid, M. Nadeem, D.J. Kang, Tin oxide coating on molybdenum oxide nanowires for high performance supercapacitor devices, Electrochim. Acta 72 (2012) 134-137.

[229] H. Zhang, X. Liu, R. Wang, R. Mi, S. Li, Y. Cui, Y. Deng, J. Mei, H. Liu, Coating of α-MoO_3 on nitrogen-doped carbon nanotubes by electrodeposition as a high-performance cathode material for lithium-ion batteries, J. Power Sources 274 (2015) 1063-1069.

[230] L.C. Yang, W.L. Guo, Y. Shi, Y.P. Wu, Graphite@MoO_3 composite as anode material for lithium ion battery in propylene carbonate-based electrolyte, J. Alloys Compd. 501 (2010) 218-220.

[231] A.C. Dillon, A.H. Mahan, R. Deshpande, P.A. Parilla, K.M. Jones, S.H. Lee, Metal oxide nano-particles for improved electrochromic and lithium-ion battery technologies, Thin Solid Films. 516 (2008) 794–797.

[232] M.F. Hussan, Z.P. Guo, Z. Chen, H.K. Liu, Carbon-coated MoO_3 nanobelts as anode materials for lithium-ion batteries, J. Power Sources 195 (2010) 2372-2376.

[233] S. Hariharan, K. Saravanan, P. Balaya, α-MoO_3: A high performance anode material for sodium-ion batteries, Electrochem. Commun. 31 (2013) 5-9.

[234] C. Wang, L. Wu, H. Wang, W. Zuo, Y. Li, J. Liu, Fabrication and shell optimization of synergistic TiO_2-MoO_3 core-shell nanowire array anode for high energy and high power lithium-ion batteries, Adv. Funct. Mater. 25 (2015) 3524-3533.

[235] C. Yang, Q. Xiang, X. Li, Y. Xu, X. Wang, X. Xie, C. Li, H. Wang, L. Wang, MoO_3 nanoplates: a high-capacity and long-life anode material for sodium-ion batteries, J. Mater. Sci. 55 (2020) 12053-12064.

[236] Y.S. Jung, S. Lee, D. Ahn, A.C. Dillon, S.-H. Lee, Electrochemical reactivity of ball-milled MoO_{3-y} as anode materials for lithium-ion batteries, J. Power Sources 188 (2009) 286-291.

[237] L.A. Riley, S.-H. Lee, L. Gedvilias, A.C. Dillon, Optimization of MoO_3 nanoparticles as negative-electrode material in high-energy lithium ion batteries, J. Power Sources 195 (2010) 588-592.

[238] X.-Y. Xue, Z.-H. Chen, L.-L. Xing, S. Yuan, Y.-J. Chen, SnO_2/α-MoO_3 core-shell nanobelts and their extraordinarily high reversible capacity as lithium-ion battery anodes, Chem. Commun. 47 (2011) 5205-5207.

[239] A.C. Dillon, L.A. Riley, Y.S. Jung, C. Ban, D. Molina, A.H. Mahan, A.S. Cavanagh, S.M. George, S.-H. Lee, HWCVD MoO_3 nanoparticles and a-Si for next generation Li-ion anodes, Thin Solid Films 519 (2011) 4495-4497.

[240] W. Tang, L. Liu, S. Tian, L. Li, Y. Yue, Y. Wu, K. Zhu, Aqueous supercapacitors of high energy density based on MoO_3 nanoplates as anode material, Chem. Commun. 47 (36) (2011) 10058-10060.

[241] M.J. Aragon, B. Leon, C. Perez-Vicente, J.L. Tirado, On the use of transition metal oxysalts as conversion electrodes in lithium-ion batteries, J. Power Sources 189 (2009) 823–827.

[242] M. Sasidharan, N. Gunawardhana, H. Noma, M. Yoshio, K. Nakashima, α-MoO_3 hollow nanospheres as an anode material for Li-ion batteries, Bull. Chem. Soc. Jpn 85 (2011) 642-646.

[243] P.M. Ette, P. Gurunathan, K. Ramesha, Self-assembled lamellar alpha-molybdenum trioxide as high performing anode material for lithium-ion batteries, J. Power Sources 278 (2015) 630-638.

[244] L.A. Riley, A.S. Cavanagh, S.M. George, Y.-S. Jung, Y. Yan, S.-H. Lee, A.C. Dillon, Conformal surface coatings to enable high volume expansion Li-ion anode materials, ChemPhysChem 11 (2010) 2124-2130.

[245] X. Zhao, M. Cao, C. Hu, Thermal oxidation synthesis hollow MoO_3 microspheres and their applications in lithium storage and gas-sensing, Mater. Res. Bull. 48 (2013) 2289-2295.

[246] A.P Varghese, B. Gangaja, S. Nair, D. Santhanagopalan, New Li-ion battery full-cells: MoO_3 nanobelts as high energy density electrode, Mater. Res. Express 6 (2019) 075003.

[247] T.A. Kerr, F. Leroux, L.F. Nazar, Surfactant-mediated incorporation of poly(*p*-phenylene) into MoO_3, Chem. Mater. 10 (1998) 2588-2591.

[248] Y. Sun, J. Wang, B. Zhao, R. Cai, R. Ran, Z. Shao, Binder-free α-MoO_3 nanobelt electrode for lithium-ion batteries utilizing van der Waals forces for film formation and connection with current collector. J. Mater. Chem. A 1 (2013) 4736–4746.

[249] Y.N. Ko, S.B. Park, K.Y. Jung, Y.C. Kang, One-pot facile synthesis of ant-cave-structured metal oxide-carbon microballs by continuous process for use as anode materials in Li-ion batteries, Nano Lett. 13 (2013) 5462-5466.

[250] Q.-D. Yang, H.-T. Xue, X.-Yang, Z. Guan, Y. Cheng, S.-W. Tsang, C.-S. Lee, Low temperature sonochemical synthesis of morphology variable MoO_3 nanostructures for performance enhanced lithium ion battery applications, Electrochim. Acta 185 (2015) 83-89.

[251] S.-H. Lee, R. Deshpande, D. Benhammou, P.A. Parilla, A.H. Mahan, A.C. Dillon, Metal oxide nanoparticles for advanced energy applications, Thin Solid Films 517 (2009) 3591-3595.

[252] T. Tao, A.M. Glushenkov, C. Zhang, H. Zhang, D. Zhou, Z. Guo, H.K. Liu, Q. Chen, H. Hu, Y. Chen, MoO_3 nanoparticles dispersed uniformly in carbon matrix: A high capacity composite anode for Li-ion batteries, J. Mater. Chem. 21 (2011) 9350-9355.

[253] C.-L. Liu, Y. Wang, C. Zhang, X.-S. Li, W.-S. Dong, In situ synthesis of α-MoO_3/graphene composites as anode materials for lithium ion batteries, Mater. Chem. Phys. 143 (2014) 1111-1118.

[254] L. Noerochim, J.Z. Wang, D. Wexler, Z. Chao, H.K. Liu, Rapid synthesis of free-standing MoO_3/graphene films by the microwave hydrothermal method as cathode for bendable lithium batteries, J. Power Sources 228 (2013) 198-205.

[255] C.L. Liu, Y. Wang, C. Zhang, X.S. Li, W.S. Dong, In situ synthesis of α-MoO_3/graphene composites as anode materials for lithium ion battery, Mater. Chem. Phys. 143 (2014) 1111-1118.

[256] K. Zhou, W. Zhou, X. Liu, Y. Sang, S. Ji, W. Li, J. Lu, L. Li, W. Niu, H. Liu, S. Chen, Ultrathin MoO_3 nanocrystals self-assembled on graphene nanosheets via oxygen bonding as supercapacitor electrodes of high capacitance and long cycle life, Nano Energy 12 (2015) 510-520.

[257] Y. Cui, Y. Zhao, H. Chen, K. Wei, S. Ni, Y. Cui, S. Shi, First-principles study of MoO_3/graphene composite as cathode material for high-performance lithium-ion batteries, Appl. Surf. Sci. 433 (2018) 1083-1093.

[258] X. Cao, B. Zheng, W. Shi, J. Yang, Z. Fan, Z. Luo, X. Rui, B. Chen, Q. Yan, H. Zhang, Reduced graphene oxide-wrapped MoO_3 composites prepared by using metal–organic frameworks as precursor for all-solid-state flexible supercapacitors, Adv. Mater. 27 (2015) 4695-4701.

[259] X. Zhang, C. Fu, J. Li, C. Yao, T. Lu, L. Pan, MoO_3/reduced graphene oxide composites as anode material for sodium ion batteries, Ceram. Int. 43 (2017) 3769-3773.

[260] G. Krishnamurthy, G. Veeresha, A facile one pot synthesis of MoO_3 on reduced graphene oxide (RGO) and electrochemical studies for energy applications, Mater. Res. Express 6 (2019) 094013.

[261] D. Stamatis, E.L. Dreizin, K. Higa, Thermal initiation of Al-MoO_3 nanocomposite materials prepared by different methods, J. Propulsion Power. 27 (2011)1079-1087.

[262] H. Sinaim, A. Phuruangrat, S. Thongtem, T. Thongtem, Synthesis and characterization of heteronanostructured Ag nanoparticles/MoO_3 nanobelts composites, Mater. Chem. Phys. 132 (2012) 358-363.

[263] Y. Zhang, B. Lin, J. Wang, P. Han, T. Xu, Y. Sun, X. Zhang, H. Yang, Polyoxometalates@ metal-organic frameworks derived porous MoO_3@ CuO as electrodes for symmetric all-solid-state supercapacitor, Electrochim. Acta 191 (2016) 795-804.

[264] O. Sachuk, N. Kopachevska, L. Kuznetsova, V. Zazhigalov, V. Starchevskyy. Influence of ultrasonic treatment on the properties of ZnO-MoO_3 oxide system, Chem. Chem. Technol. 11 (2017) 152-157.

[265] A. Martinez-Garcia, A. Kumar Thapa, R. Dharmadasa, T.Q. Nguyen, J. Jasinski, T.L. Druffel, M.K Sunkara, High rate and durable, binder free anode based on silicon loaded MoO_3 nanoplatelets, Sci. Rep. 5 (2015) 10530.

[266] Z. Yuan, L. Si, D. Wei, L. Hu, Y. Zhu, X. Li, Y. Qian, Vacuum topotactic conversion route to mesoporous orthorhombic MoO_3 nanowire bundles with enhanced electrochemical performance. J. Phys. Chem. C 118 (2014) 5091–5101.

[267] P.-J. Lu, M. Lei, J. Liu, Graphene nanosheets encapsulated α-MoO_3 nanoribbons with ultrahigh lithium ion storage properties, CrystEngComm 16 (2014) 6745-6755.

[268] J. Ni, G. Wang, J. Yang, D. Gao, J. Chen, L. Gao, Y. Li, Carbon nanotube-wired and oxygen-deficient MoO_3 nanobelts with enhanced lithium-storage capability, J. Power Sources 247 (2014) 90-94.

[269] C. Yang, H. Lu, C. Li, L. Wang, H. Wang, Spatially-confined electrochemical reactions of MoO_3 nanobelts for reversible high capacity: critical roles of glucose, Chem. Eng. J. 337 (2018) 1–9.

[270] D. Cao, Y. Dai, S. Xie, H. Wang, C. Niu, Pyrolytic synthesis of MoO_3 nanoplates within foam-like carbon nanoflakes for enhanced lithium ion storage. J. Colloid Interface Sci. 514 (2018) 686–693.

[271] F. Ma, A. Yuan, J. Xu, P. Hu, Porous α-MoO_3/MWCNT nanocomposite synthesized via a surfactant-assisted solvothermal route as a lithium-ion-battery high-capacity anode material with excellent rate capability and cyclability. ACS Appl. Mater. Interfaces 7 (2015) 15531–15541.

[272] H. Sun, D. Hanlon, D.A. Dinh, J.B. Boland, A.E. Del Rio Castillo, C. Di Giovanni, A. Ansaldo, V. Pellegrini, J.N. Coleman, F. Bonaccorso, Carbon nanotubes-bridged molybdenum trioxide nanosheets as high performance anode for lithium ion batteries, 2D Mater. 5 (2018) 015024.

[273] J. Wu, Q. Lai, C. Zhong, Hydrothermal synthesis MoO_3@$CoMoO_4$ hybrid as an anode material for high performance lithium rechargeable batteries, Funct. Mater. Lett. 12 (2019) 1850104.

[274] C. Yang, X. Zhong, Y. Jiang, Y. Yu, Reduced graphene oxide wrapped hollow molybdenum trioxide nanorod for high performance lithium-ion batteries, Chinese Chem. Lett. 28 (2017) 2231-2234.

[275] S.R Sahu, V.R. Rikka, P. Haridoss, A. Chatterjee, R. Gopalan, R. Prakash, A Novel α-MoO_3/single-walled carbon nanohorns composite as high-performance anode material for fast-charging lithium-ion battery, Adv. Energy Mater. 10 (2020) 2001627.

[276] Y. Feng, K. Wu, J. Ke, Z. Guo, X. Deng, C. Bai, Y. Sun, Q. Wang, B. Yang, H. Dong, D. Xiong, M. He, Synthesis of ternary SnO_2–MoO_3–C composite with nanosheet structure as high-capacity, high-rate and long-lifetime anode for lithium-ion batteries, Ceram. Int. (2020) doi.org/10.1016/j.ceramint.2020.12.057.

[277] S. Zhao, Z. Zha, X. Liu, H. Tian, Z. Wu, W. Li, L.-B. Sun, B. Liu, Z. Chen, Core–sheath structured MoO_3@MoS_2 composite for high-performance lithium-ion battery anodes, Energy Fuels 34 (2020) 11498-11507.

[278] Y. Teng, H. Liu, D. Liu, Y. Chen, A hierarchically nanostructured composite of MoO_3-NiO/graphene for high-performance lithium-ion batteries, J. Electrochem. En. Conv. Stor. 18 (2021) 031003.

[279] S.H. Oh, S.M. Park, D.W. Kang, Y.C. Kang, J.S. Cho, Fibrous network of highly integrated carbon nanotubes/MoO_3 composite bundles anchored with MoO_3 nanoplates for superior lithium ion battery, J. Ind. Eng. Chem. 83 (2020) 438-448.

[280] Z. Zhang, X. Chen, G. Zhang, C. Feng, Synthesis of MoO_3/V_2O_5/C composite as novel anode for Li-ion battery application, J. Nanosci. Nanotechnol. 20 (2020) 2911-2916.

[281] G. Wang, J. Ni, H. Wang, L. Gao, High-performance CNT-wired MoO_3 nanobelts for Li-storage application. J. Mater. Chem. A 1 (2013) 4112-4118.

[282] J.S. Cho, Large scale process for low crystalline MoO_3-carbon composite microspheres prepared by one-step spray pyrolysis for anodes in lithium-ion batteries, Nanomaterials 9 (2019) 539.

[283] S.H. Choi, Y.C. Kang, Crumpled graphene–molybdenum oxide composite powders: Preparation and application in lithium-ion batteries. ChemSusChem 7 (2014) 523–528.

[284] A. Kumar Mondal, S. Chen, D. Su, H. Liu, G. Wang, Fabrication and enhanced electrochemical performances of MoO_3/graphene composite as anode material for lithium-ion batteries, Int. J. Smart Grid Clean Energy 3 (2014) 142-148.

[285] A. Wold, W. Kunnmann, R.J. Arnott, A. Ferretti, Preparation and properties of sodium and potassium molybdenum bronze crystals, Inorg. Chem. 3 (1964) 545-547.

[286] W. Xia, F. Xu, C. Zhu, H.L. Xin, Q. Xu, P. Sun, L. Sun, Probing microstructure and phase evolution of α-MoO_3 nanobelts for sodium-ion batteries by in situ transmission electron microscopy. Nano Energy 27 (2016) 447–456.

[287] M.B. Sreedhara, A.L. Santhosha, A.J. Bhattacharyya, C.N.R. Rao, Composite of few-layer MoO_3 nanosheets with graphene as a high performance anode for sodium-ion batteries, J. Mater. Chem. A 4 (2016) 9466-9471.

[288] Y. Jiang, M. Sun, Ni J, L. Li, Ultrastable sodium storage in MoO_3 nanotube arrays enabled by surface phosphorylation. ACS Appl. Mater. Interfaces 11 (2019) 37761–37767.

[289] Y. Liu, B. Zhang, S. Xiao, L. Liu, Z. Wen, Y. Wu, A nanocomposite of MoO_3 coated with PPy as an anode material for aqueous sodium rechargeable batteries with excellent electrochemical performance. Electrochim Acta 116 (2014) 512–517.

[290] Y. Li, D. Wang, Q. An, B. Ren, Y. Rong, Y. Yao, Flexible electrode for long-life rechargeable sodium-ion batteries: effect of oxygen vacancy in MoO_{3-x}. J Mater Chem A 4 (2016) 5402–5405.

[291] Y. Xu, M. Zhou, X. Wang, C. Wang, L. Liang, F. Grote, M. Wu, Y. Mi, Y. Lei, Enhancement of sodium ion battery performance enabled by oxygen vacancies, Angew. Chem. Int. Ed. 54 (2015) 8768–8771.

[292] S. Li, H. Hou, Z. Huang, H. Liao, X. Qiu, X. Ji, Alternating voltage introduced [001]-oriented α-MoO_3 microrods for high-performance sodium-ion batteries. Electrochim. Acta 245 (2017) 949–956.

[293] K. Zhu, X. Wang, J. Liu,S. Li, H. Wang, L. Yang, S. Liu, T. Xie, Novel amorphous MoS_2/MoO_3/nitrogen-doped carbon composite with excellent electrochemical performance for lithium ion batteries and sodium ion batteries, ACS Sustainable Chem. Eng. 5 (2017) 8025-8034.

[294] K. Wu, J. Zhan, G. Xu, C. Zhang, D. Pan, M. Wu, MoO_3 nanosheet arrays as superior anode materials for Li- and Na-ion batteries. Nanoscale 10 (2018) 16040–16049.

[295] V. Gangaraju, D. Bhargavi, D. Rangappa, Synthesis and characterization of α-MoO_3/RGO composite as anode material for Li-ion batteries using spray drying combustion, Mater. Today Proc. 4 (2017) 12328-12332.

[296] W. Kang, Y. Wang, D. Cao, Z. Kang, D. Sun, In-situ transformation into $MoSe_2$/MoO_3 heterogeneous nanostructures with enhanced electrochemical performance as anode material for sodium ion battery, J. Alloys Compd. 743 (2018) 410-418.

[297] C.J. Machiels, W.H. Cheng, U. Chowdhry, W.E. Farneth, F. Hong, E.M. McCarron, A.W. Sleight, The effect of the structure of molybdenum oxides on the selective oxidation of methanol, Appl. Catal. 25 (1986) 249−256.

[298] T.T. Phuong Pham, P.H. Duy Nguyen, T. Tai Vo, H.H. Phuc Nguyen, C. Loc Luu Facile method for synthesis of nanosized β-MoO_3 and their catalytic behavior for selective oxidation of methanol to formaldehyde, Adv. Nat. Sci. Nanosci. Nanotechnol. 6 (2015) 045010.

[299] D. D. Yao, J.Z. Ou, K. Latham, S. Zhuiykov, A. P. O'Mullane, K. Kalantar-zadeh, Electrodeposited α- and ß-phase MoO_3 films and investigation of their gasochromic properties, Cryst. Growth Des. 12 (2012) 1865−1870.

[300] I. Juarez-Ramirez, A. Martinez-de-la-Cruz, Electrochemical lithium insertion in β-MoO_3: Novel Li_xMoO_3 bronzes, J. Solid State Electrochem. 7 (2003) 259-263.

[301] T. Mizushima, K. Fukushima, H. Ohkita, N. Kakuta, Synthesis of β-MoO_3 through evaporation of HNO_3-added molybdic acid solution and its catalytic performance in partial oxidation of methanol, Appl. Catal. A. 326 (2007) 106–112.

[302] T.M. Huong, N.H.H. Phuc, H. Ohkita, T. Mizushima, N. Kakuta, Selective preparation of β-MoO_3 and silicomolybdic acid(SMA) on MCM-41 from molybdic acid precursor and their partial oxidation performances, Stud. Surf. Sci. Catal. 175 (2010) 695–698.

[303] P.F. Carcia, E.M. McCarron III, Synthesis and properties of thin film polymorphs of molybdenum trioxide, Thin Solid Films 155 (1987) 53−63.

[304] C.N.R. Rao, J. Gopalakrishnan, K. Vidyasagar, A.K. Ganguli, A. Ramanam, L. Ganapathi, Novel metal oxides prepared by ingenious synthetic routes, J. Mater. Res. 1 (1986) 280-294.

[305] D.E. Diaz-Droguett, R. El-Far, V.M. Fuenzalida, A.L. Cabrera, In situ-Raman studies on thermally induced structural changes of porous MoO_3 prepared in vapor phase under He and H_2, Mater. Chem. Phys. 134 (2012) 631-638.

[306] N.H.H. Phuc, H. Ohkita, T. Mizushima, N. Kakuta, Simple method to prepare new structure of metastable molybdenum (VI) oxide, Mater. Lett. 76 (2012) 173-176.

[307] R. Diehl, G. Brandt, E. Salje, The crystal structure of triclinic WO_3, Acta Cryst. B 34 (1978) 1105-1111.

[308] T. Mizushima, Y. Moriya, N. H. Huy Phuc, H. Ohkita, N. Kakuta, Soft chemical transformation of α-MoO_3 to β-MoO_3 as a catalyst for vapor-phase oxidation of methanol. Catal. Commun. 13 (2011) 10-13.

[309] F. Hard, B. Gérand, G. Nowogrocki, M. Figlarz, Structural filiation between a new hydrate $MoO_3 \cdot 13H_2O$ and a new monoclinic form of MoO_3 obtained by dehydration, Solid State Ion. 32-33 (1989) 84-90.

[310] I. Juárez-Ramírez, A. Martínez-de la Cruz, Synthesis of β-MoO_3 by vacuum drying and its structural and electrochemical characterisation, Mater. Lett. 57 (2003) 1034–1039.

[311] T. Mizushima, K. Fukushima, M.H. Tran, H. Ohkita, N. Kakuta, Synthesis of β-MoO_3 by simple evaporation of molybdic acid solution containing nitric acid, Chem. Lett. 34 (2005) 986–987.

[312] J.B. Parise, E.M. McCarron III, R. Von Dreele, J.A. Goldstone, β-MoO_3 produced from a novel freeze drying route, J. Solid State Chem. 93 (1991) 193-201.

[313] D. Mariotti, H. Lindström, A.C. Bose, K. Ostrikov, Monoclinic *β*-MoO_3 nanosheets produced by atmospheric microplasma: application to lithium-ion batteries, Nanotechnology 19 (2008) 495302.

[314] W.C. Chang, X.D. Qi, J.C. Kuo, S.C. Lee, S.K. Ng, D. Chen, Post-deposition annealing control of phase and texture for the sputtered MoO_3 films, CrystEngComm 13 (2011) 5125−5132.

[315] K. Koike, R. Wada, S. Yagi, Y. Harada, S. Sasa, M. Yano, Characteristics of MoO_3 films grown by molecular beam epitaxy, Jpn. J. Appl. Phys. 53 (2014) 05FJ02.

[316] A. Kuzmin, J. Purans, Dehydration of the molybdenum trioxide hydrates $MoO_3 \cdot nH_2O$: in situ x-ray absorption spectroscopy study at the Mo K edge, J. Phys.: Condens. Matter 12 (2000) 1959-1970.

[317] G. A. Nazri, C. Julien, Heat-treatment studies of molybdenum oxide-monohydrate, Solid State Ion. 80 (1995) 271-275.

[318] McEvoy, T. M.; Stevenson, K. J.; Hupp, J. T.; Dang, X. Electrochemical preparation of molybdenum trioxide thin films: Effect of sintering on electrochromic and electroinsertion properties, Langmuir 19 (2003) 4316−4326.

[319] B. Yebka, C. Julien, G.A. Nazri, Electrochemical features of hydrated molybdenum oxides in lithium batteries, Mater. Res. Soc. Symp. Proc. 548 (1999) 229-237.

[320] K. Yamamoto, R. Shimizu, S. Shiraki, T. Hitosugi, Transparent conducting properties of Re-doped β-MoO_3 films, APL Mater. 4 (2016) 096104.

[321] T.M. McEvoy, K.J. Stevenson, Spatially resolved imaging of inhomogeneous charge transfer behavior in polymorphous molybdenum oxide. II. Correlation of localized coloration/insertion properties using spectroelectrochemical microscopy, Langmuir 21 (2005) 3529-3538.

[322] A. Rosenheim, Die darstellung von molybdänsäuredihydrayt, Z. Anorg. Chem. 50 (1906) 320.

[323] H. Peters, L. Till, K.H. Radeke, Fällungsprodukte beim ansäuern von molybdatlösungen, Z. Anorg. Allg. Chem. 365 (1969) 14-21.

[324] E.M. McCarron III, D.M. Thomas, J.C. Calabrese, Hexagonal molybdates: Crystal structure of $(Na{\cdot}2H_2O)Mo_{5.33}[H_{4.5}]_{0.67}O_{18}$, Inorg. Chem. 26 (1987) 370–373.

[325] N.A. Caiger, S. Crouch-Baker, P.G. Dickens, G.S. James, Preparation and structure of hexagonal molybdenum trioxide, J. Solid State Chem. 67 (1987) 369–673.

[326] V. Kumar, P.S. Lee, Redox active polyaniline-h-MoO_3 hollow nanorods for Improved pseudocapacitive performance. J Phys. Chem. C *119* (2015) 9041-9049.

[327] J.V. Silveira, J.V.B. Moura, C. Luz-Lima, P.T.C. Freire, A.G. Souza Filho, Laser-induced thermal effects in hexagonal MoO_3 nanorods, Vibr. Spectrosc. 98 (2018) 145-151.

[328] C. Zhu, Q. Xu, W. Liu, Y. Ren, CO_2-assisted fabrication of novel heterostructures of h-MoO_3/1T-MoS_2 for enhanced photoelectrocatalytic performance, Appl. Surf. Sci. 425 (2017) 56-62.

[329] X. Wang, W. Cui, M. Chen, Q. Xu, Supercritical CO_2-assisted phase transformation from orthorhombic to hexagonal MoO_3, Mater. Lett. 201 (2017) 129-132.

[330] Y. Song, Y. Zhao, Z. Huang, J. Zhao, Aqueous synthesis of molybdenum trioxide (h-MoO_3, α-$MoO_3{\cdot}H_2O$ and h-/α-MoO_3 composites) and their photochromic properties study, J. Alloys Compd. 693 (2017**)** 1290-1296.

[331] V. Kumar, X. Wang, P.S. Lee, Formation of hexagonal-molybdenum trioxide (h-MoO_3) nanostructures and their pseudocapacitive behavior, Nanoscale *7* (2015) 11777-11786.

[332] L. Zheng, Y. Xu, D. Jin, Y. Xie, Novel metastable hexagonal MoO_3 nanobelts: Synthesis, photochromic, and electrochromic properties. Chem. Mater. 21 (2009) 5681–5690.

[333] A. Chithambararaj, N.R. Yogamalar, A.C. Bose, Hydrothermally synthesized h-MoO_3 and α-MoO_3 nanocrystals: New findings on crystal-structure-dependent charge transport. Cryst. Growth Des. 16 (2016) 1984–1995.

[334] H.J. Lunk, H. Hartl, M.A. Hartl, M.J. Fait, I.G. Shenderovich, M. Feist, T.A. Frisk, L.L. Daemen, D. Mauder, A.A. Gurinov, Hexagonal Molybdenum Trioxide—known for 100 years and still a fount of new discoveries. Inorg. Chem. 49 (2010) 9400–9408.

[335] C. V. Ramana, V. V. Atuchin, I. B. Troitskaia, S. A. Gromilov, V. G. Kostrovsky, Low-temperature synthesis of morphology controlled metastable hexagonal molybdenum trioxide (MoO_3). Solid State Commun. 149 (2009) 6–9.

[336] S. Komaba, N. Kumagai, R. Kumagai, N. Kumagai, H. Yashiro, Molybdenum oxides synthesized by hydrothermal treatment of A_2MoO_4 (A=Li, Na, K) and electrochemical lithium intercalation into the oxides, Solid State Ion. 152-153 (2002) 319–326.

[337] J.D. Guo, P. Zavalij, M.S. Whittingham, Metastable hexagonal molybdates: Hydrothermal preparation, structure and reactivity, J. Solid State Chem. 117 (1995) 323–332.

[338] M.K. Patil, S.H. Gaikwad, S.P. Mukherjee Phase- and morphology-controlled synthesis of tunable plasmonic MoO_{3-x} nanomaterials for ultrasensitive surface-enhanced Raman spectroscopy detection, J. Phys. Chem. C 124 (2020) 21082-21093.

[339] C.C. Zhang, L. Zheng, Z.M. Zhang, R.C. Dai1, Z.P. Wang, J. W. Zhang, Z.J. Ding, Raman studies of hexagonal MoO_3 at high pressure, Phys. Status Solidi B 248 (2011) 1119–1122.

[340] J. Guo, P. Zavalij, M.S. Whittingham, Metastable hexagonal molybdates: hydrothermal preparation, structure, and reactivity, J. Solid State Chem. 117 (1995) 323-332.

[341] T.P. Feist, P.K. Davies, Soft chemical synthesis of new compounds with the hexagonal molybdenum oxide structure, Chem. Mater. 3 (1991) 1011-1012.

[342] Y. Muraoka, J.C. Grenier, S. Petit, M. Pouchard, Preparation of hexagonal MoO_3 by "Chimie Douce" reaction with NO_2, Solid State Sci. 1 (2-3) (1999) 133–148.

[343] X. Chen, W. Lei, D. Liu, J. Hao, Q. Cui, G. Zou, Synthesis and characterization of hexagonal and truncated hexagonal shaped MoO_3 nanoplates, J. Phys. Chem. C. 113 (2009) 21582–21585.

[344] R. Irmawati, M. Shafizah, The production of high purity hexagonal MoO_3 through the acid washing of as-prepared solids, Int. J. Basic Appl. Sci. 9 (2009) 241–244.

[345] O. Mougin, J.-L. Dubois, F. Mathieu, A. Rousset, Metastable hexagonal vanadium molybdate study, J. Solid State Chem. 152 (2000) 353-360.

[346] P. Jittiarprn, L. Sikong, K. Kooptarnond, W. Taweepreda, Effects of precipitation temperature on the photochromic properties of h-MoO_3. Ceram Int. 40 (2014) 13487-13495.

[347] Y. Liu, S. Yang, Y. Lu, N.V. Podval'naya, W. Chen, G.S. Zakharova, Hydrothermal synthesis of h-MoO_3 microrods and their gas sensing properties to ethanol, Appl. Surf. Sc. 359 (2015**)** 114-119.

[348] B. Han, K.-H. Lee, Y.-W. Lee, S.-J. Kim, H.-C. Park, B.-M. Hwang, D.-H. Kwak, K.-W. Park, MoO_3 nanostructured electrodes prepared via hydrothermal process for lithium ion batteries, Int. J. Electrochem. Sci. 10 (2015) 4232-4240.

[349] Z. S. Guan, Y. Zhang, Q. Zhang, D. Xu Li, Controllable size, shape and morphology of molybdic acid self-aggregated with rhodamine B to construct functional material, J. Colloid. Interface Sci. 302 (2006) 113-122.

[350] J. Song, X. Wang, X. Ni, H. Zheng, Z. Zhang, M. Ji, T. Shen, X. Wang, Preparation of hexagonal-MoO_3 and electrochemical properties of lithium intercalation into the oxide, Mater. Res. Bull. 40 (2005) 1751–1756.

[351] K. Eda, K. Chin, N. Sotani, M.S. Whittingham, $K_2Mo_4O_{13}$ phases prepared by hydrothermal synthesis. J. Solid State Chem. 177 (2004) 916–921.

[352] Y. Xu, L. Xie, Y. Zhang, X. Cao, Hydrothermal synthesis of hexagonal MoO_3 and its reversible electrochemical behavior as a cathode for Li-ion batteries, Electron. Mater. Lett. 9 (2013) 693-696.

[353] Q. Tang, L. Wang, K. Zhu, Z. Shan, X. Qin, Synthesis and electrochemical properties of h-MoO_3/graphene composite, Mater. Lett. 100 (2013) 127-129.

[354] J. Joseph, A.P. O'Mullane, K. Ostrikov, Hexagonal molybdenum trioxide (h-MoO_3) as an electrode material for rechargeable aqueous aluminum-ion batteries, ChemElectroChem 6 (2019) 6002-6008.

[355] X. Xiao, H. Song, S. Lin, Y. Zhou., X. Zhan., Z. Hu, Q. Zhang, J. Sun, B. Yang, T. Li, L. Jiao, J. Zhou, J. Tang, Y. Gogotsi, Scalable salt-templated synthesis of two-dimensional transition metal oxides, Nat. Commun. 7 (2016) 11296.

[356] J. Zhou, N. Lin, L. Wang, K. Zhang, Y. Zhu, Y. Qian, Synthesis of hexagonal MoO_3 nanorods and a study of their electrochemical performance as anode materials for lithium-ion batteries, J. Mater. Chem. A 3 (2015) 7463-7468.

[357] E. M. McCarron and J. C. Calabrese, The growth and single crystal structure of a high pressure phase of molybdenum trioxide: MoO_3-II, J. Solid State Chem. 91 (1991) 121-125.

[358] S. Åsbrink, L. Kihlborg, E. M. McCarron, High pressure single-crystal X-ray diffraction studies of MoO_3. I. Lattice parameters up to 7·4 GPa, J. Appl. Crystallogr. 21 (1988) 960-962.

[359] A. Stavenhagen, E. Engels, Ueber Molybdänbronzen, Ber. Deut. Chem. Gesell. 28 (1895) 2280-2281.

[360] M. Greenblatt, W.H. McCarroll, R. Neifeld, M. Croft, J.V. Waszczak, Quasi two-dimensional electronic properties of the lithium molybdenum bronze, $Li_{0.9}Mo_6O_{17}$, Solid State Commun. 51 (1984) 671–674.

[361] P.P. Tsai, J.A. Potenza, M. Greenblatt, H.J. Schugar, "Crystal structure of $Li_{0.33}MoO_3$, a stoichiometric, triclinic, lithium molybdenum bronze, J. Solid State Chem. 64 (1986) 47–56.

[362] M. Onoda, K. Toriumi, Y. Matsuda, M. Sato, Crystal structure of lithium molybdenum purple bronze $Li_{0.9}Mo_6O_{17}$, J. Solid State Chem. 66 (1987) 163–170.

[363] M. Greenblatt, Molybdenum oxide bronzes with quasi-low-dimensional properties, Chem. Rev. 88 (1988) 31-53.

[364] W.H. McCarroll, M. Greenblatt, Preparation of lithium molybdenum oxide bronzes by a temperature gradient flux growth technique, J. Solid State Chem. 54 (1984) 282-290.

[365] F.F. Leroux, LF. Nazar, Lithium ion battery containing molybdenum bronze, Canadian Patent CA02,222,494 A1. Assessed on 26 May 1997.

[366] G. Guzman, B. Yebka, J. Livage, C. Julien, Lithium intercalation studies in hydrated molybdenum oxides, Solid State Ion. 86-88 (1996) 407-413.

[367] B. Krebs, The crystal structure of MoO_3,$2H_2O$: a metal aquoxide with both co-ordinated and hydrate water, Chem. Soc. D Chem. Commun. (1970) 50-51.

[368] J.R. Günter, Topotactic dehydration of molybdenum trioxide hydrates, J. Solid State Chem. 5 (1972) 354-359.

[369] H.R. Oswald, J.R. Günter, E. Dubler, Topotactic decomposition and crystal structure of white molybdenum trioxide-monohydrate: prediction of structure by topotaxy, J. Solid State Chem. 13 (1975) 330-338.

[370] R.L. Fellows, M.H. Lloyd, J.F. Knight, H.L. Yakel, X-ray diffraction and thermal analysis of molybdenum(VI) oxide hemihydrate: monoclinic $MoO_3 \cdot ½H_2O$, Inorg. Chem. 22 (1983) 2468-2470.

[371] H. Luo, M. Wei, K. Wei, A new metastable phase of crystallized $MoO_3 \cdot 0.3H_2O$ nanobelts, Mater. Chem. Phys. 113 (2009) 85–90.

[372] M.A. Camacho-López, E. Haro-Poniatowski, L. Lartundo-Rojas, J. Livage, C.M. Julien, Amorphous-crystalline transition studied in hydrated MoO_3, Mater. Sci. Eng. B 135 (2006) 88–94.

[373] K. Du, W. Fu, R. Wei, H. Yang, J. Xu, L. Chang, Q. Yu, G. Zou, Ultrasonic-assisted synthesis of highly dispersed MoO_3 nanospheres using 3-mercaptopropyltrimethoxysilane, Ultrason. Sonochem. 15 (2008) 233-238.

[374] M. Afsharpour, A. Mahjoub and M. M. Amini, Synthesis of molybdenum oxide nanohybrids as efficient catalysts in oxidation of alcohols**.** J. Inorg. Organomet. Polym. Mater. 19 (2009) 298-305.

[375] M.I. Shukoor, H.A. Therese, L. Gorgishvili, G. Glasser, U. Kolb, W. Tremel, From layered molybdic acid to lower-dimensional nanostructures by intercalation of amines under ambient conditions, Chem. Mater. 18 (2006) 2144-2151.

[376] D. Chen, M. Liu, L.Yin, T. Li, Z. Yang, X. Li, B. Fan, H. Wang, R. Zhang, Z. Li, H. Xu, H. Lu, D. Yang, J. Sune, L. Gao, Single-crystalline MoO_3 nanoplates: topochemical synthesis and enhanced ethanol-sensing performance, J. Mater. Chem. 21 (2011) 9332-9342.

[377] B. Yebka, C. Julien, G.A. Nazri, Electrochemical behavior of hydrated molybdenum oxides in lithium batteries, Ionics 5 (1999) 236-243.

[378] A. Martinez-de la Cruz, I. Juárez Ramirez, Electrochemical lithium insertion into amorphous $MoO_3 \cdot 2H_2O$, J. Power Sources 133 (2004) 268–271.

[379] Z. Yuan, L. Si, Reversible lithium-ion insertion in triclinic hydrated molybdenum oxide nanobelts. J. Mater. Chem. A, 2013, 1, 15247-15251.

[380] N. Kumagai, N. Kumagai, K. Tanno, Electrochemical and structural characteristics of molybdenic acid as a new cathode material for nonaqueous lithium batteries. Electrochim. Acta 32 (1987) 1521-1526.

[381] N. Kumagai, S. Komaba, M. Abe, H. Yashiro, Hydrothermal synthesis of molybdenum oxide and lithium intercalation, Electrochem. Soc. Proc. 99-24 (1999) 215-229.

[382] N. Kumagai, S. Komaba, M. Abe, H. Yashiro, Hydrothermal synthesis of mobydenum oxide and lithium intercalation, In: *Intercalation Compounds for Battery Materials*, G.A. Nazri, M. Thackeray, T. Ohzuku (Eds.), Electrochem. Soc. Proc. 99-24 (2000) 215-229. On line at https://books.google.fr/books?hl=fr&lr=&id=Ju5viChENAwC&oi=fnd&pg=PR6&dq=intercalation+compounds+for+battery+materials.

[383] J.P. Pereira-Ramos, N. Kumagai, N. Kumagai, Low temperature molybdenum oxide as host lattice for lithium intercalation, J. Power Sources 56 (1995) 87-90.

[384] T. Sekine, C. Julien, I. Samaras, M. Jouanne, M. Balkanski, Vibrational modifications on lithium intercalation in MoS_2, Mater. Sci. Eng. B 3 (1989) 153-158.

[385] E. Hatzikraniotis, I. Samaras, K.M. Paraskevopoulos, C. Julien, Lithium intercalation studies on MoO_3 single crystals, Ionics 2 (1996) 24-28.

[386] M. Pasquali, G. Pistoia, F. Rodante, Non-stoichiometric molybdenum oxides as cathodes for lithium cells. part v. thermodynamic, kinetic and structural aspects of the behaviour of Mo_8O_{23} and $Mo_{18}O_{52}$, Solid State Ion. 6 (1982) 319-325.

[387] L.A. Bursill, Crystallographic shear in molybdenum trioxide, Proc. Math. Phys. Eng. Sci. 311 (1969) 267–290.

[388] M. Yu, H. Shao, G. Wang, F. Yang, C. Liang, P. Rozier, C.-Z. Wang, X. Lu, P. Simon, X. Feng, Interlayer gap widened α-phase molybdenum trioxide as high-rate anodes for dual-ion intercalation energy storage devices, Nat. Commun. 11 (2020) 1348.

[389] T. Li, M. Beidaghi, X. Xiao, L. Huang, Z. Hu, W. Sun, X. Chen, Y. Gogotsi, J. Zhou, Ethanol reduced molybdenum trioxide for Li-ion capacitors, Nano Energy, 26 (2016) 100-107.

[390] J.-P. Jegal, H.K. Kim, J.-S. Kim, K.-B. Kim, One-pot synthesis of mixed-valence MoO_x on carbon nanotube as an anode material for lithium ion batteries, J. Electroceram. 31 (2013) 218-223.

[391] B. Saravanakumar, R. Shobana, G. Ravi, V. Ganesh, R. Yuvakkumar, Preparation and electrochemical characterization of Mo_9O_{26} nanopowders for supercapacitors applications, Nano-Struct. Nano-Objects 19 (2019) 100340.

[392] S.S. Sunu, E. Prabhu, V. Jayaraman, K.I. Gnanasekar, T. Gnanasekaran, Gas sensing properties of PLD made MoO_3 film, Sens. Actuators B 94 (2003) 189–196.

[393] H. Simchi, B.E. McCandless, T. Meng, J.H. Boyle, W.N. Shafarman, Characterization of reactively sputtered molybdenum oxide films for solar cell application, J. Appl. Phys. 114 (2013) 13503.

[394] J. Bullock, A. Cuevas, T. Allen, C. Battaglia, Molybdenum oxide MoO_x: A versatile hole contact for silicon solar cells, Appl. Phys. Lett. 105 (2014) 232109.

[395] J.J. Jacieniak, J. Seifter, J. Jo, T. Mates, A.J. Heegeer, A solution-processed MoO_x anode interlayer for use within organic photovoltaic devices, Adv. Funct. Mater. 22 (2012) 2594–2605.

[396] K.A. Gesheva, T.M. Ivanova, G.K. Bodurov, APCVD transition metal oxides—Functional layers in smart windows, J. Phys. Conf. Ser. 559 (2014) 012002.

[397] M. Vasilopoulou, L.C. Palilis, D.G. Georgiadou, S. Kennou, I. Kostis, D. Davazoglou, P. Argitis, Barrierless hole injection through sub-bandgap occupied states in organic light emitting diodes using substoichiometric MoO_x anode interfacial layer, Appl. Phys. Lett. 110 (2012) 013311.

[398] K. Inzani, T. Grande, F. Vullum-Bruer, S.M. Selbach, A van der Waals density functional study of MoO_3 and its oxygen vacancies, J. Phys. Chem. C 120 (2016) 8959–8968.

[399] H.A. Tahini, X. Tan, S.N. Lou, J. Scott, R. Amal, Y.H. Ng, S.C. Smith, Mobile polaronic states in α-MoO_3: An ab initio investigation of the role of oxygen vacancies and alkali ions, ACS Appl. Mater. Interfaces 8 (2016) 10911–10917.

[400] K. Inzani, M. Nematollahi, F. Vullum-Bruer, T. Grande, T.W. Reenaasb, S.M. Selbach, Electronic properties of reduced molybdenum oxides, Phys. Chem. Chem. Phys. 19 (2017) 9232–9245.

[401] X.K. Hu, Y.T. Qian, Z.T. Song, J.R. Huang, R. Cao, J.Q. Xiao, Comparative study on MoO_3 and H_xMoO_3 nanobelts: structure and electric transport, Chem. Mater. 20 (2008) 1527-1733.

[402] M. Mattinen, P.J. King, L. Khriachtchev, M.J. Heikkilä, B. Fleming, S. Rushworth, K. Mizohata, K. Meinander, J. Räisänen, M. Ritala, M. Leskelä, Atomic layer deposition of crystalline molybdenum oxide thin films and phase control by post-deposition annealing, Mater. Today Chem. 9 (2018) 17–27.

[403] D.O. Scanlon, G.W. Watson, D.J. Payne, G.R. Atkinson, R.G. Egdell, D.S.L. Law, Theoretical and experimental study of the electronic structures of MoO_3 and MoO_2, J. Phys. Chem. C 114 (2010) 4636–4645.

[404] T. Zhang, C.-Y. Lee, B. Gong, B. Hoex, Thermal stability analysis of WO_x and MoO_x as hole selective contacts for Si solar cells using in situ XPS, AIP Conf. Proc. 1999 (2018) 040027.

[405] C.D. Wagner, W.M. Riggs. L.E. Davis, J.F. Moulder, G.E. Muilenberg, Handbook of X-ray Photoelectron Spectroscopy, Physical Electronics Division, Perkin-Elmer, Eden Prairie, Minnesota, 1979.

[406] Z. Li, Ch. Wang, X. Chen, X. Wang, X. Li, Y. Yamauchi, X. Xu, J. Wang, C. Lin, D. Luo, X. Wang, X.S. Zhao, MoO_x nanoparticles anchored on N-doped porous carbon as Li-ion battery electrode, Chem. Eng. J. 381 (2020) 122588.

[407] R. Zeng, H. Liu, W. Shen, A facile and controllable electrochemically fabricated nonstoichiometric MoO_x film for novel opto-electronic devices, J. Micromech. Microeng. 29 (2019) 065012.

[408] J. Yang, X. Xiao, P.Chen, Kai Zhua , Kui Chenga , K. Ye, G. Wang, D. Cao, J. Yan, Creating oxygen-vacancies in MoO_{3-x} nanobelts toward high volumetric energy-density asymmetric supercapacitors with long lifespan, Nano Energy 58 (2019) 455-465.

[409] T. Ressler, O. Timpe, T. Neisius, J. Find, G. Mestl, M. Dieterle, R. Schlögl, Time-resolved XAS investigation of the reduction/oxidation of $MoO_{3–x}$, J. Catal. 191 (2000) 75-85.

[410] Y. Hou, J. Wang, C. Hou, Y. Fan, Y. Zhai, H. Li, F. Dang, S. Chou, Oxygen vacancies promoting the electrocatalytic performance of CeO_2 nanorods as cathode materials for Li–O_2 batteries, J. Mater. Chem. A 7 (2019) 6552–6561.

[411] S. Sun, Q. Xia, J. Liu, J. Xu, F. Zan, J. Yue, S. V. Savilov, V.V. Lunin, H. Xia, Self-standing oxygen-deficient α-MoO_{3-x} nanoflake arrays as 3D cathode for advanced all-solid-state thin film lithium batteries, J. Materiomics 5 (2019) 229-236.

[412] Z.Z. Sun, C.H. Yang, G.Y. Liu, H.B. Lu, R. Zhang, L.J. Wang, H. Wang, Largely enhanced electrochemical performance in MoO_{3-x} nanobelts formed by a "sauna reaction": importance of oxygen vacancies, Electrochim. Acta 239 (2017) 16−24.

[413] G. Zhang, T. Xiong, M. Yan, L. He, X. Liao, C. He, C. Yin, H. Zhang, L. Mai, α-MoO_{3-x} by plasma etching with improved capacity and stabilized structure for lithium storage. Nano Energy 49 (2018) 555–563.

[414] Y. Yi, H. An, P. Zhang, X. Tian, P. Yang, P. Liu, T. Wang, L. Qu, M. Li, G. Yang, B. Yang, Oxygen deficiency driven conversion of polysulfide by electrocatalysis: MoO_{3-x} nanobelts for an improved lithium-sulfur battery cathode, ChemNanoMat 5 (2019) 926 – 931.

[415] Q.-L. Wu, S.-X. Zhao, L. Yu, L.-Q. Yu, X.-X. Zheng, G. Wei, In situ synthesis and electrochemical performance of MoO_{3-x} nanobelts as anode materials for lithium-ion batteries, Dalton Trans. 48 (2019) 12832-12838.

[416] U. Akin, H. Safal, Thickness dependence of dispersion parameters of the MoO_x thin films prepared using the vacuum evaporation technique, J. Alloys Compd. 647 (2015) 146-151.

[417] L. Meng, A. Yamada, Low-resistance orthorhombic MoO_{3-x} thin film derived by two-step annealing, Thin solid Films 665 (2018) 179-183.

[418] P.K. Parashar, V.K. Komarala, Sputter deposited sub-stochiometric MoO_x thin film as hole-selective contact layer for silicon based heterojunction devices, Thin Solid Films 682 (2019) 76-81.

[419] F. He, X. Yin, J. Li, S. Lin, L. Wu, X. Hao, J. Zhang, L. Feng, Characterization of sputtered MoO_x thin films with different oxygen content and their application as back contact in CdTe solar cells, Vacuum 176 (2020) 109337.

[420] M.A. Camacho-Lopez, L. Escobar-Alarcon, E. Haro-Poniatowski, Structural transformations in MoO_x thin films grown by pulsed laser deposition, Appl. Phys. A 78 (2004) 59–65.

[421] V. Bhosle, A. Tiwari, J. Narayan, Epitaxial growth and properties of MoO_x ($2<x<2.75$) films, J. Appl. Phys. 97 (2005) 083539.

[422] X. Zhang, F. You, Q. Zheng, Z. Zhang, P. Cai, X. Xue, J. Xiong, J. Zhang, Solution-processed MoO_x hole injection layer towards efficient organic light-emitting diode, Org. Electron. 39 (2016) 43–49.

[423] M. Kröger, S. Hamwi, J. Meyer, T. Riedl, W. Kowalsky, A. Kahn, Role of the deep-lying electronic states of MoO_3 in the enhancement of hole injection in organic thin films, Appl. Phys. Lett. 95 (2009) 95, 123301.

[424] W. Chen, H. Zhang, Y. Wang, Z. Ma, Z. Li, In-situ microstructural investigations by electron-beam irradiation induced crystallization of amorphous MoO_x thin films with high performance for Li-ion storage, Electrochim. Acta 144 (2014) 369–375.

[425] H. Guyot, C. Schlenker, J.P. Pougetf, R. Ayroles, C. Roucau, Evidence for an incommensurate charge density wave instability in h-Mo_4O_{11}, J. Phys. C Solid State Phys. 18 (1985) 4427-4434.

[426] J.Z. Ke, M. Yang, H.K. Zuo, H.P. Zhu, C.B. Liu, R. Chen, C. Dong, W.X. Liu, M.Y. Shi, J.F. Wang, Single crystal growth and electrical transport properties of η-Mo_4O_{11}, J. Alloys Compd. 835 (2020) 155417.

[427] S. Barber, J. Booth, D.R. Pyke, R. Reid, R.J.D. Tilley, The influence of crystallographic shear planes on the behavior of molybdenum-tungsten oxide catalysts for the selective oxidation of propene, J. Catal. 77 (1982) 180-191.

[428] L. Kihlborg, Least squares refinement of the structure of Mo_8O_{23}, Ark. Kemi 21 (1963) 461-469.

[429] R. Knorr, U. Müller, η-Mo_4O_{11} und $Mg_2Mo_3O_8$: eine neue synthese und verfeinerung ihrer kristallstrukturen, Z. Anorg. Allg. Chem. 621 (1995) 541−545.

[430] L. Kihlborg, Crystal structure studies on monoclinic and orthorhombic Mo_4O_{11}, Arkiv Kemi 21 (1963) 365−377.

[431] L. Kihlborg, Stabilization of the tunnel structure of Mo_5O_{14} by partial atom substitution, Acta Chem. Scand. 23 (1969) 1834−1835.

[432] R. L. Smith and G. S. Rohrer, Scanning probe microscopy of cleaved molybdates: α-MoO_3(010), $Mo_{18}O_{52}$(100), Mo_8O_{23}(010), and η-Mo_4O_{11}(100), J. Solid State Chem. 124 (1996) 104–115.

[433] M. Dieterle, G. Mestl, Raman spectroscopy of molybdenum oxides. Part II. Resonance Raman spectroscopic characterization of the molybdenum oxides Mo_4O_{11} and MoO_2, Phys. Chem. Chem. Phys. 4 (2002) 822–826.

[434] A. Magnéli, The crystal structure of Mo_4O_{11} (γ-molybdenum oxide), Acta Chem. Scand. 2 (1948) 861–871.

[435] L.A. Bursill, Electron microscope study of a homologous series of shear structures based on molybdenum trioxide, Acta Crystallogr. A 28 (1972) 187–191.

[436] P. Cignini, M. Icovi, S. Panero, G. Pistoia, C. Temperoni, Non-stoichiometric molybdenum oxides as cathodes for lithium cells. Part. I. Primary batteries, J. Electroanal. Chem. 102 (1979) 333–341.

[437] M. Icovi, S. Panero, A. D'Agate, G. Pistoia, C. Temperoni, Non-stoichiometric molybdenum oxides as cathodes for lithium cells. Part. II. Secondary batteries, J. Electroanal. Chem. 102 (1979) 343–349.

[438] G. Pistoia, C. Temperoni, P. Cignini, M. Icovi, S. Panero, Non-stoichiometric molybdenum oxides as cathodes for lithium cells. Part. III. Cells based on $Mo_{18}O_{52}$, J. Electroanal. Chem. 108 (1980) 169–180.

[439] P. Fiordiponti, G. Pistoia, C. Temperoni, M. Icovi, S. Panero, Non-stoichiometric molybdenum oxides as cathodes for lithium cells. Part. IV. Factors influencing the performance of Li/Mo_8O_{23} batteries, J. Electroanal. Chem. 108 (1980) 181–190.

[440] P.A. Christian, J.N. Carides, F.J. DiSalvo, J. V. Waszczak, Molybdenum oxide cathodes in secondary lithium cells, J. Electrochem. Soc. 127 (1980) 2315–2319.

[441] M. Ghedira, H. Vincent, M. Marezio, J. Marcus, G. Furcaudot, Structure crystalline du conducteur metallique bidimensionnel Mo_4O_{11}-γ, J. Solid State Chem. 56 (1985) 66-73.

[442] H. Gruber, H. Haselmair, H.P. Fritzer, On magnetic properties of some molybdenum oxides, J. Solid State Chem. 47 (1983) 84-91.

[443] H.-K. Fun, P. Yang, M. Sasaki, M. Inoue, H. Kadomatsu, Rietveld refinement of the crystal structure of γ-Mo_4O_{11}, Powder Diffraction 14 (1999) 284-288.

[444] C. Julien, B. Yebka, Electrochemical features of lithium batteries based on molybdenum-oxide compounds, in: Materials for Lithium Batteries; C. Julien, Z. Stoynov (Eds.), Kluwer Acad. Publ., Dordecht, The Netherlands (2000) pp. 263–277.

[445] E. Shembel, R. Apostolova, V. Nagirny, I. Kirsanova, Ph. Grebenkin, P. Lytvyn, Electrolytic molybdenum oxides in lithium batteries, J. Solid State Electrochem. 9 (2005) 96–105.

[446] A.M. Hashem, S.M. Abbas, A.E. Abdel-Ghany, A.E. Eid, A.A. Abdel-Khalek, S. Indris, H. Ehrenberg, A. Mauger, C.M. Julien, Blend formed by oxygen deficient $MoO_{3-\delta}$ oxides as lithium-insertion compounds, J. Alloys Compd. 686 (2016) 744-752.

[447] L. Zhou, N. Ding, J. Yang, L. Yang, Y. Zong, Z. Liu, A. Yu, Sulfur encapsulated in Mo_4O_{11}-anchored ultralight graphene for high-energy lithium sulfur batteries, ACS Sustainable Chem. Eng. 4 (2016) 3679−3687.

[448] V.P. Tysyachny, E.M. Shembel, R.D. Apostolova, V.M. Nagirny, K.E. Kylyvnyk, N.I. Eskova, Studies of the lithium ion transport properties in electrolytic molybdenum oxides, Solid state Ion. 169 (2004) 125-137.

[449] T. Ressler, J. Wienold, R. E. Jentoft, T. Neisius, Bulk structural investigation of the reduction of MoO_3 with propene and the oxidation of MoO_2 with oxygen, J. Catal. 210 (2002) 67-83.

[450] F. Kaiser, M. Schmidt, Y. Grin, I. Veremchuk, Molybdenum oxides MoO_x: spark-plasma synthesis and thermoelectric properties at elevated temperature, Chem. Mater. 32 (2020) 2025-2035.

[451] M. Hugues, N.A. Hampson, S.A.G.R. Karunathilaka, A review of cells based on lithium negative electrodes (anodes), J. Power sources 12 (1984) 83-144.

[452] B.G. Brandt, A.C. Skapski, A refinement of the crystal structure of molybdedum dioxide, Acta Chem. Scand. 21 (1967) 661-672.

[453] D.B. Rogers, R.D. Shannon, A.W. Sleight, J.L. Gillson, Crystal chemistry of metal dioxides with rutile-related structures, Inorg. Chem. 8 (1969) 841-849.

[454] E.Y. Ahn, Y.-S. Seo, J.H. Cho, I. Lee, J. Hwang, H. Jeen, Epitaxial growth and metallicity of rutile MoO_2 thin film, RSC Adv. 6 (2016) 60704–60708.

[455] Y. Shi, B. Guo, S.A. Corr, Q. Shi, Y.-S. Hu, K.R. Heier, L. Chen, R. Seshadri, G.D. Stucky, Ordered mesoporous metallic MoO_2 materials with highly reversible lithium storage capacity, Nano Lett. 9 (2009) 4215–4220.

[456] U.K. Sen, A. Shaligram, S. Mitra, Intercalation anode material for lithium ion battery based on molybdenum dioxide, ACS Appl. Mater. Interfaces 6 (2014) 14311–14319.

[457] J.R. Dahn, W. McKinnon, Structure and electrochemistry of Li_xMoO_2, Solid State Ion. 23 (1987) 1-7.

[458] D. Murphy, F. DiSalvo, J. Carides, J. Waszczak, Topochemical reactions of rutile related structures with lithium, Mater. Res. Bull. 13 (1978) 1395-1402.

[459] J.J. Auborn, Y.L. Barberio, Lithium intercalation cells without metallic lithium: $MoO_2/LiCoO_2$ and $WO_2/LiCoO_2$. J. Electrochem. Soc. 134 (1987) 638-640.

[460] H.-J. Zhang, T.-H. Wu, K.-X. Wang, X.Y. Wu, X.-T. Chen, Y.-M. Jiang, X. Wei, J.S. Chen, Uniform hierarchical MoO_2/carbon spheres with high cycling performance for lithium ion batteries, J. Mater. Chem. A 1 (2013) 12038-12043.

[461] H.J. Zhang, K.X. Wang, X.Y. Wu, Y.M. Jiang, Y.B. Zhai, C. Wang, X. Wei, J.S. Chen, MoO_2/Mo_2C heteronanotubes function as high-performance Li-ion battery electrode, Adv. Funct. Mater. 24 (2014) 3399-3404.

[462] L. Zhou, H.B. Wu, Z. Wang, X.W. Lou, Interconnected MoO_2 nanocrystals with carbon nanocoating as high-capacity anode materials for lithium-ion batteries, ACS Appl. Mater. Interfaces 3 (2011) 4853-4857.

[463] A. Kim, E. Park, H. Lee, H. Kim, Highly reversible insertion of lithium into MoO_2 as an anode material for lithium ion battery, J. Alloys Compd. 681 (2016) 301-306.

[464] A. Manthiram, C. Tsang, Synthesis of amorphous $MoO_{2+\delta}$ and is electrode performance in lithium batteries, J. Electrochem. Soc. 143 (1996) L143-L144.

[465] Y. Sun, X. Lu, W. Luo, Y. Huang, Self-assembled hierarchical MoO_2/graphene nanoarchitectures and their application as a high-performance anode material for lithium-ion batteries, ACS Nano 5 (2011) 7100-7107.

[466] J.H. Ku, J.H. Ryu, S.H. Kim, O.H. Han, S.M. Oh, Reversible lithium storage with high mobility at structural defects in amorphous molybdenum dioxide electrode, Adv. Funct. Mater. 22 (2012) 3658-3664.

[467] L. C. Yang, Q. S. Gao, Y. Tang, Y.P. Wu, R. Holze, MoO_2 Synthesized by reduction of MoO_3 with ethanol vapor as an anode material with good rate capability for the lithium ion battery, J. Power Sources 179 (2008) 357−360.

[468] S. Petnikota, K.W. Teo, L. Chen, A. Sim, S.K. Marka, M.V. Reddy, V.V.S.S. Srikanth, S. Adam, B.V.R. Chowdari, Exfoliated graphene oxide/MoO_2 composites as anode materials in lithium-ion batteries: an insight into intercalation of Li and conversion mechanism of MoO_2, ACS Appl. Mater. Interfaces 8 (2016) 10884-10896.

[469] C.A. Ellefson, O. Marin-Flores, S. Ha, M.G. Norton, Synthesis and applications of molybdenum (IV) oxide, L. Mater. Sci. 47 (2012) 2057-2071.

[470] A. Chen, C. Li, R. Tang, Y. Qi, MoO_2–ordered mesoporous carbon hybrids as anode materials with highly improved rate capability and reversible capacity for lithium-ion battery, Phys. Chem. Chem. Phys. 15 (2013) 13601-13610.

[471] L. Zeng, C. Zheng, C. Deng, X. Ding, M. Wei, MoO_2-ordered mesoporous carbon nanocomposite as an anode material for lithium-ion batteries, ACS Appl. Mater. Interfaces 5 (2013) 2182-2187.

[472] H.-J. Zhang, J. Shu, K.-X. Wang, X.-T. Chen, Y.-M. Jiang, X. Wei, J.S. Chen, Lithiation mechanism of hierarchical porous MoO_2 nanotubes fabricated through one-step carbothermal reduction, J. Mater. Chem. A 2 (2014) 80-86.

[473] Y.G. Liang, S.J. Yang, Z.H. Yi, J.T. Sun, Y.H. Zhou, Preparation, characterization and lithium-intercalation performance of different morphological molybdenum dioxide, Mater Chem. Phys. 93 (2005) 395-398.

[474] X. Zhang, X. Zeng, M. Yang, Y. Qi, Lithiated MoO_2 nanorods with greatly improved electrochemical performance for lithium ion batteries, Eur. J. Inorg. Chem. 2014 (2014) 352-356.

[475] B. Liu, X. Zhao, Y. Tian, D. Zhao, C. Hu, M. Cao, A simple reduction process to synthesize MoO_2/C composites with cage-like structure for high-performance lithium-ion batteries, Phys. Chem. Chem. Phys. 15 (2013) 8831-8837.

[476] Y. Liu, H. Zhang, P. Ouyang, Z. Li, One-pot hydrothermal synthesized MoO_2 with high reversible capacity for anode application in lithium ion battery, Electrochim. Acta 102 (2013) 429-435.

[477] Y.G. Liang, Z.H. Yi, S. Yang, L.Q. Zhou, J.T. Sun, Y.H. Zhou, Hydrothermal synthesis and lithium-intercalation properties of MoO_2 nano-particles with different morphologies, Solid State Ion. 177 (2006) 501-505.

[478] S. Hu, F. Yin, E. Uchaker, W. Chen, M. Zhang, J. Zhou, Y. Qi, G. Cao, Facile and green preparation for the formation of MoO_2-GO composites as anode material for lithium-ion batteries, J. Phys. Chem. C 118 (2014) 24890−24897.

[479] A. Andersson, S. Hansen, Ammoxidation of toluene over molybdenum oxides, Catal. Lett. 1 (1988) 377-383.

[480] J. Sloczynski, Kinetics and mechanism of molybdenum(VI) oxide reduction, J. Solid State Chem. 118 (1995) 84-92.

[481] Y. Chen, X. Di, C. Ma, C. Zhu, P. Gao, J. Li, C. Sun, Q. Ouyang, Graphene–MoO_2 hierarchical nanoarchitectures: in situ reduction synthesis and high rate cycling performance as lithium-ion battery anodes, RSC Adv. 3 (2013) 17659-17663.

[482] Q. Gao, L. Yang, X. Lu, J. Mao, Y. Zhang, Y. Wu, Y. Tang, Synthesis, characterization and lithium-storage performance of MoO_2/carbon hybrid nanowires, J. Mater. Chem. 20 (2010) 2807-2812.

[483] W. Cho, J.H. Song, J.H. Kim, Y.J. Kim, Electrochemical characteristics of nano-sized MoO_2/C composite anode materials for lithium-ion batteries, J. Appl. Electrochem. 42 (2012) 909-915.

[484] J.H. Song, H.J. Kang, K.J. Kim, Y.N. Jo, Y.J. Kim, Electrochemical characteristics of MoO_2 anode materials with various morphologies for LIB applications, ECS Meeting Abstr. MA2009-02 (2009) 479.

[485] H. Choi, S.P. Yoon, J.-J. Han, J. Kim, M.R. Othman, Continuous synthesis of molybdenum oxide microspheres by ultrasonic spray pyrolysis, J. Ind. Eng. Chem. 47 (2016) 254-259.

[486] D.-Y. Park, Y.-K. Sun, S.-T. Myung, Carbothermal synthesis of molybdenum(IV) oxide as a high rate anode for rechargeable lithium batteries, J. Power Sources 280 (2015) 1-4.

[487] Y. Zhu, S. Wang, Y. Zhong, R. Cai, L. Li, Z. Shao, Facile synthesis of a MoO_2–Mo_2C–C composite and its application as favorable anode material for lithium-ion batteries, J. Power Sources 307 (2016) 552-560.

[488] A. Manthiram, A. Dananjay, Y.T. Zhu, New route to reduced transition-metal, Chem. Mater. 6 (1994) 1601-1602.

[489] Y. Liu, Y. Qian, M. Zhang, Z. Chen, C. Wang, Preparation of nano-sized amorphous molybdenum dioxide by use of γ-ray radiation method, Mater. Res. Bull. 31 (1996) 1029-1033.

[490] L. Yang, L. Liu, Y. Zhu, X. Wang, Y. Wu, Preparation of carbon coated MoO_2 nanobelts and their high performance as anode materials for lithium ion batteries, J. Mater. Chem. 22 (2012) 13148-13152.

[491] B.K. Guo, X.P. Fang, B. Li, Y.F. Shi, C.Y. Ouyang, Y.S. Hu, Z.X. Wang, G.D. Stucky, L.Q. Chen, Synthesis and lithium storage mechanism of ultrafine MoO_2 nanorods, Chem. Mater. 24 (2012) 457-463.

[492] X.P. Fang, B.L. Guo, Y.F. Shi, B. Li, C.X. Hua, C.H. Yao, Y.C. Chang, Y.S. Hu, Z.X. Wang, G.D. Stucky, L.Q. Chen, Enhanced Li storage performance of ordered mesoporous MoO_2 via tungsten doping, Nanoscale 4 (2012) 1541-1544.

[493] L.C. Yang, Q.S. Gao, Y.H. Zhang, Y. Tang, Y.P. Wu, Tremella-like molybdenum dioxide consisting of nanosheets as an anode material for lithium ion battery, Electrochem. Commun. 10 (2008) 118-122.

[494] H. Zhang, L. Zeng, X. Wu, L. Lian, M. Wei, Synthesis of MoO_2 nanosheets by an ionic liquid route and its electrochemical properties, J. Alloys Compd. 580 (2013) 358-362.

[495] X. Zhao, H.-E. Wang, X. Chen, J. Cao, Y.Zhao, Z.G. Neale, W. Cai, J. Sui, G. Cao, Tubular MoO_2 organized by 2D assemblies for fast and durable alkali-ion storage, Energy Stor. Mater. 11 (2018) 161-169.

[496] Q. Hao, G. Cui, Y. Zhao, Z. Bakenov, Flower-like $MoSe_2$/MoO_2 composite with high capacity and long-term stability for lithium-ion battery, Nanomaterials (Basel) 9 (2019) 1256.

[497] X.L. Ji, S. Herle, Y.H. Rho, L.F. Nazar, Carbon/MoO_2 composite based on porous semi-graphitized nanorod assemblies from in situ reaction of tri-block polymer, Chem. Mater. 19 (2007) 374-383.

[498] Y. Sun, X. Hu, J.C. Yu, Q. Li, W. Luo, L. Yuan, W. Zhang, Y. Huang, Morphosynthesis of a hierarchical MoO_2 nanoarchitecture as a binder-free anode for lithium-ion batteries, Energy Environ. Sci. 4 (2011) 2870-2877.

[499] J.H. Ku, Y.S. Jung, K.T. Lee, C.H. Kim, S.M. Oh, Thermoelectrochemically activated MoO_2 powder electrode for lithium secondary batteries, J. Electrochem. Soc. 156 (2009) A688-A693.

[500] X. Zhang, X. Song, S. Gao, Y. Xu, X. Cheng, H. Zhao, L. Huo, Facile synthesis of yolk–shell MoO_2 microspheres with excellent electrochemical performance as a Li-ion battery anode, J. Mater. Chem. A 1 (2013) 6858-6864.

[501] Y. Sun, X. Hu, W. Luo, Y. Huang, Ultrafine MoO_2 nanoparticles embedded in a carbon matrix as a high-capacity and long-life anode for lithium-ion batteries, J. Mater. Chem. 22 (2012) 425−431.

[502] Z. Wang, J.S. Chen, T. Zhu, S. Madhavi, X.W. Lou, One-pot synthesis of uniform carbon-coated MoO_2 nanospheres for high-rate reversible lithium storage, Chem. Commun. 46 (2010) 6906-6908.

[503] W. Luo, X. Hu, Y. Sun, Y. Huang, Electrospinning of carbon-coated MoO_2 nanofibers with enhanced lithium-storage properties, Phys. Chem. Chem. Phys. 13 (2011) 16735-16740.

[504] L. Yang, L. Liu, Y. Zhu, X. Wang, Y. Wu, Preparation of carbon coated MoO_2 nanobelts and their high performance as anode materials for lithium ion batteries, J. Mater.

[505] Y. Zhou, I. Lee, C.W. Lee, H.S. Park, H. Son, S. Yoon, Ordered mesoporous carbon-MoO_2 nanocomposite as high performance anode material in lithium ion batteries, Bull. Korean Chem. Soc. 35 (2014) 257-260.

[506] S. Yoon, K.-N. Jung, C. S. Jin, K.-H. Shin, Synthesis of nitrided MoO_2 and its application as anode materials for lithium-ion batteries, J. Alloys Compd. 536 (2012) 179−183.

[507] J. Liu, S. Tang, Y. Lu, G. Cai, S. Liang, W. Wang, X. Chen, Synthesis of Mo_2N nanolayer coated MoO_2 hollow nanostructures as high-performance anode materials for lithium-ion batteries, Energy Environ. Sci. 6 (2013) 2691−2697.

[508] X. Liu, H. Xu, Y. Huang, X. Hu, Direct planting of ultrafine $MoO_{2+\delta}$ nanoparticles in carbon nanofibers by electrospinning: self-supported mats as binder-free and long-life anodes for lithium-ion batteries, Phys. Chem. Chem. Phys. 18 (2016) 19832-19837.

[509] M. Qing, Y. Meng, Y. Wang, X. Li, C. Zhou, Y. Liang, Z. Zhang, Q. Liu, Y. Guo, D. Xiao, Building nanoparticle-stacking MoO_2-CDs via in-situ carbon dots reduction as high-performance anode material for lithium ion and sodium ion batteries, Electrochim. Acta 319 (2019) 740-752.

[510] M. Ihsan, H. Wang, S.R. Majid, J. Yang, S.J. Kennedy, Z. Guo, H.K. Liu, MoO_2/Mo_2C/C spheres as anode materials for lithium ion batteries, Carbon 96 (2016) 1200-1207.

[511] H. Gao, C.-L. Liu, Y. Liu, Z.-H. Liu, W.-S. Dong, MoO_2-loaded porous carbon hollow spheres as anode materials for lithium-ion batteries, Mater. Chem. Phys. 147 (2014) 218-224.

[512] L.C. Yang, W. Sun, Z.W. Zhong, J.W. Liu, Q.S. Gao, R.Z. Hu, M. Zhu, Hierarchical MoO_2/N-doped carbon heteronanowires with high rate and improved long-term performance for lithium-ion batteries, J. Power Sources 306 (2016) 78-84.

[513] Z. Xu, H. Wang, Z. Li, A. Kohandehghan, J. Ding, J. Chen, K. Cui, D. Mitlin, Sulfur refines MoO_2 distribution enabling improved lithium ion battery performance, J. Phys. Chem. C 118 (2014) 18387–18396.

[514] Y. Wang, Z. Huang, Y. Wang, A new approach to synthesize MoO_2@C for lithium ion batteries, J. Mater. Chem. A 3 (2015) 21314–21320.

[515] X. Zhang, M. Gao, W. Wang, B. Liu, X. Li, Encapsulating MoO_2 nanocrystals into flexible carbon nanofibers via electrospinning for high-performance lithium storage, Polymers (Basel) 13 (2021) 22.

[516] Y. Liang, S. Yang, Z. Yi, X. Lei, J. Sun, Y. Zhou, Low temperature synthesis of a stable MoO_2 as suitable anode materials for lithium batteries, Mater. Sci. Eng. B 121 (2005) 152-155.

[517] J. Liu, S. Tang, Y. Lu, G. Cai, S. Liang, W. Wang, X. Chen, Synthesis of Mo_2N nanolayer coated MoO_2 hollow nanostructures as high-performance anode materials for lithium-ion batteries, Energy Environ. Sci. 6 (2013) 2691−2697.

[518] Z.X. Huang, Y. Wang, Y.G. Zhu, Y. Shi, J.I. Wong, H.Y. Yang, 3D graphene supported MoO_2 for high performance binder-free lithium ion battery, Nanoscale 6 (2014) 9839-9845.

[519] Y. Che, X.Y. Zhu, J.J. Li, J. Sun, Y.Y. Liu, C. Jin, C.H. Dong, Simple synthesis of MoO_2/carbon aerogel anodes for high performance lithium ion batteries from seaweed biomass, RSC Adv. 6 (2016) 106230-106236.

[520] Y.W. Wang, L. Yu, X.W. Lou, Formation of triple-shelled molybdenum–polydopamine hollow spheres and their conversion into MoO_2/carbon composite hollow spheres for lithium-ion batteries, Angew. Chem. Int. Ed. 55 (2016) 14668-14672.

[521] J.H. Ku, Y.S. Jung, K.T. Lee, C.H. Kim, S.M. Oh, Thermoelectrochemically activated MoO_2 powder electrode for lithium secondary batteries, J. Electrochem. Soc. 156 (2009) A688−A693.

[522] Y.Z. Lei, J.C. Hu, H.W. Liu, J.L. Li, Template-free synthesis of hollow core-shell MoO_2 microspheres with high lithium-Ion storage capacity, Mater. Lett. 68 (2012) 82−85.

[523] S. Yoon, A. Manthiram, Microwave-hydrothermal synthesis of $W_{0.4}Mo_{0.6}O_3$ and carbon-decorated WO_x-MoO_2 nanorod anodes for lithium ion batteries, J. Mater. Chem. 21 (2011) 4082−4085.

[524] Y. Xu, R. Yi, B. Yuan, X. Wu, M. Dunwell, Q. Lin, L.Fei, S. Deng, P. Andersen, D. Wang, H. Luo, High capacity MoO_2/graphite oxide composite anode for lithium-ion batteries, J. Phys. Chem. Lett. 3 (2012) 309−314.

[525] A. Bhaskar, M. Deepa, T.N. Rao, U.V. Varadaraju, Enhanced nanoscale conduction capability of a MoO_2/graphene composite for high performance anodes in lithium ion batteries, J. Power Sources 216 (2012) 169−178.

[526] K.H. Seng, G.D. Du, L. Li, Z.X. Chen, H.K. Liu, Z.P. Guo, Facile synthesis of graphene-molybdenum dioxide and its lithium storage properties, J. Mater. Chem. 22 (2012) 16072−16077.

[527] M. Faraji, A. Abedini, Fabrication of electrochemically interconnected MoO_3/GO/MWCNTs/graphite sheets for high performance all-solid-state symmetric supercapacitor, Int. J. Hydrogen Energy 44 (2019) 2741-2751.

[528] Q. Tang, Z. Shan, L. Wang, X. Qin, MoO_2-graphene nanocomposite as anode material for lithium-ion batteries, Electrochim. Acta 79 (2012) 148-153.

[529] R. Giardi, S. Porro, T. Topuria, L. Thompson, C.F. Pirri, H.-C. Kim, One-pot synthesis of graphene-molybdenum oxide hybrids and their application to supercapacitor electrodes, Appl. Mater. Today 1 (2015) 27-32.

[530] Y. Cui, Y. Pu, Y. Hao, W. Bao, Q. Zhuang, Synthesis and electronic/ionic transport properties of MoO_2/rGO anode for lithium ion batteries, J. Chin. Chem. Soc. 61 (2014) 1089-1092.

[531] J. Hwang, D. Yoon, B. Kweon, W. Chang, J. Kim, A simple, one-pot synthesis of molybdenum oxide-reduced graphene oxide composites in supercritical methanol and their electrochemical performance, RSC Adv. 6 (2016) 108298-108309.

[532] C. Liu, S. Luo, H. Huang, Y. Zhai, Z. Wang, Direct growth of MoO_2/reduced graphene oxide hollow sphere composites as advanced anode materials for potassium-ion batteries, ChemSusChem 12 (2019) 873-880.

[533] P. Lu, D. Xue, MoO_2/reduced graphene oxide composite electrode with improved cycling performance and high capacitance for supercapacitors, J. Nanoeng. Nanomanuf. 3 (2013) 73-78.

[534] M. Serrapede, M. Fontana, A. Gigot, M. Armandi, G. Biasotto, E. Tresso, P. Rivolo, A Facile and green synthesis of a MoO_2-reduced graphene oxide aerogel for energy storage devices, Materials (Basel) 13 (2020) 594.

[535] K. Palanisamy, Y. Kim, H. Kim, J.M. Kim, W.-S. Yoon, Self-assembled porous MoO_2/graphene microspheres towards high performance anodes for lithium ion batteries, J. Power Sources 275 (2015) 351-361.

[536] J. Huang, Z. Xu, L. Cao, Q. Zhang, H. Ouyang, J. Li, Tailoring MoO_2/graphene oxide nanostructures for stable, high-density sodium-ion battery anodes, Energy Technol. 3 (2015) 1108-1114.

[537] W. Tang, C.X. Peng, C.T. Nai, J. Su, Y.P. Liu, M.V. Reddy, M. Lin, K.P. Loh, Ultrahigh capacity due to multi-electron conversion reaction in reduced graphene oxide-wrapped MoO_2 porous nanobelts, Small 11 (2015) 2446-2453.

[538] P. Ju, Z. Zhu, X. Shao, S. Wang, C. Zhao, X. Qian, C. Zhao, 3D walnut-shaped TiO_2/RGO/MoO_2@Mo electrode exhibiting extraordinary supercapacitor performance, J. Mater. Chem. A 5 (2017) 18777-18785.

[539] Z. Xu, K. Yao, H. Fu, X. Shen, X. Duan, L. Cao, J. Huang, H. Wang, Constructing MoO_2 porous architectures using graphene oxide flexible supports for lithium io battery anodes, Global Challenges (2017) 1700050.

[540] S. Wang, B. Liu, G. Zhi, G. Xu, Q. Wang, J. Zhang, 2D layered mesoporous MoO_2/rGO composites for high performance anode materials in lithium-ion batteries, Micropor. Mesopor. Mater. 246 (2017) 14-23.

[541] X. Chen, R. Liu, L Zeng, X. Huang, Y. Fang, J. Liu, Y. Xu, Q. Chen, M. Wei, Q. Qian, Preparation of hierarchical MoO_2@RGO composite and its application for high rate performance lithium-ion batteries, Mater. Lett. 212 (2018) 198-201.

[542] F. Li, L. Li, W. Wang, J. Gao, A new facile approach to prepare reduced graphene oxide and MoO_2/reduced graphene oxide as electrode materials for oxygen reduction reactions, J. Colloid Interface Sci. 519 (2018) 194-202.

[543] M. Li, Y. Zhu, X. Ji, S. Cheng, Facile synthesis of MoO_2/Mo-GO with high initial columbic efficiency and enhanced lithiation ability, Mater. Lett. 254 (2019) 332-335.

[544] W. Devina, J. Hwang, J. Kim, Synthesis of MoO_2/Mo_2C/rGO composite in supercritical fluid and its enhanced cycling stability in Li-ion batteries, Chem. Eng. J. 345 (2018) 1-12.

[545] R. Zheng, Z. Tang, H. Wang, D. Sun, Y. Tang, Z. Xie, The fabrication of hierarchical MoO_2@MoS_2/rGO composite as high reversible anode material for lithium ion batteries, Electrochim. Acta 364 (2020) 136996.

[546] F. Xia, X. Hu, Y. Sun, W. Luo, Y. Huang, Layer-by-layer assembled MoO_2–graphene thin film as a high-capacity and binder-free anode for lithium-ion batteries, Nanoscale 4 (2012) 4707-4711.

[547] L. Guo, Y. Wang, Standing carbon-coated molybdenum dioxide nanosheets on graphene: morphology evolution and lithium ion storage properties, J. Mater. Chem. A 3 (2015) 4706− 4715.

[548] X. Wang, Y. Xiao, J. Wang, L. Sun, M. Cao, Facile fabrication of molybdenum dioxide/nitrogen-doped graphene hybrid as high performance anode material for lithium-ion batteries, J. Power Sources 274 (2015) 142−148.

[549] Y. Feng, H. Liu, One-dimensional architecture with reduced graphene oxide supporting ultrathin MoO_2 nanosheets as high performance anodes for lithium-ion batteries, Nanotechnology 30 (2019) 315602.

[550] Q. Yang, Q. Liang, J. Liu, S. Liang, S. Tang, P. Lu, Y. Lu, Ultrafine MoO_2 nanoparticles grown on graphene sheets as anode materials for lithium-ion batteries, Mater. Lett. 127 (2014) 32-35.

[551] L.E. Aleandri, R.E. McCarley, Hexagonal lithium molybdate, $LiMoO_2$: a close-packed layered structure with infinite molybdenum-molybdenum-bonded sheets, Inorg. Chem. 27 (1988) 1041-1044.

[552] J. Gopalakrishnan, V. Bhat, Oxidative extraction and ion-exchange of lithium in Li_2MoO_3: synthesis of $Li_{2-x}MoO_3$ ($0 < x \leq 2.0$) and H_2MoO_3, Mater. Res. Bull. 22 (1987) 769-774.

[553] S.J. Hibble, I.D. Fawcett, A.C. Hannon, Structure of two disordered molybdates $Li_2Mo^{IV}O_3$ and $Li_4Mo_3^{IV}O_8$, from total neutron scattering, Acta Cryst. B 53(1997) 604-612.

[554] J. Barker, M.Y. Saidi, J.L. Swoyer, Lithium insertion properties of the layered $LiMoO_2$ ($R\bar{3}m$) made by a novel carbothermal reduction method, Solid State Ion. 158 (2003) 261-267.

[555] K. Ben-Kamel, N. Amdouni, H. Groult, A. Mauger, K. Zaghib, C.M. Julien, Structural and electrochemical properties of $LiMoO_2$, J. Power Sources 202 (2012) 314-321.

[556] J. Barker, M.Y. Saidi, J.L. Swoyer, Synthesis and electrochemical insertion properties of the layered Li_xMoO_2 phases ($x = 0.74$, 0.85, and 1.00), Electrochem. Solid State Lett. 6 (2003) A252-A256.

[557] R.E. McCarley, K.H. Lii, P.A. Edwards, L.F. Brough, New extended clusters in ternary molybdenum oxides, J. Solid State Chem. 57 (1985) 17-24.

[558] S.J. Hibble, I.D. Fawcett, A.C. Hannon, The true structure and metal−metal-bonded framework of $LiMo^{III}O_2$ determined from total neutron scattering, Inorg. Chem. 36 (1997) 1749-1753.

[559] H.Y. He, D. Li, M.Q. Li, Electrochemical performance and reaction mechanism of the Li_2MoO_3 anode synthesized by ball milling and thermal reduction for lithium-ion batteries, Electrochim. Acta 224 (2017) 1–8.

[560] J. Ma, Y.N. Zhou, Y.R. Gao, X.Q. Yu, Q.Y. Kong, L. Gu, Z.X. Wang, X.Q. Yang, L.Q. Chen, Feasibility of using Li_2MoO_3 in constructing Li-rich high energy density cathode materials, Chem. Mater. 26 (2014) 3256–3262.

[561] E.C. Self, L.F. Zou, M.J. Zhang, R. Opfer, R.E. Ruther, G.M. Veith, B.H. Song, C.M. Wang, F. Wang, A. Huq, J. Nanda, Synthesis and electrochemical and structural investigations of oxidatively stable Li_2MoO_3 and xLi_2MoO_3 $(1-x)LiMO_2$ composite cathodes, Chem. Mater. 30 (2018) 5061–5068.

[562] J. Ma, R.Y. Gao, Z.X. Wang, L. Chen, Structural and electrochemical stability of Li-rich layer structured Li_2MoO_3 in air, J. Power Sources 258 (2014) 314–320.

[563] S. Kumakura, Y. Shirao, K. Kubota, S. Komaba Preparation and electrochemical properties of Li_2MoO_3/C composites for rechargeable Li-ion batteries, Phys. Chem. Chem. Phys. 18 (2016) 28556–28563.

[564] D. Li, H.Y. He, X.M. Wu, M.Q. Li, Electrochemical behavior of submicron Li_2MoO_3 as anodes in lithium-ion batteries, J Alloys Compd. 682 (2016) 759–765.

[565] G.-C. Mao, H.-T. Yu, C.-F. Guo, Y. Xie, T.-F. Yi, Li_2MoO_3 microspheres with excellent electrochemical performances as cathode material for lithium-ion battery, Ionics 26 (2020) 4401-4411.

[566] Z.Y. Yu, J.H. Hao, W.J. Li, H.X. Liu, Enhanced electrochemical performances of cobalt-doped Li_2MoO_3 cathode materials, Materials (Basel) 12 (2019) 843.

[567] Z.Y. Yu, T.L. Yu, W.J. Li, J.S. Hao, H.X. Liu, N. Sun, M.Y. Lu, J. Ma, Improved electrochemical performances of carbon-coated Li_2MoO_3 cathode materials for Li-ion batteries, Int. J. Electrochem. Sci. 13 (2018) 4504–4511.

[568] J.M. Tarascon, $Li_xMo_2O_4$: a new promising cathode material for secondary lithium cells, J. Electrochem. Soc. 134 (1987) 1345-1351.

[569] X. Liu, Y. Zhao, Nanotube Li_2MoO_4: a novel and high-capacity material as a lithium-ion battery anode, Nanoscale 6 (2014) 13660-13667.

[570] X. Liu, Y. Zhao, Y. Dong, Q. Fan, Q. Kuang, Z. Liang, X. Lin, W. Han, Q. Li, M. Wen, Synthesis of one-dimensional Li_2MoO_4 nanostructures and their electrochemical performance as anode materials for lithium-ion batteries, Electrochim. Acta 174 (2015) 315-326.

[571] S.W. Kim, D.H. Seo, X. Ma, G. Ceder, K. Kang, Electrode materials for rechargeable sodium-ion batteries: potential alternatives to current lithium ion batteries, Adv. Energy Mater. 2 (2012) 710-721.

[572] C. Delmas, Sodium and sodium-ion batteries: 50 Years of research, Adv. Energy Mater. 8 (2018) 1703137.

[573] Y.L. Bai, X.Y. Wu, Y.S. Liu, C. Ma, X. Wei, K.X. Wang, J.S. Chen, Dandelion-clockinspired preparation of core-shell TiO_2@MoS_2 composites for high performance sodium ion storage, J. Alloys Compd. 815 (2019) 152386.

[574] Z. Chen, T. Yang, H. Shi, T. Wang, M. Zhang, G. Cao, Single nozzle electrospinning synthesized MoO_2@C core shell nanofibers with high capacity and long-term stability for lithium-ion storage, Adv. Mater. Interfaces 4 (2017) 1600816.

[575] X. Xia, S. Deng, D. Xie, Y. Wang, S. Feng, J. Wu, J. Tu, Boosting sodium ion storage by anchoring MoO_2 on vertical graphene arrays, J. Mater. Chem. A 6 (2018) 15546-15552.

[576] S. Bao, S. Luo, S. Yan, Z. Wang, Q. Wang, J. Feng, Y. Wang, T. Yi, Nanosized MoO_2 spheres interspersed three-dimensional porous carbon composite as advanced anode for reversible sodium/potassium ion storage, Electrochim. Acta 307 (2019) 293-301.

[577] J. Jiang, W. Yang, H. Wang, Y. Zhao, J. Guo, J. Zhao, M. Beidaghi, L. Gao, Electrochemical performances of MoO_2/C nanocomposite for sodium ion storage: an insight into rate dependent charge/discharge mechanism, Electrochim. Acta 240 (2017) 379-387.

[578] L. Li, Z. Chen, H. Zhang, Z. Zhu, M. Zhang, The double effects of sulfur-doping on MoO_2/C nanofibers with high properties for Na-ion batteries, Appl. Surf. Sci. 455 (2018) 343-348.

[579] C. Cui, Q. Wei, L. Zhou, L. Mai, J. Ma, Facile synthesis of MoO_2@C nanoflowers as anode materials for sodium-ion batteries, Mater. Res. Bull. 94 (2017) 122-126.

[580] H. He, Y. Man, J. Yang, J. Xie, M. Xu, MoO_2 nanosheets embedded in amorphous carbon matrix for sodium-ion batteries, Roy. Soc. Open. Sci. 4 (2017) 170892-170898.

[581] C. Zhao, C. Yu, M. Zhang, H. Huang, S. Li, X. Han, X. Sun, Ultrafine MoO_2-carbon microstructures enable ultralong-life power-type sodium ion storage by enhanced pseudocapacitance, Adv. Energy Mater. 7 (2017) 1602880-1602887.

[582] A. Valdez, J. Villarreal, L. Zuniga, M. Alcoutlabi, MoS_2 and MoO_2 loaded carbon microfibers as anode materials for lithium-ion and sodium-ion batteries, ECS Trans. 85 (2018) 357-368.

[583] W. Zhang, L. Xing, J. Chen, H. Zhou, S. Liang, W. Huang, W. Li, Improving the cyclic stability of MoO_2 anode for sodium ion batteries via film-forming electrolyte additive, J. Alloys Compd. 822 (2020) 153530.